Dissertation zur Erlangung des Doktorgrades

der Fakultät für Chemie und Pharmazie

der Ludwig-Maximilians-Universität München

Explorative Study of Group I and II Phosphidosilicates

Arthur Haffner

aus

Tscheljabinsk, Russland

2021

Erklärung

Diese Dissertation wurde im Sinne von §7 der Promotionsordnung vom 28. November 2011 von Herrn Prof. Dr. Dirk Johrendt betreut.

Eidesstattliche Versicherung

Diese Dissertation wurde eigenständig und ohne unerlaubte Hilfsmittel erarbeitet.

München, 14.04.2021

_____

Arthur Haffner

Dissertation eingereicht am: 14.04.2021

1. Gutachter: Prof. Dr. Dirk Johrendt

2. Gutachter: PD Dr. Constantin Hoch

Mündliche Prüfung am 08.06.2021

Danksagung

Als erstes möchte ich mich bei PD Dr. Constantin Hoch für die Übernahme des Zweitgutachtens bedanken. Vielen Dank Tino, dass du mit Erfolg versucht hast, mich mit deiner Betreuung meiner Bachelorarbeit in die anorganische Chemie einzuführen. Es hat sehr viel Spaß gemacht mit dir unterschiedliche Syntheseideen durchgespielt und diverse kristallographische Probleme diskutiert zu haben.

Ebenso gilt mein Dank Herrn Prof. Dr. Schnick, Herrn Prof. Dr. Hubert Huppertz, Herrn Prof. Dr. Stefan Schwarzer und Herrn Prof. Dr. Konstantin Karaghiosoff für ihr Interesse an meiner Forschung und für ihre Bereitschaft als Prüfer in meiner Prüfungskommission teil zu nehmen.

Den größten Anteil daran, dass mir das Arbeiten im Labor stets Freude bereitet hat, tragen alle aktuellen und ehemaligen Kollegen meines Arbeitskreises sowie der Arbeitskreise um Prof. Dr. Wolfgang Schnick und Prof. Dr. Bettina V. Lotsch. Vielen Dank Dr. Simon und Dr. Ursula Peschke für eure Unterstützung bei meinen ersten Gehversuchen in der Röntgendiffraktometrie sowie Dr. Juliane Stahl, Dr. Tobias Rackl und Bettina Rendenbach und für eure Einkristall-Pulverproben und für die stets aufmunternden Worte, die mich hier und da zum Weitermachen angestachelt haben. Auch euch Valentin Weippert und Jakob Blahusch danke ich für die zahlreichen aufmunternden Bild- und Videocollagen und natürlich auch dir, liebe Catrin Löhnert, dass du uns alle stets mit einem Lächeln aushältst und uns zur Ordnung ermahnst, sobald das Chaos auszubrechen droht. Es freut mich sehr, Martin Weidemann, dass du dich entschlossen hast, meine Arbeit in Zukunft weiterzuführen und ich bin jetzt schon gespannt auf deine Entdeckungen. Lasse dich von etwaigen Durststrecken nicht entmutigen, sondern halte die Augen offen und zwinge das Glück anzubeißen. Ebenso möchte ich mich bei Dr. Katalin Szendrei-Temesi, Dr. Alberto von Mankowski und Anna-Katharina Hatz für unsere Diskussions- und Messsessions bedanken, die oftmals bis tief in die Nacht oder auch am Wochenende stattgefunden haben. Natürlich sind nicht diejenigen vergessen, die einen großen Anteil für diese Arbeit geleistet haben. Ich danke euch Dr. Thomas Bräuniger, Christian Minke, Dr. Otto Zeman und Dr. Simon Kloß sowie meinen Praktikanten Marlo Schöneich und Lisa Seidl.

Lieber Dirk, dir möchte ich meinen besonderen Dank aussprechen! Du hast mich nicht nur durch meine Master-Prüfung begleitet und mich so vor dem Wechsel in die organische Chemie bewahrt, sondern mich auch herzlich in deine Gruppe aufgenommen. In der anschließenden Masterarbeit als auch in dieser Arbeit hast du mir jede Freiheit gelassen, sodass ich mich auf dem gesamten Periodensystem ohne jeglichen Leistungsdruck austoben durfte. Ohne dein Vertrauen in mich als Einkristall-Gerätebetreuer und dem einhergehenden uneingeschränkten Zugang zu diesem Herzstück unserer Forschung, wäre diese Arbeit in diesem Umfang nie möglich gewesen und die anorganische Chemie hätte nicht zu meinem Hobby werden können. Es war stets eine Freude dein Interesse bei den Vorstellungen meiner Teilergebnisse in unseren Seminaren und den anschließenden Diskussionen zu bemerken. Tausend Dank!

Der größte Dank gilt meiner Familie. Lieber Papa, liebe Mama, ich kann es nicht in Worte fassen wie dankbar ich euch dafür bin, dass ihr den Mut hattet mit zwei kleinen Kindern und nicht recht viel mehr als zwei Koffern ein neues Leben in einem fremden Land zu beginnen. Ihr habt eure Ängste und Sorgen mich nie spüren lassen, sodass ich eine wunderschöne und sorgenfreie Kindheit haben durfte. Vielen Dank für eure uneingeschränkte und stetige Unterstützung, vor allem während meiner schwierigen Zeit am Gymnasium. Außerdem konnte ich ohne euch meine Frau vor nun 13 Jahren nicht kennen lernen!

Liebe Viki, du bist das Beste das mir in meinem Leben passieren konnte! Du standst immer an meiner Seite und ich konnte mich jederzeit auf dich verlassen. Egal wie anstrengend und lange meine Arbeitstage waren oder wie sehr die Chemie mich auch frustrierte, du hast mich immer wieder aufgebaut und mir ein Lächeln ins Gesicht gezaubert. Du bist immer da und das ist ein unglaublich schönes Gefühl! Ich danke dir von ganzem Herzen für 13 wunder- und liebevolle gemeinsame Jahre und freue mich auf weitere 70 Jahre mit dir an meiner Seite. Was für Überraschungen wohl die Zukunft für uns bereithält? Ach ja, du kannst auch unglaublich gut kochen (wollte der Panna so haben)!

“It is only because we accept the risk of error we can reap new discoveries.”

Rene Thom

Table of Contents

1 Introduction

One of the most important discoveries in the field of inorganic chemistry dates back to the years of 1864 and 1869 with the quest for an organizing principle of the chemical elements by Lothar Meyer and, especially, Dimitri I. Mendelejew – the periodic table of elements.[1,2] In the first prototype of the table, the elements were listed according to their ascending atomic weight and their chemical behavior. A simple but at the same time astonishing accomplishment since the atomic structure composed of protons, neutrons and electrons was still unknown. Additionally, Mendelejew himself showed the impact of this elemental arrangement by correctly predicting the unknown elements Sc, Ga, Ge and Tc, for example, or by exposing wrongly determined atom weights for some elements.[3] Today, more than 150 years later, the original table has been barely modified and complemented to 118 entries and is now not only printed on the first page in almost every chemical school- and textbook but represents every chemist's vast playground.

In contrast to the chemical discipline of organic chemistry, which mainly deals with chemical substances based on the elements of hydrogen and carbon, the inorganic chemistry contemplates the interaction of all elements of the periodic system. However, in the daily routine work of a chemical inorganic laboratory, the research is limited to stable and therefore naturally occuring elements. By the exclusion of the unstable elements, which are radioactive or only producible by nuclear reactions or decays in particle accelerators or nuclear reactors, only 86 of the known 118 elements remain for research without special precautions. At the first glance, this rather small amount seems to be manageable but the combinatorial possibilities for element combinations increase dramatically with $n![k!(n\text{-}k)!]^{-1}$ where n and k represent the number of different elements and the components in a compound.[4] Assuming only binary chemical systems the formula gives 3655 elemental combination possibilities. While a ternary system also seems bearable with 102340 combinations, the amount for quaternary systems exceed far the number of two million. Keeping in mind that chemical compounds are elemental combinations with certain stoichiometric ratios, the formula above is to be multiplied with the factor $[I^k–(I\text{-}1)]$ where I represents the maximum number of one atom type contributing to a compound or, in other words, the

highest index of a chemical sum formula. If one estimates conservatively a maximal index value of 3, than there are around 2.5 million hypothetical compounds in the ternary and 170 million in the quaternary system. Obviously, this quantity is pure combinatorial and therefore overestimated for real structures or compounds since there is no information integrated about the chemical reactivity or the plausibility of generated chemical formulas. Even though a plurality of these hypothetical substances are not existent, the discovery of the remaining existing compounds will last over the next decades or centuries with conventional methods. This implies that improved key substances for today's issues or problems may be available only in the future, most likely by a serendipitous discovery. Therefore, the prediction of desired compounds with specific properties is desirable and circumvents the difficulty of the uncountable amount of hypothetical compounds to be synthesized and investigated. Several ideas have already been described based on computational methods and combinatorial synthesis with high-throughput characterization, which may offer the screening of previously unknown and known thousands of compounds in a shorter time compared to conventional experiments.[4-17] Due to the lacking of computing resources in the past this access to new materials is still in its beginning, but some achievements have already been made demonstrated by predicting and successfully synthesizing unknown compounds for renewable energy applications, magnetic or multiferroic substances.[18-22] Contrary to the prediction of Moore's law the computing power will not be rising significantly in the next years and decades and therefore theoretical ideas and methods for structure prediction have to be improved further enabling faster processing of larger datasets.

In spite of this exciting prospective progress, the chemist's historically traditional explorative work will remain essential. Not only because the synthesis conditions have to be found for predicted substances but exotic structures leading to new phenomena or improved properties probably will stay undiscovered by calculations since they are based on libraries of known compounds and derived chemical or physical rules, thus reflecting only the current state of knowledge.[19,23,24] In that view, it is of high importance to look for new substances and structural families, with both educated chemical intuition and a little bit of naivety to enlarge the library of inorganic compounds.

However, new key substances are desired to be producible without particular efforts and composed of earth abundant and globally easy accessible elements providing large-scale production and application in different areas and devices. In this view, the most frequent and cheap elements forming our planet are oxygen and silicon with about 75 % by weight (excluding earth's core). Combining these two elements yields the structure class of silicates in which the silicon cation is coordinated tetrahedrally by

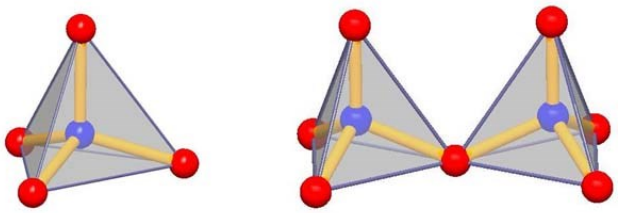

Figure 1.1 Predominant basic building block of silicates consisting of $[SiO_4]^{4-}$ tetrahedra (left), and the only condensation mode of common vertices observed in silicates (right). Silicon is shown in blue, oxygen in red and they depict structural sections of Zn_2SiO_4 and $Ca_2MgSi_2O_7$.[26,27]

four oxygen anions. The only condensation mode observed in this class is the condensation of two tetrahedra by one common oxide vertex, although the condensation by common edges was reported once for fibrous SiO_2, which was never reproduced and therefore is still elusive.[25] Given only these two possible structural motives for silicates it is astonishing that this substance class represents one of the most extensive family in inorganic chemistry with hundreds of representatives.[28] This structural plurality arises from the continuative vertex connection and the branching of the SiO_4 tetrahedra leading to the subclasses of chain- (ino-), ring- (cyclo-), sheet- (phyllo-) and framework- (tecto-) besides the ortho- (neso-) and pyrosilicates (sorosilicates) depicted in Figure 1.1. Due to their natural abundance and the relatively simple fabrication, they are broadly used in electronics, ceramics, optics, catalysis, cosmetics or food additives for instance.[28] While most of the oxidosilicates are naturally occurring, the related family of nitridosilicates does not exist in nature due to the high bond energy of elemental nitrogen (941 kJ/mol), its negative redox potential (-0.736 V)[29] and its positive electron affinity (+0.07 eV). Exceptions are Si_2N_2O and a few other transition metal nitrides found in meteorites or impact craters.[30-35] On this account, a systematic synthetic approach was required achieved by the application of nitride precursors in combination with high-pressure (up to 65 GPa) or high-temperature (well beyond 1000 °C) techniques.[36-39] Since the ionic radii of the oxide (1.26 Å) and nitride ions (1.32 Å) are almost identical and their electronegativity resemble each other with $\chi_P = 3.44$ and 3.04, respectively, to some extent a similar bonding situation and structural features as for oxosilicates, shown in Figure 1.1, are found in nitride containing analogues. But additionally, the condensation of two SiN_4 tetrahedra by common edges,[40] as described for the elusive modification of fibrous SiO_2,[25] can be found in multiple compounds. This originates most likely from the decreased electronegativity of nitrogen involving a less ionic bonding situation, which in turn decreases the charge of the silicon ions thus reducing their mutual

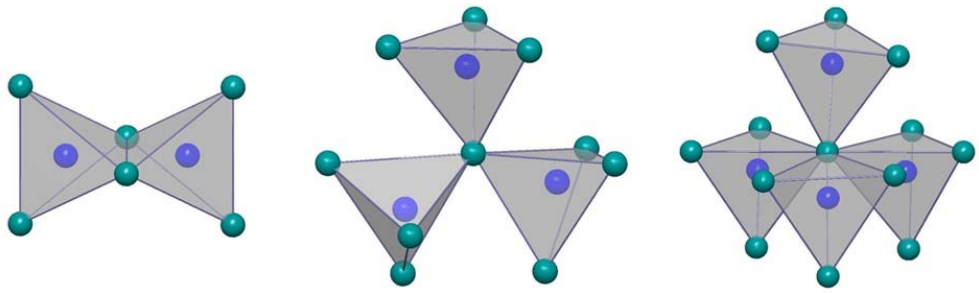

Figure 1.2 Additional structural features observed in nitridosilicates consisting in the condensation of SiN_4 tetrahedra by common edges (left), as well as triple (middle) and quadruple vertex condensation (right). Shown are structural sections of the crystal structures of $Ba_5Si_2N_6$,[40] $Ca_2Si_5N_8$ [41] and $BaYbSi_4N_7$[42] with silicon in blue and nitrogen in petrol.

Coulomb repulsion. Contrary to oxygen, the nitrogen's trivalent nature enables also the bridging of three to four SiN_4 tetrahedra by one common nitride vertex, shown in Figure 1.2.[41,42] Apparently, the structural degree of freedom is more than doubled with the substitution of oxygen by nitrogen and one would reasonably think of at least comparable known amounts of nitridosilicate materials. But in fact, they lag far behind the oxidosilicates probably due to the relatively new development of the demanding preparative methods and the high synthetic efforts. However, numerous compounds attracted immense interest because of their properties and they were discussed for high-temperature ceramics as well as for thermal and ion conductors.[43-45] Within a short time, they also became an inherent part in the application as luminescent materials in phosphor converting LEDs in the lighting industries.[36,46,47]

While nitrogen is the major constituent of the atmosphere, thus easy accessible, the second most abundant nonmetal element in earth's crust is phosphorus located in the same group of the periodic table. Although it is therefore isovalent to nitrogen, its chemical behavior is amphoteric and unique. Given the ubiquitous occurrence of oxygen, phosphorus can naturally be found almost only in oxidophosphates, that is in the oxidation state of +5,[48,49] reflecting its similarity to silicon with its potential of -1.445 V in the PO_4^{3-}/P system compared to -1.834 V for SiO_4^{4-}/Si,[29] as well as in the structural motives of nitridophosphates.[50] On the other hand, phosphorus exhibits an electron affinity of 0.746 eV[51] and a Pauling electronegativity of $\chi_P = 2.2$. This enables the formation of phosphides, which can be found in the recently discovered and extremely rare minerals of terrestrial[52-59] but mostly of meteoritic origin containing nickel and iron.[60-66] While molecular nitrogen exhibits a high bonding energy of 941 kJ/mol originating from its triple bond, it amounts approximately only one fifth in the case of phosphorus (205 kJ/mol) due to the formation of single bonds. For this tendency of homonuclear

single bonding, phosphorus is known to be the element with the greatest ability of self-bonding after carbon.[28] This can be exemplarily seen in the number of its allotropes (red (I-V), of which some are still unknown, white, black, violet, fibrous, and a few exotic representatives[67-70]) as well as in the amount of different phosphide anions in alkaline metal binaries, depicted in Figure 1.3.[71-90]

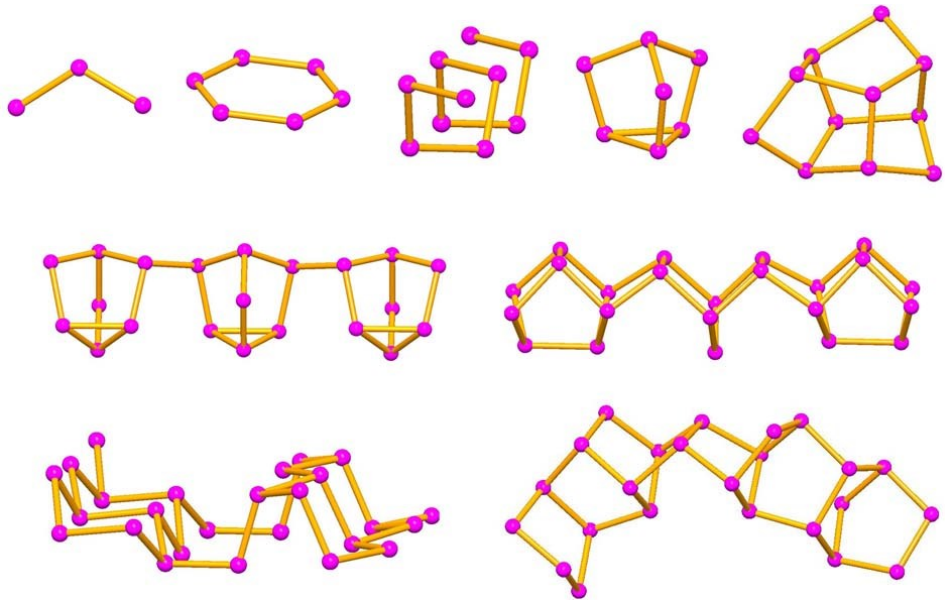

Figure 1.3 Different examples of phosphide anions in P_3^{4-},[73] P_6^{4-},[74-76] P^{1-},[77,78] P_7^{3-},[79-81] P_{11}^{3-},[82,83] P_7^{1-},[84] P_{15}^{1-},[85-87] P_5^{1-}[88,89] and P_7^{1-}[88,90] in reading order.

Thus, in analogy to the afore mentioned nitridosilicates the combination of silicon with phosphorus would lead to the isovalent class of phosphidosilicates providing all structural possibilities described before and shown in Figure 1.1 and Figure 1.2. In addition, regarding the distinct ability of homonuclear bonding one would assume the extension of the structural features in phosphidosilicates by bridging adjacent SiP_4 tetrahedra by P–P bonds, which are highly unlikely to be found in oxido- and nitridosilicates. Furthermore, phosphidosilicates are vastly distinct from their related compounds in terms of bonding situation. Silicon and phosphorus resemble each other noticeable in their adjacent position in the periodic table. The difference in their electronegativity amounts only 0.3 on the Pauling scale with χ_P (Si) = 1.9, thus causing a mainly covalent bonding. For this reason, homonuclear silicon bonding may probably occur more frequently in phosphidosilicates, in light of this only the reduced nitridosilicate $SrSi_6N_8$ is known with this peculiarity.[91] These two structural motives have been already found for example in $AlSiP_3$ and $Ca_3Si_8P_{14}$, shown in Figure 1.4.[92,93]

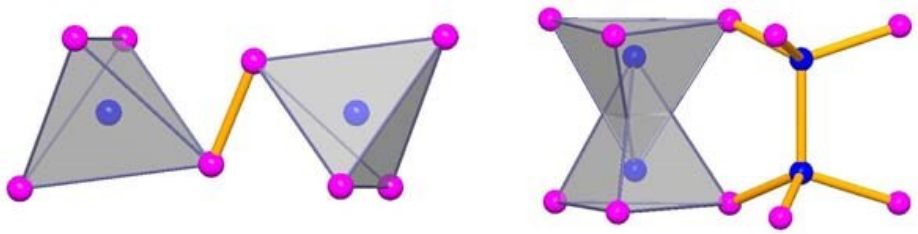

Figure 1.4 Special structural motifs observed in phosphidosilicates, namely homonuclear bonding of phosphorus (left) and silicon (right). Shown are structural sections of the crystal structures of $AlSiP_3$[92] and $Ca_3Si_8P_{14}$[93] with silicon in blue and phosphorus in pink.

This substance class complies with the previous considerations about the desire for new structures composed of abundant elements and their effortless fabrication since the production of a phophidosilicate should be feasible by simple solid-state reactions of elemental mixtures. Combining the multi-variant structural chemistry of phosphorus with silicon, its strong tendency in homonuclear bonding and the largely simple preparative methods one would expect an overwhelming structure class with hundreds of representatives comparable to the natural silicates.[94] In fact, at the beginning of this thesis only a handful of compounds were synthesized and subsequently investigated of which the most date back to the 1970's and 1980's. A compilation of all known materials in this system is visualized in the color-coded periodic system of elements in Figure 1.5 excepting only five quaternary compounds of $Na_3K_2SiP_3$,[95] $Na_4M_2SiP_4$ (M = Ca; Sr; Eu)[96] and $Ag_3Sn_2Si_3P_6$.[97] This figure shows clearly that in most ternary phosphidosilicate systems only one representative is known. On the other hand phosphidosilicates were discovered with alkaline and alkaline-earth cations and also with late transition metals but not with triels (excepting $AlSiP_3$[92]) suggesting the formation of thermodynamically very stable metal phosphide binaries mainly with NaCl, ZnS, NiAs or related type structures.[28,94]

Following the trend of semiconducting compounds in the decreasing band gap energy with increasing group number and the covalent nature of Si–P bonds,[114-116] all known phosphidosilicates (referred in Figure 1.5) are colored, ranging from bright reddish to black. Thus, phosphidosilicates are semiconductors with small band gap energies contrary to their related families of oxido- and nitridosilicates with wide band gaps leading to transparent substances. Obviously, this characteristic impedes the utilization of phosphidosilicates in lighting applications but offers an access to possible new thermoelectric substances since a high electronic but low thermal conductivity is needed.

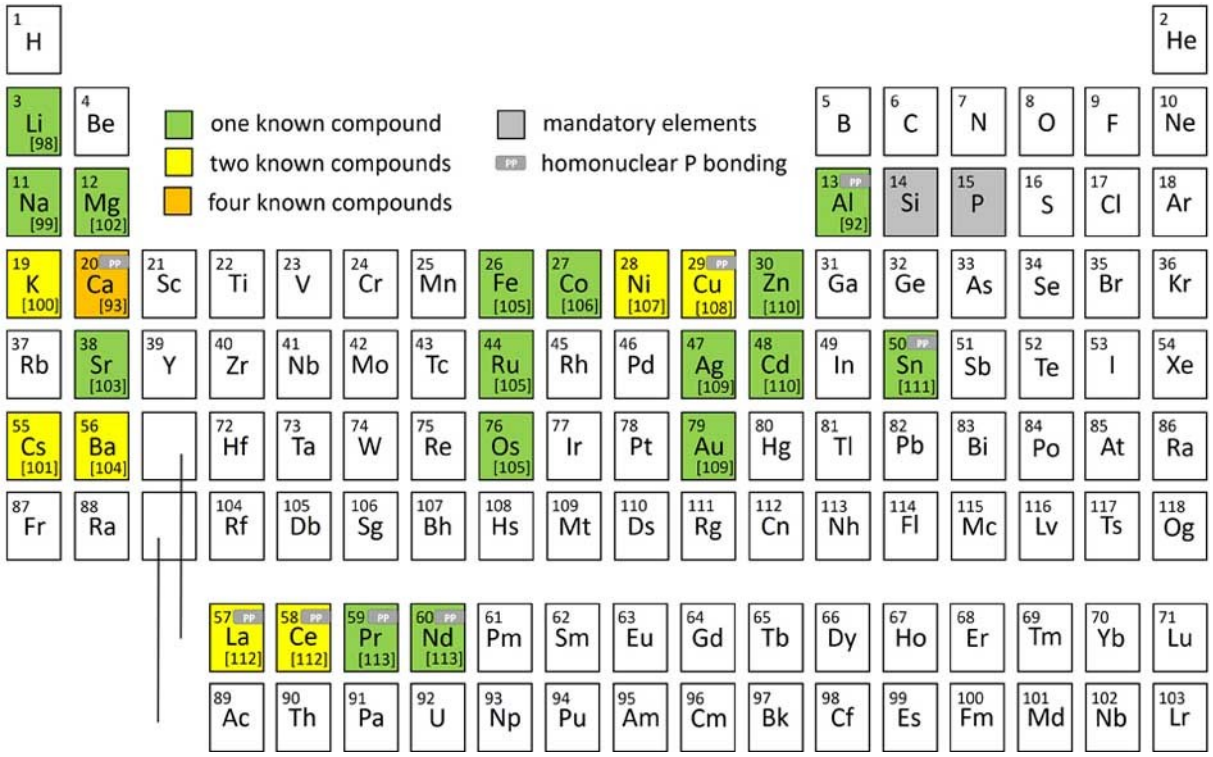

Figure 1.5 Color-coded periodic table of elements representing known ternary phosphidosilicates until the year of 2016. Element symbols shaded in green, yellow or orange typify one, two or four known ternary structures. The PP icon indicates at least one compound in this system with homonuclear phosphorus bonding.

While the first requirement is associated with a low band gap, the second premise is, by the rule of thumb, the scattering of phonons through the alternation of ionic and covalent bonding, disorder or nano-sized structural building blocks and architectures.[117-125] As the research on phosphidosilicates is still in its infancy, there are no examples of thermoelectrics yet, but recently the silicate $Ba_2Si_3P_6$ was reported to exhibit an ultralow thermal conductivity of 0.6 $Wm^{-1}K^{-1}$, originating from the mentioned alternating bonding situations of the Ba cations and the double chains of SiP_4 tetrahedra.[126] This value is comparable with the quaternary black and layered silicate $Li_{12.3}Ba_{4.35}Si_{33}P_{51}$ comprising fused defect T5 supertetrahedra (vide infra) with a similar thermal conductivity of 0.6-0.7 $Wm^{-1}K^{-1}$, representing nano-structural building units with an edge length of 1.8 nm.[127] These values are in the range of known thermoelectrics[118,128-135] and strongly emphasize further research in this field. Another and may be the most important potential application area to face the currently increasing demand of electrical energy and the ongoing human-made climate change, caused by combustion of fossil fuels, are rechargeable batteries. They can be used as storage media for mobile devices or to buffer natural fluctuations of regenerative power generation.[136,137] Batteries consist essentially of three components comprising the

cathode and anode separated by an ion-conducting electrolyte. While cathode materials have to be redox active to absorb the electrons and conducting metal ions by discharging, thus comprising metals with various possible oxidation states, the anode consists mostly of an intercalated or pure metal with a negative potential. Obviously, other electrode requirements are also crucial, for example the accessibility of the conducting ions into the electrodes or their chemical and structural stability.[138-142] For the electrolytes the most relevant property is the provision of exclusively ionic conductivity between the electrodes which would otherwise result in a short-circuit fault or self-discharge. While the currently used electrolytes are mostly based on alkali salts dissolved in aprotic solvents or polymers,[143,144] the all-solid-state batteries comprising a solid electrolyte are discussed to improve the energy densities and charging rates[145-147] and may allow the future utilization of metallic lithium anodes.[148,149] Thus, solid-state electrolytes require a rather rigid anionic framework with loosely bound cationic species and the ionic conductivity, which is strongly associated with the underlying crystal structure, is to be maximized for the utilization in all-solid-state batteries. Besides multiple strategies for this improvement an increase was observed – to some extent[150]– with a softening of the anionic structure, thus decreasing the attractive Coulomb interactions of the conducting ions, visible in chalkogenotetrelates and –pentelates.[151-165] Therefore one may expect a similar behavior for silicon and phosphorus containing structures. In that view, the investigation of this underrepresented compound family was revived with the discovery of the orthosilicate Li_8SiP_4 with a remarkably high ionic conductivity of $1.2 \cdot 10^{-4}$ S·cm^{-1} and an activation energy of 0.37 eV in 2016.[166] At the same time, Li_2SiP_2 and $LiSi_2P_3$ were found with estimated activation energies of 0.1 and 0.07 eV for the lithium ion conduction, respectively (see Chapter 2). Additionally, the SiP_4 anions in the phosphidosilicate family unexpectedly tend to cluster into large supertetrahedral entities, denominated in the Yaghi notation as T*n* where *n* represents the number of condensed tetrahedra along a supertetrahedral edge.[167] This results in large anionic structures with reduced charge density, which in turn dilutes the cations, thus yielding in numerous partially occupied sites favoring a facile ion movement through the structure. Within a few years, several new lithium phosphidosilicates were reported and the ion conductivity was raised to 10^{-3} S·cm^{-1} in $Li_{14}SiP_6$ suggesting a rapid growth of the research in the field of phosphidosilicates in future.[168,169]

This thesis addresses the research and characterization on hitherto unknown phosphidosilicate compounds with alkaline and alkaline-earth metals to find new structure motives or improved properties, which may tentatively contribute a mite facet to the solution of todays or tomorrows issues in future.

Chapter 2 of this thesis reports on the discovery and characterization of Li_2SiP_2 and $LiSi_2P_3$ showing a fast movement of lithium ions as indicated by small activation energies of 0.1 and 0.08 eV, respectively. Lithium ion batteries are discussed to be a valuable alternative for combustion engines in the transport industry and may be used as well in small electronic devices. But, in consideration of large-scale usage, the accessibility and extractability of lithium is to be considered.[170] Therefore, alternative systems should be sought for the replacement of lithium by sodium or potassium based solid-state batteries. In this view, Chapters 3, 4, and 5 deal with the discovery and the ionic conduction investigation of the heavier alkaline metal ions of sodium and potassium in the supertetrahedral solid electrolyte phosphidosilicates $Na_{23}Si_{9n+19}P_{12n+33}$ with n = 0-3, Na_2SiP_2 and T5-KSi_2P_3. In the following Chapters 6, 7, and 8, to date unknown structures with unprecedented structural motives of ternary phosphidosilicates with alkaline-earth cations are shown and some light is shed on the bonding situation in phosphidosilicates described above. Chapter 9 hints at the possibility to extend the number of constituting elements in phosphidosilicates to quaternary systems with the purpose to increase the ionic conduction by further sodium diluting with the incorporation of Ba^{2+} cations in $Na_{1.25}Ba_{0.875}Si_3P_5$ and $Na_{31}Ba_5Si_{52}P_{83}$. Further, this chapter shows once more the unpredictable ability of phosphidosilicates in the formation of supertetrahedral entities enabling fast ion migration.

References

[1] L. Meyer, *Die modernen Theorien der Chemie und ihre Bedeutung für die chemische Statik*, Maruschke & Berendt Verlag, **1864**, p. 137.

[2] D. Mendelejeff, *Z. Chem.* **1869**, *12*, 405.

[3] S. Shaik, E. Cremades, S. Alvarez, *Angew. Chem. Int. Ed.* **2019**, *58*, 13194.

[4] M. Jansen, *Angew. Chem. Int. Ed.* **2002**, *41*, 3746.

[5] A. Ludwig, *npj Comput. Mater.* **2019**, *5*, 70.

[6] O. A. von Lilienfeld, *Angew. Chem. Int. Ed.* **2018**, *57*, 4164.

[7] K. Alberi, M. B. Nardelli, A. Zakutayev, L. Mitas, S. Curtarolo, A. Jain, M. Fornari, N. Marzari, I. Takeuchi, M. L. Green, M. Kanatzidis, M. F. Toney, S. Butenko, B. Mereding, S. Lany, U. Kattner, A. Davydov, E. S. Toberer, V. Stevanovic, A. Walsh, N.-G. Park, A. Aspuru-Guzik, D.

P. Tabor, J. Nelson, J. Murphy, A. Setlur, J. Gregoire, H. Li, R. Xiao, A. Ludwig, L. W. Martin, A. M. Rappe, S.-H. Wei, J. Perkins, *J. Phys. D: Appl. Phys* **2019**, *52*,013001.

[8] H. Koinuma, I. Takeuchi, *Nat. Mater.* **2004**, *3*, 429.

[9] G. A. Landrum, H. Genin, *J. Solid State Chem.* **2003**, *176*, 587.

[10] P. Raccuglia, K. C. Elbert, P. D. F. Adler, C. Falk, M. B. Wenny, A. Mollo, M. Zeller, S. A. Friedler, J. Schrier, A. J. Norquist, *Nature* **2016**, *533*, 73.

[11] G. Hautier, C. C. Fischer, A. Jain, T. Mueller, G. Ceder, *Chem. Mater.* **2010**, *22*, 3762.

[12] A. K. Singh, J. H. Montoya, J. M. Gregoire, K. A. Persson, *Nat. Commun.* **2019**, *10*, 443.

[13] D. P. Tabor, L. M. Roch, S. K. Saikin, C. Kreisbeck, D. Sheberla, J. H. Montoya, S. Dwaraknath, M. Aykol, C. Ortiz, H. Tribukait, C. Amador-Bedolla, C. J. Barabec, B. Maruyama, K. A. Persson, A. Aspuru-Guzik, *Nat. Rev. Mater.* **2018**, *3*, 5.

[14] B. Meredig, A. Agrawal, S. Kirklin, J. E. Saal, J. W. Doak, A. Thompson, K. Zhang, A. Choudhary, C. Wolverton, *Phys. Rev. B* **2014**, *89*, 094104.

[15] A. Seko, H. Hayashi, K. Nakayama, A. Takahashi, I. Tanaka, *Phys. Rev. B* **2017**, *95*, 144110.

[16] K. T. Schütt, H. Glawe, F. Brockherde, A. Sanna, K. R. Müller, E. K. U. Gross, *Phys. Rev. B* **2014**, *89*, 205118.

[17] J. P. Janet, F. Liu, A. Nandy, C. Duan, T. Yang, S. Lin, H. J. Kulik, *Inorg. Chem.* **2019**, *58*, 10592.

[18] Y. Hinuma, T. Hatakeyama, Y. Kumagai, L. A. Burton, H. Sato, Y. Muraba, S. Iimura, H. Hiramatsu, I. Tanaka, H. Hosono, F. Oba, *Nat. Commun.* **2016**, *7*, 11962.

[19] A. Jain, Y. Shin, K. A. Persson, *Nat. Rev. Mater.* **2016**, *1*, 15004.

[20] G. Hautier, A. Jain, S. P. Ong, *J. Mater. Sic.* **2012**, *47*, 7317.

[21] L. Fu, C. L. Kane, *Phys. Rev. B* **2007**, *76*, 045302.

[22] M. König, S. Wiedemann, C. Brüne, A. Roth, H. Buhmann, L. W. Molenkamp, X.-L. Qi, S.-C. Zhang, *Science* **2007**, *318,* 766.

[23] J. R. Chamorro, T. M. McQueen, *Acc. Chem. Res.* **2018**, *51*, 2918.

[24] A. Zunger, *Nat. Rev. Chem.* **2018**, *2*, 0121.

[25] A. Weiss, A. Weiss, *Z. Anorg. Allg. Chem.* **1954**, *276*, 95.

[26] W. Schütz, *Z. Phys. Chem. B* **1936**, *31*, 292.

[27] D. E. Warren, *Z. Kristallogr.* **1930**, *74*, 131.

[28] A. F. Hollemann, E. Wiberg, N. Wiberg in *Lehrbuch der Anorganischen Chemie*, Vol. 102, Walter de Gruyter, Berlin, **2007**, p. 949.

[29] S. G. Bratsch, *J. Phys. Chem. Ref. Data* **1989**, *18*, 1.

[30] K. Keil, C. A. Andersen, *Nature* **1965**, *207*, 745.

[31] O. Silvestri, *Ann. Phys. Chem.* **1876**, *233*, 165.

[32] H. P. Nielsen, V. F. Buchwald, *Lunar Planet. Sci.* **1982**, *12*, 1343.

[33] H. J. Axon, J. Kinder, C. W. Haworth, J. W. Horsfield, *Mineral. Mag.* **1981**, *44*, 107.

[34] F. A. Brannister, Mineral. *Mag. J. Mineral. Soc.* **1941**, *26*, 36.

[35] W. H. Baur, *Nature* **1972**, *240*, 461.

[36] M. Zeuner, S. Pagano, W. Schnick, *Angew. Chem. Int. Ed.* **2011**, *50*, 7754.

[37] R. C. Liebermann, *High Pressure Research* **2011**, *31*, 493.

[38] H. Huppertz, *Z. Kristallogr.* **2004**, *219*, 330.

[39] T. Ishii, Z. Liu, T. Katsura, *Engineering* **2019**, *5*, 434.

[40] S. Pagano, S. Lupart, M. Zeuner, W. Schnick, *Angew. Chem. Int. Ed.* **2009**, *48*, 6335.

[41] T. Schlieper, W. Schnick, *Z. Anorg. Allg. Chem.* **1995**, *621*, 1037.

[42] H. Huppertz, W. Schnick, *Angew. Chem. Int. Ed.* **1996**, *35*, 1983.

[43] K. H. Jack, *J. Mater. Sci.* **1976**, *11*, 1135.

[44] H. Yamane, S. Kikkawa, M. Koizumi, *Solid State Ionics* **1987**, *25*, 183.

[45] H. Yamane, S. Kikkawa, M. Koizumi, *J. Power Sources* **1987**, *20*, 311.

[46] H. A. Höppe, *Angew. Chem. Int. Ed.* **2009**, *48*, 3572.

[47] R.-J. Xie, N. Hirosaki, *Sci. Technol. Adv. Mater.* **2007**, *8*, 588.

[48] S. N. Britvin, M. N. Murashko, Y. Vapnik, Y. S. Polekhovsky, S. V. Krivovichev, *Sci. Rep.* **2015**, *5*, 8335.

[49] A. G. Christy, *Eur. J. Mineral.* **2018**, *30*, 193.

[50] S. D. Kloß, W. Schnick, *Angew. Chem. Int. Ed.* **2019**, *58*, 7933.

[51] R. J. Peláez, C. Blondel, M. Vandevraye, C. Drag, C. Delsart, *J. Phys. B: At. Mol. Opt. Phys.* **2011**, *44*, 195009.

[52] S. N. Britvin, M. N. Murashko, Y. Vapnik, Y. S. Polekhovsky, S. V. Krivovichev, O. S. Vereshchagin, N. S. Vlasenko, V. V. Shilovskikh, A. N. Zaitsev, *Phys. Chem. Minerals* **2019**, *46*, 361.

[53] S. N. Britvin, M. N. Murashko, Y. Vapnik, Y. S. Polekhovsky, S. V. Krivovichev, O. S. Vereshchagin, V. V. Shilovskikh, N. S. Vlasenko, M. G. Krzhizhanovskaya, *Phys. Chem. Minerals* **2020**, *47*, 3.

[54] S. N. Britvin, M. N. Murashko, Y. Vapnik, Y. S. Polekhovsky, S. V. Krivovichev, O. S. Vereshchagin, V. V. Shilovskikh, M. G. Krzhizhanovskaya, *Am. Mineral.* **2020**, *105*, 422.

[55] S. N. Britvin, M. N. Murashko, Y. Vapnik, Y. S. Polekhovsky, S. V. Krivovichev, M. G. Krzhizhanovskaya, O. S. Vereshchagin, V. V. Shilovskikh, N. S. Vlasenko, *Am. Mineral.* **2020**, *105*, 428.

[56] S. N. Britvin, Y. Vapnik, Y. S. Polekhovsky, S. V. Krivovichev, M. G. Krzhizhanovskaya, L. A. Gorelova, O. S. Vereshchagin, V. V. Shilovskikh, A. N. Zaitsev, *Miner. Petrol.* **2019**, *113*, 237.

[57] R. Miyawaki, F. Hatret, M. Pasero, S. J. Mills, *Mineral. Mag.* **2019**, *83*, 887.

[58] R. Miyawaki, U. Halenius, F. Hatert, M. Pasero, S. J. Mills, *Eur. J. Mineral.* **2019**, *31*, 197.

[59] R. Miyawaki, F. Hatret, M. Pasero, S. J. Mills, *Mineral. Mag.* **2019**, *83*, 615.

[60] B. Cervelle, M. Gasperin, R. Jeanrot, A. Sandrea, *Bull. Soc. fr. Mineral. Cristallogr.* **1974**, *97*, 40.

[61] G. Pratesi, L. Bindi, V. Moggi-Cecchi, *Am. Mineral.* **2006**, *91*, 451.

[62] S. N. Britvin, N. S. Rudashevsky, S. V. Krivovichev, P. C. Burns, Y. S. Polekhovsky, *Am. Mineral.* **2002**, *87*, 1245.

[63] C. Ma, J. R. Beckett, G. R. Rossman, *Am. Mineral.* **2014**, *99*, 198.

[64] P. R. Buseck, *Science* **1969**, *165*, 169.

[65] A. V. Ivanov, M. E. Zolensky, A. Saito, K. Ohsumi, S. V. Yang, N. N. Kononkova, T. Mikouchi, *Am. Mineral.* **2000**, *85*, 1082.

[66] M. Fleischer, *Am. Mineral.* **1967**, *52*, 559.

[67] M. E. Schlesinger, *Chem. Rev.* **2002**, *102*, 4267.

[68] A. Pfitzner, M. F. Bräu, J. Zweck, G. Brunklaus, H. Eckert, *Angew. Chem. Int. Ed.* **2004**, *43*, 4228.

[69] J. Zhang, D. Zhao, D. Xiao, C. Ma, H. Du, X. Li, L. Zhang, J. Huang, H. Huang, C.-L. Jia, D. Tománek, C. Niu, *Angew. Chem. Int. Ed.* **2017**, *56*, 1850.

[70] J. L. Zhang, S. Zhao, C. Han, Z. Wang, S. Zhong, S. Sun, R. Guo, X. Zhou, C. D. Gu, K. D. Yuan, Z. Li, W. Chen, *Nano Lett.* **2016**, *16*, 4903.

[71] G. Brauer, E. Zintl, *Z. Phys. Chem. B* **1937**, *37*, 323.

[72] G. Gnutzmann, F. W. Dorn, W. Klemm, *Z. Anorg. Allg. Chem.* **1961**, *309*, 210.

[73] H. G. von Schnering, M. Hartweg, U. Hartweg, W. Hönle, *Angew. Chem.* **1989**, *101*, 98.

[74] H. P. Abicht, W. Hönle, H. G. von Schnering, *Z. Anorg. Allg. Chem.* **1984**, *519*, 7.

[75] W. Schmettow, A. Lipka, H. G. von Schnering, *Angew. Chem.* **1974**, *86*, 379.

[76] H. G. von Schnering, T. Meyer, W. Hönle, W. Schmettow, U. Hinze, W. Bauhofer, G. Kliche, *Z. Anorg. Allg. Chem.* **1987**, *553*, 261.

[77] K. Langer, R. Juza, *Naturwissenschaften* **1967**, *54*, 225.

[78] H. G. von Schnering, W. Hönle, *Z. Anorg. Allg. Chem.* **1979**, *456*, 194.

[79] V. Manriquez, W. Hönle, H. G. von Schnering, *Z. Anorg. Allg. Chem.* **1986**, *539*, 95.

[80] W. Hönle, T. Meyer, C. Mensing, H. G. von Schnering, *Z. Kristalllogr.* **1985**, *170*, 78.

[81] T. Meyer, W. Hönle, H. G. von Schnering, *Z. Anorg. Allg. Chem.* **1987**, *552*, 69.

[82] W. Wichelaus, H. G. von Schnering, *Naturwissenschaften* **1973**, *60*, 104.

[83] H. G. von Schnering, M. Somer, G. Kliche, W. Hönle, T. Meyer, J. Wolf, L. Ohse, P. B. Kempa, *Z. Anorg. Allg. Chem.* **1991**, *601*, 13.

[84] H. G. von Schnering, *Angew. Chem.* **1981**, *93*, 44.

[85] N. Eckstein, L. A. Jantke, T. F. Fässler, J. Mink, M. Drees, T. Nilges, *Eur. J. Inorg. Chem.* **2014**, *5135*.

[86] H. G. von Schnering, H. G. Schmidt, *Angew. Chem.* **1967**, *79*, 323.

[87] D. J. Olego, *Phys. Rev. B: Condens. Matter Mater. Phys.* **1985**, *31*, 2230.

[88] H. G. von Schnering, W. Wichelaus, *Naturwissenschaften* **1972**, *59*, 78.

[89] X. Chen, S. Yamanaka, *J. Alloys. Compd.* **2004**, *370*, 110.

[90] C. Grotz, M. Köpf, M. Baumgartner, L. A. Jantke, G. Raudaschl-Sieber, T. F. Fässler, T. Nilges, *Z. Anorg. Allg. Chem.* **2015**, *641*, 1395.

[91] F. Stadler, O. Oeckler, J. Senker, H. A. Höppe, P. Kroll, W. Schnick, *Angew. Chem. Int. Ed.* **2005,** *44*, 567.

[92] H. G. von Schnering, G. Menge, *J. Solid State Chem.* **1979**, *28*, 13.

[93] X. Zhang, T. Yu, C. Li, S. Wang, X. Tao, *Z. Anorg. Allg. Chem.* **2015**, *641*, 1545.

[94] U. Müller in *Anorganische Strukturchemie*, Vol. 6, Vieweg+Teubner, Wiesbaden, **2008**, p. 200.

[95] B. Eisenmann, J. Klein, M. Somer, *Z. Kristallogr.* **1991**, *197*, 275.

[96] J. Nuss, H. Kalpen, W. Hönle, M. Hartweg, H. G. von Schnering, *Z. Anorg. Allg. Chem.* **1997**, *623*, 250.

[97] W. Hönle, H. G. von Schnering, *Abstr. 6th Int. Conf. Solid Compd. Transition Elem.* **1979**, 101.

[98] R. Juza, W. Schulz, *Z. Anorg. Allg. Chem.* **1954**, *275*, 65.

[99] B. Eisenmann, M. Somer, *Z. Naturforsch. B* **1985**, *40*, 886.

[100a] B. Eisenmann, M. Somer, *Z. Naturforsch. B* **1984**, *39*, 736.

[100b] K. Feng, L. Kang, W. Yin, W. Hao, Z. Lin, J. L. Yao, Y. Wu, *J. Solid State Chem.* **2013**, *205*, 129.

[101a] B. Eisenmann, J. Klein, M. Somer, *Angew. Chem.* **1990**, *102*, 92.

[101b] B. Eisenmann, J. Klein, *J. Less-Common Met.* **1991**, *175*, 109.

[102] R. Trykozko, N. A. Goryunova, *Inorg. Mater.* **1968**, *4*, 1826.

[103] B. Eisenmann, H. Jordan, H. Schäfer, *Mater. Res. Bull.* **1982**, *17*, 95.

[104] B. Eisenmann, H. Jordan, H. Schäfer, *Z. Naturforsch. B* **1984**, *39*, 864.

[105] C. Peyrier, H. Vincent, P. Chaudouet, B. Chenevier, R. Madar, *Mater. Res. Bull.* **1995**, *30*, 357.

[106] H. Vincent, J. Kreisel, C. Perrier, O. C. Pluchery, P. Chaudouet, R. Madar, F. Genet, G. Lucazeau, *J. Solid State Chem.* **1996**, *124*, 366.

[107a] J. Wallinda, W. Jeitschko, *J. Solid State Chem.* **1995**, *114*, 476.

[107b] O. N. Ilnitskaya, V. A. Bruskov, P. Y. Zavalii, Y. B. Kuz'ma, *Inorg. Mater.* **1991**, *27*, 1108.

[108a] P. Kaiser, W. Jeitschko, *Z. Anorg. Allg. Chem.* **1996**, *622*, 53.

[108b] Y. A. Mozharivskyi, O. Lang, H. F. Franzen, *Z. Anorg. Allg. Chem.* **2000**, *626*, 2153.

[109] P. Kaiser, W. Jeitschko, *Z. Naturforsch. B* **1997**, *52*, 462.

[110] A. A. Vaipolin, E. O. Osmanov, D. N. Tret'yakov, *Inorg. Mater.* **1967**, *3*, 231.

[111] J. Y. Pivan, R. Guérin, J. Padiou, M. Sergent, *J. Solid State Chem.* **1988**, *76*, 26.

[112] H. Hayakawa, T. Sekine, S. Ono, *J. Less-Common Met.* **1975**, *41*, 197.

[113] P. Kaiser, W. Jeitschko, *J. Solid State Chem.* **1996**, *124*, 346.

[114] H. Ibach, H. Lüth in *Festkörperphysik Einführung in die Grundlagen*, Vol. 7, Springer, Berlin, **2009**, p. 443.

[115] C.-Z. Ning, L. Dou, P. Yang, *Nat. Rev. Mater.* **2017**, *2*, 17070.

[116] R. Gross, A. Marx in *Festkörperphysik*, Vol. 1, Oldenbourg, München, **2012**, p. 481.

[117] K. F. Hsu, S. Loo, F. Guo, W. Chen, J. F. Dyck, C. Uher, T. Hogan, E. K. Polychroniadis, M. G. Kanatzidis, *Science* **2004**, *303*, 818.

[118] L.-D. Zhao, S.-H. Lo, Y. Zhang, H. Sun, G. Tan, C. Uher, C. Wolverton, V. P. Dravid, M. G. Kanatzidis, *Nature* **2014**, *508*, 373.

[119] K. Kurosaki, A. Kosuga, H. Muta, M. Uno, S. Yamanaka, *Appl. Phys. Lett.* **2005**, *87*, 061919.

[120] K. Biswas, J. He, I. D. Blum, C.-I. Wu, T. P. Hogan, D. N. Seidman, V. P. Dravid, M. G. Kanatzidis, *Nature* **2012**, *489*, 414.

[121] S. R. Brown, S. M. Kauzlarich, F. Gascoin, G. J. Snyder, *Chem. Mater.* **2006**, *18*, 1873.

[122] E. Hazan, N. Madar, M. Parag, V. Casian, O. Ben-Yehuda, Y. Gelbstein, *Adv. Electron. Mater.* **2015**, *1*, 1500228.

[123] L.-D. Zhao, V. P. Dravid, M. G. Kanatzidis, *Energy Environ. Sci.* **2014**, *7*, 251.

[124] Y. Gelbstein, J. Davidow, S. N. Girard, D. Y. Chung, M. G. Kanatzidis, *Adv. Energy Mater.* **2013**, *3*, 815.

[125] B. I. Ismail, W. H. Ahmed, *Recent Patents on Electrical Engineering* **2009**, *2*, 27.

[126] J. Mark, J. Wang, K. Wu, J. G. Lo, S. Lee, K. Kovnir, *J. Am. Chem. Soc.* **2019**, *141*, 11976.

[127] A. Haffner, M. Jakob, O. Oeckler, D. Johrendt, *unpublished results.*

[128] S. N. Girard, J. He, X. Zhou, D. Shoemaker, C. M. Jaworski, C. Uher, V. P. Dravid, J. P. Heremans, M. G. Kanatzidis, *J. Am. Chem. Soc.* **2011**, *133*, 16588.

[129] W. Liu, X. Tan, K. Yin, H. Liu, X. Tang, J. Shi, Q. Zhang, C. Uher, *Phys. Rev. Lett.* **2012**, *108*, 166601.

[130] A. Saramat, G. Svensson, A. E. C. Palmqvist, C. Stiewe, E. Mueller, D. Platzek, S. G. K. Williams, D. M. Rowe, J. D. Bryan, G. D. Stucky, *J. Appl. Phys.* **2006**, *99*, 023708.

[131] J. Jiang, H. Zhu, Y. Niu, Q. Zhu, S. Song, T. Zhou, C. Wang, Z. Ren, *J. Mater. Chem. A* **2020**, *8*, 4790.

[132] B. Owens-Baird, J. Wang, S. G. Wang, Y.-S. Chen, S. Lee, D. Donadio, K. Kovnir, *J. Amer. Chem. Soc.* **2020**, *142*, 2031.

[133] J. Wang, J. Voyles, S. Grzybowski, K. Kovnir, *J. Appl. Phys.* **2020**, *127*, 055104.

[134] D. C. Schmitt, N. Haldolaarachchige, Y. Xiong, D. P. Young, R. Jin, J. Y. Chan, *J. Am. Chem. Soc.* **2012**, *134*, 5965.

[135] J. Wang, K. Kovnir, *J. Am. Chem. Soc.* **2015**, *137*, 12474.

[136] M. Armand, J. M. Tarascon, *Nature* **2008**, *451*, 652.

[137] Z. Yang, J. Zhang, M. C. W. Kintner-Meyer, X. Lu, D. Choi, J. P. Lemmon, J. Liu, *Chem. Rev.* **2011**, *111*, 3577.

[138] N. Yabuuchi, K. Kubota, M. Dahbi, S. Komaba, *Chem. Rev.* **2014**, *114*, 11636.

[139] D. Kundu, E. Talaie, V. Duffort, L. F. Nazar, *Angew. Chem. Int. Ed.* **2015**, *54*, 3431.

[140] S.-W. Kim, D.-H. Seo, X. Ma, G. Ceder, K. Kang, *Adv. Energy Mater.* **2012**, *2*, 710.

[141] M. S. Islam, R. Dominico, C. Masquelier, C. Sirisopanaporn, R. A. Armstrong, P. G. Bruce, *J. Mater. Chem.* **2011**, *21*, 9811.

[142] W. Lee, S. Muhammad, C. Sergey, H. Lee, J. Yoon, Y.-M Kang, W.-S. Yoon, *Angew. Chem. Int. Ed.* **2020**, *59*, 2578.

[143] V. Palomares, M. Casas-Cabanas, E. Castillo-Martínez, M. H. Han, T. Rojo, *Energy Environ. Sci.* **2013**, *6*, 2312.

[144] H. Kim, J. Hong, K.-Y. Park, H. Kim, S.-W. Kim, K. Kang, *Chem. Rev.* **2014**, *114*, 11788.

[145] Y.-K. Sun, *ACS Energy Let.* **2020**, *5*, 3221.

[146] Y. Lee, S. Fujiki, C. Jung, N. Suzuki, N. Yashiro, R. Omoda, D.-S. Ko, T. Shiratsuchi, T. Sugimoto, S. Ryu, J. H. Ku, T. Watanabe, Y. Park, Y. Aihara, D. Im, I. T. Han, *Nat. Energy* **2020**, *5*, 299.

[147] J. C. Bachman, S. Muy, A. Grimaud, H.-H. Chang, N. Pour, S. F. Lux, O. Paschos, F. Maglia, S. Lupart, P. Lamp, L. Giordano, Y. Shao-Horn, *Chem. Rev.* **2016**, *116*, 140.

[148] K. B. Hatzell, X. C. Chen, C. L. Cobb, N. P. Dasgupta, M. B. Dixit, L. E. Marbella, M. T. McDowell, P. P. Mukherjee, A. Verma, V. Viswanathan, A. S. Westover, W. G. Zeier, *ACS Energy Lett.* **2020**, *5*, 922.

[149] H. Liu, X.-B. Cheng, J.-Q. Huang, H. Yuan, Y. Lu, C. Yan, G.-L. Zhu, R. Xu, C.-Z. Zhao, L.-P. Hou, C. He, S. Kaskel, Q. Zhang, *ACS Energy Lett.* **2020**, *5*, 833.

[150] M. A. Kraft, S. P. Culver, M. Calderon, F. Böcher, T. Krauskopf, A. Senyshyn, C. Dietrich, A. Zevalkink, J. Janek, W. G. Zeier, *J. Am. Chem. Soc.* **2017**, *139*, 10909.

[151] N. Kamaya, K. Homma, Y. Yamakawa, M. Hirayama, R. Kanno, M. Yonemura, T. Kamiyama, Y. Kato, S. Hama, K. Kawamoto, A. Mitsui, *Nature Mater.* **2011**, *10*, 682.

[152] P. Bron, S. Johansson, K. Zick, J. Schmedt auf der Günne, S. Dehnen, B. Roling, *J. Am. Chem. Soc.* **2013**, *135*, 15694.

[153] E. Rangasamy, Z. Liu, M. Gobet, K. Pilar, G. Sahu, W. Zhou, H. Wu, S. Greenbaum, C. Liang, *J. Am. Chem. Soc.* **2015**, *137*, 1384.

[154] H. Yamane, M. Shibata, Y. Shimane, T. Junke, Y. Seino, S. Adams, K. Minami, A. Hayashi, M. Tatsumisago, *Solid State Ionics* **2007**, *178*, 1163.

[155] Y. Inoue, K. Suzuki, N. Matsui, M. Hirayama, R. Kanno, *J. Solid State Chem.* **2017**, *246*, 334.

[156] Z. Xu, R. Chen, H. Zhu, *J. Mater. Chem. A* **2019**, *7*, 12645.

[157] F. Tsuji, N. Tanibata, A. Sakuda, A. Hayashi, M. Tatsumisago, *Chem. Lett.* **2018**, *47*, 13.

[158] M. Duchardt, U. Ruschewitz, S. Adams, S. Dehnen, B. Roling, *Angew. Chem. Int. Ed.* **2018**, *57*, 1351.

[159] A. Hayashi, K. Noi, A. Sakuda, M. Tatsumisago, *Nature Commun.* **2012**, *3*, 856.

[160] S. Takeuchi, K. Suzuki, M. Hirayama, R. Kanno, *J. Solid State Chem.* **2018**, *265*, 353.

[161] L. Zhang, D. Zhang, K. Yang, X. Yan, L. Wang, J. Mi, B. Xu, Y. Li, *Adv. Sci.* **2016**, *3*, 1600089.

[162] N. Wang, K. Yang, L. Zhang, X. Yan, L. Wang, B. Xu, *J. Mater. Sci.* **2018**, *53*, 1987.

[163] Z. Yu, S.-L. Shang, J.-H. Seo, D. Wang, X. Luo, Q. Huang, S. Chen, J. Lu, X. Li, Z.-K. Liu, D. Wang, *Adv. Mater.* **2017**, *29*, 1605561.

[164] A. Hayashi, N. Masuzawa, S. Yubuchi, F. Tsuji, C. Hotehama, A. Sakuda, M. Tatsumisago, *Nature Commun.* **2019**, *10*, 5266.

[165] S. Harm, A.-K. Hatz, C. Schneider, C. Hoefer, C. Hoch, B. V. Lotsch, *Front. Chem.* **2020**, *8*, 90.

[166] L. Toffoletti, H. Kirchhain, J. Landesfeind, W. Klein, L. van Wüllen, H. A. Gasteiger, T. F. Fässler, *Chem. Eur. J.* **2016**, *22*, 17635.

[167] H. Li, J. Kim, T. L. Groy, M. O'Keeffe, O. M. Yaghi, *J. Am. Chem. Soc.* **2001**, *123*, 4867.

[168] H. Eickhoff, L. Toffoletti, W. Klein, G. Raudaschl-Sieber, T. F. Fässler, *Inorg. Chem.* **2017**, *56*, 6688.

[169] S. Strangmüller, H. Eickhoff, D. Müller, W. Klein, G. Raudaschl-Sieber, H. Kirchhain, C. Sedlmeier, V. Baran, A. Senyshyn, V. L. Deringer, L. van Wüllen, H. A. Gasteiger, T. F. Fässler, *J. Am. Chem. Soc.* **2019**, *141*, 14200.

[170] H. Vikström, S. Davidsson, M. Höök, *Applied Energy* **2013**, *110*, 252.

2 Supertetrahedral Networks and Lithium-Ion Mobility in Li_2SiP_2 and $LiSi_2P_3$

Arthur Haffner, Thomas Bräuniger, and Dirk Johrendt

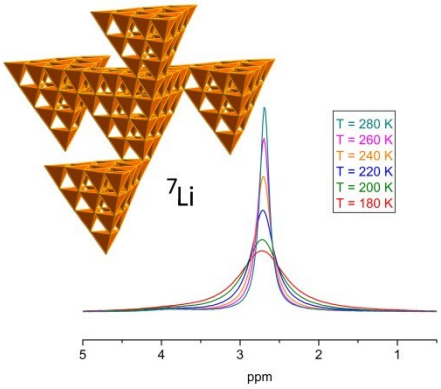

published in: *Angewandte Chemie International Edition* **2016**, *55*, 13585–13588.

2.1 Abstract

The new phosphidosilicates Li_2SiP_2 and $LiSi_2P_3$ were synthesized by heating the elements at 1123 K and characterized by single-crystal X-ray diffraction. Li_2SiP_2 ($I4_1/acd$, $Z = 32$, $a = 12.111(1)$ Å, $c = 18.658(2)$ Å) contains two interpenetrating diamond-like tetrahedral networks consisting of corner-sharing T2 supertetrahedra $[(SiP_{4/2})_4]$. Sphalerite-like interpenetrating networks of uniquely bridged T4 and T5 supertetrahedra make up the complex structure of $LiSi_2P_3$ ($I4_1/a$, $Z = 100$, $a = 18.4757(3)$ Å, $c = 35.0982(6)$ Å). The lithium ions are located in the open spaces between the supertetrahedra and coordinated by four to six phosphorus atoms. Temperature-dependent ^{7}Li solid-state MAS NMR spectroscopic data indicate high mobility of the Li^+ ions with low activation energies of 0.10 eV in Li_2SiP_2 and 0.07 eV in $LiSi_2P_3$.

2.2 Introduction

Phosphidosilicates contain SiP_4 tetrahedra that are connected via common vertices or edges to form insular entities, chains, layers, or complex three-dimensional networks. Some examples are isolated $[Si_2P_6]^{10-}$ anions in Na_5SiP_3,[1] infinite $^1_\infty[SiP_{4/2}]^{2-}$ chains in K_2SiP_2,[2] double layers of SiP_4 tetrahedra in KSi_2P_3,[3] and interpenetrating three-dimensional $[SiP_{4/2}]^{2-}$ networks in $MgSiP_2$.[4] Furthermore, several compounds such as $AlSiP_3$[5] or $Ca_3Si_8P_{14}$[6] are polyphosphides with short P-P bonds between neighboring tetrahedra, which distinguishes phosphidosilicates from structurally comparable oxido- and nitridosilicates where homonuclear bonds between oxygen or nitrogen atoms do not form. Phosphidosilicates with transition-[7-10] and rare-earth metals[11] are also known. $CdSiP_2$ and the germanate $ZnGeP_2$, with a tetragonal chalcopyrite-type structure, have attracted considerable interest as nonlinear optical materials.[12,13]

To the best of our knowledge, Li_5SiP_3, which was described by Juza et al. in 1954,[14] is the only lithium phosphidosilicate that has been reported thus far; its structure, however, has not been unambiguously assigned to date. Given the manifold structural chemistry of phosphidosilicates together with the immense interest in new materials with potential lithium ion conductivity, we have re-addressed the Li-Si-P system and came across the two new compounds Li_2SiP_2 and $LiSi_2P_3$ whose crystal structures are reported herein. ^{7}Li solid-state MAS NMR spectra serve as first indications for possible Li^+ mobility.

2.3 Results and Discussion

Li_2SiP_2 and $LiSi_2P_3$ were synthesized by heating stoichiometric mixtures of the elements in alumina crucibles sealed in silica tubes under purified argon atmosphere. Optimized heating procedures yielded dark red and black polycrystalline samples, respectively, which were sensitive to air. Small single crystals were selected for X-ray structure determination. The crystal structures were solved and refined using the tetragonal space groups $I4_1/acd$ (Li_2SiP_2) and $I4_1/a$ ($LiSi_2P_3$). Three lithium positions in Li_2SiP_2 are well defined while three of seven lithium positions in $LiSi_2P_3$ have large displacement parameters also when high-quality diffraction data collected at 100 K were used. Thus the uncertain lithium positions in $LiSi_2P_3$ may arise from possible Li mobility rather than from measurement artefacts. The crystallographic data of Li_2SiP_2 and $LiSi_2P_3$ are compiled in Table 2.1. Atomic parameters and displacement factors are given in the Supporting Information, Tables A1-A4.

Rietveld refinements of the powder X-ray patterns obtained by using the single-crystal data as starting parameters (Figure 2.1) confirm the structures and corroborate that bulk samples of both compounds are single phases without discernible impurities.

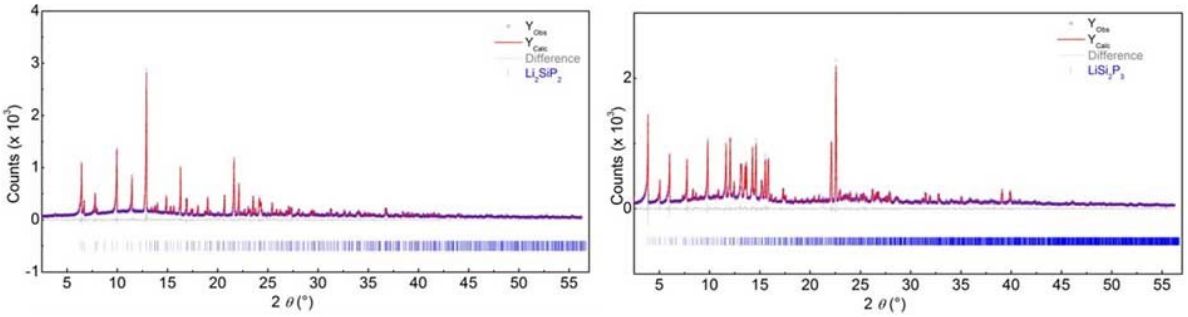

Figure 2.1 X-ray powder diffraction patterns (Y_{obs}), Rietveld fits (Y_{Calc}), and difference lines (gray) of Li_2SiP_2 (left) and $LiSi_2P_3$ (right).

Table 2.1 Crystallographic data of Li_2SiP_2 and $LiSi_2P_3$.

Formula	Li_2SiP_2	$LiSi_2P_3$
space group	$I4_1/acd$ (142)	$I4_1/a$ (88)
a / Å	12.111(1)	18.4658(6)
c / Å	18.658(2)	35.0924(12)
V_{cell} / Å^3	2736.6(5)	11966.0(9)
Z	32	100
$\rho_{X\text{-}ray}$ / g cm^{-1}	2.018	2.165
μ / mm^{-1}	1.33	1.55
θ-range / °	3.23 – 26.36	12.2 – 30.0
Reflections meas.	14645	168514
Independent refl.	704	8708
Parameters	48	340
$R\sigma$	0.026	0.018
R_{int}	0.073	0.049
R_1 ($F^2 > 2\sigma(F^2)$) / all	0.023 / 0.031	0.041 /0.056
wR_2 ($F^2 > 2\sigma(F^2)$) / all	0.042 / 0.044	0.098/ 0.104
GooF	1.111	1.036
$\Delta\rho_{min/max}$ / eÅ^{-3}	+0.29 / -0.31	+3.24 / -1.18

The SiP_4 tetrahedra (d_{Si-P} = 2.23 – 2.27 Å) in both structures are connected via common vertices to form supertetrahedral clusters (Figure 2.2). Li_2SiP_2 contains solely T2 supertetrahedra (4 SiP_4, hetero-adamantane), while the basic building block of $LiSi_2P_3$ is a double unit of T4 (20 SiP_4) and T5 (35 SiP_4) supertetrahedra sharing one common SiP_4 tetrahedron (Figure 2.2 right). The T2 units in Li_2SiP_2 share corners and form two three-dimensional interpenetrating diamond-like networks, which are a hierarchical variant of the NaTl structure.[15] Figure 2.3 shows the connectivity of the T2 centers of gravity in Li_2SiP_2. Decorating the nodes of these networks with vertex-sharing T2 supertetrahedra yields the interpenetrating six-membered rings depicted in Figure 2.3. The different colours were used to facilitate the discrimination of the otherwise identical networks. Interestingly, both networks are built up by one crystallographically independent silicon site, thus all SiP_4 as well as all T2 tetrahedra are related by symmetry. The nodes of both diamond-like networks, that is the centres of the T2 clusters are at the 8*a* site (0, ¼, 3/8) of the space group $I4_1/acd$ with the point symmetry $\bar{4}$. The supertetrahedra of the two diamond-like networks point in opposite directions. The lithium ions are located in between the supertetrahedral networks and coordinated by four or six phosphorous atoms.

With 600 atoms in the unit cell, the crystal structure of $LiSi_2P_3$ is more complex than that of Li_2SiP_2, but the structural principle is similar. The basic patterns again consist of two interpenetrating tetrahedral nets, where the nodes represent the centers of the supertetrahedra (Figure 2.4). The latter net now consists of alternating T4 and T5 clusters, thus each T4 corner is connected to four T5 corners and vice versa. Consequently, the underlying net is not derived from a diamond-type structure as in Li_2SiP_2, but analogous to a sphalerite-type (ZnS) structure.

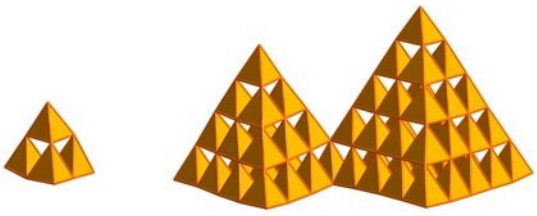

Figure 2.2 Supertetrahedral building units of Li_2SiP_2 (T2, left) and $LiSi_2P_3$ (T4 connected to T5 via one common SiP_4 tetrahedron, right).

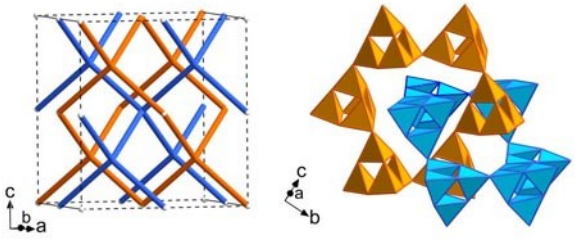

Figure 2.3 Crystal structure of Li_2SiP_2. Left: Topology of the two interpenetrating diamond-like networks. Right: Six-membered rings of T2-supertetraheda are located at each node of the network. Different colours were used to be able to distinguish between the two networks and do not indicate different types of T2 units

The nodes of the sphalerite network in the space group $I4_1/a$ are again at sites with $\bar{4}$ symmetry, namely at 4*a* (0, ¼, 1/8) and 4*b* (0, ¼, 5/8), which define the centres of the T4 and T5 supertetrahedra, respectively. Figure 2.4 shows the interpenetrating six-membered rings of alternating T4 and T5 units, always connected via one common SiP_4 tetrahedron. Like the T2 units in Li_2SiP_2, the T4 and T5 clusters of each sphalerite net in $LiSi_2P_3$ also point in opposite directions. The Li^+ ions in $LiSi_2P_3$ are distributed over the large voids between the T4 and T5 units and coordinated by four (Li1, Li5, Li7) or six (Li2, Li3, Li4) phosphorus atoms within 3.4 Å. One Li atom (Li6) has only three neighbours.

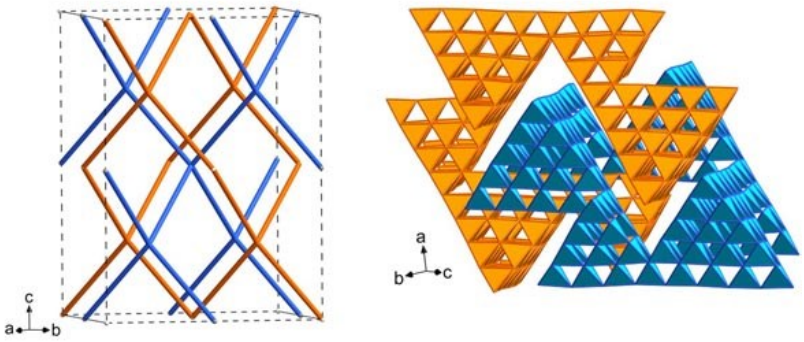

Figure 2.4 Crystal structure of $LiSi_2P_3$. Left: Topology of the two interpenetrating sphalerite-like networks. Right: Six-membered rings of alternating T4 and T5 supertetrahedra are located at each node of the network. Different colours were used to be able to distinguish between the two nets and do not indicate different types of T units.

Both phosphidosilicates crystallize in hitherto unknown structure types that are different from the known homologous nitridosilicates. Li_2SiN_2[16] consists of two interpenetrating networks of vertex-sharing T2 supertetrahedra (4 SiN_4) and is thus comparable to Li_2SiP_2, but has a different topology. The ^{7}Li MAS NMR spectrum of Li_2SiN_2 shows one resonance at 1.7 ppm with a full width at half maximum (FWHM) of 7.5 ppm. $LiSi_2N_3$ is isotypic to the oxidosilicate Li_2SiO_3,[17] which is a Wurtzite variant. Interpenetrating diamond-like nets of vertex-sharing T5 supertetrahedra were recently found in the nitridoaluminate $Ca_{18.75}Li_{10.5}[Al_{39}N_{55}]:Eu^{2+}$.[18] In general, supertetrahedral structures have thus far been more commonly observed in open-framework chalcogenides, predominantly with indium.[19,20] In the present phospidosilicates, the “pores” are filled with the second network.

In the ^{7}Li NMR spectra of the compounds (Figure 2.5), only a single resonance was observed at 2.0 and 2.7 ppm for Li_2SiP_2 and $LiSi_2P_3$, respectively. As three/seven lithium sites are present in the crystal structures, more resonances were expected. However, upon cooling, the single resonances broaden

considerably, which is a clear sign of an exchange process taking place. To obtain more detailed information on the ^{7}Li mobility, we also measured the spin-lattice relaxation times T_1, by applying the saturation recovery method and assuming monoexponential recovery (see Supporting Information for details). A logarithmic plot of the relaxation rates ($1/T_1$) versus the inverse temperature shows good linear correlations (Figure 2.5) as would be expected in the so-called low-temperature regime.[21,22] The slopes of the linear fits yield the activation energies for the ion motion, which were determined to be 0.07 eV for $LiSi_2P_3$, and 0.10 eV for Li_2SiP_2. The compound with the higher activation energy also shows a larger residual line width close to room temperature, as one would expect. These activation energies are comparatively low and consistent with very fast lithium motion. However, it is known that data extracted only from the low-temperature regime need to be treated with caution. In particular, a flattening may occur at the low temperature flank ("stretched exponential"), which would lower the activation energies extracted from that region[21,22]. For a full characterisation of the lithium mobility in $LiSi_2P_3$ and Li_2SiP_2, more comprehensive NMR studies are necessary (wider temperature windows and/or different magnetic fields), which is beyond the scope of the current work.

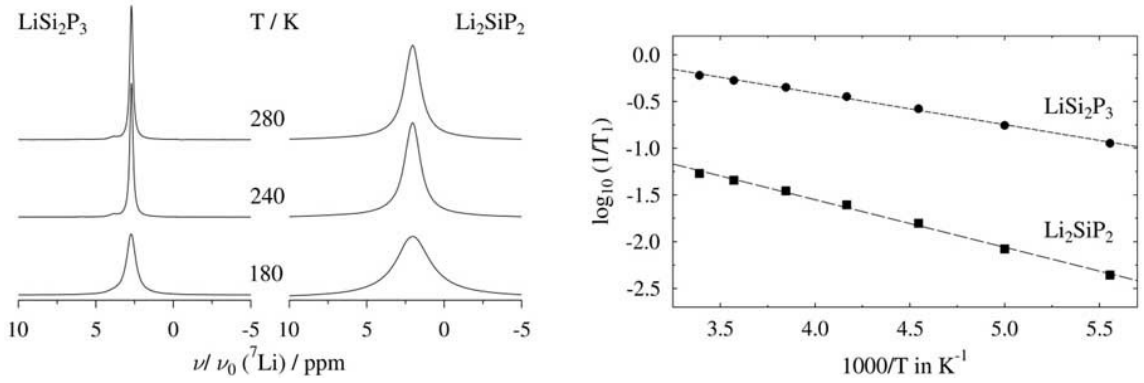

Figure 2.5 ^{7}Li NMR spectra of $LiSi_2P_3$ and Li_2SiP_2. Left: 10 kHz MAS spectra at the indicated temperatures. Right: Temperature dependence of the spin-lattice relaxation rates ($1/T_1$). The slopes of the linear fits allow for determination of the activation energies of the lithium mobility (see text for details).

2.4 Conclusion

In conclusion, we have found the new phosphidosilicates Li_2SiP_2 and $LiSi_2P_3$, which display unusual crystal structures that consist of interpenetrating networks of vertex-sharing T2, T4, and T5 supertetrahedra. The network topologies are based on the diamond-type structure in Li_2SiP_2 and a

sphalerite-type structure in $LiSi_2P_3$. The lithium ions are located in the open spaces between the large supertetrahedral clusters and mobile according to temperature-dependent ^{7}Li solid-state MAS NMR spectroscopy. The low activation energies of 0.10 eV (Li_2SiP_2) and 0.07 eV ($LiSi_2P_3$) are consistent with very fast lithium motion.

2.5 Experimental Section

Li_2SiP_2 and $LiSi_2P_3$ were obtained by heating Li metal (99.8 %, Alfa Aesar), Si powder (99.8 %, smart elements), and P (> 99%, chempur) in alumina crucibles welded in silica tubes under purified argon atmospheres. The optimized heating procedures

$$Li_2SiP_2: 295K \xrightarrow{20\ K/h} 473K \xrightarrow{50\ K/h} 933K \xrightarrow{200\ K/h} 1123K\,(20h) \xrightarrow{-10\ K/h} 450K \xrightarrow{fast} 295K$$

$$LiSi_2P_3: 295K \xrightarrow{20\ K/h} 473K \xrightarrow{50\ K/h} 933K \xrightarrow{100\ K/h} 1223K\,(20h) \xrightarrow{-10\ K/h} 450K \xrightarrow{fast} 295K$$

yielded dark read polycrystalline and air-sensitive samples. X-ray powder patterns were obtained with a Stoe Stadi-P diffractometer (Mo-Kα1) equipped with a Stoe Mythen 1k detector and fitted using Topas.[23] Single-crystal data were collected using Bruker D8 Venture (Mo-Kα1, rotating anode, Photon-II CPAD detector) or Bruker D8 Quest (Mo-Kα1 Photon-I detector) diffractometers. The crystal structures were solved and refined with the Jana[24] and Shelxl[25] packages. Further details on the crystal structure investigation may be obtained from the Fachinformationszentrum Karlsruhe, 76344 Eggenstein-Leopoldshafen, Germany, (email: crysdata@fiz-karlsruhe.de) on quoting the depository numbers CSD-431573 (Li_2SiP_2) and CSD-431584 ($LiSi_2P_3$). The ^{7}Li-NMR MAS spectra were recorded on a Bruker Avance-III 500 spectrometer at a Larmor frequency of $\nu_0(^7Li)$= 194.41 MHz, using a commercial 4 mm MAS probe.

2.6 References

[1] B. Eisenmann, M. Somer, *Z. Naturforsch. B* **1985**, *40*, 886.

[2] B. Eisenmann, M. Somer, *Z. Naturforsch. B* **1984**, *39*, 736.

[3] K. Feng, L. Kang, W. Yin, W. Hao, Z. Lin, J. Yao, Y. Wu, *J. Solid State Chem.* **2013**, *205*, 129.

[4] A. J. SpringThorpe, J. G. Harrison, *Nature* **1969**, *222*, 977.

[5] H. G. von Schnering, G. Menge, *J. Solid State Chem.* **1979**, *28*, 13.

[6] X. Zhang, T. Yu, C. Li, S. Wang, X. Tao, *Z. Anorg. Allg. Chem.* **2015**, *641*, 1545.

[7] J. Wallinda, W. Jeitschko, *J. Solid State Chem.* **1995**, *114*, 476.

[8] H. Vincent, J. Kreisel, C. Perrier, O. ChaixPluchery, P. Chaudouet, R. Madar, F. Genet, G. Lucazeau, *J. Solid State Chem.* **1996**, *124*, 366.

[9] P. Kaiser, W. Jeitschko, *Z. Naturforsch. B* **1997**, *52*, 462.

[10] P. Kaiser, W. Jeitschko, *Z. Anorg. Allg. Chem.* **1996**, *622*, 53.

[11] P. Kaiser, W. Jeitschko, *J. Solid State Chem.* **1996**, *124*, 346.

[12] Z. W. Zhang, D. T. Reid, S. C. Kumar, M. Ebrahim-Zadeh, P. G. Schunemann, K. T. Zawilski, C. R. Howle, *Opt. Lett.* **2013**, *38*, 5110.

[13] B. Q. Yao, Y. J. Shen, X. M. Duan, T. Y. Dai, Y. L. Ju, Y. Z. Wang, *Opt. Lett.* **2014**, *39*, 6589.

[14] R. Juza, W. Schulz, *Z. Anorg. Allg. Chem.* **1954**, *275*, 65.

[15] M. O'Keeffe, M. Eddaoudi, H. Li, T. Reineke, O. M. Yaghi, *J. Solid State Chem.* **2000**, *152*, 3.

[16] S. Pagano, M. Zeuner, S. Hug, W. Schnick, *European Journal of Inorganic Chemistry* **2009**, *2009*, 1579.

[17] M. Orth, W. Schnick, *Z. Anorg. Allg. Chem.* **1999**, *625*, 1426.

[18] P. Wagatha, P. Pust, V. Weiler, A. S. Wochnik, P. J. Schmidt, C. Scheu, W. Schnick, *Chem. Mater.* **2016**, *28*, 1220.

[19] G. Férey, *Angew. Chem. Int. Ed.* **2003**, *42*, 2576.

[20] H. L. Li, A. Laine, M. O'Keeffe, O. M. Yaghi, *Science* **1999**, *283*, 1145.

[21] R. Böhmer, K. R. Jeffrey, M. Vogel, *Progress in Nuclear Magnetic Resonance Spectroscopy* **2007**, *50*, 87.

[22] A. Kuhn, M. Kunze, P. Sreeraj, H.-D. Wiemhöfer, V. Thangadurai, M. Wilkening, P. Heitjans, *Solid State Nuclear Magnetic Resonance* **2012**, *42*, 2.

[23] A. Coelho, *TOPAS-Academic, Version 4.1, Coelho Software*, Brisbane, **2007**.

[24] V. Petricek, M. Dusek, L. Palatinus, *Z. Kristallogr.* **2014**, *229*, 345.

[25] G. M. Sheldrick, *Acta Crystallogr., Sect. A: Found. Crystallogr.* **2008**, *A64*, 112.

3 Fast Sodium-Ion Conductivity in Supertetrahedral Phosphidosilicates

Arthur Haffner, Anna-Katharina Hatz, Igor Moudrakovski, Bettina V. Lotsch, and Dirk Johrendt

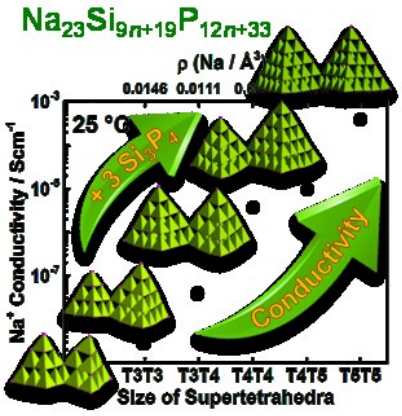

published in: *Angewandte Chemie International Edition* **2018**, *57*, 6155–6160.

3.1 Abstract

Fast sodium-ion conductors are key components of Na-based all-solid-state batteries which hold promise for large-scale storage of electrical power. We report the synthesis, crystal-structure determination, and Na^+-ion conductivities of six new Na-ion conductors, the phosphidosilicates $Na_{19}Si_{13}P_{25}$, $Na_{23}Si_{19}P_{33}$, $Na_{23}Si_{28}P_{45}$, $Na_{23}Si_{37}P_{57}$, *LT*-$NaSi_2P_3$ and *HT*-$NaSi_2P_3$, based entirely on earth-abundant elements. They have SiP_4 tetrahedra assembled interpenetrating networks of T3 to T5 supertetrahedral clusters and can be hierarchically assigned to sphalerite- or diamond-type structures. ^{23}Na solid-state NMR spectra and geometrical pathway analysis show Na^+-ion mobility between the supertetrahedral cluster networks. Electrochemical impedance spectroscopy shows Na^+-ion conductivities up to σ (Na^+) = $4 \cdot 10^{-4}$ Scm^{-1}. The conductivities increase with the size of the supertetrahedral clusters through dilution of Na^+-ions as the charge density of the anionic networks decreases.

3.2 Introduction

A supertetrahedron or supertetrahedral cluster is a segment of the sphalerite-type structure. The number of constituting tetrahedra in a T*n* supertetrahedron is $t_n = n(n+1)(n+2)/6$ where *n* is the number of tetrahedra along the cluster edges.[1] Crystal structures with supertetrahedra T*n* up to T5 have been found for example in indium-based chalcogenides, such as $Cd_4In_{16}S_{35}^{14-}$, $Cd_4In_{16}S_{33}^{10-}$ and $Cu_7In_{28}S_{53}^{15-}$, and were discussed as pathways to new open framework structures.[1-5] On the other hand, supertetrahedra are often connected via vertices and form rather dense interpenetrating networks. Examples are ZnI_2,[6] Li_2SiN_2 (T2),[7] $Na_6B_{10}S_{18}$ (T3),[8] and $Ca_{18.75}Li_{10.5}[Al_{39}N_{55}]:Eu^{2+}$ (T5).[9] These interpenetrating supertetrahedral networks do not exhibit large pores, but their topology enforces an inhomogeneous distribution of the cations by confining them into the spaces between the large clusters. This introduces limitations to the coordination of the cations, which may be weaker bonded in more irregular surroundings by the anions of the cluster surfaces. Thus, supertetrahedral anionic networks potentially favor the mobility of the cations and are therefore candidates for fast ion conductivity. The recently reported Li^+-ion mobility in the phosphidosilicates Li_2SiP_2[10] and $LiSi_2P_3$[11] with supertetrahedral networks based on SiP_4 entities supports this concept.

Because of the versatile structural chemistry of phosphidosilicates [12-17] and the immense interest in new, earth-abundant solid-state ionic conductors, we have now addressed sodium phosphidosilicates. Though sodium-based batteries [18,19] and solid-state Na^+ electrolytes are intensively investigated,[20-25] Na_5SiP_3[13] is the only hitherto known SiP based compound. In the system Na-Si-P we came across the six new compounds $Na_{19}Si_{13}P_{25}$, $Na_{23}Si_{19}P_{33}$, $Na_{23}Si_{28}P_{45}$, $Na_{23}Si_{37}P_{57}$ and *LT*-/*HT*-$NaSi_2P_3$ (low-temperature (*LT*) and high-temperature (*HT*) polymorphs), whose crystal structures are reported herein. ^{23}Na solid-state MAS NMR spectra, T_1-relaxometry and impedance spectroscopy were used to quantify the Na^+-ion conductivity, which increases with the supertetrahedral cluster size.

3.3 Results and Discussion

Table 3.1 summarizes the results of the X-ray crystal structure determinations. All compounds exhibit SiP_4 based supertetrahedral clusters. $Na_{19}Si_{13}P_{25}$ has two different motives (Figure 2.1): the first is a T3 supertetrahedron. The second contains two edge-sharing SiP_4 tetrahedra bridged by another vertex sharing SiP_4 tetrahedron with an additional P–P single bond (217.6 pm). Each T3 supertetrahedron shares three vertices with the Si_3P_8 unit. The fourth vertex of the T3 tetrahedron is connected via a single

Table 3.1 Crystallographic data of $Na_{19}Si_{13}P_{25}$, $Na_{23}Si_{19}P_{33}$, $Na_{23}Si_{28}P_{45}$, $Na_{23}Si_{37}P_{57}$, *LT*-$NaSi_2P_3$ and *HT*-$NaSi_2P_3$.

Formula	$Na_{19}Si_{13}P_{25}$	$Na_{23}Si_{19}P_{33}$	$Na_{23}Si_{28}P_{45}$	$Na_{23}Si_{37}P_{57}$	*LT*-$NaSi_2P_3$	*HT*-$NaSi_2P_3$
space group	$P\bar{1}$ (2)	$C2/c$ (15)	$P2_1/c$ (14)	$C2/c$ (15)	$I4_1/a$ (88)	$I4_1/acd$ (142)
a / Å	13.3550 (5)	28.4985 (10)	19.1630 (8)	34.1017 (18)	19.5431 (6)	20.8976 (13)
b / Å	15.3909 (5)	16.3175 (6)	23.4038 (11)	16.5140 (9)	19.5431 (6)	20.8976 (13)
c / Å	15.4609 (6)	13.8732 (5)	19.0220 (8)	19.5764 (11)	34.5317 (11)	40.081 (2)
α / °	118.0540 (10)	90	90	90	90	90
β / °	111.7050 (10)	102.3510 (10)	104.3020 (10)	111.528 (2)	90	90
γ / °	93.0540 (10)	90	90	90	90	90
V_{cell} / Å^3	2503.64 (16)	6302.1 (4)	8266.7 (6)	10255.5 (10)	13188.8 (9)	17504 (2)
Z	2	4	4	4	100	128
$\rho_{x\text{-}ray}$ / g cm^{-3}	2.091	2.197	2.177	2.159	2.167	2.090
μ / mm^{-1}	1.317	1.402	1.442	1.463	1.491	1.438
Θ-range / °	2.543–27.5	2.496–30.508	2.203–25.681	2.214–30.507	2.359–30.508	2.198–30.557
refl. measured	81805	100893	186348	120166	158298	257162
independent refl.	11484	9634	15704	15633	10080	6714
Parameters	517	343	880	557	378	251
R_σ	0.0228	0.0154	0.0616	0.0364	0.0273	0.0164
R_{int}	0.0362	0.0313	0.1119	0.0562	0.0610	0.0618
R_1 ($F^2 > 2\sigma(F^2)$) / all	0.0361 / 0.0455	0.0284 / 0.0349	0.0641 / 0.1188	0.0457 / 0.0762	0.0334 / 0.0586	0.0443 / 0.0618
wR_2 ($F^2 > 2\sigma(F^2)$) / all	0.0907 / 0.0943	0.0705 / 0.0741	0.1157 / 0.1345	0.1122 / 0.1279	0.0632 / 0.0708	0.1244 / 0.1387
GooF	1.042	1.063	1.022	1.035	1.013	1.171
$\Delta\rho_{max/min}$ / e Å^3	+1.755/-1.474	+1.816/-0.929	+2.826/-1.086	+2.105/-1.004	+0.953/-0.788	+1.597/-1.290

P–P bond (221.4 pm) to the Si_3P_8 unit, leading to a P_3-chain (Figure 3.1). The charge neutral formula is $(Na^{+1})_{19}(Si^{+4})_{13}(P^{-1})(P^{-2})_2(P^{-3})_{22}$. Condensation of the two motives forms a three-dimensional sphalerite-like network. The voids are interpenetrated with a second crystallographically independent but symmetrically equivalent network. Figure 3.1 shows the connectivity of the Si_3P_8 and T3 entities and emphasizes the interpenetration of the six-membered rings.

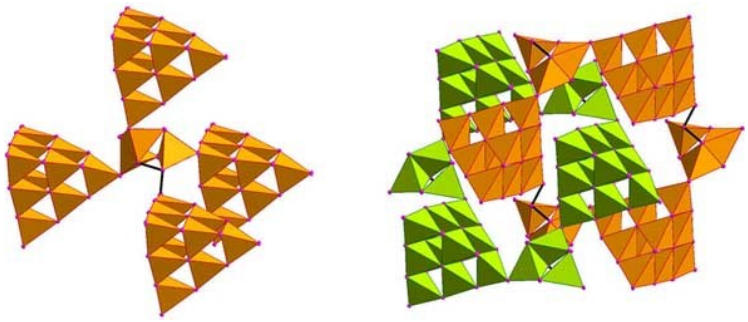

Figure 3.1 Crystal structure of $Na_{19}Si_{13}P_{25}$. Left. Connectivity of T3 and Si_3P_8 entities with two single P–P bonds (221.4 and 217.6 pm, black lines) leading to a P_3-chain. Right: Interpenetrating six-membered rings of alternating building units. See text for details.

$Na_{23}Si_{19}P_{33}$ contains solely T3 tetrahedra whereas in $Na_{23}Si_{37}P_{57}$ only T4 tetrahedra occur (Figure 3.2). Every T3 tetrahedron is connected to three T3 by common vertices and to a fourth T3 by sharing one SiP_4 tetrahedron. This anionic structure is isotypic to $Li_9B_{19}S_{33}$.[26] $Na_{23}Si_{37}P_{57}$ has this motif the other way round with T4 units: only one vertex linkage but three fusions occur, which means that two supertetrahedra share one common SiP_4 unit (Figure 3.2). $Na_{23}Si_{28}P_{45}$ contains T3 and T4 tetrahedra, whereby every T3 shares vertices to two other T3, one T4 and is fused with another T4 tetrahedra (Figure 3.3). Every T4 cluster is fused with two other T4, one T3 and vertex shared with one T3 entity (Figure 3.3). Four different six-membered supertetrahedral ring motives occur (Figure B10 in the Supporting Information), leading to six interpenetration modes (Figure 3.3, for details see Supporting Information). In contrast to the complex patterns of $Na_{23}Si_{28}P_{45}$ the crystal structures of *LT*-$NaSi_2P_3$ and *HT*-$NaSi_2P_3$ are relatively simple. In *LT*-$NaSi_2P_3$ every T4 cluster is coordinated tetrahedrally by four T5 tetrahedra and vice versa by sharing one SiP_4 unit (Figure 3.4). *HT*-$NaSi_2P_3$ contains solely T5 units tetrahedrally connected by four other T5 entities as depicted in Figure 3.4.

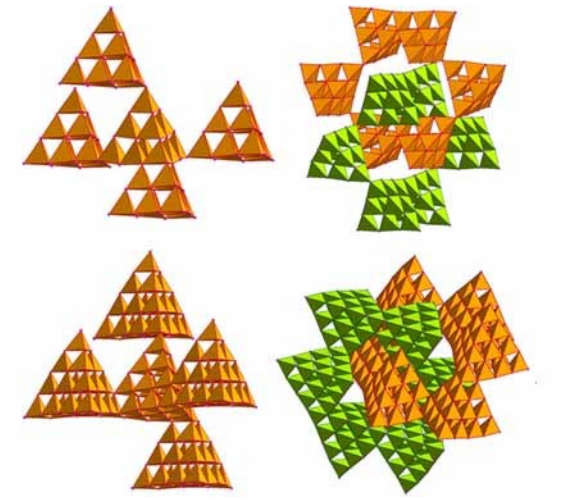

Figure 3.2 Crystal structures of $Na_{23}Si_{19}P_{33}$ (top) and $Na_{23}Si_{37}P_{57}$ (bottom). The connected T3 or T4 entities form interpenetrating networks of six-membered rings (right).

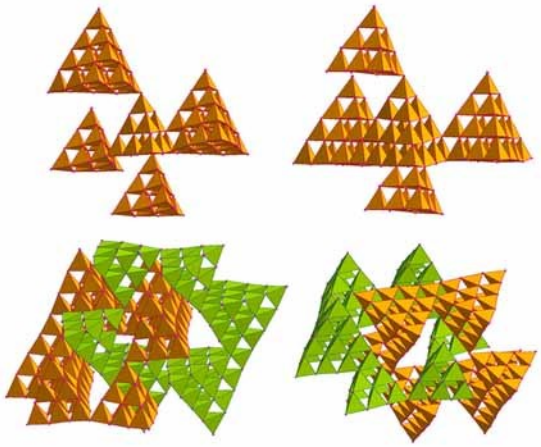

Figure 3.3 Crystal structure of $Na_{23}Si_{28}P_{45}$. Top: Connectivities of the T3 and T4 clusters. Bottom: Two out of six modes of interpenetrating six-membered rings of T3 and T4 supertetrahedra.

The resulting tetrahedral networks are interpenetrated by a second network (Figure 3.4, right). The T5 supertetrahedra in *LT*-$NaSi_2P_3$ and *HT*-$NaSi_2P_3$ lack one Si atom in their centers. This was already observed in other T5 compounds, namely $[In_{34}S_{54}]^{6-}$,[27] $LiSi_2P_3$[11] and *HP*-B_2S_3.[28] The infinite connection of SiP_4 supertetrahedra formally gives SiP with sphalerite-type structure. Assuming Si^{4+} and P^{3-} ions, SiP is not electroneutral and Si vacancies are required, leading to Si_3P_4, which is unknown. However, Si_3P_4 was investigated theoretically by DFT methods yielding a pseudo-cubic structure with similar lattice parameters (a = 502.7 pm and c = 499.8 pm) [29] as those derived from a T5 supertetrahedron (a = 494 to 534 pm). Therefore, the reason for the absence of one Si in the center of the T5 entities is the tendency to attain charge neutrality in the interior of the cluster.

The sodium ions are located between the supertetrahedral networks as shown in Figure 3.5 and exhibit irregular NaP_x polyhedra. The Na–P distances measure between 271.1 pm up to extremely elongated 398.0 pm. The extremely elongated ones may not be considered to the coordination. Octahedral and trigonal prismatic coordination predominates, while trigonal bipyramids and trigonal and quadratic pyramids also occur. Additionally, *HT*-$NaSi_2P_3$ contains higher coordinated Na^+-ions such as twofold capped trigonal prisms. Moreover, many Na^+-ions reveal large anisotropic thermal displacement ellipsoids (Figure 3.5) and relatively high residual electron densities in their vicinities. While all Na^+ sites are fully occupied in $Na_{19}Si_{13}P_{25}$ and $Na_{23}Si_{19}P_{33}$, some are partially occupied in the other compounds (Table 3.2, and Tables B1-B6). This deficiency is ascribed to the incorporation of Na^+-ions into the

increasing voids between the supertetrahedral anionic networks with constant charges (except $Na_{19}Si_{13}P_{25}$). These findings are typical for compounds that exhibit a high mobility of Na^+-ions and thus suggest a possible (high) sodium ion conductivity.[30]

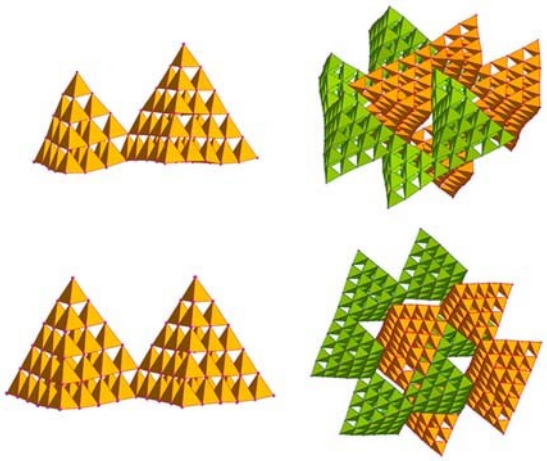

Figure 3.4 Crystal structures of *LT*-$NaSi_2P_3$ (top) and *HT*-$NaSi_2P_3$ (bottom). The connected T4/T5 or T5/T5 entities form interpenetrating networks of six-membered rings (right).

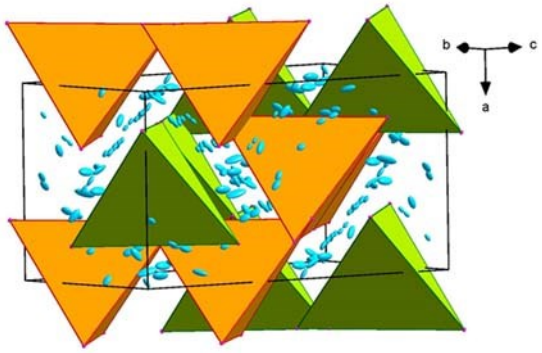

Figure 3.5 Unit cell of *HT*-$NaSi_2P_3$. Super-tetrahedral entities are depicted as enlarged single tetrahedra. Na^+ ions (blue) are located between the tetrahedral networks with increased anisotropic displacement ellipsoids..

Table 3.2 Average occupancies and sodium densities in $Na_{19}Si_{13}P_{25}$ (T3), $Na_{23}Si_{19}P_{33}$ (T3T3), $Na_{23}Si_{28}P_{45}$ (T3T4), $Na_{23}Si_{37}P_{57}$ (T4T4), *LT*-$NaSi_2P_3$ (T4T5) and *HT*-$NaSi_2P_3$ (T5T5).

Compound	T3	T3T3	T3T4	T4T4	T4T5	T5T5
Ø-occ (Na)	1	1	0.958	0.821	0.625	0.571
ρ (NaÅ^{-3})	0.0152	0.0146	0.0111	0.0090	0.0076	0.0073

Na^+-ion mobility is supported by solid-state NMR measurements both under static and MAS conditions. In spite of a variety of distinct crystallographic Na sites with diverse coordination, ^{23}Na MAS NMR spectra of virtually every compound demonstrate a single and relatively sharp resonance (Figure 3.6). The broader signal of $Na_{23}Si_{19}P_{33}$ is likely a result of both second-order quadrupolar broadening and overlap of several signals (cf. Figure 3.6). Less effective motional averaging of the different chemical environments experienced by the Na^+-ions results in a broader linewidth indicating lower Na^+-ion

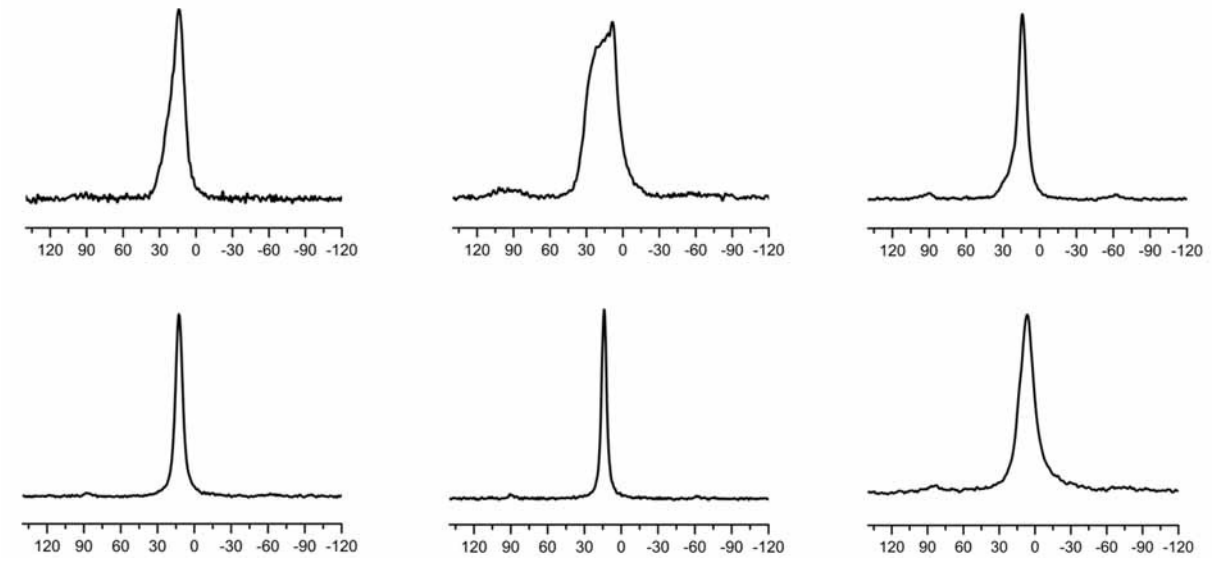

Figure 3.6 ^{23}Na MAS NMR spectra (ν_{rot} = 10 kHz) at room temperature of $Na_{19}Si_{13}P_{25}$ (top, left), $Na_{23}Si_{19}P_{33}$ (top, middle), $Na_{23}Si_{28}P_{45}$ (top, right), $Na_{23}Si_{37}P_{57}$ (bottom, left), *LT*-$NaSi_2P_3$ (bottom, middle) and *HT*-$NaSi_2P_3$ (bottom, right). δ (^{23}Na) = 14.04, 8.63, 14.19, 12.61, 13.98, 6.6 ppm and FWHM (^{23}Na) = 12.89, 27.50, 8.01, 6.82, 4.81 and 14.53 ppm.

mobility. The relatively sharp signals of the other compounds mean enhanced averaging. The overall signal's width roughly decreases with increasing size of the tetrahedral building units. The sharpest signal belongs to *LT*-$NaSi_2P_3$, which consists of T4 and T5 tetrahedra and indicates enhanced Na^+-ion mobility.

Possible Na^+-ion migration pathways were extracted from geometrical analysis with Topos[31] using covalent radii for silicon and phosphorus.[32] The calculations resulted in a rather isotropic distribution of pathways. Four large channels occur in all compounds (Figure B42-B47). With increasing supertetrahedral building units, the width of these channels increases. Shorter pathways connect the channels along every supertetrahedral face, leading to almost three-dimensional sodium migration pathways (Figures B42-B47). Such isotropic trajectories are desirable for fast ion conduction, since blocking effects have less impact on 3D compared to lower dimensional ion diffusion. Na^+-ion conductivities were determined by impedance spectroscopy. DC galvanostatic polarization measurements (Figure B49) revealed negligible contributions of electronic conductivity to the overall conductivity, which is desired in the context of solid electrolytes for battery applications. The ionic conductivities of all compounds (T3-T5T5) at 25 °C are plotted in Figure 3.7 as a function of size of their supertetrahedral entities. In addition, the sodium density in the compounds is given in the upper *x*-axis.

For a detailed description of the data analysis see Figure B50-B55 in the Supporting Information. All samples were sintered below their synthesis temperature to avoid decomposition (T3-T4T4 at 400 °C; T4T5 and T5T5 additionally at 800 °C, marked #). σ_{total} (black; Figure 3.7) refers to the total ionic conductivity including all grain boundary contributions of at least four samples of each compound. The conductivities of samples with optimized morphologies with only one semicircle in the EIS are plotted in orange (σ_{best}; Figure 3.7). The total ionic conductivity clearly increases with supertetrahedra size from $1.76 \cdot 10^{-9}$ Scm^{-1} to $4.0 \cdot 10^{-4}$ Scm^{-1}. This trend is also valid if only the grain boundary process at higher

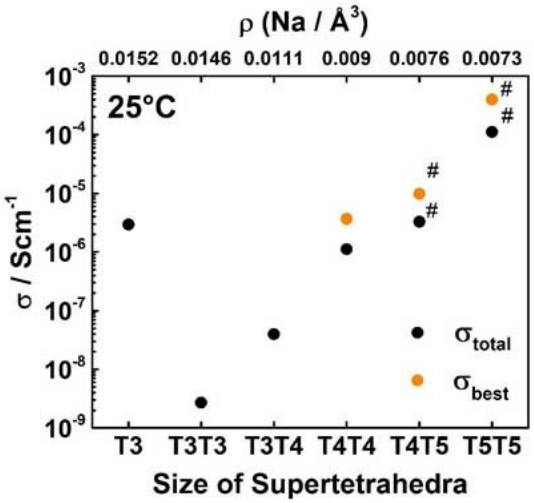

Figure 3.7 Ionic conductivity at 25 °C increases with the size of the supertetrahedral entities in the Na-Si-P structures and with a decrease in sodium density ρ(NaÅ^{-3}). For details see text.

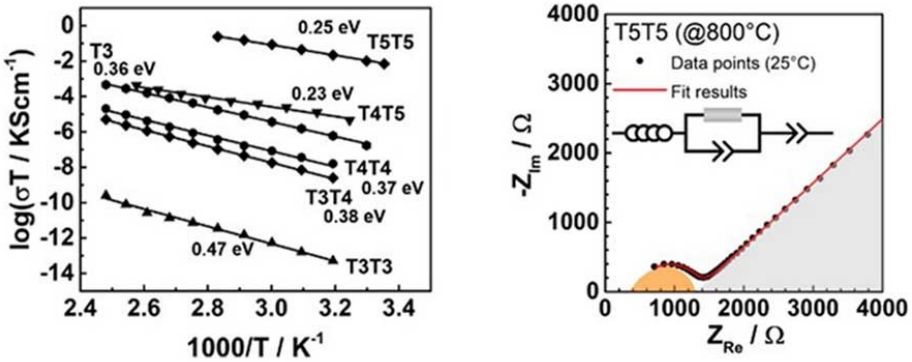

Figure 3.8 Comparison of the activation energies of all compounds (left). Complex impedance plot of T5T5 sintered at 800 °C (right). For details see text.

frequencies (cf. Figure B57) is evaluated and if the "best" samples with only one grain boundary contribution are compared (orange; Figure 3.7). Figure B58 shows a plot including the data of T4T5 and T5T5 samples sintered at 400 °C. The increase in conductivity is rationalized by the increasing space between the supertetrahedra as observed in the pathway analysis. By enlarging the supertetrahedra all channels and shorter connecting pathways become broader. Moreover, the relation between the phases T3T3 to T5T5 can be rationalized by adding 3×"Si_3P_4" to the formulae: $Na_{23}Si_{19}P_{33}$ (T3T3) + 3×"Si_3P_4" → $Na_{23}Si_{28}P_{45}$ (T3T4) + 3×"Si_3P_4" → $Na_{23}Si_{37}P_{57}$ (T4T4) + 3×"Si_3P_4" → $Na_{23}Si_{46}P_{69}$ (T4T5 or T5T5). The general formula is $Na_{23}Si_{9n+19}P_{12n+33}$ (n = 0-3). Adding charge neutral "Si_3P_4" to the anionic framework reduces the charge density, thus reduces the effective charge acting on the Na^+ ions. Besides, the Na^+ ions are "diluted", that is, the Na density decreases and the number of partially occupied Na sites increases, which in turn increases the conductivity (cf. Tables 3.2, Tables B1-B6 and Figure 3.7). In Figure 3.8, the activation energies (E_a) obtained from the grain boundary process at higher frequencies and from the measurements showing only one semicircle [cf. SI Eq. (5)] confirm the facilitation of the Na^+-ion movement in the larger structures. In general, a lower E_a is associated with a more facile movement of the ions.[33] We find that the activation energies decrease dramatically along the series T3T3 to T5T5 with increasing supertetrahedra size and Na^+-ion conductivity from 0.47 eV to 0.23 eV. The E_a of the two fastest materials *LT*-$NaSi_2P_3$ (T4T5, 0.23 eV) and *HT*-$NaSi_2P_3$ (T5T5, 0.25 eV) are even lower compared to existing fast Na^+-ion conductors like Na_3PS_4 (0.29 eV)[22], Na_3SbS_4 (0.25 eV)[23], $Na_3P_{0.5}As_{0.5}S_4$ (0.27 eV)[34] and $Na_3Zr_2(SiO_4)_2(PO_4)$ (0.26 eV)[24]. $Na_{19}Si_{13}P_{25}$ (T3) does not follow the described trend. Its total conductivity of $2.9 \cdot 10^{-6}$ Scm^{-1} is close to that of $Na_{23}Si_{37}P_{57}$ (T4T4, $3.7 \cdot 10^{-6}$ Scm^{-1}) and its E_a of 0.36 eV is very close to that of the T4T4 sample. The relatively high conductivity may be connected to the low density of 2.091 g cm^{-3}. Apparently, the replacement of a T3 supertetrahedron by a Si_3P_8 unit in $Na_{19}Si_{13}P_{25}$ creates extra space for the movement of Na^+-ions. *HT*-$NaSi_2P_3$ (T5T5) exhibits the highest total ionic conductivity of $4 \cdot 10^{-4}$ Scm^{-1} at 25 °C. (cf. Figure 3.8). Thus, *HT*-$NaSi_2P_3$ is comparable with very fast Na^+-ion conductors, such as Na_3PS_4[22] ($2 \cdot 10^{-4}$ Scm^{-1}) and NASICON-type $Na_{3.4}Sc_2(SiO_4)_{0.4}(PO_4)_{2.6}$[35,36] ($7 \cdot 10^{-4}$ Scm^{-1}), but slightly slower than materials such as NASICON produced by Ceramtec[37], β-Alumina[38], $Na_{3.1}Zr_{1.95}Mg_{0.5}Si_2PO_{12}$[39], Na_3SbS_4[23], $Na_{11}Sn_2PS_{12}$[40, 41], $NaCB_9H_{10}$[25] and $Na(C_9H_{10})(CB_{11}H_{12})$[42] with conductivities of 10^{-3}-10^{-2} Scm^{-1}.

For a deeper understanding of the origin and bulk vs. grain boundary contributions to the conductivity, the capacitance of the semicircle in the EIS has to be considered: assuming a realistic relative permittivity ε between 1-100 for a non-ferroelectric solid like *HT*-$NaSi_2P_3$, the bulk capacitance calculated by C=

$\varepsilon_0\varepsilon A/d$ with ε_0 being the vacuum permittivity should be in the low pF range.[43] Here, in Figure 3.8 and in a measurement of T5T5 at -60 °C (Figure B56), the capacitance is in the range of 20-100 pF and thus much larger than the expected bulk value. Consequently, we attribute the semicircle to a grain boundary process where ion transport is limited by geometrical current constriction effects. [44-46] The bulk properties of T5T5 are concealed by the grain boundary contributions and could not be deconvoluted. The bulk conductivity of this material thus potentially exceeds $4{\cdot}10^{-4}$ Scm^{-1} at ambient conditions. This assumption is corroborated by ^{23}Na-T_1-relaxometry data showing a low E_a of 0.11 eV for T5T5 (Figure 3.9). This suggests fast ion dynamics in the bulk, similar to β-Alumina. The grain boundary E_a of polycrystalline β-Alumina is 0.26 eV ($\sigma_{GB}=1{\cdot}10^{-3}$ Scm^{-1}), while the bulk E_a amounts to only 0.15 eV ($\sigma_{bulk}=8{\cdot}10^{-3}$ Scm^{-1}).[38] For T4T5 similar results were obtained.

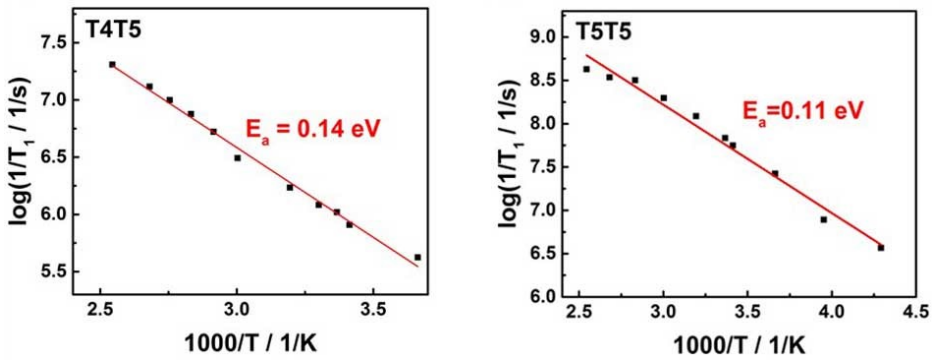

Figure 3.9 Temperature dependence of the ^{23}Na-T_1-relaxation time in the samples T4T5 (left) and T5T5 (right).

3.4 Conclusion

In summary, the herein reported phosphidosilicates are fast Na^+-ion conductors and our systematic study shows that the conductivity increases with the size of the supertetrahedra. It is demonstrated that the enhanced conductivity is due to the dilution of the Na^+ ions since the anionic charge of the supertetrahedral networks remains constant (except $Na_{19}Si_{13}P_{25}$). *HT*-$NaSi_2P_3$ with the largest supertetrahedral entities (T5) exhibits the highest total conductivity of up to $4{\cdot}10^{-4}$ Scm^{-1} at 25 °C which is competitive to known fast ionic conductors.[22,35,36] Impedance and NMR data indicate the existence of an even more facile and fast bulk conductivity, motivating additional research on the family of sodium phosphidosilicates for Na^+-ion conduction.

3.5 Experimental Section

All experiments and measurements were performed in an argon filled glovebox. The compounds were synthesized by solid state reactions of the elements in alumina crucibles at 750 to 1100 °C. Further details on elemental analysis, NMR, electrochemical spectroscopy are in the Supporting Information. CCDC 1816420-1816425 contain the supplementary crystallographic data for this paper. These data can be obtained free of charge from The Cambridge Crystallographic Data Centre.

3.6 References

[1] H. Li, J. Kim, T. L. Groy, M. O'Keeffe, O. M. Yaghi, *J. Am. Chem. Soc.* **2001**, *123*, 4867.

[2] C. Wang, Y. Li, X. Bu, N. Zheng, O. Zivkovic, C.-S. Yang, P. Feng, *J. Am. Chem. Soc.* **2001**, *123*, 11506.

[3] L. Wang, T. Wu, F. Zuo, X. Zhao, X. Bu, J. Wu, P. Feng, *J. Am. Chem. Soc.* **2010**, *132*, 3283.

[4] H. Li, A. Laine, M. O'Keeffe, O. M. Yaghi, *Science* **1999**, *283*, 1145.

[5] G. Férey, *Angew. Chem. Int. Ed.* **2003**, *42*, 2576.

[6] P. H. Fourcroy, D. Carre, J. Rivet, *Acta Crystallogr. B* **1978**, *34*, 3160.

[7] S. Pagano, M. Zeuner, S. Hug, W. Schnick, *Eur. J. Inorg. Chem.* **2009**, 1579.

[8] A. Hammerschmidt, P. z. Hebel, F. Hiltmann, B. Krebs, *Z. Anorg. Allg. Chem.* **1996**, *622*, 76.

[9] P. Wagatha, P. Pust, V. Weiler, A. S. Wochnik, P. J. Schmidt, C. Scheu, W. Schnick, *Chem. Mater.* **2016**, *28*, 1220.

[10] L. Toffoletti, H. Kirchhain, J. Landesfeind, W. Klein, L. v. Wüllen, H. A. Gasteiger, T. F. Fässler, *Chem. Eur. J.* **2016**, *22*, 17635.

[11] A. Haffner, T. Bräuniger, D. Johrendt, *Angew. Chem. Int. Ed.* **2016**, *55*, 13585.

[12] B. Eisenmann, H. Jordan, H. Schäfer, *Mater. Res. Bull.* **1982**, *17*, 95.

[13] B. Eisenmann, M. Somer, *Z. Naturforsch. B* **1985**, *40*, 886.

[14] B. Eisenmann, M. Somer, *Z. Naturforsch. B* **1984**, *39*, 736.

[15] B. Eisenmann, J. Klein, *J. Less-Common Met.* **1991**, *175*, 109.

[16] K. Feng, L. Kang, W. Yin, W. Hao, Z. Lin, J. Yao, Y. Wu, *J. Solid State Chem.* **2013**, *205*, 129.

[17] A. J. Springthorpe, J. G. Harrison, *Nature* **1969**, *222*, 977.

[18] D. Kundu, E. Talaie, V. Duffort, L. F. Nazar, *Angew. Chem. Int. Ed.* **2015**, *54*, 3431-3448; Angew. Chem. **2015,** *127*, 3495-3513.

[19] N. Yabuuchi, K. Kubota, M. Dahbi, S. Komaba, *Chemical Reviews* **2014**, *114*, 11636-11682.

[20] J. W. Fergus, *Solid State Ion.* **2012**, *227*, 102.

[21] Zhang, L.; Yang, K.; Mi, J.; Lu, L.; Zhao, L.; Wang, L.; Li, Y.; Zeng, H., *Adv. Energy Mater.* **2015,** *5*, 1501294.

[22] A. Hayashi, K. Noi, A. Sakuda, M. Tatsumisago, *Nat. Commun.* **2012**, *3*, 856.

[23] L. Zhang, D. Zhang, K. Yang, X. Yan, L. Wang, J. Mi, B. Xu, Y. Li, *Adv. Sci.* **2016**, *3*, 1600089.

[24] Q. Ma, M. Guin, S. Naqash, C.-L. Tsai, F. Tietz, O. Guillon, *Chem. Mater.* **2016**, *28*, 4821.

[25] W. S. Tang, M. Matsuo, H. Wu, V. Stavila, W. Zhou, A. A. Talin, A. V. Soloninin, R. V. Skoryunov, O. A. Babanova, A. V. Skripov, A. Unemoto, S.-I. Orimo, T. J. Udovic, *Adv. Energy Mater.* **2016**, *6*, 1502237.

[26] F. Hiltmann, P. z. Hebel, A. Hammerschmidt, B. Krebs, *Z. Anorg. Allg. Chem.* **1993**, *619*, 293.

[27] C. Wang, X. Bu, N. Zheng, P. Feng, *J. Am. Chem. Soc.* **2002**, *124*, 10268.

[28] T. Sasaki, H. Takizawa, K. Uheda, T. Yamashita, T. Endo, *J. Solid State Chem.* **2002**, *166*, 164.

[29] M. Huang, Y. P. Feng, A. T. L. Lim, J. C. Zheng, *Phys. Rev. B* **2004**, *69*, 054112.

[30] Lasia, A. In *Modern Aspects of Electrochemistry*; Conway, B. E., Bockris, J. O. M., White, R. E., Eds.; Springer US: Boston, MA, 2002, p 143.

[31] V. A. Balatov, A. P. Shevchenko, *Topos Professional*, 4.0, Samara State University: Samara, 2010.

[32] A. Haffner, D. Johrendt, *Z. Anorg. Allg. Chem.* **2017**, *643*, 1717.

[33] J. C. Bachman, S. Muy, A. Grimaud, H.-H. Chang, N. Pour, S. F. Lux, O. Paschos, F. Maglia, S. Lupart, P. Lamp, L. Giordano, Y. Shao-Horn, *Chem. Rev.* **2016**, *116*, 140.

[34] Z. Yu, S.-L. Shang, J.-H. Seo, D. Wang, X. Luo, Q. Huang, S. Chen, J. Lu, X. Li, Z.-K. Liu, D. Wang, *Adv. Mater.* **2017**, *29*, 1605561.

[35] M. Kaus, M. Guin, M. Yavuz, M. Knapp, F. Tietz, O. Guillon, H. Ehrenberg, S. Indris, *J. Phys. Chem. C* **2017**, *121*, 1449.

[36] M. Guin, F. Tietz, O. Guillon, *Solid State Ion.* **2016**, *293*, 18.

[37] W. G. Coors, J. H. Gordon, S. G. Menzer, US 2010/0297537 A1, 2010.

[38] A. Hooper, *J. Phys. D: Appl. Phys.* **1977**, *10*, 1487.

[39] S. Song, H. M. Duong, A. M. Korsunsky, N. Hu, L. Lu, *Sci. Rep.* **2016**, *6*, 32330.

[40] Duchardt, M.; Ruschewitz, U.; Adams, S.; Dehnen, S.; Roling, B., *Angew. Chem. Int. Ed.* **2018,** *57*, 1351-1355.

[41] Zhang, Z.; Ramos, E.; Lalere, F.; Assoud, A.; Kaup, K.; Hartman, P.; Nazar, L. F., *Energy Environ. Sci.* **2018,** *11*, 87-93.

[42] W. S. Tang, K. Yoshida, A. V. Soloninin, R. V. Skoryunov, O. A. Babanova, A. V. Skripov, M. Dimitrievska, V. Stavila, S.-I.Orimo, T. J. Udovic, *ACS Energy Lett.* **2016**, *1*, 659.

[43] J. R. Macdonald, W. B. Johnson, In *Impedance Spectroscopy*; John Wiley & Sons, Inc.: 2005, p 1.

[44] J. Fleig, J. Maier, *J. Am. Ceram. Soc.* **1999**, *82*, 3485.

[45] A. Kuhn, V. Duppel, B. V. Lotsch, *Energy Environ. Sci.* **2013**, *6*, 3548.

[46] P. Bron, S. Johansson, K. Zick, J. Schmedt auf der Günne, S. Dehnen, B. Roling, *J. Am. Chem. Soc.* **2013**, *135*, 15694.

4 Synthesis and Structure of the Sodium Phosphidosilicate Na_2SiP_2

Arthur Haffner, Anna-Katharina Hatz, Constantin Hoch, Bettina V. Lotsch, and Dirk Johrendt

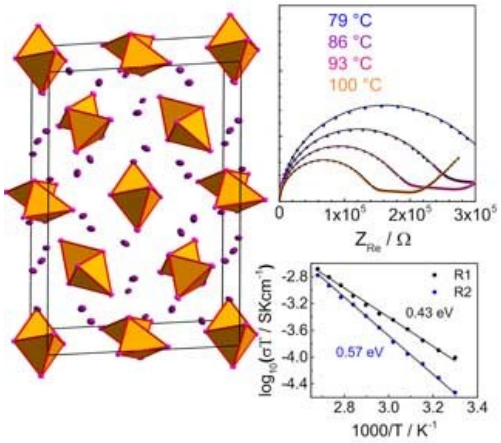

published in: *European Journal of Inorganic Chemistry* **2020**, 617-621.

4.1 Abstract

Ion conductors of light alkaline metals based on earth-abundant elements are important components for all-solid-state batteries. The new sodium-rich phosphidosilicate Na_2SiP_2 was synthesized by solid state reaction of stoichiometric amounts of the elements at 973 K and characterized by single-crystal X-ray diffraction (space group *Pccn* (no. 56), a = 12.7929(5) Å, b = 22.3109(9) Å, c = 6.0522(2) Å and Z = 16) and solid-state NMR under MAS conditions. The compound forms dark-red twinned crystals, and its crystal structure contains edge-sharing SiP_4 tetrahedra connected to infinite $_\infty{}^1[SiP_{4/2}]$ chains. The sodium ions between the chains are fairly mobile. Electrochemical impedance spectroscopy shows a total ionic conductivity of $\sigma(Na^+, 373\ K) = 2.3 \cdot 10^{-6}$ Scm^{-1} with an activation energy of E_a = 0.43 eV, and galvanostatic polarization reveals mixed conduction behavior with a transference number of 0.8.

4.2 Introduction

Fast lithium and sodium ion conductors composed of earth abundant elements as potential components of all solid-state batteries attract immense interest.[1-5] Recently, several phosphidosilicates with isolated or condensed SiP_4 tetrahedra have demonstrated lithium or sodium ion conductivity, for example Li_8SiP_4,[6] Li_2SiP_2,[6,7] $LiSi_2P_3$,[7] and the series $Na_{23}Si_{9n+19}P_{12n+33}$ (n = 0-3).[8] These compounds have also been studied in the framework of the electrochemical mechanism of SiP_2/Li anodes.[9,10] Except Li_8SiP_4 with isolated $[SiP_4]^{8-}$ tetrahedra, the crystal structures feature networks of interpenetrating T2-T5 supertetrahedra according to the *Yaghi* notation.[7,8,11] It was shown that larger supertetrahedral entities favour the ion conductivity by diluting the alkali metal ions between the lower charged clusters.[8] Nevertheless there is currently no reason to believe that supertetrahedral structures are generally needed for facile ion movement in phosphidosilicates. Since the actual structural requirements for fast ion conductivity are still not fully understood, it is reasonable to search for further compounds in this system. The supertetrahedral compounds in the system Na-Si-P are rather sodium-poor and the only known sodium-rich compound is Na_5SiP_3.[12] Therefore we focused on the sodium-rich part of the system and came across Na_2SiP_2 which turned out to be structurally quite different from the lithium analogue reported earlier.[6,7] Here we report the synthesis, crystal structure, NMR and impedance spectroscopy of Na_2SiP_2.

4.3 Results and Discussion

The crystal structure of Na_2SiP_2 was solved from single-crystal diffraction data using direct methods.[13] The diffraction patterns of several measured single-crystals showed pseudo-hexagonal metric, but a structure solution using hexagonal symmetry failed. One specimen showed unequal contributions of the twin domains, so the feigned hexagonal intensity distribution was broken. From this dataset, a structure model with orthorhombic symmetry could be derived under the assumption of a merohedral *drilling* by a rotation of 120 ° around (0 0 1). From the expected three sets of *drilling* domains, only two were observed in the diffraction pattern. One additional domain occurs twinned by the mirror plane (1 1 0) yielding in volume fractions of 16.8 and 13.5 %. Note that this twinning originates not from phase transitions but is caused by the metric of the orthorhombic unit cell ($b/a \approx \sqrt{3}$), leading to oriented adhering of crystal domains while growth of the contact twins. Figure 4.1 (left) shows the pseudo-hexagonal diffraction pattern of the $hk2$ plane with the three interfering lattices marked in blue (main domain), green and purple (minor components). The reflections of the main domain show little intensity deviations (a, highlighted in red) compared to the other two highlighted areas (b and c), where

only every second reflection belongs to the main component, discernible by alternating intensities. Figure 4.1 (right) shows a non-integer 0.5*kl*-plane, where no reflections of the main domain are visible, but of the two minor components. All atom positions were refined with anisotropic thermal displacement parameters. Data on structure refinement and the fractional coordinates are compiled in Table 4.1 and Table 4.2 (CCDC 1946908).

Table 4.1 Crystallographic data for the refinement of Na_2SiP_2.

Formula	Na_2SiP_2
formula mass / g·mol^{-1}	136.01
space group	*Pccn* (no. 56)
a / Å	12.7929(5)
b / Å	22.3109(9)
c / Å	6.0522(2)
V / Å^3	1727.43(11)
Z	16
$\rho_{X\text{-}ray}$ / g·cm^{-1}	2.092
μ / mm^{-1}	1.262
radiation	Mo-Kα
θ-range / °	3.168 – 30.682
reflections measured	28523
independent reflections	4104
refined parameters	94
R_σ	0.0225
R_{int} (main component)	0.0404
*R*1 ($F^2 > 2\sigma(F^2)$ / all)	0.0389 / 0.0455
w*R*2 ($F^2 > 2\sigma(F^2)$ / all)	0.0852 / 0.0881
GooF	1.118
BASF factor 1	0.16745
BASF factor 2	0.13472
$\Delta\rho_{max}$, $\Delta\rho_{min}$ / e·Å^3	0.634, -1.460

Table 4.2 Fractional atom coordinates, Wyckoff positions and equivalent displacement parameters of Na_2SiP_2.

Atom	Wyckoff position	*x*	*y*	*z*	U_{eq} / Å²
P1	8*e*	0.03221(7)	0.07405(4)	0.00206(16)	0.01376(16)
P2	8*e*	0.12998(6)	0.50881(4)	0.00362(16)	0.01327(15)
P3	8*e*	0.16116(7)	0.19518(4)	0.43788(14)	0.01279(16)
P4	8*e*	0.66053(8)	0.19606(5)	0.18775(16)	0.0198(2)
Si1	8e	0.50140(8)	0.00021(5)	0.25362(14)	0.01086(15)
Si2	4d	¼	¾	0.0615(3)	0.0157(3)
Si3	4c	¼	¼	0.1882(2)	0.0102(2)
Na1	8*e*	0.00974(14)	0.20996(8)	0.0224(3)	0.0330(4)
Na2	8*e*	0.24880(16)	0.08638(8)	0.2294(3)	0.0275(3)
Na3	8*e*	0.30558(15)	0.59216(9)	0.0123(4)	0.0408(5)
Na4	8*e*	0.50940(12)	0.11973(7)	0.0096(3)	0.0272(3)

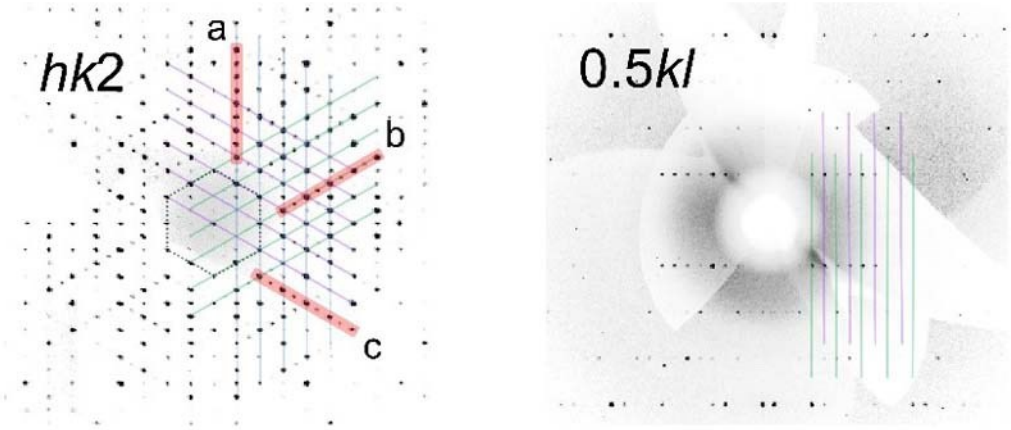

Figure 4.1 Left: *hk*2-plane with the three interfering lattices marked blue (main component), green and purple (minor components). The red highlighted areas indicate the violation of the hexagonal symmetry. Right: 0.5*kl*-plane with reflections of the two minor components only.

The phosphidosilicate polyanion in Na_2SiP_2 is composed of three crystallographic independent SiP_4 tetrahedra, sharing common edges along [001] and assembling three independent $_\infty^1[SiP_2]^{2-}$ chains

(Figure 4.2). The Si–P distances range between 2.244 and 2.273 Å as typical in phosphidosilicates. With 94.98 to 121.95°, the P–Si–P angles show considerable deviation from the ideal tetrahedral angle, whereas the mean value of 109.77° is still close to it. The sodium cations reside on general Wyckoff positions between the tetrahedra chains coordinated by P atoms and form distorted trigonal bipyramids (Na1), octahedra (Na2 and Na4) and trigonal prisms (Na3) with two elongated Na–P distances (see Figure 4.3).

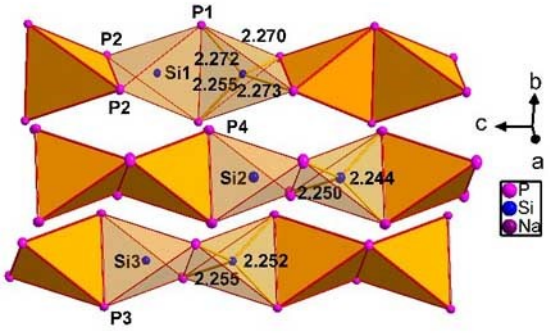

Figure 4.2 Three independent $_\infty{}^1[SiP_2]^{2-}$ chains of edge-sharing SiP_4 tetrahedra in Na_2SiP_2 with Si–P distances.

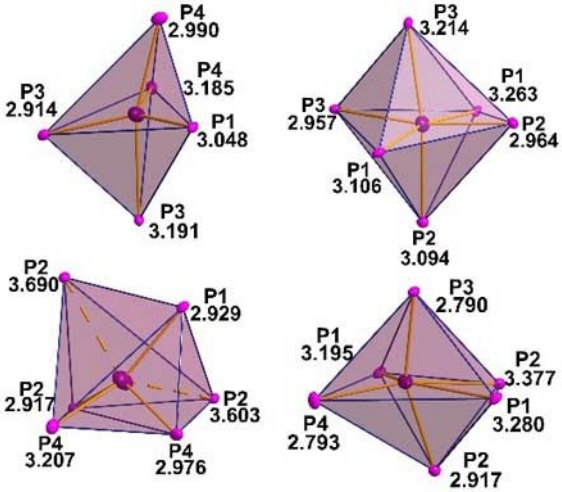

Figure 4.3 Distorted NaP_x polyhedra in Na_2SiP_2 (top, left: $Na1P_5$ trigonal bipyramid; top, right: $Na2P_6$ octahedron; bottom, left: $Na3P_6$ trigonal prism; bottom, right: $Na4P_6$ octahedron).

The measured reflection patterns indicated a hexagonal crystal symmetry in which no structure solution was possible. The underlying hexagonal motif appears in the topology of a hexagonal rod packing of the anionic bars along the *c*-axis (Figure 4.4) as well as in the *b*/*a* ratio with only 0.69 % deviation from √3. By decorating these bars with silicon and phosphorus ions to edge-shared $_\infty{}^1[SiP_2]^{2-}$ chains, the hexagonal symmetry reduces to orthorhombic with splitting into three crystallographically independent SiP_2 chains. The symmetry reduction creates a pseudo-merohedral *drilling* with a *C*-centered orthorhombic unit cell. For the tetrahedra chain composed of Si1, P1 and P2 this centering is nearly accomplished whereas it is infringed by the two other tetrahedra chains. As depicted in Figure 4.4, the tetrahedra chain with Si3 slightly shift along [001] whereas the symmetry equivalent chain displaces in the opposing direction. The same occurs in the chain assembled of Si2 and P4 with a larger offset. In

case of the sodium ions the discussed centering is also valid if a minor displacement is taken into account. In contrast to Li_2SiP_2,[7] where the constituting SiP_4 tetrahedra assemble interpenetrating T2 supertetrahedral networks, the structural motif of K_2SiP_2 [14] and Cs_2SiP_2[15] with K_2ZnO_2 type structure [16] are rather similar to Na_2SiP_2, where the tetrahedra chains are arranged along the *c*-axis as well. Due to the chain orientation with respect to the *ab*-plane there are two differently oriented, but topologically identical chains in K_2SiP_2 whereas in Na_2SiP_2 three types occur (symmetrically inequivalent due to shift in the *z* parameter, Figure 4.4) leading to nearly the same *c*- and almost doubled *a* and *b* cell parameters involving quadruplicating of respective Wyckoff sites. The majority of representatives of the K_2ZnO_2-type structure are sulfides or selenides with relatively big cations separating the tetrahedra chains like in A_2CoX_2 [17] or A_2MnX_2[18] or in the compounds $A_3Fe_2X_4$ [19-21] (A = K, Rb, Cs; X = S, Se) with the $Tl_3Fe_2S_4$-type structure. There are fewer examples of tetrahedra chains surrounded by cations smaller than potassium like in Na_2ZnS_2,[22] $Na_2Co(S;Se)_2$[17] or $Na_3Fe_2(S;Se)_4$.[23, 24] Decreasing the amount of the separating counterions leads to $KFeSe_2$-type structure[25] with edge condensed tetrahedra chains as well. The effect of substitution of Cs^+ in $CsGa(S;Se)_2$ by smaller cations Rb^+ or K^+ was investigated, and it turned out that the structure changes when about 30 % of the Cs^+ ions are replaced.[26] These findings may suggest that chains of edge condensed tetrahedra are stabilized by the amount and size of the counterions. NMR spectra of all constituting nuclei were collected under MAS conditions with rotation frequencies of 10 kHz of a pure polycrystalline sample (see Figure 4.5).

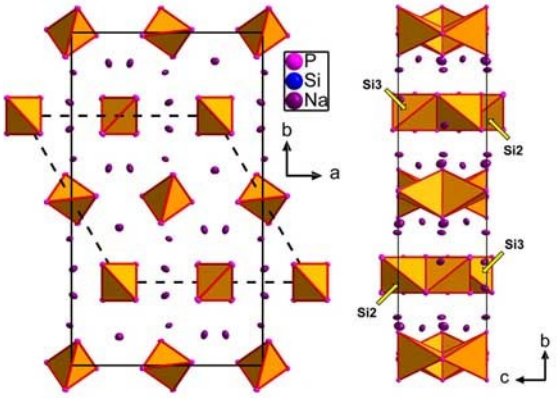

Figure 4.4 Unit cell of Na_2SiP_2 with $_\infty^1[SiP_2]^{2-}$ tetrahedra chains in [001] direction and the pseudo-hexagonal unit cell (left) and view along the *a*-axis with opposing displacement of the tetrahedra chains (right).

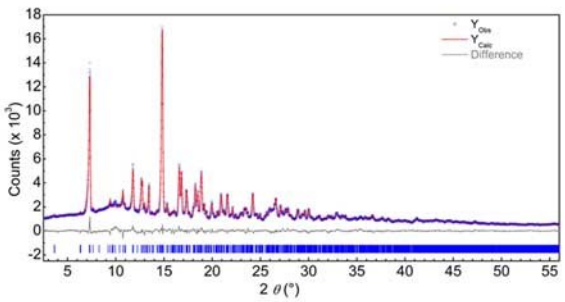

Figure 4.5 X-Ray powder pattern of Na_2SiP_2 (blue) with Rietveld fit (red) and difference plot (grey).

As it is depicted in Figure 4.6, Na_2SiP_2 has four resonance frequencies for phosphorus at δ (^{31}P) = -74.7, -71.4, -52.6 and -34.8 ppm with the first two at nearly the same chemical shift. Integrating the intensities including rotation sidebands yields a 1:1:1:1 ratio indicating four magnetically inequivalent phosphorus atoms in the structure. The resonances with nearly the same chemical shift are assigned to P3 and P4 with almost the same Si–P distances and both with five sodium ions in vicinity. P3 induces the resonance in the shielded region due to the larger chemical shift anisotropy than P4, seen on the greater intensity on the rotation sideband pattern, whereas the downfield signals belong to the Si1 tetrahedra chain with slightly elongated Si–P distances. Following the observation described by Monconduit et al. for compounds in the Li-Si-P system, a resonance is shifted into the upfield region with increasing negative charge density at a particular phosphorus atom in ^{31}P-NMR spectra.[9] Assuming the same behavior towards sodium ions, the resonance at δ (^{31}P) = -52.6 ppm can be assigned to P2 with seven by contrast to P1 with six sodium ions in vicinity (the limit was set to 3.7 Å for this approach). In the silicon spectrum three broad resonances were detected in agreement with the structure model at δ (^{29}Si) = -59.0, -39.3 and -35.5 ppm. The additional signal at 48 ppm differs in line shape and is assigned to background noise. Opposing the structure model, in the sodium spectrum only one signal is visible with a shoulder in the high field region at δ (^{23}Na) = 8.1 ppm instead of four distinct resonances. As it was shown for sodium based supertetrahedral ionic conductors,[8] this observation can arise from similar chemical environment or from fast exchange processes. Since Na_2SiP_2 comprises three different NaP_x polyhedra, one single sodium resonance indicates fast dynamics.

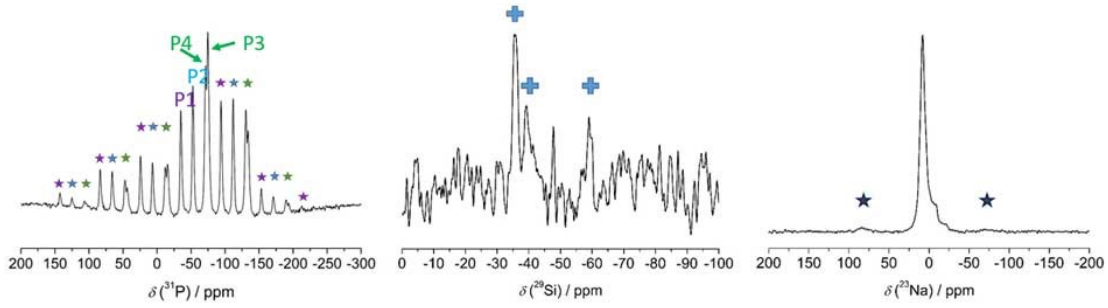

Figure 4.6 ^{31}P (left), ^{29}Si (middle) and ^{23}Na (right) MAS-NMR spectra at 10 kHz of Na_2SiP_2 with star-marked rotation side bands. Respective chemical shifts are δ (^{31}P) = -74.7, -71.4, -52.6 and -34.8 ppm, δ (^{29}Si) = -59.0, -39.3 and -35.5 ppm (marked with crosses) and δ (^{23}Na) = 8.1 ppm.

Ionic conduction was quantified by electrochemical impedance spectroscopy. Spectra measured from 303 to 373 K (cf. Figure 4.7, top left) reveal two distorted semicircles at higher frequencies and a spike at

lower frequencies which results from polarization of sodium ions at the blocking electrodes. The data were fitted to the equivalent circuit shown in Figure 4.7 (bottom, left) comprising of two parallel resistances (R) and constant phase element (CPE)-entities, representing the semicircles, in series to a CPE for the electrode polarization. These elements are placed in parallel to a capacitor (C) representing a stray capacitance of about 80 pF. According to the Brug formula $C_{eff} = Q^{1/\alpha}R^{(1/\alpha-1)}$ an effective capacitance (C_{efl}) of a CPE in parallel to a resistance was calculated resulting C_{efl}(CPE1) = 30 pF and C_{eff}(CPE2) = 0.23 nF.[27] These values indicate that only grain boundary processes or current constriction phenomena are visible.[28, 29] The bulk properties could not be resolved and only the total ionic conductivity σ (Na^+) of $2.3 \cdot 10^{-6}$ Scm^{-1} at 373 K was calculated from the sum of R1+R2=R by $\sigma(Na^+) = L\cdot(RA)^{-1}$ with L being the thickness and A the area of the sample. Since the grain boundary thickness is unknown, the activation energies of the two processes were calculated with the conductivity derived from the formula above using R1 and R2, respectively. A low activation energy of 0.43 eV for the high frequency process (CPE1R1) and a significantly higher one of 0.57 eV for CPE2R2, possibly stemming from highly resistive grain boundaries, were obtained. The DC galvanostatic polarization measurement in Figure 4.7 (bottom, right), measured with stainless steel electrodes at 368 K, determines an electronic conductivity of σ (e^-) = $7.9 \cdot 10^{-9}$ Scm^{-1}, which is roughly one order of magnitude lower than the σ (Na^+) of $6.8 \cdot 10^{-9}$ Scm^{-1} of this sample leading to a transference number of 0.8. This classifies the material as a sort of mixed ionic electronic conductor being unsuitable for the application as solid electrolyte, but potentially interesting in SiP_2 electrode material research.

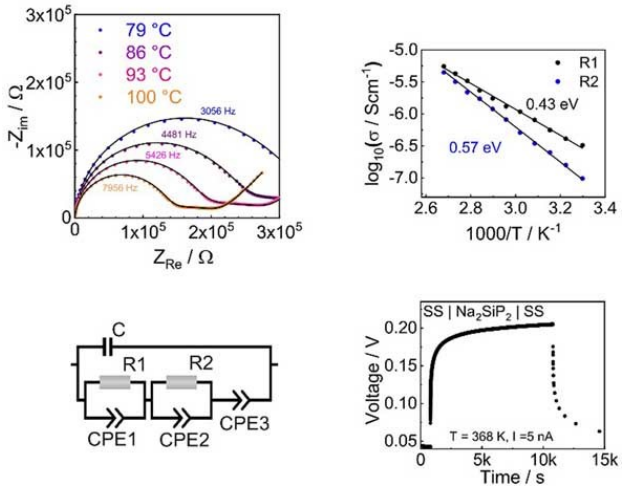

Figure 4.7 Selection of temperature dependent AC impedance spectra of Na_2SiP_2 (top, left) fitted to the equivalent circuit (bottom, left). Plot of the activation energy showing 0.43 eV for R1 in parallel CPE ≈ $3\cdot10^{-11}$ F and 0.57 eV for R2 in parallel to CPE ≈ $2\cdot10^{-10}$ F (top, right) and DC galvanostatic polarization measured with stainless steel electrodes showing a σ_{eon} of $7.9\cdot10^{-9}$ S/cm at 368 K (bottom, right).

4.4 Conclusion

Na_2SiP_2 is a new phosphidosilicate with a SiS_2-like arrangement of $_\infty^1[SiP_2]^{2-}$ chains and fairly mobile sodium ions between them. The crystal structure differs from the related potassium compound with K_2ZnO_2-type structure by three crystallographically different tetrahedra chains instead of one and feigns hexagonal symmetry. Impedance data show mobile sodium ions at elevated temperatures and polarization experiments reveal mixed ionic and electronic conduction behaviour, making this compound potentially interesting in SiP_2 electrode material research. Na_2SiP_2 enriches the family of phosphidosilicates and encourages continuative research in the field of the Si-P-system with light alkali metals for low-cost energy storage applications.

4.5 Experimental Section

Synthesis. Na_2SiP_2 was prepared by solid-state reaction of a stoichiometric mixture of metallic sodium (67.6 mg, Alfa Aesar, 99.8 %), silicon powder (41.3 mg, Smart Elements, 99.8 %) and red phosphorus (91.1 mg, Chempur, > 99 %). The reaction mixture was ground and filled in alumina crucibles under inert conditions in an argon-filled glovebox with concentrations of O_2 and H_2O < 0.1 ppm. This mixture was sealed in a silica ampoule and fired in a tube furnace to 100 °C within 5 h before the temperature was raised to 700 °C and maintained for 40 h. After cooling to room temperature, the still inhomogeneous product was ground thoroughly and reheated to the same reaction temperature twice yielding a polycrystalline and highly moisture-sensitive red powder.

Single-Crystal X-ray Diffraction. Crystals of sufficient quality for diffraction experiments were selected under dried paraffin oil and sealed in oil-filled glass capillaries (Hilgenberg GmbH, Germany, inner diameter 0.1 mm). Diffraction data were collected on a Bruker D8 Quest diffractometer equipped with a microfocus Mo-Kα X-ray source, Göbel mirror optics and Photon II detector. For data reduction and absorption correction the software package APEX3 [30] was used. Space group determination was carried out with XPREP [31] based on systematically absent reflections. SHELX-97 [13] was used for structure solution and refinement. Visualization of the crystal structure was carried out with Diamond [32] software. CCDC 1946908 (for Na_2SiP_2) contains the supplementary crystallographic data for this paper. These data can be obtained free of charge from The Cambridge Crystallographic Data Centre.

Powder X-ray Diffraction. For powder X-ray diffraction a phase pure polycrystalline sample was ground and sealed in Hilgenberg glass capillaries to avoid hydrolysis. Data were collected on a Stadi P powder diffractometer (STOE & Cie GmbH, Darmstadt, Germany) equipped with a Mythen 1K detector

(Dectris, Baden, Switzerland) in Debye-Scherrer geometry with a Ge(111) monochromator and Mo-Kα1 radiation. Rietveld refinement based on single-crystal diffraction data was performed with TOPAS [33] software.

Solid-State MAS-NMR. Polycrystalline samples of Na_2SiP_2 were loaded into a commercial 4 mm zirconia rotor. Spectra of ^{23}Na, ^{29}Si and ^{31}P were acquired on a Bruker Avance III 500 with a magnetic field of 11.74 T in MAS conditions (ν_{rot} = 10 kHz) and Larmor frequencies of $\nu_0(^{23}Na)$ = 132.33 MHz, $\nu_0(^{29}Si)$ = 99.38 MHz and $\nu_0(^{31}P)$ = 202.48 MHz. All spectra were indirectly referenced to ^{1}H in 100 % TMS at -0.1240 ppm.

Electrical Conductivity. For DC conductivity measurements and AC impedance spectroscopy, an Ivium compactstat.h (24 bit) in a two-electrode setup using a home-build Swagelok cell was applied. Prior to the measurements a polycrystalline sample was compacted to a pellet with 5 mm in diameter and 1 mm of thickness by uniaxial cold pressing (22 kN) and annealed for 10 h at 400 °C. Then, the pellet was sandwiched between indium foil (Alfa Aesar, 0.127 mm of thickness, 99.99 %) to enhance contact with the Swagelok cell. No reactions between the pellet and the indium foil were observed. For DC measurements stainless steel electrodes were applied. All measurements were carried out under inert conditions and the amplitude of the AC voltage was 100 mV. Collected data were analyzed by RelaxIS3 software from rhd instruments.

4.6 References

[1] F. Zheng, M. Kotobuki, S. Song, M. O. Lai, L. Lu, *J. Power Sources* **2018**, *389*, 198.

[2] R. Chen, W. Qu, X. Guo, L. Li, F. Wu, *Mater. Horiz.* **2016**, *3*, 487.

[3] Y. Wang, S. Song, C. Xu, N. Hu, J. Molenda, L. Lu, *Nano Materials Science* **2019**, *1*, 91.

[4] B. V. Lotsch, J. Maier, *J. Electroceram.* **2017**, *38*, 128.

[5] Z. Zhang, Y. Shao, B. V. Lotsch, Y.-S. Hu, H. Li, J. Janek, L. F. Nazar, C.-W. Nan, J. Maier, M. Armand, L. Chen, *Energy Environ. Sci.* **2018**, *11*, 1945.

[6] L. Toffoletti, H. Kirchhain, J. Landesfeind, W. Klein, L. van Wüllen, H. A. Gasteiger, T. F. Fässler, *Chem. Eur. J.* **2016**, *22*, 17635.

[7] A. Haffner, T. Bräuniger, D. Johrendt, *Angew. Chem. Int. Ed.* **2016**, *55*, 13585.

[8] A. Haffner, A.-K. Hatz, I. Moudrakovski, B. V. Lotsch, D. Johrendt, *Angew. Chem. Int. Ed.* **2018**, *57*, 6155.

[9] G. Coquil, B. Fraisse, N. Dupré, L. Monconduit, *ACS Appl. Energy Mater.* **2018**, *1*, 3778-3789.

[10] D. Duveau, S. S. Israel, J. Fullenwarth, F. Cunin, L. Monconduit, *J. Mater. Chem. A* **2016**, *4*, 3228.

[11] H. Li, J. Kim, T. L. Groy, M. O'Keeffe, O. M. Yaghi, *J. Am. Chem. Soc.* **2001**, *123*, 4867.

[12] B. Eisenmann, M. Somer, *Z. Naturforsch. B* **1985**, *40*, 886.

[13] G. M. Sheldrick, *Acta crystallogr. A* **2008**, *64*, 112.

[14] B. Eisenmann, M. Somer, *Z. Naturforsch. B* **1984**, *39*, 736.

[15] B. Eisenmann, J. Klein, *J. Less.-Common Met.* **1991**, *175*, 109.

[16] E. Vielhaber, R. Hoppe, *Z. Anorg. Allg. Chem.* **1968**, *360*, 7.

[17] W. Bronger, C. Bomba, *J. Less-Common Met.* **1990**, *158*, 169.

[18] W. Bronger, H. Balk-Hardtdegen, D. Schmitz, *Z. Anorg. Allg. Chem.* **1989**, *574*, 99.

[19] W. Bronger, U. Ruschewitz, P. Müller, *J. Alloy. Compd.* **1995**, *218*, 22.

[20] W. Bronger, H. S. Genin, P. Müller, *Z. Anorg. Allg. Chem.* **1999**, *625*, 274.

[21] K. O. Klepp, S. Pantschov, H. Boller, *Z. Kristallogr.* **2000**, *215*, 5.

[22] K. O. Klepp, W. Bronger, *Rev. Chim. Miner.* **1983**, *20*, 682.

[23] H. Boller, H. Blaha, *Monatsh. Chem.* **1983**, *114*, 145.

[24] K. O. Klepp, W. Sparlinek, *Z. Kristallogr.* **1996**, *211*, 626.

[25] W. Bronger, A. Kyas, P. Müller, *J. Solid State Chem.* **1987**, *70*, 262.

[26] D. Friedrich, M. Schlosser, M. Etter, A. Pfitzner, *Crystals* **2017**, *7*, 379.

[27] G. J. Brug, A. L. G. van den Eeden, M. Sluyters-Rehbach, J. H. Sluyters, *J. Electroanal. Chem.* **1984**, *176*, 275.

[28] J. T. S. Irvine, D. C. Sinclair, A. R. West, *Adv. Mater.* **1990**, *2*, 132.

[29] J. Fleig, J. Maier, *J. Am. Ceram. Soc.* **1999**, *82*, 3485.

[30] APEX3, Version 2016.5-0, Brucker AXS Inc., Madison, Wisconsin, **2016**.

[31] XPREP, Version 2008/2, Bruker AXS Inc., Karlsruhe, Germany, **2008**.

[32] K. Brandenburg, Diamond, Version 3.2k, Crystal Impact GbR, Bonn, Germany, **2014**.

[33] A. Coelho, TOPAS-Academic, Version 4.1, Coelho Software, Brisbane, Australia, **2007**.

5 Polymorphism and fast Potassium-Ion Conduction in the T5 Supertetrahedral Phosphidosilicate KSi_2P_3

Arthur Haffner, Anna-Katharina Hatz, Otto E. O. Zeman, Constantin Hoch, Bettina V. Lotsch, and Dirk Johrendt

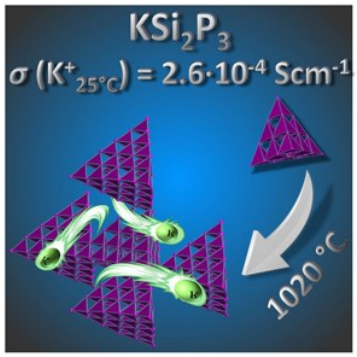

published in: *Angewandte Chemie International Edition* **2021**, *60*, 13641-13646.

5.1 Abstract

The all-solid-state battery (ASSB) is a promising candidate for electrochemical energy storage. In view of the limited availability of lithium, however, alternative systems based on earth-abundant and inexpensive elements are urgently sought. Besides well-studied sodium compounds, potassium-based systems offer the advantage of low cost and a large electrochemical window, but are hardly explored. Here we report the synthesis and crystal structure of K-ion conducting T5 KSi_2P_3 inspired by recent discoveries of fast ion conductors in alkaline phosphidosilicates. KSi_2P_3 is composed of SiP_4 tetrahedra forming interpenetrating networks of large T5 supertetrahedra. The compound passes through a reconstructive phase transition from the known T3 to the new tetragonal T5 polymorph at 1020 °C with enantiotropic displacive phase transitions upon cooling at about 155 °C and 80 °C. The potassium ions are located in large channels between the T5 supertetrahedral networks and show facile movement through the structure. The bulk ionic conductivity is up to $2.6 \cdot 10^{-4}$ S/cm at 25 °C with an average activation energy of 0.20 eV. This is remarkable high for a potassium ion conductor at room temperature, and marks KSi_2P_3 as the first non-oxide solid potassium ion conductor.

5.2 Introduction

All-solid-state batteries (ASSB) with solid instead of liquid electrolytes are traded as the next generation energy storage devices because they provide higher energy densities and faster charging rates than conventional systems.[1-6] For the development of ASSBs, the solid electrolyte is a critical component and its ionic conductivity a key performance indicator. So far, several lithium ion conducting materials are well investigated. Garnets such as doped $Li_7La_3Zr_2O_{12}$ and $Li_{1.4}Al_{0.4}Ti_{1.6}(PO_4)_3$ exhibit bulk ionic conductivities up to 10^{-3} S/cm at room temperature. Similar and even higher lithium ion conductivities in the range of $1.6{\cdot}10^{-4}$ to $2.5{\cdot}10^{-2}$ S/cm were found in ternary lithium thiophosphates,[7] halide argyrodites,[8-9] $Li_{10}GeP_2S_{12}$-type materials[10] and rare-earth halides.[11-13] Recently, it became apparent that phosphidosilicates may be promising candidates for solid electrolytes. These compound contain SiP_4 tetrahedra, which are isolated in Li_8SiP_4,[14] while in $Li_{10}Si_2P_6$ or $Li_3Si_3P_7$[15] the tetrahedra are condensed via edges or vertices to reduce the charge. The SiP_4 tetrahedra in Li_2SiP_2 form interpenetrating networks of T2 supertetrahedra,[14] while in $LiSi_2P_3$ fused T4 and T5 entities are present.[16] The lithium ion conductivities are between $4{\cdot}10^{-7}$ S/cm (Li_2SiP_2) [14] and $1{\cdot}10^{-3}$ S/cm ($Li_{14}SiP_6$)[17] with activation energies of 0.49 to 0.30 eV, respectively. NMR data of $LiSi_2P_3$ reveal an activation energy of about 0.1 eV indicating an even more facile ion transport in this compound. However, lithium batteries for large scale applications are restricted by the availability and cost of lithium.[18-22] Therefore, systems with earth abundant cheap alternatives such as sodium or potassium are requested. Solid sodium electrolytes like Na_3PS_4[23] or NaSICON-type $Na_{3.4}Sc_2(SiO_4)_{0.4}(PO_4)_{2.6}$[24-25] have conductivities on the order of $2{\cdot}10^{-4}$ S/cm and $7{\cdot}10^{-4}$ S/cm, respectively. β-Alumina,[26] Na_3SbS_4[27-28] or $Na_{11}Sn_2PS_{12}$[29-30] exceed these conductivities by about one order of magnitude. The phosphidosilicates $Na_{23}Si_{9n+19}P_{12n+33}$ based on interpenetrating networks of fused T3 to T5 supertetrahedra turned out to be competitive.[31] *HT*-$NaSi_2P_3$ exhibits solely T5 entities and shows a total sodium ion conductivity of $4{\cdot}10^{-4}$ S/cm with a low activation energy (E_a) of 0.25 eV. NMR data reveal an even lower activation energy of 0.11 eV, suggesting a facile Na hopping process. While sodium is much more abundant than lithium, it has a less negative electrode potential (-2.71 V) compared to lithium (-3.04 V). In contrast, potassium has a lower potential than Na (-2.93 V) that enables an improved cell output voltage.

Since the availability and low cost of potassium are comparable with those of sodium, the exploration of potassium ion batteries (KIBs) appears promising. So far, studies on KIBs employing potassium metal anodes, solid electrolytes and cathodes such as Prussian blue with remarkable capacities and cycling stabilities were reported.[32-35] Surprisingly, only a few solid potassium ion electrolytes are known (Figure

5.1, for data and references see Table C8). These materials are oxides and show conductivities in a reasonable range for applications (10^{-4}-10^{-2} S/cm) only at high temperatures of 300-400 °C. The only exception is polycrystalline $K_2Fe_4O_7$ with a conductivity of $5{\cdot}10^{-2}$ S/cm at room temperature. However, single crystal impedance spectroscopy shows that the potassium ion migration in this compound is predominantly two-dimensional. [34]

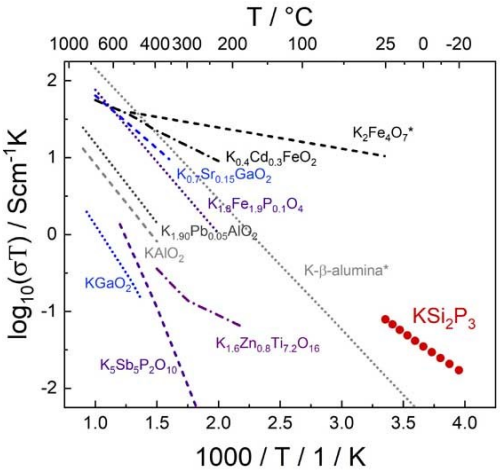

Figure 5.1 K^+-ion conductivities of known materials and of KSi_2P_3-*mC*928 (sample 2c in Table C9). Asterisks indicate single-crystal data. References and activation energies are in Table C8.

In this work, we address the family of potassium phosphidosilicates as possible solid electrolytes. Currently only the compounds K_2SiP_2[36] and the layered T3 KSi_2P_3[37] are known in this system. Both are not promising as ion conductors because of the lack of partial occupied potassium sites. Here we report three new polymorphs of KSi_2P_3 with T5 supertetrahedral structures related to the sodium ion conductor $NaSi_2P_3$.[31] The polymorphs are characterized by X-ray powder diffraction based on the single-crystal data of the high temperature polymorph. Electrochemical impedance and MAS-NMR spectra of the new monoclinic modification revealed a remarkably high σ_{bulk} (K^+) up to $2.6{\cdot}10^{-4}$ S/cm at 25 °C, and a low activation energy of 0.20 eV. This material hence qualifies as the first non-oxide fast solid potassium ion conductor.

5.3 Results and Discussion

KSi_2P_3 with the space group *C*2/*c* was first described by Feng *et al.*[37] and is denominated as KSi_2P_3-*mC*96 in the following. It contains SiP_4 tetrahedra which form T3 supertetrahedra according to the Yaghi

nomenclature.[38] These T3 entities are fused by one common SiP_4 tetrahedron resulting in a layered structure with the K^+ ions located on two fully occupied general Wyckoff sites between T3 supertetrahedral layers (see inset of Figure 5.2). This structure is stable upon heating to 1000 °C. We find a mixture of two phases at 1020 °C before KSi_2P_3-*mC*96 is completely transformed to a tetragonal modification at 1040°C, denoted as KSi_2P_3-*tI*960. Figure 5.2 shows the high temperature diffraction patterns. The additional reflection at about 9.8° indicates crystallization of the silica capillary. We were able to solve and refine the structure of this metastable high temperature polymorph quenched to room temperature with single-crystals. For details we refer to the experimental section in the Supporting Information. Table 5.1 summarizes the single-crystal data of KSi_2P_3-*tI*960 in space group $I4_1/acd$ (No. 142).[39] Atom positions and displacement factors are given in Tables C1 and C2 of the Supporting Information. KSi_2P_3-*tI*960 is also built from SiP_4 tetrahedra, but now forming three-dimensional networks of T5 supertetrahedra as shown in Figure 5.3.

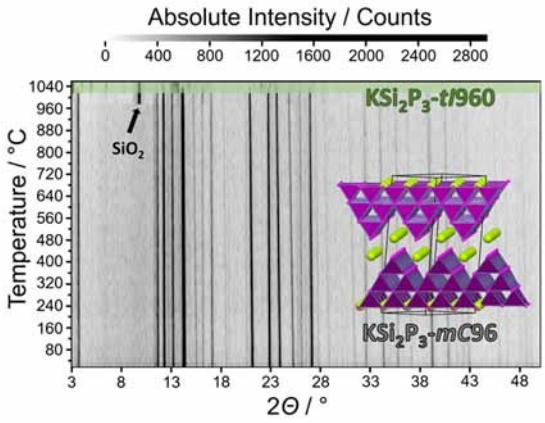

Figure 5.2 High temperature Mo-$K\alpha_1$ X-ray powder diffraction patterns of a KSi_2P_3-*mC*96 sample with a phase transition to KSi_2P_3-*tI*960 at about 1020 °C (highlighted in green). Inset shows the crystal structure of the known KSi_2P_3-*mC*96 compound.

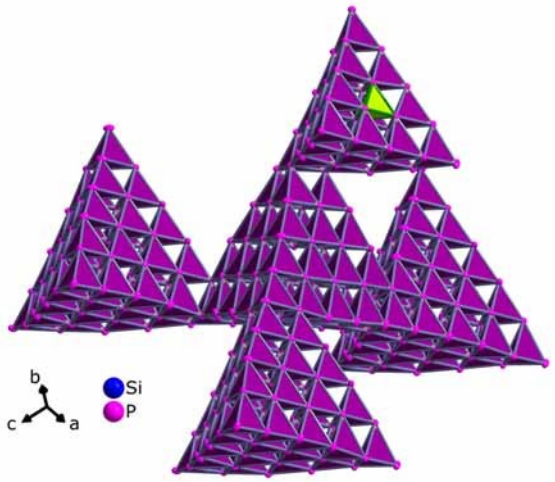

Figure 5.3 Three-dimensional fused T5 supertetrahedra composed of SiP_4 tetrahedra in KSi_2P_3-*tI*960. Every T5 cluster lacks a central silicon atom indicated by the green empty tetrahedron in the upper T5 cluster, where one layer of SiP_4 tetrahedra was removed for clarity.

Every T5 cluster features a missing silicon site in its center, affecting the adjacent four phosphorus atoms by shifting them slightly towards the vacancy. This leads to shorter average P–P distances of 3.2 Å compared to 3.7 Å of the phosphorus atoms not neighboring the missing site. This appears counter-intuitive but has been already observed in several T5 supertetrahedral compounds, such as B_2S_3,[40]

$LiSi_2P_3$,[16] *HT*- and *LT*-$NaSi_2P_3$[31] or UCR-15.[41] A likely explanation could be the preservation of charge neutrality in the interior of the T5 entity, since the T5 cluster is a section of the sphalerite-type structure with silicon defects resulting in the sum formula of Si_3P_4. However, this binary compound has not been confirmed experimentally, but predicted by DFT calculations.[42-43] The T5 clusters share one common SiP_4 tetrahedron resulting in a three-dimensional anionic network with giant voids interpenetrated by a second crystallographically equivalent network. These can be ascribed hierarchically to a diamond type network, resembling the structure of homeotypic *HT*-$NaSi_2P_3$.[31]

Table 5.1 Single crystal data of the high temperature polymorph KSi_2P_3-*tI*960, measured at 25 °C on a Bruker D8 Quest diffractometer.

Formula	KSi_2P_3-*tI*960
space group	$I4_1/acd$ (No. 142)
a / Å	21.9221(15)
c / Å	39.868(3)
V_{cell} / Å^3	19160(3)
Z	128
$\rho_{X\text{-}ray}$ / g·cm^{-3}	2.088
λ / Å	0.71073 (Mo-Kα)
μ / mm^{-1}	1.937
Θ-range / °	2.120 – 30.586
reflections measured	459701
independent reflections	7358
parameters	283
R_σ	0.0095
R_{int}	0.0452
R_1 ($F^2>2\sigma(F^2)$) / all	0.0391 / 0.0438
wR_2 ($F^2>2\sigma(F^2)$) / all	0.0919 / 0.0951
Goof	1.102
restraints	1
$\Delta\rho_{max/min}$ / e·Å^{-3}	+1.610 / -1.374

The potassium ions reside in big cavities of the supertetrahedral networks with large displacement factors and an average occupancy of 0.4. All eleven potassium positions are partially occupied and thus disordered (see Figure 5.4), similar to *HT*-$NaSi_2P_3$, which indicates mobility of potassium ions already at room temperature. KSi_2P_3-*tI*960 goes through displacive phase transitions upon cooling. As shown in Figure 5.5, KSi_2P_3-*tI*960 exhibits a splitting of the most intense reflections at a diffraction angle range of 13.1 to 13.7° (Mo-$K\alpha_1$) at 155 °C. Two of these split reflections approach each other while the third moves towards a higher angle of about 14° beginning at 80 °C, indicating a third phase transition. These phase transitions occur upon heating and cooling of a KSi_2P_3 sample making this T5 compound enantiotropic (see Figure 5.5).

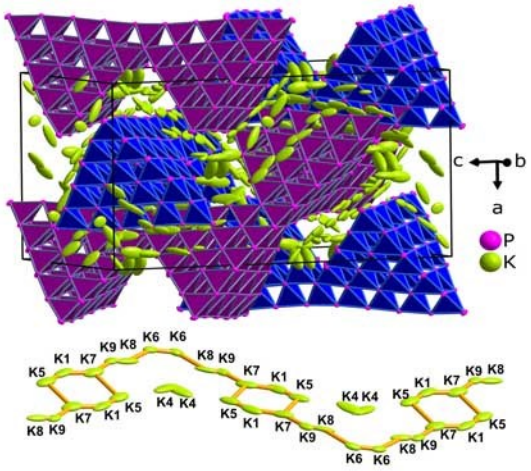

Figure 5.4 Unit cell of KSi_2P_3-*tI*960 with large displacements of the K ions (top, ellipsoids with 90 % probability) and K positions in the voids along [111] indicating a possible ion migration pathway (bottom, ellipsoids with 50 % probability).

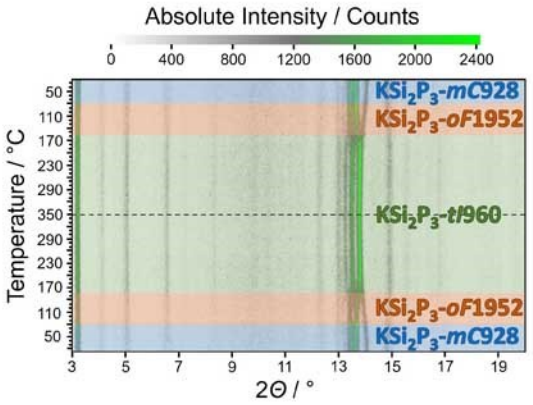

Figure 5.5 High temperature X-ray powder diffraction (Mo-$K\alpha_1$) of a KSi_2P_3-*mC*928 sample upon heating to 350 °C and subsequent cooling. KSi_2P_3-*mC*928 (highlighted in blue) transforms at 80 °C to KSi_2P_3-*oF*1952 (orange) before a further phase transition at 155 °C yields KSi_2P_3-*tI*960 (green). The same phase transitions are observable upon cooling making the T5 compound enantiotropic.

We were not able to synthesize suitable single-crystals of the two low temperature modifications mainly due to twinning. Therefore, we stabilized the different modifications for powder diffraction analysis at ambient conditions. While the room temperature modification is easily producible with conventional

solid-state methods, small amounts of the other modification could only be obtained by a modified synthesis as described in the Supporting Information. The Cu-Kα_1 diffraction patterns and Rietveld fits of the respective modifications are shown in Figure 5.6 (enlarged in the SI Figures C1-3) highlighting their most prominent differences consisting in the splitting, the intensity distribution, and the shifting towards higher diffraction angles of the indicated reflections. Acceptable refinements were obtained by *translationsgleiche* (*t*2) symmetry reductions from tetragonal KSi_2P_3-*tI*960 (spacegroup $I4_1/acd$) to the orthorhombic and monoclinic subgroups of KSi_2P_3-*oF*1952 (*Fddd*) and KSi_2P_3-*mC*928 (*C*2/*c*). The potassium positions were calculated from the symmetry reduced single-crystal structure data of KSi_2P_3-*tI*960. Therefore, these positions do not strictly follow the *Bärnighausen tree* while silicon and phosphorus do. The displacive phase transitions are mainly contractions of the crystal structure as visible in Table 5.2, thus increasing the crystallographic density along with the symmetry reduction (note that the cell parameters given in Table 5.2 appear dissimilar due to different space groups).

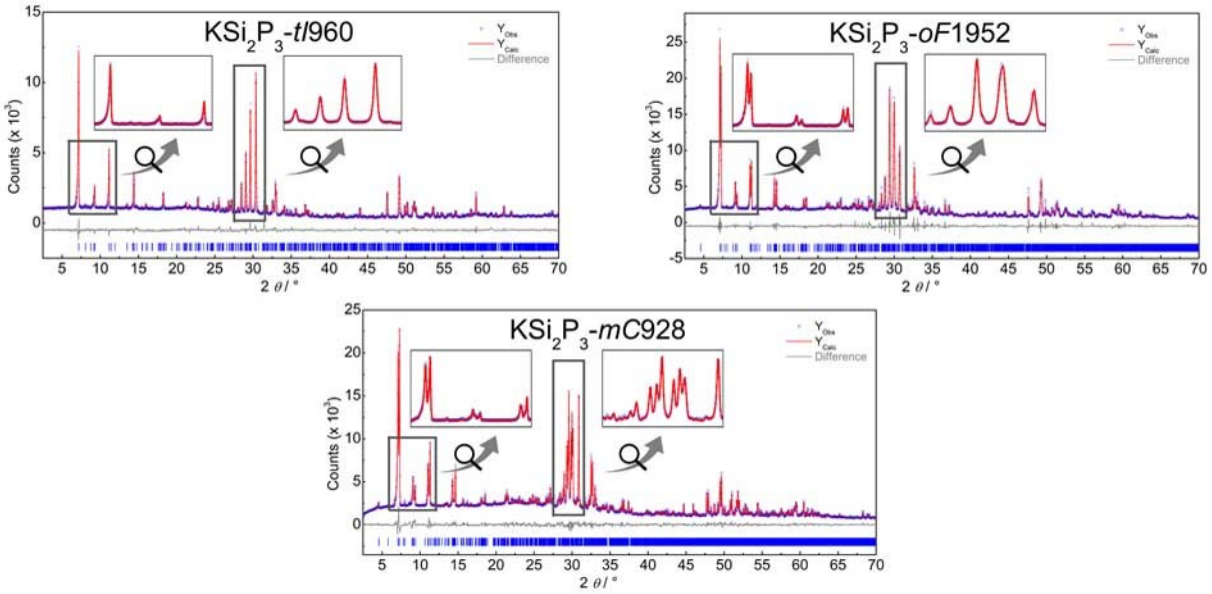

Figure 5.6 X-ray powder diffraction patterns (Cu-Kα_1) of tetragonal (top, left), orthorhombic (top, right) and monoclinic (bottom) KSi_2P_3.

We have confirmed the composition and structure model of KSi_2P_3-*mC*928 with EDX (Figure C4, Table C7) and MAS-NMR measurements. The ^{29}Si spectrum (Figure C5) has broad signals between δ (^{29}Si) = -12 to -26 ppm originating from 32 crystallographically inequivalent silicon atoms on general Wyckoff sites. Since the structure of KSi_2P_3-*mC*928 is homeotypic to *HT*-$NaSi_2P_3$, the ^{31}P spectra are comparable

Table 5.2 Rietveld refinement results of the T5 KSi_2P_3 modifications.

Modification	KSi_2P_3-*tI*960	KSi_2P_3-*oF*1952	KSi_2P_3-*mC*928
space group	$I4_1/acd$ (No. 142)	*Fddd* (No. 70)	*C*2/*c* (No. 15)
stability range / °C	> 155	155 – 80	< 80
a / Å	21.8826(3)	31.5291(10)	31.8337(4)
b / Å	21.8826(3)	30.5475(5)	30.4796(3)
c / Å	40.2923(8)	39.9611(13)	25.2909(2)
β / °	90	90	128.7029(8)
V_{cell} / Å^3	19293.8(6)	38487(2)	19150.3(4)
$\rho_{X\text{-}ray}$ / g·cm^{-3}	2.07651(6)	2.08417(12)	2.11092(5)

as shown in Figure 5.7. KSi_2P_3-*mC*928 exhibits four broad signals within almost the same chemical shift range compared to the tetragonal sodium phase. Integration of these signals in the KSi_2P_3-*mC*928 spectrum yields the same intensity distribution of 4:4:3:1 as in *HT*-$NaSi_2P_3$.[31] The resonance pattern of KSi_2P_3-*mC*928 is more complicated than that of *HT*-$NaSi_2P_3$ due to the symmetry reduction from tetragonal to monoclinic, which leads to splitting of all resonances and impeding a simple intensity assignment to the respective phosphorus atoms. Assuming that the upfield signal at δ (^{31}P) = -298.7 ppm is the result of only one phosphorus atom, a sectional intensity integration of the whole spectrum is possible. It results in 49 distinct atoms being very close to the number of 48 atoms as predicted by X-ray diffraction. Hence, the NMR measurements are in line with the structure.

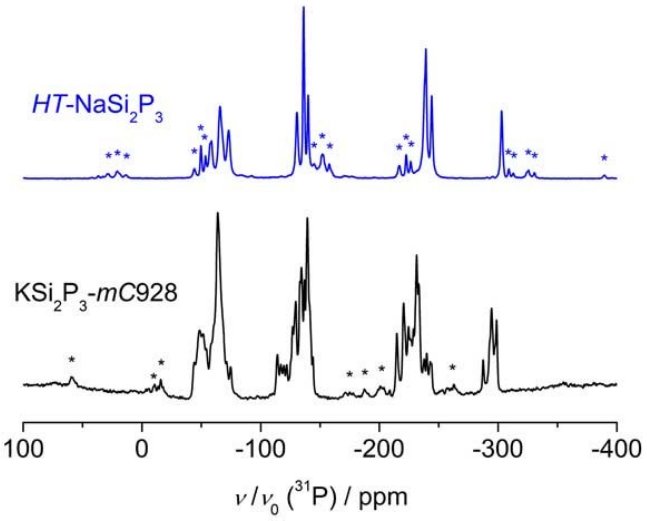

Figure 5.7 Normalized ^{31}P MAS-NMR spectra of *HT*-$NaSi_2P_3$ (top, blue) and KSi_2P_3-*mC*928 (bottom, black) at 25 kHz and a magnetic field of B_0 = 11.7 T. Asterisks indicate rotational side bands.

We have identified possible migration pathways of all polymorphs of KSi_2P_3 from geometrical calculations yielding four large channels through the structure, which are connected by short passages along every supertetrahedral face. This indicates a 3D ion conduction similar to $NaSi_2P_3$. The calculated migration paths are visualized in Figure C6-C8 in the Supporting Information.

We have shown recently that ionic conductivity in supertetrahedral phosphidosilicates increases with increasing cluster size. [31] In view of the T5 structure of KSi_2P_3, high K-ion mobility seems more likely than in the T3 structure. We applied electrochemical impedance spectroscopy (EIS) and potentiostatic polarization measurements as described in the SI on several samples from different batches to assess the ionic and electronic conductivity. All results are listed in Table C9 and C10, and a representative impedance spectrum at -20 °C (sample 2b in Table C9) is shown in Figure 5.8. The measurements were performed at low temperatures to deconvolute the bulk properties of the material and to avoid phase changes that already occur at 80 °C, which may influence the performance. The spectrum contains high and low frequency contributions followed by a spike resulting from the polarization of K ions at the blocking electrodes at low frequencies. The spectrum is fitted with the equivalent circuit model depicted in the inset in Figure 5.8. For the high frequency semicircle modelled by R1-CPE1, an effective capacitance $C_{eff} = (Q/(R^{\alpha-1}))^{1/\alpha}$ of 8 pF is calculated that corresponds to a relative permittivity of 24. This is a typical value for the bulk contributions of a solid inorganic material.[44] The low frequency semicircle (R2-CPE2) possesses a much larger C_{eff} of $9 \cdot 10^{-7}$ F, thus it presumably stems from grain boundaries or a surface layer.[44] The low frequency semicircle CPE3 models the polarization of ions at the electrode. The measured ionic conductivities σ_{bulk} (K^+) of nine samples from three different batches (cf. Table C9) are between $0.13 \cdot 10^{-4}$ and $2.6 \cdot 10^{-4}$ S/cm with an average activation energy of 0.20±0.04 eV. The scatter of conductivities is typical for a solid ion conductor as previously revealed in a round robin study of sulfide electrolytes,[45] and can be rationalized by batch to batch variations as well as differences in pellet preparation, annealing and sputtering of each sample. The highest bulk conductivity we found is $2.6 \cdot 10^{-4}$ S/cm at room temperature with an activation energy of 0.21 eV (plotted in Figure C9), which is consistent with the averaged activation energy of the high frequency semicircle of all samples (0.20±0.04 eV). This result is directly compared to literature data in Figure 5.1, highlighting its uniqueness as first non-oxide K ion conductor with high ionic conductivity at room temperature and below (down to -20 °C) and a low activation energy, indicating facile ion migration within the large channels of the structure. KSi_2P_3 exhibits an even higher ionic conductivity than K-β-Alumina single-crystals. Compared to other

potassium ion conductors, KSi_2P_3 contains neither redox active transition metals nor expensive or rare elements.

The measured total ionic conductivity ranges from $0.045 \cdot 10^{-4}$ to $2.0 \cdot 10^{-4}$ S/cm and can be calculated from R_{tot} as sum of R1+R2 with $\sigma_{tot} = d/(A \cdot R_{tot})$ with d being the thickness and A the area of the sample. This shows that even the total ionic conductivity is reasonably fast for an ionic conductor at room temperature. The activation energy of the low frequency semicircle (R2-CPE2) of 0.19±0.03 eV resembles the activation energy of the bulk process (also cf. Figure C9). Thus, there is no indication of the presence of highly resistive grain boundaries. The similar activation energy rather points to a current constriction phenomenon that could result from a limited contact area between the grains, which is consistent with the low geometrical density of 77±3 % of the sample pellets.[46] Therefore, by optimizing the sample preparation and microstructure, the total conductivity may be enhanced further.

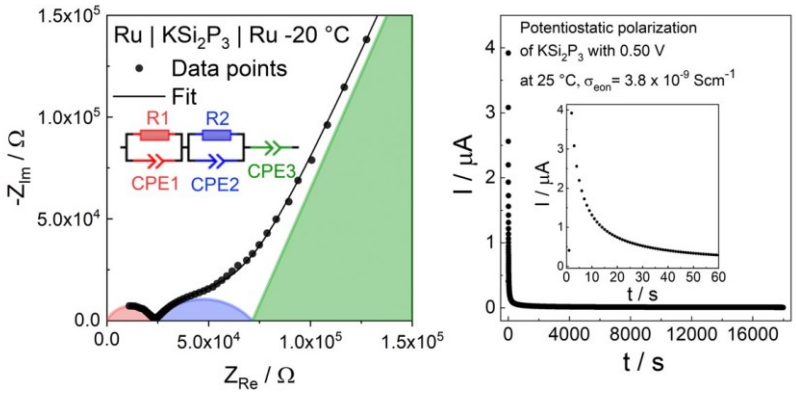

Figure 5.8 Left: Impedance spectra of KSi_2P_3 at -20 °C (sample 6 in Table C9), fitted with the equivalent circuit model shown in the inset. The spectrum can be deconvoluted into bulk (high frequency semicircle R1CPE1) and surface/interlayer contributions (low frequency semicircle). Right: Potentiostatic polarization curve over 5 h showing a low electronic conductivity of 3.8×10^{-9} S/cm. Inset shows data at short times.

The partial electronic conductivity was measured by a potentiostatic polarization experiment over several hours at 0.25 and 0.5 V for several samples (cf. Table C10). A representative plot is shown in Figure 5.8 (right). The electronic conductivity ranges from $0.09 \cdot 10^{-8}$ to $1.1 \cdot 10^{-8}$ S/cm, resulting in a transference number $\tau_i = \sigma_{ion}/(\sigma_{ion}+\sigma_{eon})$ of 0.9998. This suggests that this material can be classified as a predominantly ionic conductor.

5.4 Conclusion

In summary, we have identified three new polymorphs of KSi_2P_3 with T5 supertetrahedra and K-ion conductivities up to $2.6 \cdot 10^{-4}$ S/cm at 25 °C. The hitherto known modification consists of T3 supertetrahedra without partially occupied K sites, which hampers ion conduction. We demonstrate fast potassium ion conduction through three-dimensional connected voids between the large T5 supertetrahedra. KSi_2P_3 contains low cost, non-redox active and abundant elements. As the first non-oxide solid material, KSi_2P_3 extents the compositional space of solid potassium ion conductors, which is key for the rational design of further potassium solid electrolytes. Further investigations must show whether these compounds are suitable for use in batteries.

5.5 Experimental Section

Due to the moisture sensitivity of the title compound all experiments and sample manipulations were conducted at inert conditions in argon filled gloveboxes. The synthesis and further experimental details are compiled in the Supporting Information.

5.6 References

[1] M. Armand, J. M. Tarascon, *Nature* **2008**, *451*, 652.

[2] J. C. Bachman, S. Muy, A. Grimaud, H. H. Chang, N. Pour, S. F. Lux, O. Paschos, F. Maglia, S. Lupart, P. Lamp, L. Giordano, Y. Shao-Horn, *Chem. Rev.* **2016**, *116*, 140.

[3] Y. Wang, S. Song, C. Xu, N. Hu, J. Molenda, L. Lu, *Nano Materials Science* **2019**, *1*, 91.

[4] Z. Zhang, Y. Shao, B. Lotsch, Y.-S. Hu, H. Li, J. Janek, L. F. Nazar, C.-W. Nan, J. Maier, M. Armand, L. Chen, *Energy Environ. Sci.* **2018**, *11*, 1945.

[5] R. Chen, W. Qu, X. Guo, L. Li, F. Wu, *Mater. Horizons* **2016**, *3*, 487.

[6] Y.-G. Lee, S. Fujiki, C. Jung, N. Suzuki, N. Yashiro, R. Omoda, D.-S. Ko, T. Shiratsuchi, T. Sugimoto, S. Ryu, J. H. Ku, T. Watanabe, Y. Park, Y. Aihara, D. Im, I. T. Han, *Nat. Energy* **2020**, *5*, 299.

[7] Z. Liu, W. Fu, E. A. Payzant, X. Yu, Z. Wu, N. J. Dudney, J. Kiggans, K. Hong, A. J. Rondinone, C. Liang, *J. Am. Chem. Soc.* **2013**, *135*, 975.

[8] M. A. Kraft, S. P. Culver, M. Calderon, F. Böcher, T. Krauskopf, A. Senyshyn, C. Dietrich, A. Zevalkink, J. Janek, W. G. Zeier, *J. Am. Chem. Soc.* **2017**, *139*, 10909.

[9] M. A. Kraft, S. Ohno, T. Zinkevich, R. Koerver, S. P. Culver, T. Fuchs, A. Senyshyn, S. Indris, B. J. Morgan, W. G. Zeier, *J. Am. Chem. Soc.* **2018**, *140*, 16330.

[10] N. Kamaya, K. Homma, Y. Yamakawa, M. Hirayama, R. Kanno, M. Yonemura, T. Kamiyama, Y. Kato, S. Hama, K. Kawamoto, A. Mitsui, *Nat. Mater.* **2011**, *10*, 682.

[11] X. Li, J. Liang, J. Luo, M. Norouzi Banis, C. Wang, W. Li, S. Deng, C. Yu, F. Zhao, Y. Hu, T.-K. Sham, L. Zhang, S. Zhao, S. Lu, H. Huang, R. Li, K. R. Adair, X. Sun, *Energy Environ. Sci.* **2019**, *12*, 2665.

[12] H.-J. Steiner, H. D. Lutz, *Z. Anorg. Allg. Chem.* **1992**, *613*, 26.

[13] T. Asano, A. Sakai, S. Ouchi, M. Sakaida, A. Miyazaki, S. Hasegawa, *Adv. Mater.* **2018**, *30*, 1803075.

[14] L. Toffoletti, H. Kirchhain, J. Landesfeind, W. Klein, L. van Wüllen, H. A. Gasteiger, T. F. Fässler, *Chem. - Eur. J.* **2016**, *22*, 17635.

[15] H. Eickhoff, L. Toffoletti, W. Klein, G. Raudaschl-Sieber, T. F. Fässler, *Inorg. Chem.* **2017**, *56*, 6688.

[16] A. Haffner, T. Bräuniger, D. Johrendt, *Angew. Chem. Int. Ed.* **2016**, *55*, 13585.

[17] S. Strangmüller, H. Eickhoff, D. Müller, W. Klein, G. Raudaschl-Sieber, H. Kirchhain, C. Sedlmeier, V. Baran, A. Senyshyn, V. L. Deringer, L. van Wüllen, H. A. Gasteiger, T. F. Fässler, *J. Am. Chem. Soc.* **2019**, *141*, 14200.

[18] K. Vignarooban, R. Kushagra, A. Elango, P. Badami, B. E. Mellander, X. Xu, T. G. Tucker, C. Nam, A. M. Kannan, *Int. J. Hydrogen Energy* **2016**, *41*, 2829.

[19] M. Sawicki, L. L. Shaw, *RSC Adv.* **2015**, *5*, 53129.

[20] N. Yabuuchi, K. Kubota, M. Dahbi, S. Komaba, *Chem. Rev.* **2014**, *114*, 11636.

[21] H. Pan, Y.-S. Hu, L. Chen, *Energy Environ. Sci.* **2013**, 6, 2338.

[22] H. Vikström, S. Davidsson, M. Höök, *Appl. Energy* **2013**, *110*, 252.

[23] A. Hayashi, K. Noi, A. Sakuda, M. Tatsumisago, *Nat. Commun.* **2012**, *3*, 856.

[24] M. Kaus, M. Guin, M. Yavuz, M. Knapp, F. Tietz, O. Guillon, H. Ehrenberg, S. Indris, *J. Phys. Chem. C* **2017**, *121*, 1449.

[25] M. Guin, F. Tietz, O. Guillon, *Solid State Ionics* **2016**, *293*, 18.

[26] A. Hooper, *J. Phys. D: Appl. Phys.* **1977**, *10*, 1487.

[27] L. Zhang, D. Zhang, K. Yang, X. Yan, L. Wang, J. Mi, B. Xu, Y. Li, *Adv. Sci.* **2016**, *3*, 1600089.

[28] A. Hayashi, N. Masuzawa, S. Yubuchi, F. Tsuji, C. Hotehama, A. Sakuda, M. Tatsumisago, *Nat. Commun.* **2019**, *10*, 5266.

[29] Z. Zhang, E. Ramos, F. Lalère, A. Assoud, K. Kaup, P. Hartman, L. F. Nazar, *Energy Environ. Sci.* **2018**, *11*, 87.

[30] M. Duchardt, U. Ruschewitz, S. Adams, S. Dehnen, B. Roling, *Angew. Chem. Int. Ed.* **2018**, *57*, 1351.

[31] A. Haffner, A.-K. Hatz, I. Moudrakovski, B. V. Lotsch, D. Johrendt, *Angew. Chem. Int. Ed.* **2018**, *57*, 6155.

[32] S. Komaba, T. Hasegawa, M. Dahbi, K. Kubota, *Electrochem. Commun.* **2015**, *60*, 172.

[33] J. C. Pramudita, D. Sehrawat, D. Goonetilleke, N. Sharma, *Adv. Energy Mater.* **2017**, *7*, 1602911.

[34] H. Yuan, H. Li, T. Zhang, G. Li, T. He, F. Du, S. Feng, *J. Mater. Chem. A* **2018**, *6*, 8413.

[35] A. Eftekhari, *J. Power Sources* **2004**, *126*, 221.

[36] B. Eisenmann, M. Somer, *Z. Naturforsch. B* **1984**, *39*, 736.

[37] K. Feng, L. Kang, W. Yin, W. Hao, Z. Lin, J. Yao, Y. Wu, *J. Solid State Chem.* **2013**, *205*, 129.

[38] H. Li, J. Kim, T. L. Groy, M. O'Keeffe, O. M. Yaghi, *J. Am. Chem. Soc.* **2001**, *123*, 4867.

[39] CCDC 2058594 contains the supplementary crystallographic data for this paper. These data can be obtained free of charge from the FIZ Karlsruhe via www.ccdc.cam.ac.uk/structures.

[40] T. Sasaki, H. Takizawa, K. Uheda, T. Yamashita, T. Endo, *J. Solid State Chem.* **2002**, *166*, 164.

[41] C. Wang, X. Bu, N. Zheng, P. Feng, *J. Am. Chem. Soc.* **2002**, *124*, 10268.

[42] M. Huang, Y. P. Feng, A. T. L. Lim, J. C. Zheng, *Phys. Rev. B* **2004**, *69*, 054112.

[43] G. Gopal Khan, S. J. Clark, N. R. Bandyopadhyay, *Int. J. Mod. Phys. B* **2010**, *24*, 5487.

[44] J. T. S. Irvine, D. C. Sinclair, A. R. West, *Adv. Mater.* **1990**, *2*, 132.

[45] S. Ohno, T. Bernges, J. Buchheim, M. Duchardt, A.-K. Hatz, M. A. Kraft, H. Kwak, A. L. Santhosha, Z. Liu, N. Minafra, F. Tsuji, A. Sakuda, R. Schlem, S. Xiong, Z. Zhang, P. Adelhelm, H. Chen, A. Hayashi, Y. S. Jung, B. V. Lotsch, B. Roling, N. M. Vargas-Barbosa, W. G. Zeier, *ACS Energy Lett.* **2020**, 910.

[46] J. Fleig, J. Maier, *J. Am. Ceram. Soc.* **1999**, *82*, 3485-3493.

6 The Phosphidosilicates $SrSi_7P_{10}$ and $BaSi_7P_{10}$

Arthur Haffner, Valentin Weippert, and Dirk Johrendt

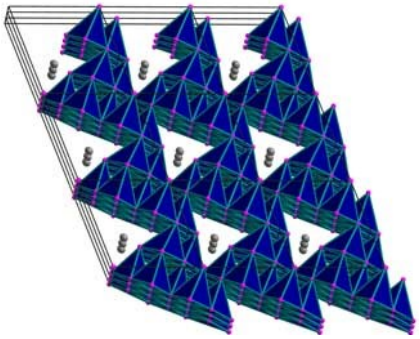

published in: *Zeitschrift für Anorganische und Allgemeine Chemie* **2021**, *647*, 326-330.

6.1 Abstract

The new phosphidosilicates $SrSi_7P_{10}$ and $BaSi_7P_{10}$ were synthesized by solid-state reactions, and their crystal structures determined by single-crystal X-ray diffraction [$P1$, $Z = 1$, $SrSi_7P_{10}$: $a = 6.1521(1)$ Å, $b = 8.0420(2)$ Å, $c = 8.1374(2)$ Å, $\alpha = 106.854(1)°$, $\beta = 99.020(1)°$, $\gamma = 105.190(1)°$; $BaSi_7P_{10}$: $a = 6.1537(1)$ Å, $b = 8.0423(2)$ Å, $c = 8.1401(2)$ Å, $\alpha = 106.863(1)°$, $\beta = 99.050(1)°$, $\gamma = 105.188(1)°$]. The compounds crystallize in a new triclinic structure type with vertex sharing SiP_4 tetrahedra, which assemble a non-centrosymmetric diamond-like network of T2 supertetrahedra. The alkaline earth cations reside in cuboctahedral voids. ^{31}P solid-state MAS-NMR spectra confirm the crystal structure. $SrSi_7P_{10}$ and $BaSi_7P_{10}$ exhibit the lowest charged SiP network in phosphidosilicates so far. Full-potential DFT calculations classify both compounds as semiconductors with small indirect band gaps of 1.1 eV.

6.2 Introduction

Posphidosilicates gain increasing attention due to its versatile structure chemistry and the abundance of its constituting elements. Relatively few representatives with alkaline and alkaline earth metals were reported in the 1970s and 1980s. The *ortho*-compounds AE_4SiP_4 (AE = Ca, Sr, Ba)[1] contain isolated SiP_4 tetrahedra, whereas edge- or vertex-condensed tetrahedra occur in Na_5SiP_3,[2] K_2SiP_2[3] or $Ba_3Si_4P_6$.[4] Networks of vertex-shared SiP_4 tetrahedra were observed likewise in $MgSiP_2$ with chalcopyrite-type structure.[5] Only recently, further alkaline and alkaline earth phosphidosilicates were reported, which comprise homonuclear Si–Si or P–P bonding, or with SiP_4 tetrahedra which coalesce into supertetrahedral entities.[6-12] Examples with P–P bonds are the compounds AE_2SiP_4[13-15] (AE = Sr, Ba, Eu), where all phosphorus atoms form dimers. Additionally, *Mark et al.* demonstrated the thermal conductivity and SHG responses of $Ba_2Si_3P_6$ making this compound potentially interesting for IR-NLO materials.[16] Most of the known alkaline earth phosphidosilicates are relatively rich of AE^{2+} cations resulting in highly charged SiP frameworks. The only known Si-P binary compounds are SiP and SiP_2 with either Si–Si or P–P bonds,[17,18] whereas the Si_3N_4 analogue Si_3P_4 has been predicted only theoretically,[19] one may ask for compounds with lower charged networks closer to Si_3P_4. Therefore, we now focused on AE^{2+}-poor phosphidosilicates and found $SrSi_7P_{10}$ and $BaSi_7P_{10}$ with the lowest charged SiP network so far known in phosphidosilicates.

6.3 Results and Discussion

The title compounds were synthesized by solid-state reactions and several annealing steps of respective elemental mixtures under argon atmosphere in alumina or glassy-carbon crucibles. After the procedure, polycrystalline black powders with 1.1 % and 5.1 % silicon as impurities were obtained (Figure 6.1).

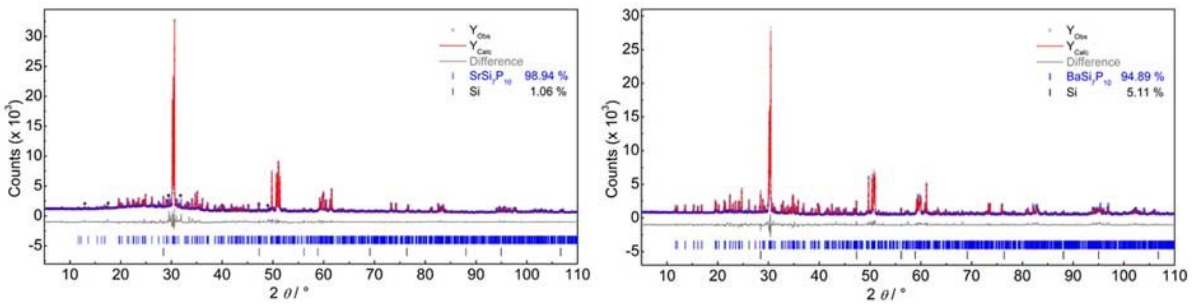

Figure 6.1 X-ray powder diffraction patterns of $SrSi_7P_{10}$ (left) and $BaSi_7P_{10}$ (right) displayed as blue circles with Rietveld-fit (red line) and difference (grey line). Both samples contain minor amounts of unreacted Si and in the $SrSi_7P_{10}$ sample an additional unknown phase (marked with asterisks).

Small single-crystals were selected from the samples for EDX analysis and single-crystal X-ray diffraction. The EDX analysis confirmed the chemical composition and the X-ray diffraction data revealed triclinic unit cells in space group *P*1 with almost identical lattice parameters for both compounds. The crystal structures were solved by direct methods and refined using least-squares methods with SHELX. Crystallographic data are compiled in Table 6.1.

Table 6.1 Single-crystal data of $SrSi_7P_{10}$ and $BaSi_7P_{10}$.

Formula	$SrSi_7P_{10}$	$BaSi_7P_{10}$
space group	*P*1 (no. 1)	*P*1 (no. 1)
a / Å	6.1521(1)	6.1537(1)
b / Å	8.0420(2)	8.0423(2)
c / Å	8.1374(2)	8.1401(2)
α / °	106.854(1)	106.863(1)
β / °	99.020(1)	99.050(1)
γ / °	105.190(1)	105.188(1)
V_{cell} / Å^3	359.844(14)	359.998(14)
Z	1	1
$\rho_{X\text{-}ray}$ / g·cm^{-3}	2.741	2.969
μ / mm^{-1}	5.411	4.422
Θ-range / °	2.799 - 36.362	2.702 - 30.760
T / K	295(2)	295(2)
reflections measured	14508	15294
independent reflections	6659	4411
parameters	163	163
R_σ	0.0712	0.0293
R_{int}	0.0282	0.0354
R_1 ($F^2>2\sigma(F^2)$) / all	0.0279 / 0.0341	0.0254 / 0.0283
wR_2 ($F^2>2\sigma(F^2)$) / all	0.0552 / 0.0583	0.0580 / 0.0593
Goof	0.711	1.073
Flack *x*	0.017(4)	0.047(6)
$\Delta\rho_{max/min}$ / e·Å^{-3}	+0.549 / -0.695	+0.928 / -1.206

The basic building units of these compounds are SiP_4 tetrahedra condensed by vertices to T2 supertetrahedra (Figure 6.2, yellow) according to the *Yaghi* [20] notation. By zigzag fusion of these entities, which was sparely observed in related compounds,[6, 10-11, 21-28] chains are formed, depicted in turquoise in Figure 6.2. Further vertex-edge condensation of these fused T2-chain motifs – to the best of our knowledge only once observed [29] – yields in T2-layers, which are propagating in the *ab* plane, visualized by condensation of the blue T2 chains in Figure 6.2. These layers are stacked along the *c* axis with symmetrically equivalent layers, exclusively by common T2 vertices, resulting in a dense three-dimensional network (see Figure 6.3). In addition, one SiP_4 tetrahedron belongs to no T2 supertetrahedron but links the layers discussed above, twice by vertex and twice by vertex-edge connection, enlarging the condensation degree of the anionic $[Si_7P_{10}]^{2-}$ network.

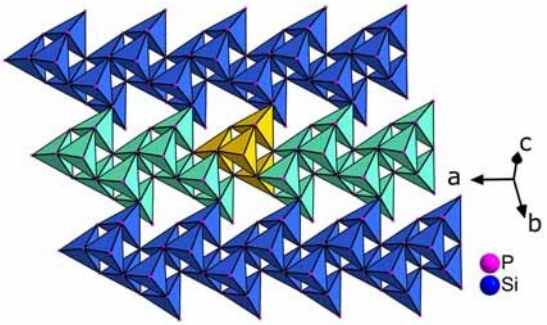

Figure 6.2 View on the *ab* plane of a supertetrahedral layer of $SrSi_7P_{10}$ composed of zigzag fused T2 entities (yellow) to chains (turquoise) linked by vertex-edge connections with other symmetrically equivalent T2 chains.

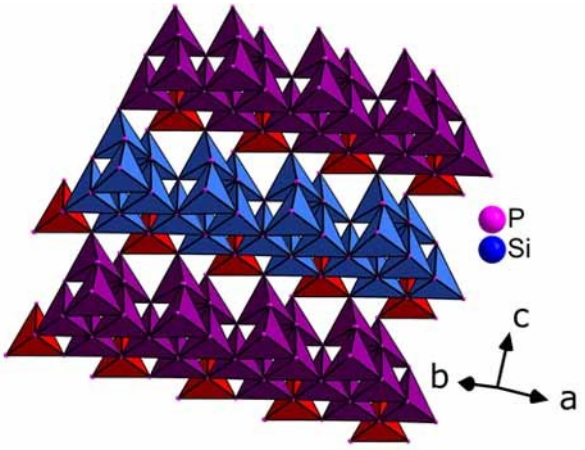

Figure 6.3 T2 layers stacked along the *c* axis by common vertices and the linkage of the only SiP_4 tetrahedron not belonging to supertetrahedral entities in $SrSi_7P_{10}$ (red).

This supertetrahedral T2 network topologically complies with a distorted diamond-type network, if one considers only the centers of the supertetrahedra. The distortion of the diamond network arises from the different condensation modes. The alkaline earth cations reside in the supertetrahedral networks forming distorted SrP_{12} and BaP_{12} cuboctahedra, shown in Figure 6.4. Given the rigid anionic network, it is not surprising that the interatomic distances between the alkaline earth and phosphorus atoms have almost identic average values of 3.47 Å for the strontium and 3.50 Å for the barium compound. Consequently, the thermal displacement parameter of Sr is almost doubled compared to $BaSi_7P_{10}$ (Figure 6.4). On the other hand, the *AE*–P distances exceed the typical values observed in other alkaline earth

phosphides and phosphidosilicates, which are in the range of 3.1 Å and 3.3 Å for Sr and Ba, respectively. The longer distances correspond to the unusual high coordination number of 12, and both effects explain the increased thermal displacements of the Ba and Sr sites.

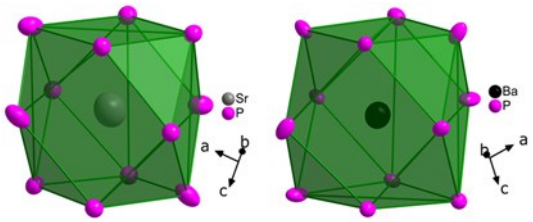

Figure 6.4 SrP_{12} (left) and BaP_{12} (right) cuboctahedra. Thermal displacement parameters of Sr and Ba are enlarged in comparison with P atoms. Ellipsoids are drawn with 99 % probability.

Because of the relatively symmetric coordination of the alkaline earth cations, we examined the barium nuclei with solid-state NMR measurements under MAS conditions. However, the ^{137}Ba nuclei induce no detectible resonance frequency. This originates from large quadrupolar interactions yielding in only few examples for ^{137}Ba NMR experiments. [30,31] In contrast, the ^{31}P NMR spectrum reveals nine resonance frequencies at δ (^{31}P) = −170.3, −166.9, −157.4, −140.7, −131.0, −115.4, −104.5, −48.5 and −31.0 ppm with equal intensities except the resonance at −157.4 ppm with a doubled one (see Figure 6.5, bottom left). This agrees with the crystal structure with ten crystallographically independent phosphorus atoms. A similar NMR pattern was obtained for the $SrSi_7P_{10}$ sample with resonance frequencies of δ (^{31}P) = −170.0, −164.5, −154.8, −139.3, −131.9, −110.3, −98.8, −36.9 and −16.3 ppm, depicted in Figure 6.5 (top left). In contrast, the silicon spectra show only two asymmetric resonance frequencies at δ (^{29}Si) = -29.1 and -22.3 ppm for $SrSi_7P_{10}$ (Figure 6.5, top right) and one asymmetric at δ (^{29}Si) = -26.9 ppm for $BaSi_7P_{10}$ (Figure 6.5, bottom right) instead of seven discrete signals originating from similar chemical shifts. However, the signals occur in the same chemical shift range known from other condensed phosphidosilicates. Unreacted elemental silicon detected by powder X-ray diffraction was not observed in the spectra which would cause a resonance frequency at δ (^{29}Si) = -82.0 ppm. The title compounds are charge neutral according to $Ba^{2+}(Si^{4+})_7(P^{3-})_{10}$ and expectedly semiconducting with relatively small bandgaps according to the black color. DFT calculations of the still unknown binary Si_3P_4 with a pseudo-cubic structure predicted a small gap of 0.134 eV (GGA, certainly too small).[17] Our full potential electronic band structure calculations of both phases reveal almost identical indirect bandgaps of 1.1 eV

for $SrSi_7P_{10}$ and $BaSi_7P_{10}$, respectively. Figure 6.6 shows the band structure of the barium compound. Additionally, we have calculated atom charges using the Bader approach,[32] which gives $Ba^{1.49+}(Si^{1.93+})_7(P^{1.5-})_{10}$.

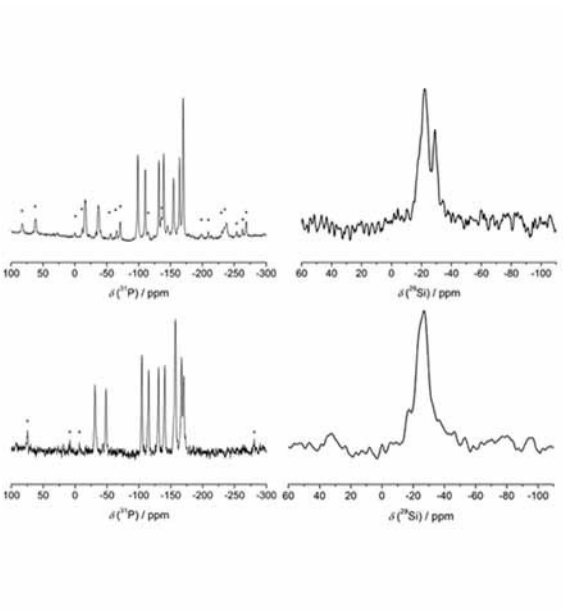

Figure 6.5 ^{31}P and ^{29}Si solid-state NMR spectra under MAS conditions of $SrSi_7P_{10}$ (top) and $BaSi_7P_{10}$ (bottom). Rotation side bands are marked with asterisks; chemical shifts are given in the text.

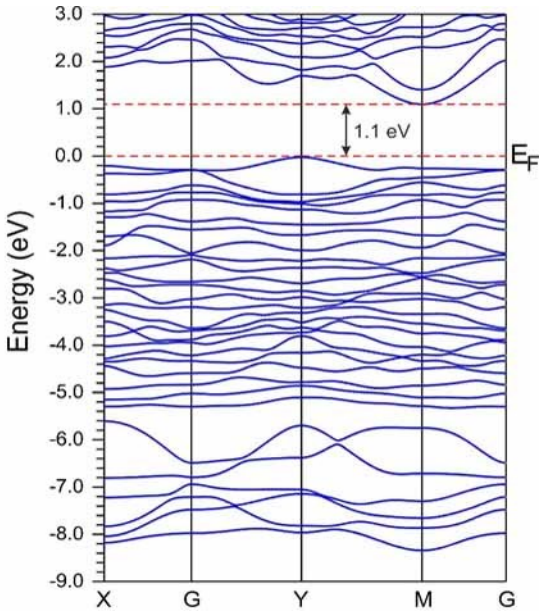

Figure 6.6. Electronic band structure of $BaSi_7P_{10}$. The energy zero is taken at the Fermi level

6.4 Conclusion

$SrSi_7P_{10}$ and $BaSi_7P_{10}$ crystalize in a new triclinic structure type with vertex sharing SiP_4 tetrahedra assembling T2 supertetrahedra. These entities are fused and linked to form dense non-centrosymmetric anionic networks, which are hierarchical variants of the diamond-type structure. The alkaline earth cations reside in cuboctahedral voids of the framework with slightly elongated *AE*–P distances compared to related phosphides and phosphidosilicates. The crystal structures were validated by solid-state ^{31}P MAS-NMR. Full potential DFT calculations reveal indirect bandgaps of ca. 1.1 eV for $SrSi_7P_{10}$ and $BaSi_7P_{10}$, respectively, which may be interesting with respect to potential thermoelectric properties. Moreover, in view of the still unknown binary Si_3P_4, the new compounds $SrSi_7P_{10}$ and $BaSi_7P_{10}$ exhibit the lowest charged SiP network in phosphidosilicates so far.

6.5 Experimental Section

Synthesis. Stoichiometric mixtures of Sr metal (SMT Metalle Wimmer, 99.95 %) or Ba metal (Sigma Aldrich, 99.99 %) were mixed with silicon powder (Smart Elements, 99.8 %) and red phosphorus (Chempur, > 99 %) and filled in alumina or glassy-carbon crucibles and welded in silica ampoules under argon atmosphere. The ampoules were placed in tube furnaces and heated to 950 °C for 90 h. The intermediates were homogenized, compacted to a pellet and heated twice at the same temperature for 40 h. The products were black powders stable in air for days and contained 1 % and 5 % silicon impurities, respectively

Single-Crystal X-ray Diffraction. Glass-like black shards were isolated under paraffin oil and transferred into oil filled glass capillaries. Diffraction pattern were recorded using a Bruker D8 Quest diffractometer with a molybdenum X-ray source, Göbel mirror optics and Photon II detector. Reflection data for unit cell determination revealed frequent twinning. Concerning the low symmetry of the compounds, reflections of the whole Ewald's sphere were measured for complete single-crystal datasets. Indexing, integration and absorption correction were performed using APEX3 software.[33] Structure solution and refinement was carried out by SHELXL[34] software and the results were plotted with Diamond.[35] The refinements were conducted without twinning by inversion due to the almost zero Flack parameters given in Table 6.1.

Further details of the crystal structures investigations may be obtained from the joint CCDC/FIZ Karlsruhe online deposition service (Fax: +49-7247-808-666; E-Mail: crysdata@fiz-karlsruhe.de, http://www.fiz-karlsruhe.de/request for deposited data.html) on quoting the depository numbers CSD-2022066 and CSD-2022067.

X-ray Powder Diffraction. Polycrystalline samples were loaded in Hilgenberg glass capillaries and sealed under argon atmosphere to avoid potential hydrolysis of intermediates formed by incomplete reactions. Diffraction patterns of respective compounds were acquired with a Stoe-Stadi P diffractometer in Debye-Scherrer geometry, Ge(111) monochromator and Mythen 1K detector (Dectris) using Cu-$K_{\alpha 1}$ radiation. Based on the single-crystal data the powder diffraction patterns were indexed and refined with Topas. [36]

Solid-State MAS-NMR Spectroscopy. Polycrystalline samples were filled in commercial 2.5 mm rotors for the phosphorus and in 4 mm rotors for the silicon spectra. Data collection was performed in a Bruker Avance III 500 spectrometer with a 11.74 T magnetic field under MAS conditions with a rotation and a

Larmor frequency of 25 kHz and ν_0 (^{31}P) = 202.48 MHz for the phosphorus and of 10 kHz and ν_0 (^{29}Si) = 99.36 MHz for the silicon spectra. All spectra were indirectly referenced to ^{1}H in 100 % TMS at -0.1240 ppm for the 2.5 mm probes and to ^{1}H in 0.1 % TMS in $CDCl_3$ at 0 ppm for the 4 mm probes.

EDX Analysis. Chemical compositions were verified with an EVO MA-10 scanning electron microscope equipped with a Bruker X-Flash 410-M X-ray detector and a field emission gun as electron beam source. Samples were placed on adhesive and conductive carbon pads and inserted into the SEM. The QUANTAX 200 software was used for data processing.

Electronic Structure Calculations. Band structure calculations were performed with the full-potential-linear-augmented plane-wave (FLAPW) method and WIEN2k software package.[37] Electronic correlations and exchanges were considered with utilising PBE[38] and mBJ[39] functionals. Prior to the calculations, the structure models were relaxed yielding no significant changes of the atomic positions.

6.6 References

[1] B. Eisenmann, H. Jordan, H. Schäfer, *Mat. Res. Bull.* **1982**, *17*, 95-99.

[2] B. Eisenmann, M. Somer, *Z. Naturforsch. B* **1985**, *40*, 886-890.

[3] B. Eisenmann, M. Somer, *Z. Naturforsch. B* **1984**, *39*, 736-738.

[4] B. Eisenmann, H. Jordan, H. Schäfer, *Z. Naturforsch. B* **1984**, *39*, 864-867.

[5] A. J. Springthorpe, J. G. Harrison, *Nature* **1969**, *222*, 977.

[6] A. Haffner, T. Bräuniger, D. Johrendt, *Angew. Chem. Int. Ed.* **2016**, *55*, 13585-13588.

[7] L. Toffoletti, H. Kirchhain, J. Landesfeind, W. Klein, L. van Wüllen, H. A. Gasteiger, T. F. Fässler, *Chem. Eur. J.* **2016**, *22*, 17635-17645.

[8] H. Eickhoff, L. Toffoletti, W. Klein, G. Raudaschl-Sieber, T. F. Fässler, *Inorg. Chem.* **2017**, *56*, 6688-6694.

[9] A. Haffner, A. K. Hatz, C. Hoch, B. V. Lotsch, and D. Johrendt, *Eur. J. Inorg. Chem.* **2020**, 617 (2020).

[10] A. Haffner, A.-K. Hatz, I. Moudrakovski, B. V. Lotsch, D. Johrendt, *Angew. Chem. Int. Ed.* **2018**, *57*, 6155-6160.

[11] K. Feng, L. Kang, W. Yin, W. Hao, Z. Lin, J. Yao, Y. Wu, *J. Solid State Chem.* **2013**, *205*, 129-133.

[12] X. Zhang, T. Yu, C. Li, S. Wang, X. Tao, *Z. Anorg. Allg. Chem.* **2015**, *641*, 1545-1549.

[13] A. Haffner, D. Johrendt, *Z. Anorg. Allg. Chem.* **2017**, *643*, 1717-1720.

[14] J. Mark, J.-A. Dolyniuk, N. Tran, K. Kovnir, *Z. Anorg. Allg. Chem.* **2019**, *645*, 242-247.

[15] A. Haffner, V. Weippert, and D. Johrendt, *Z. Anorg. Allg. Chem.* **2020**, *646*, 120 -124.

[16] J. Mark, J. Wang, K. Wu, J. G. Lo, S. Lee, K. Kovnir, *J. Am. Chem. Soc.* **2019**, *141*, 11976-11983.

[17] T. Wadsten, *Chem. Scr.* **1975**, *8*, 63-69.

[18] T. K. Chattopadhyay, H. G. von Schnering, *Z. Kristallogr. – Cryst. Mater.* **1984**, *167*, 1-12.

[19] M. Huang, Y. P. Feng, A. T. L. Lim, J. C. Zheng, *Phys. Rev. B* **2004**, *69*, 054112.

[20] H. Li, J. Kim, T. L. Groy, M. O'Keeffe, O. M. Yaghi, *J. Am. Chem. Soc.* **2001**, *123*, 4867-4868.

[21] T. Sasaki, H. Takizawa, K. Uheda, T. Yamashita, T. Endo, *J. Solid State Chem.* **2002**, *166*, 164-170.

[22] F. Hiltmann, P. zum Hebel, A. Hammerschmidt, B. Krebs, *Z. Anorg. Allg. Chem.* **1993**, *619*, 293-302.

[23] V. Weippert, A. Haffner, A. Stamatopoulos, D. Johrendt, *J. Am. Chem. Soc.* **2019**, *141*, 11245-11252.

[24] H. Lin, J.-N. Shen, L. Chen, L.-M. Wu, *Inorg. Chem.* **2013**, *52*, 10726-10728.

[25] W. Khan, S. Goumri-Said, *RSC Adv.* **2015**, *5*, 9455-9461.

[26] H. Li, C. D. Malliakas, Z. Liu, J. A. Peters, H. Jin, C. D. Morris, L. Zhao, B. W. Wessels, A. J. Freeman, M. G. Kanatzidis, *Chem. Mater.* **2012**, *24*, 4434-4441.

[27] J. H. Liao, M. G. Kanatzidis, *Chem. Mater.* **1993**, *5*, 1561-1569.

[28] H.-W. Ma, G.-C. Guo, M.-S. Wang, G.-W. Zhou, S.-H. Lin, Z.-C. Dong, J.-S. Huang, *Inorg. Chem.* **2003**, *42*, 1366-1370.

[29] H. Wang, H. Yang, W. Wang, C. Xue, Y. Zhang, M. Luo, D. Hu, J. Lin, D. Li, T. Wu, *CrystEngComm* **2017**, *19*, 4709-4712.

[30] S. F. Dec, M. F. Davis, G. E. Maciel, C. E. Bronnimann, J. J. Fitzgerald, S. S. Han, *Inorg. Chem.* **1993**, *32*, 955-959.

[31] K. J. D. MacKenzie, R. H. Meinhold, *Ceram. Int.* **2000**, *26*, 87-92.

[32] R. F. W. Bader, *Atoms in Molecules - A Quantum Theory*, Oxford University Press, London, **1990**.

[33] 2016.5-0 ed., Brucker AXS Inc., Madison, Wisconsin, **2016**.

[34] G. M. Sheldrick, *Acta Crystallogr. A* **2008**, *64*, 112-122.

[35] K. Brandenburg, 3.2k ed., Crystal Impact GbR, Bonn, Germany, **2014**.

[36] A. Coelho, 4.1 ed., Coelho Software, Brisbane, Australia, **2007**.

[37] P. Blaha, K. Schwarz, G. K. H. Madsen, D. Kvasnicka, J. Luitz, Wien2k, An Augmented Plane Wave and Local Orbital Program for Calculating Crystal Properties ed., TU Wien, Vienna, Austria, ISBN3-9501031-1-2, **2006**.

[38] J. P. Perdew, K. Burke, M. Ernzerhof, *Phys. Rev. Lett.* **1996**, *77*, 3865-3868.

[39] F. Tran, P. Blaha, *Phys. Rev. Lett.* **2009**, *102*, 226401

7 Synthesis, Crystal Structure, and Chemical Bonding of Ba_2SiP_4

Arthur Haffner and Dirk Johrendt

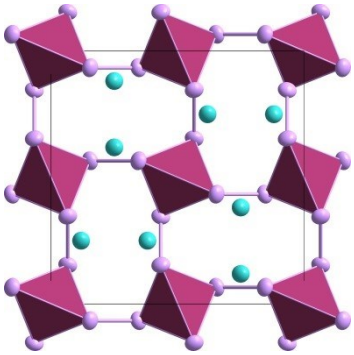

published in: *Zeitschrift für Anorganische und Allgemeine Chemie* **2017**, *643*, 1717-1720.

7.1 Abstract

Ba_2SiP_4 was synthesized by heating of the elements at 1173 K and the crystal structure was determined from single-crystal X-ray diffraction [$I\bar{4}2d$, a = 990.57(3) pm, c = 731.80(3) pm; Z = 4]. The novel structure is homeotypic to hp-Zn_2SiO_4 but the SiP_4-tetrahedra are exclusively bridged via P—P bonds [d(P—P) = 222 pm] which is hitherto unprecedented. The three-dimensional SiP_4 network is analogous to β-cristobalite if oxygen is formally replaced by a P—P dimer. Barium fills the voids and is coordinated by eight phosphorus atoms. DFT calculations indicate covalent Si—P and P—P bonding and an indirect energy gap of ca. 1 eV.

7.2 Introduction

Ternary phosphidosilicates of weak electronegative metals contain SiP_4-tetrahedra which can occur isolated as in the *ortho*-compounds Ba_4SiP_4 [1] and Li_8SiP_4[2] but more common are SiP_4- tetrahedra connected via vertices or edges to form insular entities, chains, layers, or complex three-dimensional networks. Examples are isolated $[Si_2P_6]^{10-}$ anions in Na_5SiP_3,[3] infinite $^1\infty[SiP_{4/2}]^{2-}$ chains in K_2SiP_2,[4] double layers of SiP_4-tetrahedra in KSi_2P_3 or interpenetrating three dimensional $[SiP_{4/2}]^{2-}$ networks in $MgSiP_2$.[5] Phosphidosilicates with transition metals[6-9] and rare-earth metals[10] are likewise known. $CdSiP_2$ and the germanate $ZnGeP_2$ with the tetragonal chalcopyrite-type structure have been studied as nonlinear optical materials.[11,12] Recently reported Li-phosphidosilicates like $LiSi_2P_3$ [13] and Li_2SiP_2 [2] attract considerable interest as Li ion conductors. Due to the same fundamental tetrahedral building unit, the structural chemistry of phosphidosilicates resembles to some extend those of the much bigger families of oxido- and nitridosilicates. One important difference is the possible formation of homonuclear P—P bonds, which can bridge neighboring SiP_4 tetrahedra. Such polyphosphide formation is an additional structural degree of freedom in this class of materials, because such bonds between the anions are unknown (and unlikely) in oxido- and nitridosilicates. Examples for phosphidosilicates with P—P bonds are $LaSi_2P_6$[10] which contains not less than four different polyphosphide units $(P_n)^{(n+2)-}$ with n = 3–6, or the recently published $Li_3Si_3P_7$ with polyphosphide chains.[14] P_2-dimers were found in $AlSiP_3$[15] or $Ca_3Si_8P_{14}$[16] with P—P distances around 220 pm as typical for single bonds.

All hitherto known phosphidosilicates with $[P_n]^{x-}$ groups contain also terminal P atoms and no compound is known, where *all* SiP_4 tetrahedra are connected by P—P bonds. In this paper, we report the synthesis, crystal structure, and chemical bonding of the new phosphidosilicate Ba_2SiP_4 which fills this gap.

7.3 Results and Discussion

Ba_2SiP_4 was synthesized from the elements as an almost black, air and moisture sensitive polycrystalline powder. Single crystals suitable for X-ray diffraction were selected directly from the samples. Ba_2SiP_4 crystallizes tetragonal body-centred in the non-centrosymmetric space group type $I\bar{4}2d$ (no. 122) with the lattice parameters a = 990.57(3) pm and c = 731.80(3) pm. The structure was solved by direct methods and refined with SHELXL.[17] Results of the structure determination together with selected interatomic distances are compiled in Table 7.1.

Table 7.1 Crystallographic data of Ba_2SiP_4.

Formula	Ba_2SiP_4
M_r / g·mol^{-1}	426.65
Crystal system, space group	tetragonal, $I\bar{4}2d$
Temperature / K	298
a / pm	990.57(3)
c / pm	731.80(3)
V / Å^3	718.06(5)
Z	4
Radiation type	Mo-Kα
μ / mm^{-1}	11.84
Crystal size / mm	0.13 × 0.09 × 0.06
Diffractometer	Bruker D8 Quest
Absorption correction	Multi-scan
T_{min}, T_{max}	0.335, 0.705
No. meas., indep., obs. [$I > 2\sigma(I)$] reflections	7860, 789, 775
R_{int}	0.038
$(\sin\theta/\lambda)_{max}$ / Å^{-1}	0.803
$R[F^2 > 2\sigma(F^2)]$, $wR(F^2)$, S	0.013, 0.036, 1.20
No. of reflections	789
No. of parameters	17
$\Delta\rho_{max}$, $\Delta\rho_{min}$ / e·Å^{-3}	0.73, −1.06
Absolute structure parameter	0.012 (10)

Atom positions and equivalent displacement parameters

Atom	Wyck	x	y	z	U_{eq}
Ba	8*d*	0.61890(2)	¼	1/8	0.01079(7)
Si	4*a*	0	0	0	0.0068(3)
P	16*e*	0.93388(8)	0.15431(8)	0.20396(1)	0.00967(14)

Selected interatomic distances / pm and angles / °.

Ba–P (2x)	326.58(8)	Ba–P (2x)	349.41(8)

Ba–P (2x)	331.17(8)	Si–P (4x)	223.45(8)
Ba–P (2x)	339.05(8)	P–P	222.01(15)
P–Si–P (2x)	96.18(4)	P–Si–P (6x)	116.50(2)

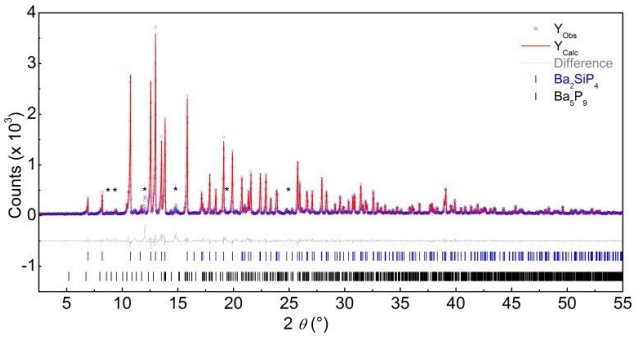

Figure 7.1 X-ray powder pattern of the Ba_2SiP_4 sample (blue circles) with Rietveld fit (red line) and difference (grey line).

The single crystal data were used to index and refine the X-ray powder pattern (Figure 7.1). The Rietveld-fit yielded Ba_2SiP_4 as the main component (ca. 90 wt%) with Ba_5P_9 (ca. 8 wt%) and an unidentified minor phase as impurities. The sample was further characterized by ^{29}Si and ^{31}P solid-state MAS-NMR spectroscopy. Both spectra (Figure 7.2) show one single resonance at δ (Si) = 24.8 ppm and δ (P) = -79.8 ppm, respectively, indicating one silicon and one phosphorus site in agreement with the single crystal structure determination. The ^{31}P spectrum reveals additional weak signals from the impurity phases. The NMR resonances have linewidths (fwhm) of ≈ 500 Hz for ^{31}P and ≈ 205 Hz for ^{29}Si, which makes the distinction of possible *J* couplings impossible. The spinning side bands of the ^{31}P spectrum cover a range of about 200 ppm, which indicates a fairly large anisotropy of the chemical shift tensor, as expected for the Si–P–P–Si motive.[14]

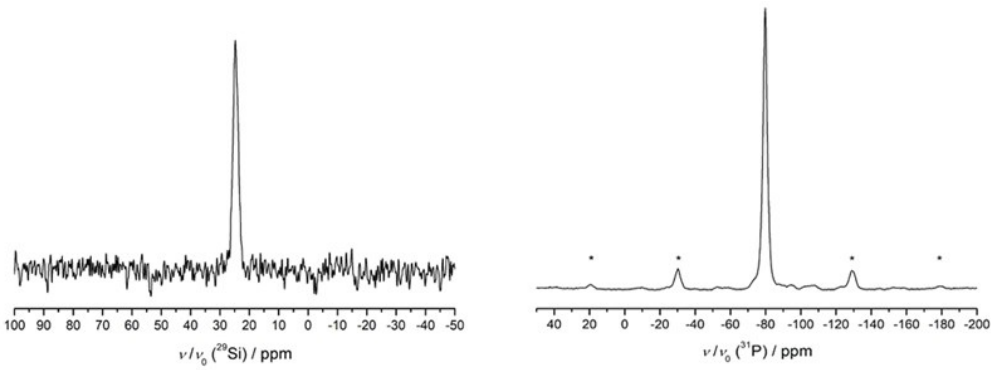

Figure 7.2 ^{29}Si (left) and ^{31}P (right) solid-state MAS-NMR spectra of the Ba_2SiP_4-sample.

Ba_2SiP_4 crystallizes in a new structure type with slightly distorted SiP_4 tetrahedra [d(Si—P) = 223.45(8) pm] which are exclusively connected via homonuclear P—P bonds [d(P—P) = 221.01(15) pm] to form a three-dimensional network with barium atoms in the lacunae (Figure 7.3).

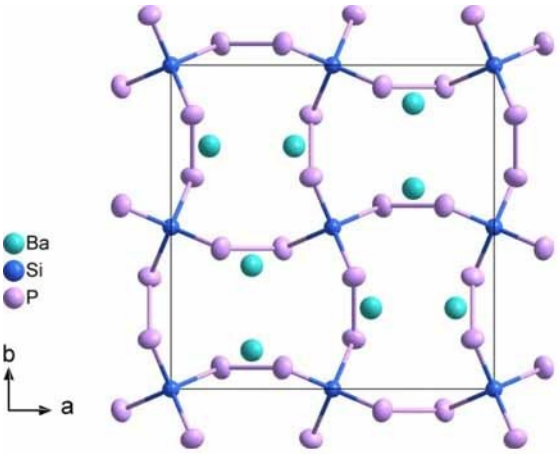

Figure 7.3 Crystal structure of Ba_2SiP_4. Ellipsoids represent 98 % probability.

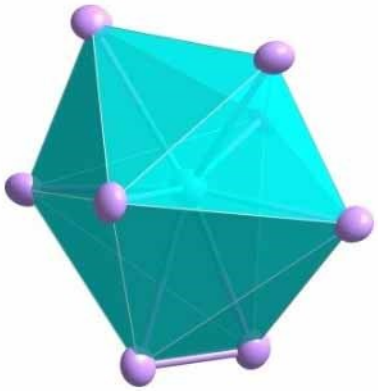

Figure 7.4 Coordination of the barium atom in Ba_2SiP_4. Ellipsoids represent 98 % probability.

Barium is eightfold coordinated by phosphorus [d(Ba—P) = 326.58(8) pm – 349.41(8) pm]. The coordination polyhedra may be described as a pentagonal bipyramid where one vertex is a P_2 dimer (Figure 7.4). Ba_2SiP_4 represents a new structure type, which is related to the high-pressure phase of Zn_2SiO_4 (Willemite).[18] The latter has no bonds between the tetrahedra, but crystallizes in the same tetragonal space group $I\bar{4}2d$ with atoms at the same Wyckoff positions. The coordinates of oxygen in Zn_2SiO_4 and of phosphorus in Ba_2SiP_4 are quite different, which may formally be interpreted as opposing rotation of the neighboring tetrahedra as illustrated in Figure 7.5. Because the phosphorus coordinates are very different from those of oxygen in Zn_2SiO_4, one cannot refer both structures as isotypic but at best as homeotypic.[19] A further structural relation is the similarity of the SiP_4 network in Ba_2SiP_4 and the $SiO_{4/2}$ network in β-cristobalite (ordered model in space group $I\bar{4}2d$).[20] Indeed the positions of the P_2 dimer midpoints almost exactly coincide with the oxygen sites of tetragonal SiO_2. However, the P_2 dimers, which formally replace oxygen atoms elongate the tetrahedra network in Ba_2SiP_4 significantly along the a and b axes. Thus the c/a value becomes 0.74, which is far from the pseudo-cubic metric of tetragonal SiO_2 (c/a = 1.414). This deformation is also necessary to form the appropriate coordination of the barium ions.

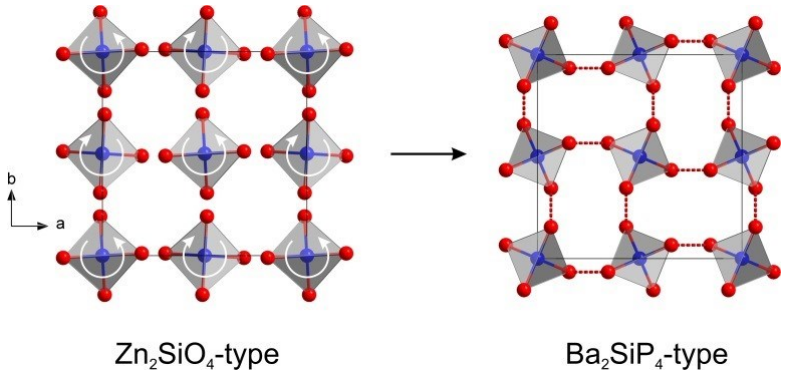

Figure 7.5 Relation between the hp-Zn_2SiO_4 and Ba_2SiP_4 type structures through rotations of the tetrahedra.

Though the crystal chemistry of phosphido-, oxido-, and nitridosilicates have certain similarities based on the SiX_4 tetrahedra (X = O, N, P) as common building units, the bonding situation is expectably different. The main reason is the lower electronegativity of the 3p element phosphorus (χ_P = 2.1) in comparison to the 2p elements oxygen (χ_P = 3.7) and nitrogen (χ_P = 3.0). Thus Si—P bonds are significantly more covalent and one may argue if these compounds are true phosphidosilicates or better named as silicon-phosphides. To shed some light on the bonding situation we have performed relativistic DFT electronic band structure calculations of Ba_2SiP_4. Figure 7.6 shows the total DOS and atom-resolved density-of-states (pDOS). Ba_2SiP_4 is a semiconductor with a calculated indirect energy gap of ca. 0.9 eV. DFT generally underestimates the gap, therefore the experimental value is certainly bigger. The valence band is dominated by phosphorus 3p states and the top of the conduction band is formed by a mixture of phosphorus and barium states with small contributions of silicon. The pDOS of silicon shows significant occupied Si-3p states, which indicates that silicon is far from a Si^{4+} state as expected. Integrations of the pDOS reveal charges of $Ba^{1.35+}$, $Si^{0.25+}$, and $P^{0.74-}$. The topological analysis of the electron density using the Bader formalism[21] results charges of $Ba^{1.33+}$, $Si^{1.72+}$, and $P^{1.10-}$. Both charge assignments are consistent with a polyanionic $[SiP_4]^{\delta-}$ network with predominantly covalent Si-P bonds. This is further supported by the electron localization function (ELF)[22,23] shown in Figure 7.7. High ELF values (ca. 0.9) occur along the Si—P and P—P bonds indicating their mainly covalent character. Note that the ELF basin of the Si—P bond is almost halfway between the atoms, which further supports the weak iconicity of the Si-P bond. The distinct lone pairs at the phosphorus atoms are likely visualized by the ELF.

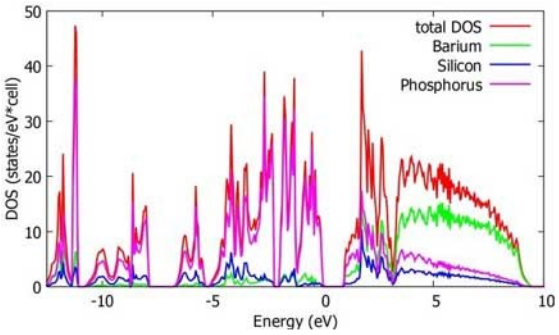

Figure 7.6 Total and atom-resolved density-of-states of Ba_2SiP_4. The energy zero is taken at the fermi level.

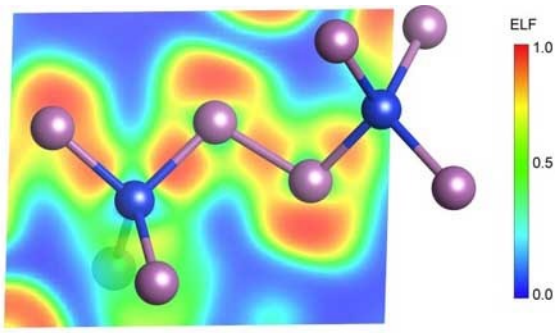

Figure 7.7 Electron localization function (ELF) of Ba_2SiP_4. ELF is given in a plane defined through the atoms of the P2 dimer and the left silicon atom.

7.4 Conclusion

Ba_2SiP_4 represents a novel phosphidosilicate, where the SiP_4 tetrahedra are exclusively bridged via homonuclear P_2 dimers. The structure is homeotypic to hp-Zn_2SiO_4 and formally emerges from the silicate by opposing rotations of neighbouring tetrahedra. The SiP_4 network of Ba_2SiP_4 is likewise related to the tetragonal β-cristobalite structure of SiO_2 by formally replacing the oxygen atoms with P_2 dimers. Ba_2SiP_4 is a semiconductor with an indirect bad gap around 1 eV. Electronic density of states, Bader-, and ELF analysis suggest strong covalent Si-P bonds and only small positive charge at the silicon atom.

7.5 Experimental Section

Synthesis. Ba_2SiP_4 was obtained by heating stoichiometric amounts of Ba metal (99.99 % SIGMA-ALDRICH), Si powder (99.8 %, SMART ELEMENTS) and red phosphorus (> 99 %, CHEMPUR) up to 1173 K with a 100 $K \cdot h^{-1}$ heating rate for 20 h in alumina crucibles welded in silica tubes under purified argon atmosphere. To prevent incomplete reaction the ground product was annealed at 1123 K twice leading to a polycrystalline and air sensitive black sample.

Single-Crystal X-ray Diffraction. A suited single-crystal was selected from the sample and welded in a Hilgenberg glass capillary under paraffin oil. Diffraction data were recorded on a Bruker D8 Quest diffractometer with Photon-I detector at room temperature using Mo-Kα radiation (λ = 0.71073 Å). The single-crystal structure was solved by using direct methods and refined with SHELXL crystallographic software package.[17]

X-ray Powder Diffraction. Measurements were performed with a Stoe Stadi-P diffractometer equipped with a Stoe Mythen 1k detector at ambient temperature using Mo-Kα1 radiation (λ = 0.71073 Å). The Topas package[24] was used for Rietveld refinement.

Nuclear Magnetic Resonance. ^{29}Si- and ^{31}P-specta were measured on a Bruker Avance-III 500 spectrometer with a magnetic field of 11.74 T under MAS conditions at a Larmor frequency of ν_0 (^{29}Si) = 99.38 MHz and ν_0 (^{31}P) = 202.48 MHz. A commercial zirconia rotor (4 mm) was used with a rotation frequency of 10 kHz.

EDX-Analysis. EDX measurements were carried out with an EVO-MA 10 (Zeiss) scanning electron microscope using Bruker X-Flash 410-M detector for elemental analysis. Received data were analysed using QUANTAX 200 software package. Signals of oxygen were not taken into account due to partial hydrolysis of the samples by contact with air.

DFT calculations. Electronic structure calculations were performed using the Vienna ab initio simulation package (VASP),[25,26] which is based on density functional theory (DFT) and plane wave basis sets. Projector-augmented waves (PAW)[27] were used and contributions of correlation and exchange were treated in the generalized-gradient approximation (GGA).[28] The PAW eigenstates were projected onto localized crystal orbitals using LOBSTER.[29]

Further details of the crystal structure investigations may be obtained from the Fachinformationszentrum Karlsruhe, 76344 Eggstein-Leopoldshafen, Germany (Fax: +49-7247-808-666; E-Mail: crysdata@fiz-karlsruhe.de, http://www.fiz-karlsruhe.de/request for deposited data.html) on quoting the depository number CSD-433493.

7.6 References

[1] B. Eisenmann, H. Jordan, H. Schäfer, *Mater. Res. Bull.* **1982**, *17*, 95.

[2] L. Toffoletti, H. Kirchhain, J. Landesfeind, W. Klein, L. van Wüllen, H. A. Gasteiger, T. F. Fässler, *Chemistry – A European Journal* **2016**, *22*, 17635.

[3] B. Eisenmann, M. Somer, *Z. Naturforsch. B* **1985**, *40*, 886.

[4] B. Eisenmann, M. Somer, *Z. Naturforsch. B* **1984**, *39*, 736.

[5] A. J. SpringThorpe, J. G. Harrison, *Nature* **1969**, *222*, 977.

[6] J. Wallinda, W. Jeitschko, *J. Solid State Chem.* **1995**, *114*, 476.

[7] H. Vincent, J. Kreisel, C. Perrier, O. Chaix-Pluchery, P. Chaudouet, R. Madar, F. Genet, G. Lucazeau, *J. Solid State Chem.* **1996**, *124*, 366.

[8] P. Kaiser, W. Jeitschko, *Z. Naturforsch. B* **1997**, *52*, 462.

[9] P. Kaiser, W. Jeitschko, *Z. Anorg. Allg. Chem.* **1996**, *622*, 53.

[10] P. Kaiser, W. Jeitschko, *J. Solid State Chem.* **1996**, *124*, 346.

[11] Z. W. Zhang, D. T. Reid, S. C. Kumar, M. Ebrahim-Zadeh, P. G. Schunemann, K. T. Zawilski, C. R. Howle, *Opt. Lett.* **2013**, *38*, 5110.

[12] B. Q. Yao, Y. J. Shen, X. M. Duan, T. Y. Dai, Y. L. Ju, Y. Z. Wang, *Opt. Lett.* **2014**, *39*, 6589.

[13] A. Haffner, T. Brauniger, D. Johrendt, *Angew. Chem. Int. Ed.* **2016**, *55*, 13585.

[14] H. Eickhoff, L. Toffoletti, W. Klein, G. Raudaschl-Sieber, T. F. Fässler, *Inorg. Chem.* **2017**, *56*, 6688.

[15] H. G. von Schnering, G. Menge, *J. Solid State Chem.* **1979**, *28*, 13.

[16] X. Zhang, T. Yu, C. Li, S. Wang, X. Tao, *Z. Anorg. Allg. Chem.* **2015**, *641*, 1545.

[17] G. M. Sheldrick, *Acta Crystallogr., Sect. A: Found. Crystallogr.* **2008**, *A64*, 112.

[18] F. Marumo, Y. Syono, *Acta Cryst. B* **1971**, *27*, 1868.

[19] U. Müller, *Z. Anorg. Allg. Chem.* **2004**, *630*, 1519.

[20] A. F. Wright, A. J. Leadbetter, *Philos. Mag.* **1975**, *31*, 1391.

[21] G. Henkelman, A. Arnaldsson, H. Jónsson, *Comput. Mat. Sci.* **2006**, *36*, 354.

[22] A. Savin, R. Nesper, S. Wengert, T. F. Fässler, *Angew. Chem. Int. Ed.* **1997**, *36*, 1808.

[23] T. F. Fässler, A. Savin, *Chem. Unserer Zeit* **1997**, *31*, 110.

[24] A. Coelho, *TOPAS-Academic, Version 4.1, Coelho Software*, Brisbane, **2007**.

[25] G. Kresse, J. Furthmüller, *Comput. Mat. Sci.* **1996**, *6*, 15.

[26] G. Kresse, D. Joubert, *Phys. Rev. B* **1999**, *59*, 1758.

[27] P. E. Blöchl, *Phys. Rev. B* **1994**, *50*, 17953.

[28] J. P. Perdew, K. Burke, M. Ernzerhof, *Phys. Rev. Lett.* **1996**, *77*, 3865.

[29] S. Maintz, V. L. Deringer, A. L. Tchougreeff, R. Dronskowski, *J. Comput. Chem.* **2013**, *34*, 2557.

8 Polymorphism of Ba_2SiP_4

Arthur Haffner, Valentin Weippert, and Dirk Johrendt

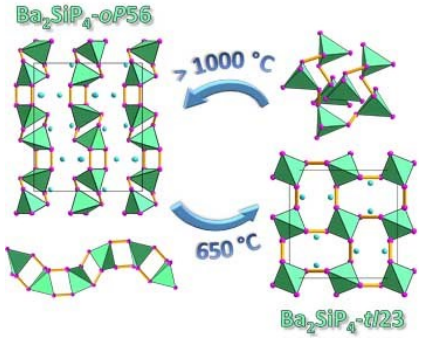

published in: *Zeitschrift für Anorganische und Allgemeine Chemie* **2020**, *646*, 120-124.

8.1 Abstract

The three-dimensional SiP_4 network in the known phosphidosilicate Ba_2SiP_4-*tI*28 is analoguos to β-cristobalite if oxygen is formally replaced by P–P dimers. Here we report a second polymorph Ba_2SiP_4-*oP*56 [*Pnma*, a = 12.3710(4) Å, b = 14.6296(7) Å, c = 7.9783(3) Å; Z = 8] with chains of SiP_4 tetrahedra connected by P–P bonds, reminiscent to the elusive fibrous SiO_2. Ba_2SiP_4 is enantiotropic. The high temperature polymorph Ba_2SiP_4-*oP*56 transforms to the low-temperature phase Ba_2SiP_4-*tI*28 at 650 °C and reconstructs to the high-temperature modification at 1100 °C. DFT calculations predict an indirect optical band gap of about 1.7 eV.

8.2 Introduction

Phosphidosilicates are known since the 1980s and attract anew considerable interest due to its broad structural variety involving compounds with versatile properties. The structures based on SiP_4 tetrahedra as anionic basic building unit are closely related to oxido- and nitridosilicates indicating a large structural variety. The nesosilicates Li_8SiP_4,[1] EA_4SiP_4 (*EA* = Ca, Sr, Ba)[2] or $Na_4EA_2SiP_4$ (*EA* = Ca, Sr, Eu)[3] are rare examples of isolated highly charged $[SiP_4]^{8-}$ anions. More common are SiP_4 anions with reduced charge density achieved by different condensation degrees leading to chain, layer or three-dimensional network motifs. $A_{10}Si_2P_6$ (*A* = Li, Na)[4,5] exhibits edge-shared $[Si_2P_6]^{10-}$ entities whereas the charge density is decreased furthermore by edge condensation of these units to infinite $[SiP_2]^{2-}$ chains found in K_2SiP_2.[6] Interestingly, to date layered phosphidosilicates were only observed with supertetrahedral entities constituted of vertex sharing SiP_4 tetrahedra in $CaSiP_2$ [7] and KSi_2P_3.[8] In contrast, the introduction of small and weak electronegative metals yields three-dimensional structures of vertex-shared tetrahedra[9,10] or supertetrahedra with sizes ranged from T2 to T5 [11] and the feature of supertetrahedral fusion in Li_2SiP_2, $LiSi_2P_3$ [12] and $Na_{23}Si_{9n+19}P_{12n+33}$ with n = 0-3.[13] To the best of our knowledge this uncommon condensation mode was sparely observed only in KSi_2P_3,[8] B_2S_3,[14] $Li_9B_{19}S_{33}$,[15] $M_{15}Tr_{22}As_{32}$ and $M_3Ga_6As_8$ (*M* = Sr, Eu; *Tr* = Ga, In) [16] and a few other mixed-metal T3 chalcogenides.[17-21]

The possibility of the formation of homonuclear phosphorus bonding distinguishes the family of phosphidosilicates from the oxido- and nitridosilicates. Isolated P–P bonding was described in $AlSiP_3$,[22] $Ca_3Si_8P_{14}$,[7] $Ba_2Si_3P_6$ [23] and $Ba_4Si_3P_8$,[24] for example, whereas in $LaSi_2P_6$ up to four different polyphosphide anions $(P_n)^{-(n+2)}$ with n = 3-6 and in $Li_3Si_3P_7$ [4] polyphosphide chains exist. Tetragonal Ba_2SiP_4-*tI*28 [25] is the first example where all SiP_4 tetrahedra are connected by P–P bonds. Currently the Ba-Si-P ternary system attracts attention regarding possible NLO and thermoelectric properties.[23] Therefore, we focused upon this compounds and found the high-temperature enantiotropic polymorph Ba_2SiP_4-*oP*56, in which all SiP_4 tetrahedra are linked by homonuclear phosphorus bonds, as well, being the second example for this structure motif.

8.3 Results and Discussion

Ba_2SiP_4-*oP*56 was synthesized by solid-state reactions of stoichiometric amounts of respective elements under inert conditions revealing air sensitive polycrystalline black powders. Single crystals suitable for

single-crystal X-ray diffraction were selected under dried paraffin oil. The compound crystallizes in a primitive orthorhombic unit cell in space group *Pnma* with lattice parameters a = 12.3710(4) Å, b = 14.6296(7) Å and c = 7.9783(3) Å. The structure was solved and refined using the SHELX [26] package. Crystallographic data of Ba_2SiP_4-*oP*56 are given in Table 8.1, fractional coordinates and equivalent displacement parameters in Table 8.2. Based on this data the powder pattern of a polycrystalline sample was indexed and refined yielding in about 94 wt% of the targeted phase with small impurities of the low-temperature polymorph Ba_2SiP_4-*tI*28,[25] Ba_3P_4 [27] and a minor unidentified phase (Figure 8.1).

Table 8.1 Crystallographic data of Ba_2SiP_4-*oP*56.

Formula	Ba_2SiP_4
space group	*Pnma* (no. 62)
a / Å	12.3710(4)
b / Å	14.6296(7)
c / Å	7.9783(3)
V_{cell} / Å^3	1443.93(10)
Z	8
$\rho_{X\text{-}ray}$ / g·cm^{-3}	3.925
μ / mm^{-1}	11.773
Θ-range / °	2.785 – 30.527
reflections measured	14530
independent reflections	2286
parameters	67
R_σ	0.0343
R_{int}	0.0596
R_1 ($F^2>2\sigma(F^2)$) / all	0.0281 / 0.0448
wR_2 ($F^2>2\sigma(F^2)$) / all	0.0470 / 0.0509
Goof	1.095
$\Delta\rho_{max/min}$ / e·Å^{-3}	1.536 / -1.293

Table 8.2 Fractional coordinates, Wyckoff positions and equivalent displacement parameters of Ba_2SiP_4-*oP*56.

Atom	Wyckoff position	*x*	*y*	*z*	U_{eq} / Å²
Ba1	8*d*	0.34858 (2)	0.51347(2)	0.38205(4)	0.01148(7)
Ba2	4*c*	0.26291(4)	1/4	0.22464(6)	0.01343(9)
Ba3	4*c*	0.43469(4)	1/4	0.72852(6)	0.0173(1)
Si1	8*d*	0.04023(11)	0.11551(10)	0.38639(17)	0.0094(2)
P1	8*d*	0.01981(11)	0.17373(9)	0.12824(17)	0.0116(2)
P2	8*d*	0.09964(10)	0.51730(9)	0.28240(15)	0.0108(2)
P3	8*d*	0.16274(11)	0.17243(10)	0.57072(17)	0.0136(3)
P4	8*d*	0.37387(10)	0.10051(9)	0.00761(16)	0.0104(2)

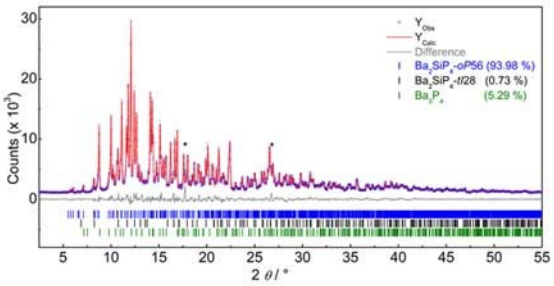

Figure 8.1 X-ray powder pattern of the Ba_2SiP_4-*oP*56 sample (blue circles) with Rietveld fit (red line) and difference (grey line). Small amounts of Ba_2SiP_4-*tI*28 and Ba_3P_4, beside an unknown impurity, marked with asterisks, were detected.

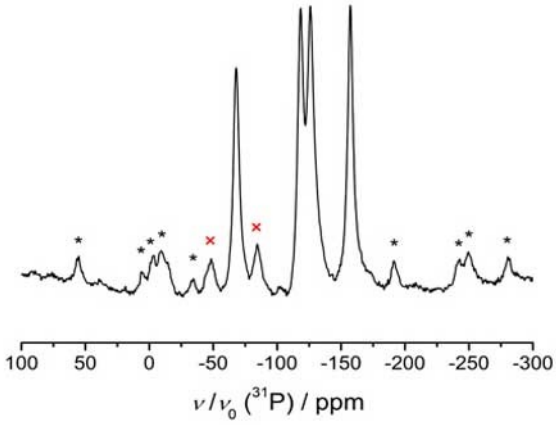

Figure 8.2 ^{31}P solid-state MAS-NMR spectrum of Ba_2SiP_4-*oP*56. Rotation side bands are marked with asterisks and resonance frequencies of the Ba_3P_4 impurity with red crosses.

The polycrystalline sample was further investigated by solid-state MAS-NMR and EDX, confirming the elemental composition. Figure 8.2 shows the ^{31}P spectrum with four distinct resonance frequencies at δ (^{31}P) = –67.98, –118.33, –125.92, –157.23 ppm, each with the same intensity indicating four magnetically inequivalent phosphorus atoms with the same multiplicity, which is in accordance with the single crystal

structure. The examined sample contains 5 wt% Ba_3P_4 in Sr_3As_4 type structure with two crystallographic different phosphorus atoms.[27] This impurity is visible in the ^{31}P NMR spectrum with two additional resonance frequencies at δ (^{31}P) = –48.35 and –84.40 ppm (see Figure 8.2, red crosses).

Ba_2SiP_4-*oP*56 crystallizes in a new structure type with a unique structural motif composed of SiP_4 tetrahedra. As in Ba_2SiP_4-*tI*28, P–P bonds [$\varnothing d$(P-P) = 2.23 Å] link all SiP_4 tetrahedra, but here the connectivity generates chains along the *b* axis (Figure 8.3). The chains form a distorted hexagonal rod packing, similar to the chains of edge-sharing $SiS_{4/2}$ tetrahedra in SiS_2.[28] As we mentioned earlier, the three-dimensional network in Ba_2SiP_4-*tI*28 is analogous to β-cristobalite, if one replaces the oxygen atoms in SiO_2 by P_2 dimers. In this sense, the new chain structure of Ba_2SiP_4-*oP*56 would be the analogue of the fibrous SiO_2, which is still elusive.[29] The Ba^{2+} cations are located between the anionic chains in strongly distorted polyhedra, which are gyro-elongated square pyramids (Ba1) with one, cubes (Ba2) with three or elongated square bipyramids (Ba3) with five homonuclear phosphorus bonds as depicted in Figure 8.4.

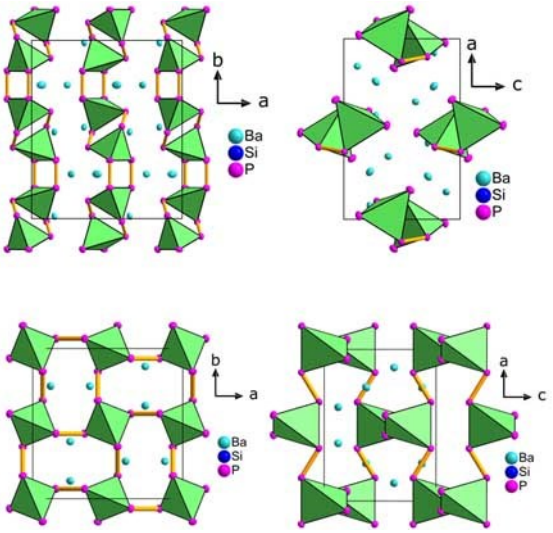

Figure 8.3 Crystal structure of Ba_2SiP_4-*oP*56 with view along [001] (top, left) and along [010] (top, right) and Ba_2SiP_4-*tI*28 with respective viewing directions (bottom). Ellipsoids are drawn with 90 % probability.

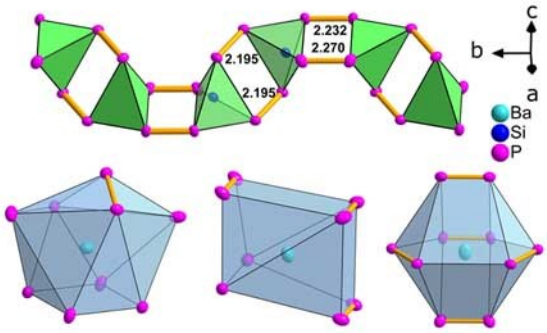

Figure 8.4 $_\infty^1[SiP_4]^{4-}$ chain motif of pseudo edge-condensed SiP_4 tetrahedra (top) and Ba coordinations containing homonuclear phosphorus bonds of Ba1 (left), Ba2 (middle) and Ba3 (right). All BaP_x polyhedra are strongly distorted.

Ba_2SiP_4-*oP*56 does not form if the solid state reactions are carried out at increased temperatures of 1100 °C with the slow cooling rates used for Ba_2SiP_4-*tI*28.[25] A nearly phase-pure sample could only be obtained by faster cooling rates from −10 $K \cdot h^{-1}$ to −50 $K \cdot h^{-1}$. We examined the phase transition of Ba_2SiP_4-*oP*56 to Ba_2SiP_4-*tI*28 by high-temperature powder diffraction yielding no transition until about 600 °C, before a mixture of both modifications occurs near 650 °C. At 700 °C, Ba_2SiP_4-*oP*56 is almost completely transformed to Ba_2SiP_4-*tI*28, which persists upon cooling to room temperature (Figure 8.5). The additional reflection at about $2\Theta = 12$ ° above 850 °C is probably caused by crystallizing of the silica capillary. On the other hand Ba_2SiP_4-*oP*56 can also be obtained from Ba_2SiP_4-*tI*28 if the same heating protocol is applied with faster cooling, thus Ba_2SiP_4 is enantiotropic with reconstructive phase transitions.

For the estimation of the electronic properties of Ba_2SiP_4-*oP*56 DFT calculations were performed. Figure 8.6 shows the electronic band structure and the atom-resolved density-of-states for Ba_2SiP_4-*oP*56. The valence band is dominated by the P-3p states with some contributions of Si-3p and Ba-5d. The energy gap is 1.11 eV using the PBE and increases to 1.65 eV with the mBJ functional. The valence band maximum is located at the *I*-point in the Brillouin zone and the conduction band minimum occurs at *T*, which means that the calculation predicts an indirect band gap.

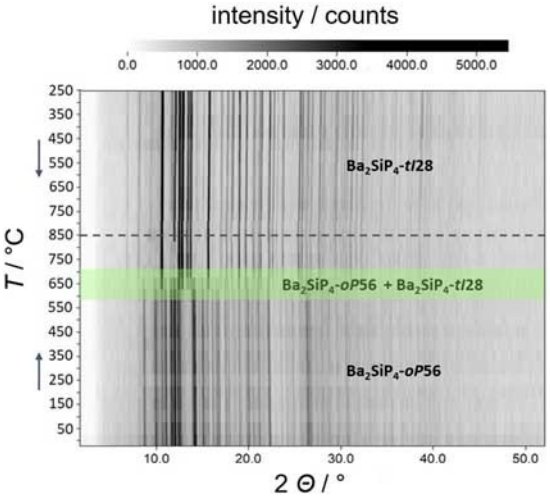

Figure 8.5 High-temperature powder diffraction pattern of Ba_2SiP_4. The sample was heated to 850 °C (marked with dashed line) and then cooled to 250 °C. Phase transition occurs between 600 and 700 °C (highlighted in green).

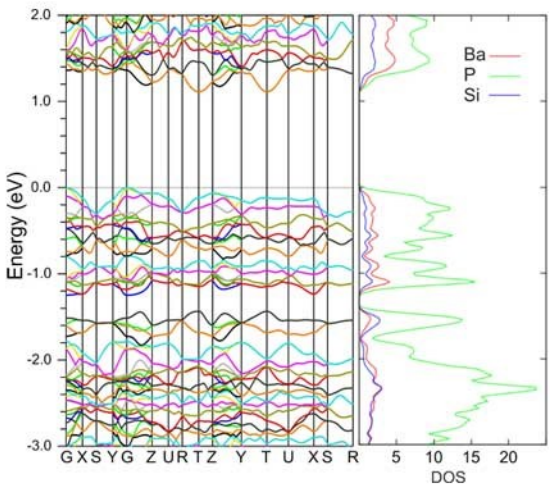

Figure 8.6 Electronic band structure (left) and atom-resolved DOS (right) for Ba_2SiP_4-*oP*56. The energy zero is taken at the Fermi level

8.4 Conclusion

Ba_2SiP_4-*oP*56 crystallizes in a new structure type constituting the second example of a phosphidosilicate with all phosphorus atoms connected by P–P bonds. The crystal structure comprises SiP_4 tetrahedra bridged via P–P bonds, leading to $_\infty^1[SiP_4]^{4-}$ chains. While the network of tetragonal polymorph Ba_2SiP_4-*tI*28 is analogous to the β-cristobalite type if one replaces oxygen by P_2 dimers, the chains in the new compound Ba_2SiP_4-*oP*56 are analogous to SiS_2, and reminiscent to the elusive fibrous SiO_2. A phase transition from Ba_2SiP_4-*oP*56 to Ba_2SiP_4-*tI*28 occurs at around 650 °C whereas we expect the re-transition well beyond 1000 °C, which we were not able to determine. Solid-state MAS-NMR data and its EDX fully confirm the structure. DFT calculations reveal an indirect band gap of around 1.7 eV in agreement with the black color of the compound.

8.5 Experimental Section

Synthesis. Ba_2SiP_4-*oP*56 was obtained by two different routes. Either a stoichiometric mixture of respective elements (Ba, 99.99 %, Sigma Aldrich; Si, 99.8 %, SMART ELEMENTS; P_{red}, > 99 %, CHEMPUR) or a phase-pure sample of Ba_2SiP_4-*tI*28 was heated to 1100 °C with a 50 $K{\cdot}h^{-1}$ rate for the elemental or with a 200 $K{\cdot}h^{-1}$ rate for the Ba_2SiP_4-*tI*28 route in alumina crucibles welded in argon filled silica ampoules. This temperature was held for 40 h before it was decreased to 450 °C with a relatively fast cooling rate of -50 $K{\cdot}h^{-1}$. After cooling to room temperature the targeted product was received as polycrystalline and air sensitive black powder.

Single-Crystal X-ray Diffraction. Due to air sensitivity single crystals of sufficient quality were selected under dried paraffin oil and transferred in oil filled and fused Hilgenberg glass capillaries with 0.2 mm in diameter. Diffraction data were collected by a Bruker D8 Venture diffractometer with a rotating anode, Göbel mirror optics and a Photon II detector. Reflection indexing, data reduction and absorption correction were processed by the Bruker software APEX3.[30] Based on systematically absent reflections the space group of Ba_2SiP_4-*oP*56 was identified with XPREP.[31] Final solution and refinement of the crystal structure were performed with direct methods implemented in the SHELX software package.[26] For visualisation of the crystal structure Diamond [32] software was chosen.

Powder X-ray Diffraction. A ground sample was loaded and sealed in a glass capillary with 0.2 mm in diameter (Hilgenberg GmbH) to avoid hydrolysis. Diffraction patterns were recorded on a Stadi-P powder diffractometer in Debye-Scherrer setup (STOE & Cie GmbH) equipped with a Ge

monochromator, a Mythen 1K detector (Dectris) and Mo-Kα_1 radiation. Diffractograms were indexed and refined using the single-crystal structure model and the Rietveld method implemented in the TOPAS [33] software.

Temperature-Dependent Powder X-ray Diffraction. For the investigation of the phase transition a ground sample was loaded into a silica capillary with 0.5 mm in diameter (Hilgenberg GmbH) and sealed with grease for pressure compensation while heating. Data were collected under argon atmosphere also on a Stadi-P diffractometer (STOE & Cie) with a Ge monochromator, an IP-PSD detector, a resistance graphite furnance and Mo-Kα_1 radiation. The sample was heated to 850 °C and cooled to room temperature in steps of 50 °C with a 5 °K·min^{-1} rate. At each step, the temperature was kept constant and a diffraction pattern was collected. We were not able to measure the retransition from Ba_2SiP_4-*tI*28 to Ba_2SiP_4-*oP*56 beyond 1000 °C because of the limited chemical stability of the silica capillaries.

Solid-State MAS-NMR Spectroscopy. For the nuclear magnetic resonance spectrum of the ^{31}P nuclei a polycrystalline sample of Ba_2SiP_4-*oP*56 was loaded into a commercial zirconia rotor with 2.5 mm in diameter and placed into a Bruker Avance III 500 spectrometer device with a magnetic field of 11.74 T. The sample was rotated under MAS conditions with a frequency of 25 kHz and a Larmor frequency of ν_0 (^{31}P) = 202.5 MHz.

EDX Analysis. For elemental analysis, a sample was prepared under argon atmosphere onto adhesive and conductive carbon pads, which were inserted into an EVO-MA 10 (Zeiss) scanning electron microscope quickly. An electron beam was generated by a field emission gun. Characteristic X-ray radiation was detected by X-Flash 410-M (Bruker) and processed with QUANTAX 200 software package. Oxygen signals were not taken into account due to partial hydrolysis while inserting the sample.

Electronic Structure Calculations. The electronic band structure was calculated using the full-potential-linear-augmented plane-wave (FLAPW) method with the WIEN2k package.[34] Exchange and correlation were treated with the PBE[35] or mBJ[36] functionals. The experimental lattice parameters and atom positions were used for the band and DOS calculations shown in Figure 8.6. Tentatively optimizations of the atom positions showed no significant changes.

8.6 References

[1] L. Toffoletti, H. Kirchhain, J. Landesfeind, W. Klein, L. van Wüllen, H. A. Gasteiger, T. F. Fässler, *Chem. Eur. J.* **2016**, *22*, 17635.

[2] B. Eisenmann, H. Jordan, H. Schäfer, *Mater. Res. Bull.***1982**, *17*, 95.

[3] J. Nuss, H. Kalpen, W. Hönle, M. Hartweg, H. G. von Schnering, *Z. Anorg. Allg. Chem.* **1997**, *623*, 205.

[4] H. Eickhoff, L. Toffoletti, W. Klein, G. Raudaschl-Sieber, T. F. Fässler, *Inorg. Chem.* **2017**, *56*, 6688.

[5] B. Eisenmann, M. Somer, *Z. Naturforsch. B* **1985**, *40*, 886.

[6] B. Eisenmann, M. Somer, *Z. Naturforsch. B* **1984**, *39*, 736.

[7] X. Zhang, T. Yu, C. Li, S. Wang, X. Tao, *Z. Anorg. Allg. Chem.* **2015**, *641*, 1545.

[8] K. Feng, L. Kang, W. Yin, W. Hao, Z. Lin, J. Yao, Y. Wu, *J. Solid State Chem.* **2013**, *205*, 129.

[9] A. J. Springthorpe, J. G. Harrison, *Nature* **1969**, *222*, 977.

[10] A. A. Vaipolin, E. O. Osmanov ; D. N. Tretyakov, *Inorg. Mater.* **1967**, *3*, 231.

[11] H. Li, J. Kim, T. L. Groy, M. O'Keeffe, O. M. Yaghi, *J. Am. Chem. Soc.* **2001**, *123*, 4867.

[12] A. Haffner, T. Bräuniger, D. Johrendt, *Angew. Chem. Int. Ed.* **2016**, *55*, 13585.

[13] A. Haffner, A.-K. Hatz, I. Moudrakovski, B. V. Lotsch, D. Johrendt, *Angew. Chem. Int. Ed.* **2018**, *57*, 6155.

[14] T. Sasaki, H. Takizawa, K. Uheda, T. Yamashita, T. Endo, *J. Solid State Chem.* **2002**, *166*, 164-170.

[15] F. Hiltmann, P. zum Hebel, A. Hammerschmidt, B. Krebs, *Z. Anorg. Allg. Chem.* **1993**, *619*, 293.

[16] V. Weippert, A. Haffner, A. Stamatopoulos, D. Johrendt, *J. Am. Chem. Soc.* **2019**, *141*, 11245.

[17] H. Lin, J.-N. Shen, L. Chen, L.-M. Wu, *Inorg. Chem.* **2013**, *52*, 10726.

[18] W. Khan, S. Goumri-Said, *RSC Adv.* **2015**, *5*, 9455.

[19] H. Li, C. D. Malliakas, Z. Liu, J. A. Peters, H. Jin, C. D. Morris, L. Zhao, B. W. Wessels, A. J. Freeman, M. G. Kanatzidis, *Chem. Mater.* **2012**, *24*, 4434.

[20] J. H. Liao, M. G. Kanatzidis, *Chem. Mater.* **1993**, *5*, 1561.

[21] H.-W. Ma, G.-C. Guo, M.-S. Wang, G.-W. Zhou, S.-H. Lin, Z.-C. Dong, J.-S. Huang, *Inorg. Chem.* **2003**, *42*, 1366.

[22] H. G. von Schnering, G. Menge, *J. Solid State Chem.* **1979**, *28*, 13.

[23] J. Mark, J. Wang, K. Wu, J. G. Lo, S. Lee, K. Kovnir, *J. Am. Chem. Soc.* **2019**, *141*, 11976.

[24] J. Mark, J.-A. Dolyniuk, N. Tran, K. Kovnir, *Z. Anorg. Allg. Chem.* **2019**, *645*, 242.

[25] A. Haffner, D. Johrendt, *Z. Anorg. Allg. Chem.* **2017**, *643*, 1717.

[26] G. M. Sheldrick, *Acta Crystallogr. A* **2008**, *64*, 112.

[27] H.-G. von Schnering, M. Wittmann, D. Sommer, *Z. Anorg. Allg. Chem.* **1984**, *510*, 61.

[28] W. Büssem, H. Fischer, E. Gruner, *Naturwissenschaften* **1935**, *23*, 740.

[29] A. Weiss, A. Weiss, *Z. Anorg. Allg. Chem.* **1954**, *276*, 95.

[30] Bruker AXS Inc., APEX3 Version 2016.5-0, Madison, Wisconsin, **2016**.

[31] Bruker AXS Inc., XPREP Version 2008/2, Karlsruhe, Germany, **2008**.

[32] K. Brandenburg, Diamond Version 3.2k, Crystal Impact GbR, Bonn, Germany, **2014**.

[33] A. Coelho, Topas Academic Version 4.1, Coelho Software, Brisbane, Australia, **2007**.

[34] P. Blaha, K. Schwarz, G.K.H. Madsen, D. Kvasnicka, J. Luitz, Wien2k, An Augmented Plane Wave and Local Orbital Program for Calculating Crystal Properties, TU Wien, Vienna, Austria, ISBN3-9501031-1-2, 2006.

[35] J.P. Perdew, S. Burke, M. Ernzerhof, *Phys. Rev. Lett.* **1996**, *77*, 3865.

[36] F. Tran, P. Blaha, *Phys. Rev. Lett.* **2009**, *102*, 226401

9 Supertetrahedral Anions in the Phosphidosilicates $Na_{1.25}Ba_{0.875}Si_3P_5$ and $Na_{31}Ba_5Si_{52}P_{83}$

Arthur Haffner, Otto E. O. Zeman, Thomas Bräuniger, and Dirk Johrendt

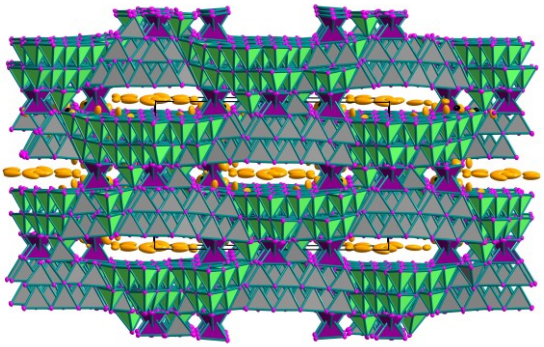

published in: *Dalton Transactions*, **2021**, DOI: 10.1039/D1DT01234G

9.1 Abstract

Solid ionic conductors are one key component of all-solid-state batteries, and recent studies with lithium, sodium and potassium phosphidosilicates revealed remarkable ion conduction capabilities in these compounds. We report the synthesis and crystal structures of two quaternary phosphidosilicates with sodium and barium, which crystallize in new structure types. $Na_{1.25}Ba_{0.875}Si_3P_5$ contains layers of T3 supertetrahedra, while $Na_{31}Ba_5Si_{52}P_{83}$ forms defect T5 entities and contains Si-Si bonds and P_3 trimers. Though T_1-relaxometry data indicate a relatively low activation energy for Na^+ migration of 0.16 eV, the crystal structures lack sufficient three-dimensional migration paths necessary for fast sodium ion conductivity.

9.2 Introduction

Supertetrahedra composed of vertex sharing basic tetrahedra represent sections of the cubic sphalerite type structure. The Yaghi notation denominates them as T*n* in which *n* is the number of fundamental tetrahedra along the supertetrahedron edges.[1] Several hybrid compounds contain inorganic supertetrahedral entities, mostly based on chalcogenides, including organic spacers, and they are discussed as pathways to new open framework compounds or as optic materials.[1-18] Supertetrahedral entities likewise occur in purely inorganic solid-state compounds, especially for small *n*. $In_{19}B_{34}O_{74}(OH)_{11}$[19] and $Li_{47}B_3P_{14}N_{42}$[20] contain T2 entities beside other bridging basic BO_4 and PN_4 tetrahedra. However, compounds solely built of supertetrahedra are more common. $Li_{10}P_4N_{10}$ or $Li_{13}P_4N_{10}X_3$ (with X = Cl, Br) comprise isolated supertetrahedral clusters[21] which are condensed by common vertices in other compounds to form either layered structures ($TlGaSe_2$[22] and $RbCuSnS_3$[23] type) or three-dimensional networks. [24-34] Supertetrahedra larger than T3 are rare in purely solid-state compounds, although many examples are known in chalcogenides (see above), and they occur in $Ca_{18.75}Li_{10.5}[Al_{39}N_{55}]:Eu^{2+}$,[35] $Na_{23}Si_{28}P_{45}$, $Na_{23}Si_{37}P_{57}$, ASi_2P_3 (A = Li, Na, K), [36-38] B_2S_3[39] and $M_{15}Tr_{22}As_{32}$ (M = Sr, Eu; Tr = Ga, In). [40] Most of these supertetrahedra share one basic tetrahedron, while the only known purely inorganic T6 compounds $M_3Ga_6As_8$ (M = Sr, Eu) even share T2 entities. [40]

The three-dimensional channels in supertetrahedral phosphidosilicates resemble to zeolites, but the phosphide based anionic network is significantly more polarizable. This is desirable for fast ion conduction[41, 42] and makes the Si-P a promising system for solid-state electrolytes.

We have recently shown that phosphidosilicates with diamond- or sphalerite-like interpenetrating networks of T3-T5 entities can enable fast lithium, sodium, and potassium ion conduction in large 3D channels between the supertetrahedra. [36-38] The main reasons for the ion mobility are the low charge density of the large polymeric anions and the dilution of the alkaline ions in the interstitial space over many sites. Following this concept, one may further dilute the alkaline with bigger alkaline earth ions, which may enlarge the space between the supertetrahedra and thus the migration pathways. Moreover, the alkaline ions in the consequently bigger coordination polyhedra should be weaker bonded and thus more mobile. $NaSi_2P_3$ with networks of T5-supertetrahedra exhibits fast Na^+ conductivity, therefore $Ba_{0.25}Na_{1.5}Si_4P_6$ seemed to be a promising target compound to test the hypothesis. Here we report the crystal structures of two new quaternary phosphidosilicates with supertetrahedral structures, and show that though the activation energy from T_1-relaxometry is small, the lack of three-dimensional migration paths probably impedes ion migration.

9.3 Results and Discussion

Attempts to synthesize $Ba_{0.25}Na_{1.5}Si_4P_6$ by heating corresponding mixtures of the elements under argon atmosphere yielded inhomogeneous black polycrystalline and air-sensitive samples. X-ray structure determinations with selected single crystals revealed $Na_{1.25}Ba_{0.875}Si_3P_5$ and $Na_{31}Ba_5Si_{52}P_{83}$ as main components (Table 9.1, for detailed crystallographic data see the SI).

Table 9.1 Crystallographic data of $Na_{1.25}Ba_{0.875}Si_3P_5$ and $Na_{31}Ba_5Si_{52}P_{83}$.

Formula	$Na_{1.25}Ba_{0.875}Si_3P_5$	$Na_{31}Ba_5Si_{52}P_{83}$
formula mass / g·cm^{-1}	388.03	5430.58
crystal system	orthorhombic	monoclinic
space group	*Cmcm* (no. 63)	*C*2/*c* (no. 15)
a / Å	7.1678(2)	21.2704(4)
b / Å	34.0730(8)	30.6728(6)
c / Å	11.0890(2)	25.3238(10)
β / °	90	113.502(1)
V_{cell} / Å^3	2708.2(1)	15151.3(5)
Z	12	4
$\rho_{X\text{-}ray}$ / g·cm^{-3}	2.855	2.381
μ / mm^{-1}	5.126	2.693
radiation	Mo-Kα	Mo-Kα
Θ-range / °	2.191 - 30.561	2.200 – 30.549
reflections measured	49160	375109
independent reflections	2327	23197
parameters	100	807
restraints	1	2
R_σ	0.0085	0.0250
R_{int}	0.0256	0.0615
R_1 ($F^2>2\sigma(F^2)$) / all	0.0278 / 0.0292	0.0455 / 0.0602
wR_2 ($F^2>2\sigma(F^2)$) / all	0.0665 / 0.0675	0.1017 / 0.1090
Goof	1.109	1.053
$\Delta\rho_{max}$, $\Delta\rho_{min}$ / e·Å^{-3}	+2.051 / -2.688	+3.025 / -3.545

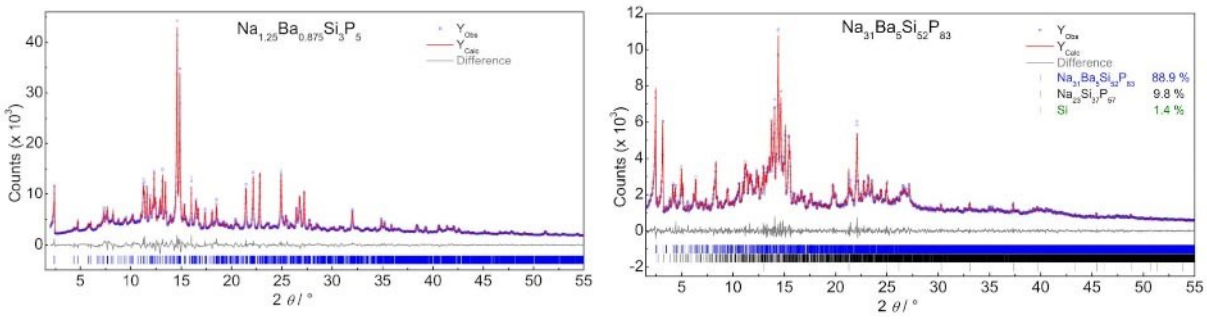

Figure 9.1 Mo-Kα_1 X-ray powder patterns of $Na_{1.25}Ba_{0.875}Si_3P_5$ (left) and $Na_{31}Ba_5Si_{52}P_{83}$ (right) depicted by blue circles with Rietveldfit (red line) and according difference (grey line). The later sample contains minor impurities of $Na_{23}Si_{37}P_{57}$ and unreacted silicon.

Correspondingly optimized synthesis protocols resulted in single-phased samples of $Na_{1.25}Ba_{0.875}Si_3P_5$, while samples of $Na_{31}Ba_5Si_{52}P_{83}$ contained 10 % $Na_{23}Si_{37}P_{57}$[37] and traces of silicon as impurities (Figure 9.1).

The crystal structure of $Na_{1.25}Ba_{0.875}Si_3P_5$ (Figure 9.2) contains SiP_4 tetrahedra ($d_{Si\text{-}P}$ = 2.191-2.291 Å) combined to T3 supertetrahedra, which in turn are connected to form layers parallel to the *ac* plane. These layers are stacked with opposing orientations along the *b* axis. Shifts of every second layer by *a*/2 result in an ABA'B' stacking, which is different from the otherwise similar $RbCuSnS_3$ type with T3 layers.[23, 25, 47-49] The supertetrahedral layers interlock like saw teeth, and are separated by sodium and barium atoms at either uniform or Ba/Na mixed sites as shown in Figure 9.2. The fully occupied Ba3 is in a trigonal prism with two additional phosphorus atoms over the square faces ($d_{Ba\text{-}P}$ = 3.218-3.612 Å). Na2 in a distorted octahedron ($d_{Na\text{-}P}$ = 2.781-3.080 Å) is 82 %, and Na4 in a trigonal prism ($d_{Na\text{-}P}$ = 3.192-3.242 Å) is 73 % occupied. The electron densities at the two remaining cation sites are in between those of sodium and barium. Therefore, one cannot distinguish between partial Ba or Ba/Na mixed occupations or even a mixed occupation with an occupancy sum of less than 100 %. We used Ba/Na mixed sites and constrained the occupancy sums to unity, which resulted in an almost charge neutral structure but increased thermal displacements for the cations, which in turn is correlated to the respective occupancy factors. Nevertheless, due to the before mentioned indistinguishability by laboratory X-ray analysis, we tried to verify the crystal structure model with NMR and EDX measurements (*vide infra*). Figure 9.2 shows the connectivity of the cation coordination polyhedra and reveals, that the fully occupied Ba3 position (yellow polyhedra) blocks the migration path for Na^+ ions between the layers along the *b* direction. For interatomic distances and further crystallographic details

on the SiP connectivity within the T3 entities and the network topology we refer to Table D3 and Figure D1 and D3 in the SI.

$Na_{1.25}Ba_{0.875}Si_3P_5$ contains seven crystallographically different phosphorus sites, which distribute over three different multiplicities, namely 1×4*c* (*m*2*m*), 1×16*h* (1), 3×8*f* (*m*..) and 2×8*g* (..*m*). The signals of the ^{31}P solid-state MAS-NMR spectrum (Figure 9.3, left) confirms this sequence and thus the structure model. The ^{23}Na MAS-NMR (Figure 9.3, right) shows a central-transition at 3.6 ppm with a distinct shoulder in the downfield region. Integrating these signals gives a ratio of 1:1.52, which is compatible with the ratio between the mixed occupied Ba/Na and the solely occupied Na sites with 1:1.72 from the crystal structure. EDX elemental analysis further corroborates the cation distribution in $Na_{1.25}Ba_{0.875}Si_3P_5$ (Table D8).

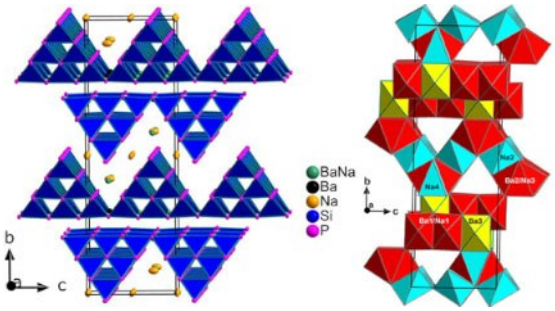

Figure 9.2 Left: Single-crystal structure of $Na_{1.25}Ba_{0.875}Si_3P_5$ composed of vertex-condensed and fused T3 supertetrahedra. Right: Cation coordination in $Na_{1.25}Ba_{0.875}Si_3P_5$. Yellow polyhedra are centred by Ba3 (100 %) and blue polyhedra by Na2 or Na4 (82 %, 73 %) whereas red polyhedra comprise mixed occupancies of Ba1/Na1 or Ba2/Na3.

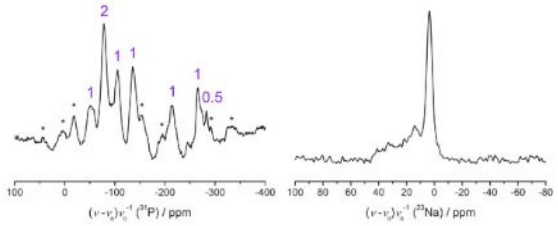

Figure 9.3 Solid-state MAS-NMR spectra of phosphorus and sodium at rotation frequencies of 12 and 10 kHz, respectively. Chemical shifts are δ (^{31}P) = -50.6, -78.0, -105.2, -135.8, -214.4, -265.5, -282.5 ppm and a ^{23}Na line position of 3.6 ppm.

$Na_{31}Ba_5Si_{52}P_{83}$ forms a more complex structure with 684 atoms in the unit cell. Ten SiP_4 tetrahedra each form T3 units (yellow, orange and turquoise in Figure 9.4, and a ball-stick model is shown in Figure D2 in the SI), three of which are linked by sharing one SiP_4 tetrahedron. This results in fragments of T5 supertetrahedra in such a way that T5 entities lack four SiP_4 tetrahedra or one T2 vertex. In these voids are the tenfold phosphorus-coordinated barium atoms (Figure 9.4). Two of the T3 clusters comprise Si-Si bonds in Si-SiP_3 tetrahedra (purple polyhedra in Figure 9.4). Such Si-Si bonds are rare and, to the best of our knowledge, have only been observed in $BaCuSi_2P_3$,[50] $Ca_3Si_2P_4$, $Ca_3Si_8P_{14}$[26] and in the reduced nitridosilicate $SrSi_6N_8$.[51] Si and P are hardly distinguishable by X-ray diffraction. We have identified

the Si-Si bonds by refining the occupation factors and based on the different lengths of Si-P (∅ 2.23 Å) and Si-Si bonds (∅ 2.30 Å) in the Si_2P_6 groups. The defect T5 clusters are vertex condensed with two T5, and share one SiP_4 tetrahedron with two equivalent T5 entities (Figure 9.4). The Si-Si bonds connect a crystallographically equivalent motif of defect T5 units with opposite orientation, forming a dense single network (Figure 9.5, ball-stick model is given in Figure D2) unlike to $Na_{23}Si_{9n+19}P_{12n+33}$, $LiSi_2P_3$, and KSi_2P_3 with two interpenetrating networks, respectively.[36-38] The topology of this unprecedented 26-nodal network is shown in Figure D4 in the SI. The distortions arrise from different connectivities of the T3 supertetrahedra by homonuclear silicon bonds, vertex condensations and fusions. This supertetrahedral network contains large cavities proceeding in *c* direction (Figure 9.6). These cavities contain sodium ions exclusively, as desired for possible Na^+ conduction. While the Ba2 site in the T2-void of the defective T5 entities is fully occupied (Figure 9.4), the Ba1 and Ba3 sites show occupancies near to 50 % and 100 %, respectively, and were therefore constrained to these values. The sodium atoms are distributed over 19 crystallographic sites, eight of which are disordered with occupations between 49 % and 90 %. Those sodium positions with occupancies near to 50 % were also constrained providing realistic interatomic distances to other partially occupied cation sites and charge neutrality of the whole unit cell.

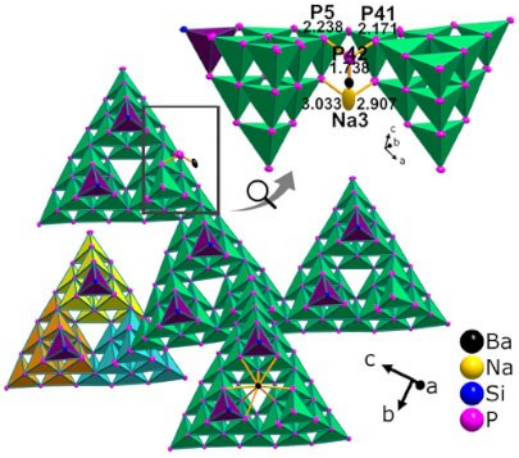

Figure 9.4 Basic building units of $Na_{31}Ba_5Si_{52}P_{83}$ composed of fused T3 supertetrahedra (yellow, orange and turquoise) and their connection among each other. Every T3 triplet is topped by one Ba ion, shown only for the undermost triplet for clarity. Si-SiP_3 tetrahedra are depicted in violet. Inset shows an additional P atom not connected to silicon but forming a P_3-trimer (see text for details).

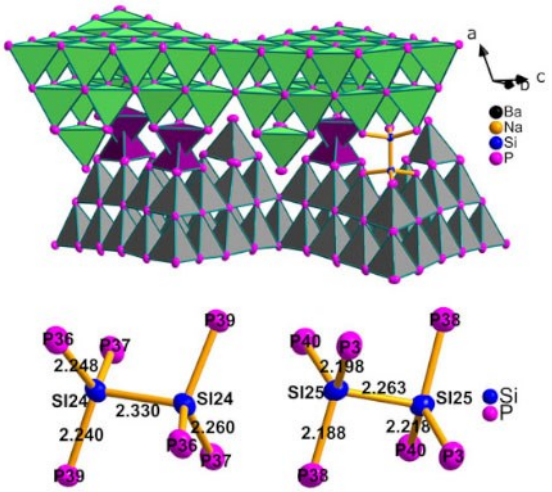

Figure 9.5 Condensation of the opposing supertetrahedral layers in $Na_{31}Ba_5Si_{52}P_{83}$ exclusively by two silicon-silicon dumbbells depicted as violet tetrahedra (top) and ball-and-stick model with interatomic distances in Å (bottom, further distances in Table D6 in the SI)

The thermal displacements of the sodium atoms exceed those of the barium atoms which is desirable in view of possible ion migration although the displacement and occupancy factors correlate. Additionally, the difference map revealed a residual electron density near Ba2 (1.738 Å, Ba2 with 50 % occ.), P5 and P41 with distances of 2.238 Å and 2.171 Å, respectively, which are typical for homonuclear phosphorus

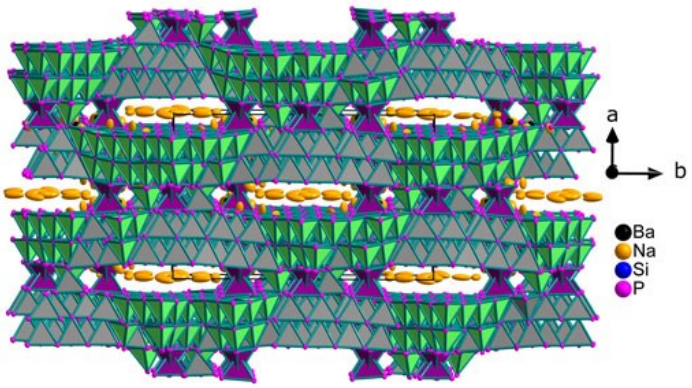

Figure 9.6 Crystal structure of $Na_{31}Ba_5Si_{52}P_{83}$ with large channels filled with Na ions propagating in *c* direction.

bonds. The occupation refinement of this position yielded also near 50 % of phosphorus. Therefore we assume this position as P42 site (d(P42-Na3) = 3.033 Å) leading to a P_3 trimer present if the Ba2 position is unoccupied. This motif occurs also in $Na_{19}Si_{13}P_{25}$.[37] Therefore the formally ionic formula is $(Na^+)_{31}(Ba^{2+})_5(Si^{4+})_{48}(Si^{3+})_4(P^{3-})_{80}(P^{2-})_2(P^{1-})$. Further interatomic distances are listed in Table D6 in the SI.

Solid-state NMR methods are suitable to verify the crystal structure and allow first insights into possible atom exchange processes. No resonance frequency of the ^{137}Ba nuclei (spin I = 3/2) was observed due to strong quadrupolar interactions, which massively broaden the resonance lines. Figure 9.7 shows the MAS-spectra of ^{31}P and ^{23}Na nuclei. As the single-crystal model of this compound comprises 42 independent phosphorus atoms on general Wyckoff sites (8*f*) the resonance frequencies in the ^{31}P spectrum overlap and sum up to broad resonance bands. Solely one asymmetric signal at δ (^{31}P) = -227.1 ppm is quite isolated, which is marked with an asterisk in Figure 9.7. Assuming this signal belongs to two magnetically independent phosphorus atoms due to the asymmetric line shape, the whole spectrum can be referenced to its intensity. This results in 44 magnetically independent phosphorus atoms instead of 41.5. However, the sample contains a small amount of $Na_{23}Si_{37}P_{57}$ as impurity, which cannot be de-convoluted. Therefore, the ^{31}P spectrum can only be taken as an indication of the plausibility of the crystal structure. In contrast, the ^{23}Na spectrum is surprisingly simple. Only one single resonance

frequency occurs at 13.4 ppm (see Figure 9.7, right) without a shoulder as in the case of $Na_{1.25}Ba_{0.875}Si_3P_5$. For this reason a mixed occupancy of the Ba sites with Na were not taken into account, as it would considerably broaden the ^{23}Na resonance. Since there are 19 crystallographically different sodium positions distributed onto 17 general Wyckoff sites 8*f* (1) and two 4*e* (2), a single resonance frequency indicates fast exchange processes of the sodium atoms. The FWHM is around 1.1 kHz, which is in the same range as in the Na^+ ion conductor *HT*-$NaSi_2P_3$ (1.9 kHz). Since this structure provides large channels solely filled with Na ions, we assume predominantly one-dimensional ion migration, although these channels are linked by small pathways along the T3 faces (calculated pathways are in the SI). Unfortunately, we were not successful in producing single-phased samples to test the ionic conductivity directly by impedance spectroscopy. Therefore, as a first test for possible Na^+ ion mobility, NMR T_1-relaxometry provides activation energies independent of sample morphologies and constriction phenomena. Spin-lattice relaxation times T_1 have been measured using the saturation recovery method and assuming bi-exponential recovery (see SI for details).

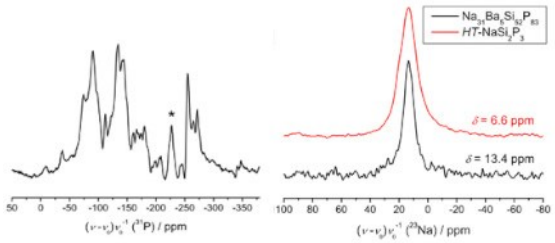

Figure 9.7 Solid-state MAS-NMR spectra of phosphorus and sodium at rotation frequencies of 25 kHz, respectively. Chemical shifts are δ (^{31}P) = -37.7 to -179.7, 208.5 and -245.7 to 271.3 ppm and a ^{23}Na line position of 13.4 ppm. For comparison, the ^{23}Na spectrum of *HT*-$NaSi_2P_3$ is plotted in red.

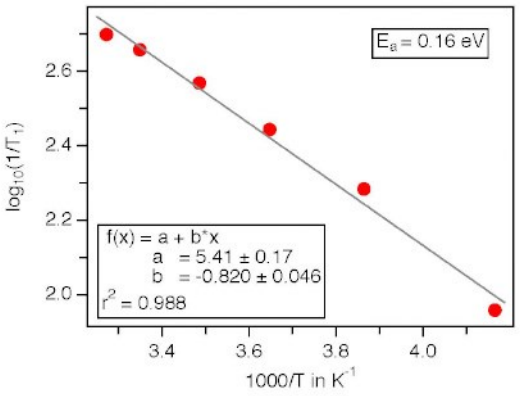

Figure 9.8 Temperature dependence of the spin-lattice relaxation rates ($1/T_1$) of ^{23}Na nuclei in $Na_{31}Ba_5Si_{52}P_{83}$. The slope of the linear fit gives the activation energy of the sodium mobility. See the SI for details.

Figure 9.8 shows a logarithmic plot of the inverse relaxation rates $1/T_1$ versus the inversetemperature. As expected in the low temperature regime,[52] the plot shows a good linear correlation. The slope of the linear fit gives the activation energy of the Na^+ ion motion of 0.16 eV, which is relatively small. This does not necessarily reflect ion conductivity, but a correlation of small activation energies with fast ion diffusion is often observed.[42, 53, 54] Moreover, this activation energy is in a similar range as those

determined for the fast sodium ion conductor $NaSi_2P_3$ (E_a = 0.11 - 0.14 eV; σ (Na^+) = $4 \cdot 10^{-4}$ Scm^{-1} at 25 °C).[37] Therefore, we assume similar values for the predominantly one-dimensional Na^+ ion conductivity in $Na_{31}Ba_5Si_{52}P_{83}$ though we do not expect overall high ion conductivity in polycrystalline material because ion movement is blocked at the boundaries of randomly oriented grains.

9.4 Conclusion

$Na_{1.25}Ba_{0.875}Si_3P_5$ and $Na_{31}Ba_5Si_{52}P_{83}$ are new quaternary phosphidosilicates with complex crystal structures based on supertetrahedral entities together with rare motifs like Si-Si bonds and P_3 trimers. The concept formulated at the beginning, according to which the incorporation of larger Ba cations could improve ion conduction, did not work out insofar as the new structures do not have sufficient three-dimensional ion migration paths. Nevertheless, our results show that such quaternary phosphidosilicates do exist and can form remarkable new structures. We assume that there are many more related compounds to discover, among which can also be good ionic conductors.

9.5 Experimental Section

Synthesis. Both compounds were synthesized by solid-state reactions of stoichiometric mixtures of the elements. Na (99.8 %, Alfa Aesar), Ba (99.99 %, SMT Metalle Wimmer), Si powder (99.8 %, Smart Elements) and red P (> 99 %, Chempur) were filled in alumina crucibles and sealed in silica ampoules under inert conditions. $Na_{1.25}Ba_{0.875}Si_3P_5$ was prepared in a three-step synthesis by heating to 700 °C within 7 h and a reaction time of 20 h in a tube furnace with intermediate homogenisation. After homogenization, the intermediate was heated to 900 °C within 9 h and 20 h of reaction time twice leading to phase pure samples. For $Na_{31}Ba_5Si_{52}P_{83}$ the elemental mixture was heated to 850 °C with a 50 °C/h heating rate and maintained for 150 h bevor the furnace was cooled down with 20 °C/h. Both compounds are polycrystalline, moisture sensitive black powders.

Single-Crystal X-ray Diffraction. Due to air and moisture sensitivity of both compounds, plate-like crystals have been selected and sealed in glass capillaries under dried paraffin oil. Single-crystal datasets were collected with a Bruker D8 Quest diffractometer with Göbel mirror optics, Mo-Kα radiation, and Photon II detector. Integration and absorption correction were processed with APEX 3 software.[43] For single-crystal structure solution and refinement the direct methods in the SHELX[44] software package

were applied and the final structures presented by Diamond.[45] CCDC-2076577 and 2076578 contain the supplementary crystallographic data for this paper.

Powder X-ray Diffraction. Powdered samples were filled into Hilgenberg glass capillaries and sealed under argon. Diffraction data were collected using a Stoe Stadi P diffractometer (Debye-Scherrer geometry, Mythen 1k detector, Ge(111) monochromator, Mo-Kα1 radiation). Based on the single-crystal structure data the powder patterns were refined with the Topas software.[46] The results are shown in Table D5 in the SI.

Solid-State MAS-NMR. The spectra were acquired on a Bruker Avance III 500 spectrometer with Larmor frequencies of $\nu_0(^{23}Na)$ = 132.33 MHz and $\nu_0(^{31}P)$ = 202.51 MHz using a commercial 4 mm MAS probe. The phosphorus spectrum of $Na_{31}Ba_5Si_{52}P_{83}$ was obtained using a 2.5 mm zirconia rotor. Spectra were referenced indirectly to ^1H in 0.1 % TMS in $CDCl_3$ at 0 ppm for the 4 mm and to ^1H in 100 % TMS at -0.124 ppm for the 2.5 mm rotor.

Elemental Analysis. Elemental compositions were examined with energy dispersive X-ray spectroscopy. Polycrystalline samples were stuck onto electro conductive carbon pads and inserted quickly into a scanning electron microscope (EVO MA-10, Zeiss). Characteristic radiation was collected by a Bruker X-Flash 410-M detector using 20 kV acceleration voltage.

9.6 References

[1] H. Li, J. Kim, T. L. Groy, M. O'Keeffe, O. M. Yaghi, *J. Am. Chem. Soc.* **2001**, *123*, 4867.

[2] H. Li, A. Laine, M. O'Keeffe, O. M. Yaghi, *Science* **1999**, *283*, 1145.

[3] C. Wang, Y. Li, X. Bu, N. Zheng, O. Zivkovic, C.-S. Yang, P. Feng, *J. Am. Chem. Soc.* **2001**, *123*, 11506.

[4] L. Wang, T. Wu, F. Zuo, X. Zhao, X. Bu, J. Wu, P. Feng, *J. Am. Chem. Soc.* **2010**, *132*, 3283.

[5] C. Wang, X. Bu, N. Zheng, P. Feng, *J. Am. Chem. Soc.* **2002**, *124*, 10268.

[6] L. Wang, T. Wu, X. Bu, X. Zhao, F. Zuo, P. Feng, *Inorg. Chem.* **2013**, *52*, 2259.

[7] C. L. Cahill, Y. Ko, J. B. Parise, *Chem. Mater.* **1998**, *10*, 19.

[8] C. L. Cahill, J. B. Parise, *J. Chem. Soc., Dalton Trans.* **2000**, 1475.

[9] M. K. Leszczyński, I. Justyniak, K. Zelga, J. Lewiński, *Dalton Trans.* **2017**, *46*, 12404.

[10] P. Vaqueiro, S. Makin, Y. Tong, S. J. Ewing, *Dalton Trans.* **2017**, *46*, 3816.

[11] Z.-Q. Li, C.-J. Mo, Y. Guo, N.-N. Xu, Q.-Y. Zhu, J. Dai, *J. Mater. Chem. A* **2017**, *5*, 8519.

[12] W.-W. Xiong, J.-R. Li, B. Hu, B. Tan, R.-F. Li, X.-Y. Huang, *Chem. Sci.* **2012**, *3*, 1200.

[13] D. Pitzschke, C. Näther, W. Bensch, *Solid State Sci.* **2002**, *4*, 1167.

[14] H. Wang, W. Wang, D. Hu, M. Luo, C. Xue, D. Li, T. Wu, *Inorg. Chem.* **2018**, *57*, 6710.

[15] X. Xu, W. Wang, D. Liu, D. Hu, T. Wu, X. Bu, P. Feng, *J. Am. Chem. Soc.* **2018**, *140*, 888.

[16] H. Wang, H. Yang, W. Wang, C. Xue, Y. Zhang, M. Luo, D. Hu, J. Lin, D. Li, T. Wu, *CrystEngComm* **2017**, *19*, 4709.

[17] X.-M. Zhang, D. Sarma, Y.-Q. Wu, L. Wang, Z.-X. Ning, F.-Q. Zhang, M. G. Kanatzidis, *J. Am. Chem. Soc.* **2016**, *138*, 5543.

[18] Q. Lin, X. Bu, P. Feng, *Chem. Commun.* **2014**, *50*, 4044.

[19] D. Vitzthum, K. Wurst, J. Prock, P. Brüggeller, H. Huppertz, *Inorg. Chem.* **2016**, *55*, 11473.

[20] E. M. Bertschler, T. Bräuniger, C. Dietrich, J. Janek, W. Schnick, *Angew. Chem. Int. Ed.* **2017**, *56*, 4806.

[21] E.-M. Bertschler, C. Dietrich, T. Leichtweiß, J. Janek, W. Schnick, *Chem. Eur. J.* **2018**, *24*, 196.

[22] D. Müller, F. E. Poltmann, H. Hahn, *Z. Naturforsch. B* **1974**, *29*, 117.

[23] J. H. Liao, M. G. Kanatzidis, *Chem. Mater.* **1993**, *5*, 1561.

[24] D. Schwarzenbach, *Z. Kristallogr.* **1969**, *128*, 97.

[25] K. Feng, L. Kang, W. Yin, W. Hao, Z. Lin, J. Yao, Y. Wu, *J. Solid State Chem.* **2013**, *205*, 129.

[26] X. Zhang, T. Yu, C. Li, S. Wang, X. Tao, *Z. Anorg. Allg. Chem.* **2015**, *641*, 1545.

[27] A. Hammerschmidt, A. Lindemann, M. Döch, B. Krebs, *Solid State Sci.* **2002**, *4*, 1449.

[28] A. Hammerschmidt, P. zum Hebel, F. Hiltmann, B. Krebs, *Z. Anorg. Allg. Chem.* **1996**, *622*, 76.

[29] F. Hiltmann, P. zum Hebel, A. Hammerschmidt, B. Krebs, *Z. Anorg. Allg. Chem.* **1993**, *619*, 293.

[30] L. Toffoletti, H. Kirchhain, J. Landesfeind, W. Klein, L. van Wüllen, H. A. Gasteiger, T. F. Fässler, *Chem. Eur. J.* **2016**, *22*, 17635.

[31] H. Eickhoff, C. Sedlmeier, W. Klein, G. Raudaschl-Sieber, H. A. Gasteiger, T. F. Fässler, *Z. Anorg. Allg. Chem.* **2020**, *646*, 95.

[32] V. Weippert, A. Haffner, D. Johrendt, *Z. Naturforsch. B* **2020**, *75*, 983.

[33] T. M. F. Restle, V. L. Deringer, J. Meyer, G. Raudaschl-Sieber, T. F. Fässler, *Chem. Sci.* **2021**, *12*, 1278.

[34] K. Kaup, A. Assoud, J. Liu, L. F. Nazar, *Angew. Chem. Int. Ed.* **2021**, *60*, 6975.

[35] P. Wagatha, P. Pust, V. Weiler, A. S. Wochnik, P. J. Schmidt, C. Scheu, W. Schnick, *Chem. Mater.* **2016**, *28*, 1220.

[36] A. Haffner, T. Bräuniger, D. Johrendt, *Angew. Chem. Int. Ed.* **2016**, *55*, 13585.

[37] A. Haffner, A.-K. Hatz, I. Moudrakovski, B. V. Lotsch, D. Johrendt, *Angew. Chem. Int. Ed.* **2018**, *57*, 6155.

[38] A. Haffner, A.-K. Hatz, O. E. O. Zeman, C. Hoch, B. V. Lotsch, D. Johrendt, *Angew. Chem. Int. Ed.* **2021**, DOI: 10.1002/anie.202101187.

[39] T. Sasaki, H. Takizawa, K. Uheda, T. Yamashita, T. Endo, *J. Solid State Chem.* **2002**, *166*, 164.

[40] V. Weippert, A. Haffner, A. Stamatopoulos, D. Johrendt, *J. Am. Chem. Soc.* **2019**, *141*, 11245.

[41] A. R. West, *Solid State Chemistry and its Applications*, Wiley, West Sussex, United Kingdom, 2 edn., **2014**.

[42] M. A. Kraft, S. P. Culver, M. Calderon, F. Böcher, T. Krauskopf, A. Senyshyn, C. Dietrich, A. Zevalkink, J. Janek, W. G. Zeier, *J. Am. Chem. Soc.* **2017**, *139*, 10909.

[43] APEX3, Bruker AXS Inc., Madison, Wisconsin, **2016**.

[44] G. M. Sheldrick, *Acta Crystallogr. Sect. A* **2008**, *64*, 112.

[45] K. Brandenburg, Crystal Impact GbR, Bonn, **2014**.

[46] A. Coelho, TOPAS-Academic, Coelho Software, Brisbane, **2007**.

[47] H. Li, C. D. Malliakas, J. A. Peters, Z. Liu, J. Im, H. Jin, C. D. Morris, L.-D. Zhao, B. W. Wessels, A. J. Freeman, M. G. Kanatzidis, *Chem. Mater.* **2013**, *25*, 2089.

[48] H. Li, C. D. Malliakas, Z. Liu, J. A. Peters, H. Jin, C. D. Morris, L. Zhao, B. W. Wessels, A. J. Freeman, M. G. Kanatzidis, *Chem. Mater.* **2012**, *24*, 4434.

[49] H. Lin, J.-N. Shen, L. Chen, L.-M. Wu, *Inorg. Chem.* **2013**, *52*, 10726.

[50] P. Yox, S. J. Lee, L.-l. Wang, D. Jing, K. Kovnir, *Inorg. Chem.* **2021**, DOI: 10.1021/acs.inorgchem.0c03636.

[51] F. Stadler, O. Oeckler, J. Senker, H. A. Höppe, P. Kroll, W. Schnick, *Angew. Chem. Int. Ed.* **2005**, *44*, 567.

[52] R. Böhmer, K. R. Jeffrey, M. Vogel, *Prog. Nucl. Mag. Res. Sp.* **2007**, *50*, 87.

[53] G. Sahu, E. Rangasamy, J. Li, Y. Chen, K. An, N. Dudney, C. Liang, *J. Mater. Chem. A* **2014**, *2*, 10396.

[54] M. Sharma, S. Yashonath, *J. Chem. Phys.* **2008**, *129*, 144103.

10 Summary

This thesis emphasizes the multifaceted chemistry of the underrepresented class of phosphidosilicates in literature. Although the basic building unit in phosphidosilicates consisting in SiP_4 tetrahedra is very simple, their possible condensation modes, which are briefly outlined in the introduction, increase the structural degree of freedom compared to the related class of its oxido or nitrido analogues. On the other hand, this thesis hints the peculiarity of the silicon-phosphorus-system to form relatively dense structures by applying low concentrations of alkaline or alkaline earth counter ions, which can be derived from supertetrahedral motifs.

The chapters in the first part of this thesis, dealing with alkaline metal phosphidosilicates, serve as examples for the formation of silicon-phosphorus supertetrahedra. Chapter 2 deals with the discovery of Li_2SiP_2 and $LiSi_2P_3$ and their unusual crystal structures. While in Li_2SiP_2 only T2 supertetrahedra, in $LiSi_2P_3$, T4 as well as T5 clusters are formed. By common vertices or by fusion diamond- or sphalerite-like networks with large voids are built, which are interpenetrated by an equivalent network preserving a collapse of the crystal structure. The lithium counter ions for the charge compensation of the anionic network are located between these supertetrahedral networks and induce only one single and very sharp resonance in the presented NMR spectra indicating their facile movement already at room temperature. For an estimation and insight into these exchange processes temperature dependent NMR measurements were performed, which revealed very low activation energies for the exchange processes.

In Chapter 3, the clustering of the SiP_4 tatrahedra into supertetrahedral entities is corroborated by the synthesis of the sodium phosphidosilicate series of $Na_{23}Si_{9n+19}P_{12n+33}$ with n = 0-3 and $Na_{19}Si_{13}P_{25}$. Here, supertetrahedra can be found ranging from T3 to T5 entities arranged in related networks as discussed for the lithium compounds. Likewise, the sodium ions reveal a single resonance in NMR measurements due to exchange processes with low activation energies for the two $NaSi_2P_3$ polymorphes, in line with the values of Li_2SiP_2 and $LiSi_2P_3$. Further, the improvement of the ionic conductivity is shown from the compound comprising solely T3 entities to *HT*-$NaSi_2P_3$ with exclusively T5 units originating from the expansion of possible migration paths and the increase of partial occupied sodium sites. Electrical

measurements give also low activation energies with associated high ion conductivities, but suggest on the other hand the probable enhancement of the conduction values by more sophisticated sample preparation techniques.

Surprisingly no supertetrahedral sodium analogue to Li_2SiP_2 was found, whereas K_2SiP_2 and Cs_2SiP_2 are also known, but differ in structure. Therefore, Chapter 4 targets the synthesis and crystal structure of the sodium compound Na_2SiP_2. Here all SiP_4 tetrahedra are condensed by common edges to form a SiS_2-like arrangement of three crystallographic independent $_\infty^1[SiP_2]^{2-}$ chains, separated by sodium ions. NMR investigations confirmed the crystal structure and electrochemical measurements revealed a mixed conduction behavior of Na_2SiP_2 with a low performance.

Chapter 5 illustrates the quest for the lithium and sodium analogue T5 compound KSi_2P_3, driven by chemical intuition, since a compound is already known with the same stoichiometry but composed of layers of fused T3 entities. Although the solely-T5-KSi_2P_3 structure is no longer surprising at this stage, it reveals though unexpected behavior. The publication presents the reconstructive phase transition from the known T3 to the T5 polymorph at temperatures beyond 1000 °C. In addition, this T5 compound passes through two more displacive phase transitions close to room temperature making this compound enantiotropic. Although potassium ions are almost twice as heavy and markedly larger than sodium ions, electrospectroscopic data reveal comparable high ion conductivities and low activation energies. The potassium nuclei inhibit the estimation of the activation energies by NMR measurements, but it is assumed that more sophisticated sample preparation techniques will be able to increase the measured ionic conductivity as well. However, besides the promising ion conductivities of the supertetrahedral alkaline metal phosphidosilicates, they have to prove their suitability for utilization in solid-state-batteries in further studies.

While the first section of this thesis covers “light” alkaline phosphidosilicates dealing with lithium, sodium or potassium, the second part focuses on the incorporation of alkaline earth elements into the ternary Si-P system. $SrSi_7P_{10}$ and the isotypic $BaSi_7P_{10}$ introduced in Chapter 6 comprise a highly condensed anionic network, which can be derived from fused and vertex-condensed T2 entities in a dimond type network. The Sr^{2+} and Ba^{2+} ions reside in cuboctahedral voids within the network. The cell parameters of both compounds are nearly identical, owed to the rigid network, and the alkaline earth cations show large displacement ellipsoids indicating disorder in the cuboctahedra.

Covalent bonding in the SiP_4 tetrahedra was verified by theoretical calculations on Ba_2SiP_4, were all SiP_4 tetrahedra are interconnected by homonuclear phosphorus bonds as shown in Chapter 7. The anionic network of the crystal structure resemble the β-cristobalite structure if one considers the P_2 dimers as oxygen ions and the compound exhibits an indirect band gap of 0.9 eV. This compound was additionally found to be a low temperature modification and the reversible reconstructive phase transitions are shown in Chapter 8. In the high temperature modification the SiP_4 tetrahedra are condensed by P–P bonds as well, but now $^1_\infty[SiP_4]^{4-}$ chains are formed reminiscent to the elusive fibrous SiO_2. This polymorph is also a semiconductor with an indirect band gap of about 1.7 eV.

The third and last section of this thesis indicates that quaternary phosphidosilicates are also attainable, of which only very few examples are known. To improve the ionic conductivity in the discussed sodium phosphidosilicates series $Na_{23}Si_{9n+19}P_{12n+33}$, larger Ba^{2+} ions were incorporated into the Na–Si–P system, resulting in two new compounds described in Chapter 9. $Na_{1.25}Ba_{0.875}Si_3P_5$ and $Na_{31}Ba_5Si_{52}P_{83}$ both are built of fused T3 entities, which form defect T5 clusters for the latter compound. Instead of one additionally fused T3 entity, which would yield a regular T5 tetrahedron, it is replaced by a Ba cation. Homonuclear silicon bonds, as discussed in the Introduction, link the T3 entities to a three-dimensional structure, with large ion migration channels similar to those mentioned in the first part of the thesis. While the barium cations are distributed almost isotropic between the supertetrahedra in the first compound, they tend to cluster not in the huge channels for $Na_{31}Ba_5Si_{52}P_{83}$ which are therefore filled with sodium ions only. Unfortunately, these channels are rather one-dimensional which impede electrospectroscopic measurements due to blocking effects but temperature dependent NMR measurements indicate mobile sodium ions with a low activation energy of 0.16 eV.

11 Outlook

The objective of this thesis was to shed light onto the barely explored structure family of phosphidosilicates with alkaline and alkaline earth cations by an explorative study. It was shown that phosphidosilicates unexpectedly tend to cluster into supertetrahedral entities when only small amounts of counter ions are available in the solid-state reactions. This tendency promotes a fast ionic conduction for respective alkaline phosphidosilicates due to the formation of large migration paths and partially occupied cation sites. Together with one of the simplest solid-state preparation technique consisting in the bare heating of elemental mixtures, these compounds could be prepared in large-scale if they demonstrate their suitability for respective applications by further research. Additionally, this thesis illustrates the versatile structure chemistry of the Si–P system and hints at the existence of numerous yet unknown substances in this family. The investigations of new phosphidosilicates start to revive since within only the last four years about 20 new ternary structures were reported, whereof more than the half are presented herein (cf. Figure 11.1 and Figure 1.5).

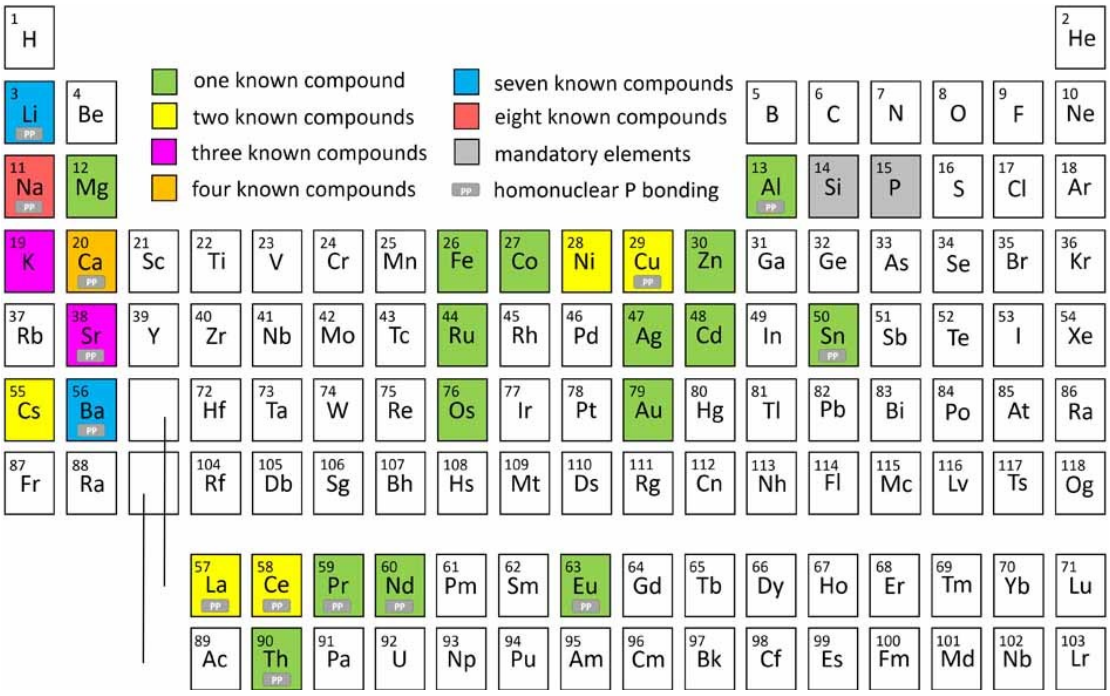

Figure 11.1 Color-coded periodic table of elements representing known ternary compounds in the family class of phosphidosilicates until the end of the year 2020.

On the other hand, this thesis highlights the need for additional research on several issues. Beside the exploration of other ternary phosphidosilicates, which may be overlooked – for example $K_{21}Si_{20}P_{35}$ composed of SiP_4 double-chains comprising homonuclear silicon bonding – this family is to be extended to quaternary or multinary systems, as it was done in Chapter 9. This approach offers a great prospect of success since the compounds $Li_{12.3}Ba_{4.35}Si_{33}P_{51}$, mentioned already in Chapter 1, $Li_4(Sr;Ca)_2SiP_4$ and $Li_{16}Ba_4Si_3P_{12}$ were already synthesized and investigated and are to be published. Likewise, a multi-anion strategy may offer similar achievements for example by the incorporation of halides in $Ba_4(Cu;Ag;Au)Si_{10}P_{16}Cl$ or the combination of nitrido- with phosphido- to nitridophophidosilicates. The latter idea may require more sophisticated preparation techniques, but in principle, it appears to be possible since in the related compound class of aluminates the yet unknown oxido-phosphidoaluminate $(Sr;Ba)Al_2P_2O$, which is surprisingly structurally related to the nitridophosphate $Ce_4Li_3P_{18}N_{35}$, was detected as a result of the reaction of the alumina crucibles with phosphidosilicate reaction mixtures. However, the biggest challenge, comparing Figure 11.1, is the development of a synthetic access to transition metal phosphidosilicates since the thermal treatment of elemental mixtures mostly yields stable transition metal phosphides. These compounds may be very interesting regarding their potential application as electrode materials in power storage devices. Approaches to overcome this hindrance are the usage of metathesis or the utilization of ionic or metallic fluxing agents. However, experiments applying these strategies failed so far. Another approach may be the raise of the reaction temperature well beyond 1100 °C, involving additional problems in the inadvertent reaction of alumina or metallic crucibles. By applying boron nitride crucibles within the multi anvil high-pressure and high-temperature synthesis route this issues may be overcome.

The published articles within this cumulative dissertation just scratched the surface of the phosphidosilicate compound space and there will definitely be an exciting progress in this field in the next years to come.

A Appendix – Supporting Information for Chapter 2

A.1 Crystallographic Data on Supertetrahedral Lithium Phosphidosilicates

Table A1 Fractional atomic coordinates, isotropic or equivalent displacement parameters and occupation factors for Li_2SiP_2.

Atom	Wyckoff Symbol	*x*	*y*	*z*	U_{eq} / Å^2	Occ.
P1	32*g*	0.53452 (4)	0.03715 (4	0.12236 (3)	0.01111 (14)	1
P2	16*e*	¾	0.06796 (6	0	0.00887 (17)	1
P3	16*d*	½	¼	−0.01885 (4)	0.01041 (18)	1
Si4	32*g*	0.62070 (4)	0.16757 (4)	0.05714 (3)	0.00790 (14)	1
Li5	16*f*	0.5949 (3)	−0.1551 (3)	1/8	0.0176 (11)	1
Li6	32*g*	0.6218 (4)	−0.0910 (4)	−0.0317 (2)	0.0273 (10)	1
Li7	16*f*	0.8496 (5)	0.0996 (5)	0.1/8	0.0372 (16)	1

Table A2 Atomic displacement parameters for Li_2SiP_2 in Å^2.

Atom	U_{11}	U_{22}	U_{33}	U_{12}	U_{13}	U_{23}
P1	0.0117 (3)	0.0080 (3)	0.0136 (3)	0.0000 (2)	0.0040 (2)	0.0003 (2)
P2	0.0081 (4)	0.0076 (4)	0.0109 (4)	0.000	0.0032 (3)	0.000
P3	0.0112 (4)	0.0114 (4)	0.0086 (3)	0.0012 (3)	0.000	0.000
Si4	0.0074 (3)	0.0075 (3)	0.0088 (3)	0.0002 (2)	0.0013 (2)	−0.0014 (2)
Li5	0.0179 (17)	0.0179 (17)	0.017 (3)	0.006 (2)	0.0002 (15)	−0.0002 (15)
Li6	0.031 (2)	0.023 (2)	0.028 (2)	−0.0079 (18)	−0.0015 (18)	−0.0020 (18)
Li7	0.042 (2)	0.042 (2)	0.028 (3)	0.014 (3)	−0.004 (2)	0.004 (2)

Table A3 Fractional atomic coordinates, isotropic or equivalent displacement parameters and occupation factors for $LiSi_2P_3$.

Atom	Wyckoff Symbol	*x*	*y*	*z*	U_{eq} / Å^2	Occ.
P1	16*f*	0.12311 (3)	0.60581 (3)	0.02134 (2)	0.00745 (12)	1
P2	4*a*	0	3/4	7/8	0.0127 (2)	1
P3	16*f*	0.28192(3)	0.73051 (3)	0.01259 (2)	0.00868 (12)	1
P4	16*f*	0.40050 (3)	0.55428 (3)	0.01369 (2)	0.00837 (12)	1
P5	16*f*	0.26621 (3)	0.58344 (3)	−0.05746 (2)	0.00735 (11)	1
P6	16*f*	0.44184 (3)	0.83696 (3)	0.01494 (2)	0.00763 (12)	1
P7	16*f*	0.42620 (3)	0.70327 (3)	0.09258 (2)	0.00750 (11)	1
P8	16*f*	0.25470 (3)	0.58392 (3)	0.09079 (2)	0.00826 (12)	1
P9	16*f*	−0.01525 (3)	0.61041 (3)	−0.04969 (2)	0.00963 (12)	1

P10	16*f*	0.14488 (3)	0.74709 (3)	–0.04954 (2)	0.00982 (12)	1
P11	16*f*	0.38600 (3)	0.55776 (3)	0.16397 (2)	0.00757(12)	1
P12	16*f*	0.13051 (3)	0.59683 (3)	–0.12641 (2)	0.00973 (12)	1
P13	16*f*	0.28120 (3)	0.71848 (3)	0.16405 (2)	0.00777 (12)	1
P14	16*f*	0.42446 (3)	0.69470 (4)	–0.05717 (2)	0.01060 (12)	1
P15	16*f*	0.23441 (4)	0.44450 (3)	0.01961 (2)	0.01153 (13)	1
P16	16*f*	0.27719 (3)	0.72235 (4)	–0.12784 (2)	0.01166 (13)	1
P17	16*f*	0.14680 (3)	0.75021 (3)	0.08921 (2)	0.01023 (12)	1
P18	16*f*	0.36848 (3)	0.42415 (3)	0.08996 (2)	0.01012 (12)	1
P19	8*e*	0	3/4	0.02306 (3)	0.01175 (17)	1
P20	16*f*	0.10850 (4)	0.46520 (3)	–0.05073 (2)	0.01239 (13)	1
Si21	16*f*	0.34021 (3)	0.64277 (4)	0.12448 (2)	0.00712 (13)	1
Si22	16*f*	0.20015 (4)	0.66820 (4)	–0.08893 (2)	0.00822 (13)	1
Si23	16*f*	0.18685 (4)	0.52961 (4)	–0.01660 (2)	0.00769 (13)	1
Si24	16*f*	0.34443 (3)	0.64373 (4)	–0.01892 (2)	0.00746 (12)	1
Si25	16*f*	0.20691 (3)	0.67240 (4)	0.05353 (2)	0.00787 (13)	1
Si26	16*f*	0.44866 (4)	0.48230 (3)	0.12555 (2)	0.00748 (13)	1
Si27	16*f*	–0.07609 (4)	0.68604 (4)	–0.08811 (2)	0.01260 (14)	1
Si28	8*e*	1/2	3/4	–0.01809 (3)	0.00771 (17)	1
Si29	16*f*	0.06190 (4)	0.68289(4)	–0.01686 (2)	0.00847 (13)	1
Si30	16*f*	0.31544 (4)	0.50512 (3)	0.05249 (2)	0.00792 (13)	1
Si31	16*f*	0.36459 (3)	0.77607 (3)	0.05288 (2)	0.00687 (13)	1
Si32	16*f*	0.04949 (4)	0.53906 (3)	–0.08877 (2)	0.00813 (13)	1
Si33	16*f*	0.47125 (3)	0.61833 (3)	0.05368 (2)	0.00705 (13)	1
Li1	16*f*	0.4848 (4)	0.4154 (4)	0.0460 (2)	0.038 (2)	0.99(2)
Li2	16*f*	0.1365 (4)	0.4882 (4)	0.0699 (2)	0.036 (2)	0.92(2)
Li3	16*f*	0.2829 (4)	0.4576 (4)	0.1472 (2)	0.040 (2)	0.99(2)
Li4	8*c*	0	½	0	0.051 (5)	0.83(3)
Li5	16*f*	0.3341 (6)	0.2977 (4)	0.0738 (3)	0.081 (4)	1
Li6	16*f*	0.4004 (7)	0.6624 (7)	–0.1257 (3)	0.077 (4)*	0.93(2)
Li7	16*f*	0.1087 (5)	0.8338 (5)	0.0361 (3)	0.064 (3)*	1

Table A4 Atomic displacement parameters for $LiSi_2P_3$ in **Å²**.

Atom	U_{11}	U_{22}	U_{33}	U_{12}	U_{13}	U_{23}
P1	0.0083 (3)	0.0073 (3)	0.0067 (3)	–0.0002 (2)	–0.0018 (2)	0.0004 (2)
P2	0.0127 (4)	0.0127 (4)	0.0127 (6)	0.000	0.000	0.000
P3	0.0085 (3)	0.0099 (3)	0.0077 (3)	–0.0010 (2)	–0.0011 (2)	–0.0009 (2)
P4	0.0082 (3)	0.0090 (3)	0.0079 (3)	–0.0007 (2)	–0.0015 (2)	0.0002 (2)
P5	0.0082 (3)	0.0072 (3)	0.0066 (3)	–0.0004 (2)	–0.0013 (2)	0.0003 (2)
P6	0.0080 (3)	0.0088 (3)	0.0061 (3)	–0.0010 (2)	0.0004 (2)	0.0001 (2)
P7	0.0079 (3)	0.0077 (3)	0.0069 (3)	–0.0003 (2)	–0.0009 (2)	–0.0004 (2)
P8	0.0086 (3)	0.0084 (3)	0.0078 (3)	–0.0005 (2)	–0.0020 (2)	–0.0007 (2)
P9	0.0091 (3)	0.0093 (3)	0.0104 (3)	0.0005 (2)	–0.0020 (2)	–0.0014 (2)
P10	0.0100 (3)	0.0098 (3)	0.0096 (3)	0.0001 (2)	0.0004 (2)	0.0005 (2)
P11	0.0079 (3)	0.0071 (3)	0.0077 (3)	–0.0003 (2)	–0.0019 (2)	0.0002 (2)
P12	0.0099 (3)	0.0109 (3)	0.0084 (3)	–0.0018 (2)	–0.0011 (2)	0.0008 (2)
P13	0.0076 (3)	0.0085 (3)	0.0072 (3)	0.0006 (2)	–0.0004 (2)	–0.0010 (2)
P14	0.0106 (3)	0.0145 (3)	0.0067 (3)	–0.0050 (2)	–0.0013 (2)	–0.0001 (2)
P15	0.0142 (3)	0.0075 (3)	0.0129 (3)	–0.0011 (2)	–0.0067 (2)	0.0016 (2)
P16	0.0075 (3)	0.0134 (3)	0.0141 (3)	0.0020 (2)	0.0009 (2)	0.0069 (2)
P17	0.0079 (3)	0.0114 (3)	0.0114 (3)	–0.0001 (2)	–0.0014 (2)	–0.0044 (2)
P18	0.0126 (3)	0.0067 (3)	0.0111 (3)	–0.0006 (2)	–0.0059 (2)	0.0008 (2)
P19	0.0154 (4)	0.0117 (4)	0.0081 (4)	0.0054 (3)	0.000	0.000
P20	0.0155 (3)	0.0070 (3)	0.0147 (3)	–0.0021 (2)	–0.0093 (2)	0.0019 (2)
Si21	0.0078 (3)	0.0071 (3)	0.0064 (3)	0.0006 (2)	–0.0011 (2)	–0.0004 (2)
Si22	0.0079 (3)	0.0083 (3)	0.0084 (3)	0.0005 (2)	–0.0014 (2)	0.0015 (2)
Si23	0.0084 (3)	0.0075 (3)	0.0072 (3)	–0.0010 (2)	–0.0015 (2)	0.0000 (2)
Si24	0.0074 (3)	0.0086 (3)	0.0064 (3)	–0.0014 (2)	–0.0012 (2)	0.0000 (2)
Si25	0.0078 (3)	0.0084 (3)	0.0073 (3)	–0.0001 (2)	–0.0012 (2)	–0.0014 (2)
Si26	0.0083 (3)	0.0069 (3)	0.0072 (3)	–0.0001 (2)	–0.0018 (2)	0.0005 (2)
Si27	0.0134 (3)	0.0125 (3)	0.0119 (3)	0.0044 (2)	–0.0048 (2)	–0.0043 (2)
Si28	0.0079 (4)	0.0085 (4)	0.0067 (4)	–0.0018 (3)	0.000	0.000
Si29	0.0093 (3)	0.0082 (3)	0.0079 (3)	0.0010 (2)	–0.0015 (2)	0.0001 (2)
Si30	0.0084 (3)	0.0072 (3)	0.0082 (3)	–0.0004 (2)	–0.0019 (2)	0.0005 (2)
Si31	0.0071 (3)	0.0072 (3)	0.0064 (3)	–0.0009 (2)	0.0003 (2)	–0.0012 (2)
Si32	0.0081 (3)	0.0068 (3)	0.0095 (3)	–0.0005 (2)	–0.0022 (2)	0.0001 (2)
Si33	0.0068 (3)	0.0076 (3)	0.0067 (3)	0.0000 (2)	–0.0004 (2)	0.0008 (2)

Li1	0.040(4)	0.035(4)	0.041(4)	-0.021(3)	0.008 (3)	0.002(3)
Li2	0.039(4)	0.038(4)	0.035(4)	0.012(3)	0.019 (3)	-0.001(3)
Li3	0.039(4)	0.042 (4)	0.040 (4)	0.010(3)	0.018(3)	-0.009(3)
Li4	0.061(9)	0.041(7)	0.057(8)	0.025(6)	0.036(7)	0.017(6)
Li5	0.099 (7)	0.019(3)	0.107 (7)	–0.018(4)	0.074(7)	–0.020 (4)
Li6	isotropic					
Li7	isotropic					

A.2 NMR Spectroscopy

To obtain the ^{7}Li-NMR spin-lattice relaxation time (T_1) at different temperatures, the saturation recovery technique was used. The integrated intensities were then fitted using a mono-exponential function, which adequately described the data (see Figure A1).

To determine an estimate of the activation energies, the following expression for the relaxation rates was used:

$$R_1 = \frac{1}{T_1} = \frac{2}{3} G(0) \left[\frac{\tau_c}{1+(\omega_0 \tau_c)^2} + \frac{4\tau_c}{1+(2\omega_0 \tau_c)^2} \right] \qquad (1)$$

Here, ω_0 is the Larmor frequency, and the τ_c are characteristic correlation times, which are assumed to follow an Arrhenius type of behaviour with activation energy E_a:

$$\tau_c = \tau_0 \, exp\left(\frac{E_a}{k_B T}\right) \qquad (2)$$

In the so-called low-temperature regime ($\omega_0 \tau_c >> 1$), Equation (1) reduces to the following form, wich can be linearized and fitted to extract the activation energies:

$$R_1 = \frac{1}{T_1} = \frac{4}{3} G(0) \frac{1}{\omega_0^2 \tau_0} exp\left(-\frac{E_A}{k_B T}\right) \qquad (3)$$

B Appendix – Supporting Information for Chapter 3

B.1 Experimental Procedures on Supertetrahedral Sodium Phosphidosilicates

Synthesis. Due to the sensitivity of the educts and products to air moisture all experiments and measurements were performed in an argon filled glovebox (Unilab, MBraun, O_2 < 0.1 ppm, H_2O < 0.1 ppm). All reactions were carried out in alumina crucibles welded under purified argon atmosphere in silica tubes which were placed in tube furnaces.

$Na_{23}Si_{19}P_{33}$ was synthesized by heating stoichiometric amounts of metallic Na (Alfa Aesar, 99.8 %), Si powder (Smart Elements, 99.8 %) and red phosphorus (Chempur, > 99 %) as multi-phase product. A phase-pure sample could only be prepared by using *in situ* formed 7.5 equivalents of Na_2S in addition as crystallization agent. Therefore, 41.9 mg of sodium were heated with 25.6 mg of Si, 49.0 mg P and 11.5 mg of sulfur (Merck, 99.0 %) to 100 °C (20 °C/h) before the temperature was increased to 850 °C with a 100 °C /h rate. This temperature was maintained for 40 h, slowly cooled down (10 °C/h) to 450 °C and finally quenched to room temperature. To eliminate Na_2S the sample was washed several times with dry methanol. Sorbed methanol was removed in high vacuum. ICP and elemental analysis revealed absence of sulfur, carbon, oxygen and hydrogen in the product.

$Na_{23}Si_{28}P_{45}$ was prepared by heating 19.5 mg of elemental Na with 29.0 mg Si and 51.4 mg of red phosphorus with the same temperature program to 900 °C for 60 h before the reaction was slowly cooled down to 450 °C and quenched to room temperature.

In the same way $Na_{23}Si_{37}P_{57}$ was synthesized with 31.7 mg Na, 62.4 mg Si and 105.9 mg P. The reaction time was decreased to 40 h.

LT-$NaSi_2P_3$ was obtained by reaction of stoichiometric amounts of the elements. Therefore, 26.7 mg Na, 65.3 mg Si and 108.0 mg P were reacted with the same heating protocol to 1000 °C. The reaction time was set to 40 h and the sample was cooled down with a 5 °C/h rate to 450 °C before the sample was quenched to room temperature. The multi-phased sample was ground and reheated leading to a phase-pure product.

HT-$NaSi_2P_3$ was synthesized from *LT*-$NaSi_2P_3$ as starting material. Therefore, *LT*-$NaSi_2P_3$ was ground thoroughly and filled in alumina crucibles. These were placed and welded in thick-walled silica tubes (2 mm) to withstand the high phosphorus pressure during reaction. These ampoules were welded a second time in tight-fitting silica tubes for further enhancing stability. These setups were welded a third time in larger silica tubes for sustaining an inert argon atmosphere in case of cracking of the first two tubes. This

3-layered set-up was heated to 1100 °C for 50 h before the temperature was decreased to 450 °C with 20 °C/h. In case of non-phase-pure samples this procedure was repeated.

$Na_{19}Si_{13}P_{25}$ was synthesized by reaction of 27.7 mg Na, 23.2 mg Si and 49.1 mg P not above 750 °C for 40 h. After homogenization this procedure was repeated twice.

Single-Crystal X-ray Diffraction. Suited crystals were selected under paraffin oil to prevent hydrolysis and sealed in oil filled Hilgenberg glass capillaries. Diffraction data were collected on a Bruker D8 Quest diffractometer equipped with a Photon-I detector at ambient temperatures using Mo-Kα radiation (λ = 0.71073 Å). The structures were solved and refined using SHELX97.

X-ray Powder Diffraction. Polycrystalline samples were ground and sealed in Hilgenberg glass capillaries under argon atmosphere. Measurements were carried out on a Stoe Stadi-P powder diffractometer with a Stoe Mythen-1k detector and a Ge monochromator in Debye-Scherrer geometry at room temperature using Mo-Kα radiation. For Rietveld refinement the Topas package was used.

EDX Measurements. Samples for energy dispersive X-ray spectroscopy were prepared by placing single crystals on conductive and adhesive carbon pads. These were inserted quickly in an EVO-Ma 10 scanning electron microscope (Zeiss) equipped with a field emission gun at an acceleration voltage not above 15 kV. For elemental analysis a Bruker X-Flash 410-M detector was used and received data were analyzed with the QUANTAX 200 software package. Signals of oxygen were not taken into account due to partial hydrolysis of the samples by short contact with air during sample insertion.

Nuclear Magnetic Resonance. ^{23}Na, ^{29}Si and ^{31}P spectra of powdered samples were measured on a Bruker Avance III 500 (magnetic field of 11.74 T) under MAS conditions at Larmor frequencies of ν_0 (^{23}Na) = 132.33 MHz, ν_0 (^{29}Si) = 99.38 MHz and ν_0 (^{31}P) = 202.49 MHz and on a Bruker Avance III 400 spectrometer (magnetic field 9.4 T) at Lamor frequencies of ν_0 (^{23}Na) = 105.79 MHz, and ν_0 (^{31}P) = 161.9 MHz. For ^{23}Na and ^{29}Si spectra a zirconia rotor with 4 mm diameter with a rotation frequency of 10 kHz was used while ^{31}P spectra were recorded at a rotation frequency of 50 kHz in a 1.3 mm or at 16 kHz in a 4 mm rotor. Variable temperature ^{23}Na-T_1-relaxation time measurements were performed on stationary samples at 9.4 T in order to determine the activation energies for Na^+-ion mobility. The temperature in the experiments was controlled using a Bruker BVT3000 temperature controller.

Electrical Conductivity Measurements. Electrochemical impedance spectroscopy and galvanostatic polarization measurements were performed with an Ivium compactstat.h (24 bit instrument) in a two-electrode setup using a home-built impedance cell which was kept under argon atmosphere during all

measurements. Before measuring, the samples were ground thoroughly and compacted to a pellet of about 1 mm thickness and 5 mm in diameter by uniaxial cold pressing (500 MPa). All pellets were subsequently annealed at 400 °C for 10 h in glassy carbon crucibles under purified argon atmosphere. Additionally, pellets of *LT*- and *HT*-$NaSi_2P_3$ were annealed at 800 °C. After annealing, the pellets were sandwiched between indium foil (Alfa Aesar, 0.127 mm of thickness, 99.99% (metals basis)) to enhance the contact with the measuring cells. No reactions between In and the samples were observed. The applied root mean square AC voltage was between 10-100 mV with a higher voltage for the less conducting samples. The analysis of the impedance spectra was carried out by means of the RelaxIS software from rhd instruments.

B.2 Crystallographic Data on Supertetrahedral Sodium Phosphidosilicates

Table B1 Fractional atomic coordinates and equivalent thermal displacement parameters for $Na_{19}Si_{13}P_{25}$.

Atom	Wyckoff Symbol	*x*	*y*	*z*	U_{eq} / Å^2
P1	2*i*	0.01458 (6)	0.40324 (5)	0.08750 (6)	0.00944 (13)
P2	2*i*	0.01898 (6)	0.40738 (5)	0.33334 (6)	0.00977 (14)
P3	2*i*	0.06603 (6)	0.39863 (5)	0.72214 (6)	0.01108 (14)
P4	2*i*	0.09190 (6)	0.19480 (6)	0.90106 (6)	0.01401 (15)
P5	2*i*	0.09273 (6)	0.84754 (5)	0.44804 (6)	0.01190 (14)
P6	2*i*	0.09714 (6)	0.20479 (6)	0.38150 (6)	0.01707 (16)
P7	2*i*	0.09879 (6)	0.19435 (5)	0.13958 (6)	0.01121 (14)
P8	2*i*	0.16207 (6)	0.86078 (5)	0.09007 (6)	0.01244 (14)
P9	2*i*	0.20224 (6)	0.66644 (5)	0.27243 (6)	0.01208 (14)
P10	2*i*	0.21058 (6)	0.66610 (5)	0.51667 (6)	0.01350 (15)
P11	2*i*	0.24343 (6)	0.10719 (6)	0.65492 (6)	0.01319 (15)
P12	2*i*	0.27725 (6)	0.47032 (5)	0.08499 (6)	0.01219 (14)
P13	2*i*	0.28883 (6)	0.46665 (5)	0.32396 (6)	0.00999 (14)
P14	2*i*	0.28999 (6)	0.47568 (6)	0.56498 (6)	0.01341 (15)
P15	2*i*	0.29307 (7)	0.03026 (6)	0.45126 (7)	0.02120 (17)
P16	2*i*	0.32741 (6)	0.12727 (6)	0.81610 (6)	0.01409 (15)
P17	2*i*	0.36479 (6)	0.25813 (6)	0.13539 (6)	0.01587 (15)
P18	2*i*	0.36825 (7)	0.26292 (6)	0.37097 (6)	0.01765 (16)
P19	2*i*	0.39249 (7)	0.31518 (6)	0.63087 (6)	0.01975 (17)
P20	2*i*	0.40919 (6)	0.92806 (6)	0.07004 (6)	0.01578 (15)
P21	2*i*	0.54715 (6)	0.18329 (6)	0.74298 (7)	0.01851 (16)

P22	2*i*	0.60352 (7)	0.07942 (6)	0.35375 (7)	0.02150 (18)
P23	2*i*	0.63984 (6)	0.70444 (6)	0.08421 (6)	0.01508 (15)
P24	2*i*	0.75099 (6)	0.34971 (5)	0.09819 (6)	0.01165 (14)
P25	2*i*	0.83748 (6)	0.14530 (6)	0.15687 (6)	0.01396 (15)
Si1	2*i*	0.01372 (6)	0.23632 (6)	0.01382 (6)	0.00987 (15)
Si2	2*i*	0.01582 (6)	0.24037 (6)	0.25335 (6)	0.01051 (15)
Si3	2*i*	0.06867 (6)	0.56140 (6)	0.80125 (6)	0.00906 (14)
Si4	2*i*	0.11596 (6)	0.68960 (6)	0.37850 (6)	0.00949 (14)
Si5	2*i*	0.19563 (6)	0.50146 (6)	0.19387 (6)	0.00951 (14)
Si6	2*i*	0.20057 (6)	0.50221 (6)	0.43162 (6)	0.00963 (15)
Si7	2*i*	0.26786 (6)	0.30258 (6)	0.01348 (6)	0.01106 (15)
Si8	2*i*	0.27666 (6)	0.30601 (6)	0.47594 (6)	0.01229 (15)
Si9	2*i*	0.27760 (6)	0.29624 (6)	0.24260 (6)	0.01096 (15)
Si10	2*i*	0.37785 (7)	0.16812 (6)	0.62228 (6)	0.01348 (16)
Si11	2*i*	0.47959 (6)	0.08361 (6)	0.78751 (6)	0.01181 (15)
Si12	2*i*	0.73841 (6)	0.04345 (6)	0.46084 (6)	0.01272 (16)
Si13	2*i*	0.76065 (6)	0.18502 (6)	0.02698 (6)	0.01027 (15)
Na1	2*i*	0.0267 (2)	0.01173 (14)	0.1628 (2)	0.0705 (7)
Na2	2*i*	0.04089 (12)	0.38378 (11)	0.52204 (11)	0.0301 (3)
Na3	2*i*	0.04727 (11)	0.40635 (10)	0.90900 (10)	0.0223 (3)
Na4	2*i*	0.06619 (13)	0.07026 (14)	0.45236 (14)	0.0401 (4)
Na5	2*i*	0.12204 (11)	0.23224 (11)	0.74648 (11)	0.0260 (3)
Na6	2*i*	0.14254 (12)	0.84154 (10)	0.26631 (11)	0.0280 (3)
Na7	2*i*	0.2225 (2)	0.04768 (18)	0.0657 (3)	0.0923 (9)
Na8	2*i*	0.22733 (11)	0.67618 (11)	0.09566 (11)	0.0250 (3)
Na9	2*i*	0.28106 (17)	0.4316 (2)	0.7492 (2)	0.0942 (10)
Na10	2*i*	0.35285 (16)	0.03557 (15)	0.29066 (15)	0.0560 (5)
Na11	2*i*	0.3716 (2)	0.0228 (2)	0.9399 (2)	0.0957 (10)
Na12	2*i*	0.45184 (16)	0.61703 (13)	0.10586 (18)	0.0565 (6)
Na13	2*i*	0.47376 (11)	0.48149 (10)	0.26437 (11)	0.0255 (3)
Na14	2*i*	0.53550 (11)	0.26049 (12)	0.05804 (12)	0.0308 (3)
Na15	2*i*	0.55155 (14)	0.24492 (17)	0.31718 (17)	0.0543 (5)
Na16	2*i*	0.57862 (16)	0.27835 (19)	0.55815 (16)	0.0723 (7)
Na17	2*i*	0.79415 (11)	0.35190 (11)	0.30292 (11)	0.0260 (3)
Na18	2*i*	0.82125 (16)	0.13804 (13)	0.33876 (13)	0.0410 (4)

Na19	1*h*	0.5000	0.5000	0.5000	0.0416 (6)
Na20	1*f*	0.5000	0.0000	0.5000	0.1154 (17)

Table B2 Fractional atomic coordinates and equivalent thermal displacement parameters for $Na_{23}Si_{19}P_{33}$.

Atom	Wyckoff Symbol	*x*	*y*	*z*	U_{eq} / Å^2
P1	8*f*	0.03955 (2)	0.15532 (3)	0.37825 (3)	0.00793 (8)
P2	8*f*	0.05030 (2)	0.01206 (3)	0.70661 (3)	0.01035 (8)
P3	8*f*	0.05506 (2)	0.31232 (3)	0.18660 (3)	0.00952 (8)
P4	8*f*	0.06946 (2)	0.12786 (3)	0.02366 (3)	0.00879 (8)
P5	8*f*	0.13005 (2)	0.32656 (3)	0.43414 (3)	0.01223 (9)
P6	8*f*	0.14407 (2)	0.14300 (3)	0.28316 (3)	0.00896 (8)
P7	8*f*	0.15488 (2)	0.46589 (3)	0.22467 (3)	0.01142 (8)
P8	8*f*	0.15907 (2)	0.03346 (3)	0.62597 (3)	0.01082 (8)
P9	8*f*	0.16619 (2)	0.28639 (3)	0.08012 (3)	0.00906 (8)
P10	8*f*	0.23986 (2)	0.29527 (3)	0.32908 (3)	0.01212 (8)
P11	8*f*	0.25401 (2)	0.12992 (3)	0.18687 (3)	0.01066 (8)
P12	8*f*	0.26971 (2)	0.03255 (3)	0.52006 (3)	0.01014 (8)
P13	8*f*	0.31871 (2)	0.38843 (3)	0.06780 (3)	0.01039 (8)
P14	8*f*	0.40578 (2)	0.23744 (3)	0.17508 (3)	0.01102 (8)
P15	8*f*	0.42349 (2)	0.05755 (3)	0.01435 (3)	0.01212 (8)
P16	8*f*	0.51752 (2)	0.21912 (3)	0.06869 (3)	0.01310 (9)
P17	4*e*	0.0000	0.57416 (4)	0.2500	0.01032 (11)
Si1	8*f*	0.02039 (2)	0.22291 (3)	0.06892 (3)	0.00842 (8)
Si2	8*f*	0.09293 (2)	0.23920 (3)	0.31918 (3)	0.00841 (8)
Si3	8*f*	0.10758 (2)	0.05954 (3)	0.15971 (3)	0.00830 (8)
Si4	8*f*	0.11343 (2)	0.37471 (3)	0.12073 (3)	0.00864 (8)
Si5	8*f*	0.18720 (2)	0.38782 (3)	0.35964 (3)	0.00918 (8)
Si6	8*f*	0.19828 (2)	0.21351 (3)	0.21704 (3)	0.00829 (8)
Si7	8*f*	0.21425 (2)	0.04378 (3)	0.07195 (3)	0.00824 (8)
Si8	8*f*	0.37337 (2)	0.30197 (3)	0.03399 (3)	0.00830 (8)
Si9	8*f*	0.45934 (2)	0.15359 (3)	0.12455 (3)	0.00915 (9)
Si10	4*e*	0.0000	0.07676 (4)	0.2500	0.00788 (11)
Na1	8*f*	0.00984 (4)	0.42050 (7)	0.43871 (9)	0.0469 (3)
Na2	8*f*	0.07756 (3)	0.45655 (6)	0.31513 (7)	0.0306 (2)
Na3	8*f*	0.08375 (4)	0.15390 (6)	0.61137 (10)	0.0423 (3)

Na4	8*f*	0.10975 (3)	0.00853 (5)	0.40551 (6)	0.02455 (18)
Na5	8*f*	0.20040 (3)	0.17476 (6)	0.48032 (7)	0.0325 (2)
Na6	8*f*	0.25706 (4)	0.46335 (7)	0.19478 (8)	0.0387 (2)
Na7	8*f*	0.30261 (5)	0.12549 (9)	0.38452 (7)	0.0545 (4)
Na8	8*f*	0.31528 (4)	0.29047 (7)	0.22881 (8)	0.0399 (3)
Na9	8*f*	0.33663 (3)	0.09645 (5)	0.09127 (7)	0.02456 (18)
Na10	8*f*	0.41582 (4)	0.09643 (8)	0.34842 (11)	0.0549 (3)
Na11	4*e*	0.0000	0.83159 (8)	0.2500	0.0347 (3)
Na12	4*c*	0.2500	0.2500	0.0000	0.0253 (3)
Na13	4*a*	0.0000	0.0000	0.0000	0.0299 (3)

Table B3 Fractional atomic coordinates, equivalent thermal displacement parameters and occupation factors for $Na_{23}Si_{28}P_{45}$.

Atom	**Wyckoff Symbol**	***x***	***y***	***z***	U_{eq} / **Å²**	**Occ.**
P1	4*e*	0.04883 (10)	0.35598 (8)	0.09089 (10)	0.0084 (4)	1
P2	4*e*	0.05016 (10)	0.22378 (8)	0.42543 (10)	0.0093 (4)	1
P3	4*e*	0.05031 (10)	0.28771 (8)	0.25308 (9)	0.0085 (4)	1
P4	4*e*	0.05978 (10)	0.19749 (8)	0.08731 (10)	0.0097 (4)	1
P5	4*e*	0.06276 (10)	0.06004 (8)	0.44000 (10)	0.0105 (4)	1
P6	4*e*	0.06865 (10)	0.13087 (8)	0.26911 (10)	0.0116 (4)	1
P7	4*e*	0.07594 (10)	0.46296 (8)	0.37115 (10)	0.0119 (4)	1
P8	4*e*	0.07846 (10)	0.52716 (8)	0.78782 (10)	0.0098 (4)	1
P9	4*e*	0.08117 (10)	0.04650 (8)	0.11113 (10)	0.0105 (4)	1
P10	4*e*	0.08404 (10)	0.60512 (8)	0.62225 (10)	0.0106 (4)	1
P11	4*e*	0.08853 (10)	0.54334 (8)	0.21086 (10)	0.0104 (4)	1
P12	4*e*	0.08913 (10)	0.61637 (8)	0.38891 (10)	0.0105 (4)	1
P13	4*e*	0.10081 (10)	0.70438 (8)	0.22576 (10)	0.0098 (4)	1
P14	4*e*	0.10573 (10)	0.63855 (9)	0.05724 (10)	0.0156 (4)	1
P15	4*e*	0.10728 (10)	0.77224 (8)	0.40038 (10)	0.0115 (4)	1
P16	4*e*	0.21091 (10)	0.29997 (8)	0.40604 (10)	0.0111 (4)	1
P17	4*e*	0.21337 (10)	0.36117 (8)	0.23933 (9)	0.0100 (4)	1
P18	4*e*	0.21774 (10)	0.43154 (8)	0.08746 (10)	0.0119 (4)	1
P19	4*e*	0.21979 (10)	0.27630 (8)	0.07612 (9)	0.0088 (4)	1
P20	4*e*	0.22641 (10)	0.21109 (8)	0.24893 (10)	0.0105 (4)	1
P21	4*e*	0.22744 (10)	0.14589 (8)	0.42384 (10)	0.0093 (4)	1

P22	4*e*	0.23206 (10)	0.82144 (8)	0.11358 (10)	0.0113 (4)	1
P23	4*e*	0.23235 (11)	0.12647 (8)	0.08648 (10)	0.0141 (4)	1
P24	4*e*	0.24023 (10)	0.52865 (8)	0.37062 (10)	0.0120 (4)	1
P25	4*e*	0.24607 (10)	0.05954 (8)	0.27299 (10)	0.0101 (4)	1
P26	4*e*	0.25028 (10)	0.52317 (8)	0.61460 (9)	0.0089 (4)	1
P27	4*e*	0.25173 (10)	0.61303 (9)	0.20326 (10)	0.0130 (4)	1
P28	4*e*	0.42123 (11)	0.45642 (8)	0.38215 (10)	0.0135 (4)	1
P29	4*e*	0.42443 (10)	0.05096 (8)	0.13224 (10)	0.0129 (4)	1
P30	4*e*	0.44436 (10)	0.37275 (8)	0.23081 (10)	0.0094 (4)	1
P31	4*e*	0.44894 (11)	0.31107 (8)	0.41121 (11)	0.0152 (4)	1
P32	4*e*	0.45026 (13)	0.43602 (9)	0.05848 (11)	0.0234 (5)	1
P33	4*e*	0.45901 (11)	0.15397 (8)	0.41492 (10)	0.0124 (4)	1
P34	4*e*	0.46174 (10)	0.27614 (8)	0.08455 (10)	0.0123 (4)	1
P35	4*e*	0.46362 (10)	0.21997 (8)	0.25527 (10)	0.0118 (4)	1
P36	4*e*	0.57883 (10)	0.02647 (8)	0.29780 (10)	0.0128 (4)	1
P37	4*e*	0.59681 (10)	0.10951 (8)	0.13809 (10)	0.0128 (4)	1
P38	4*e*	0.59978 (10)	0.46783 (8)	0.21074 (11)	0.0133 (4)	1
P39	4*e*	0.60104 (10)	0.39557 (8)	0.39182 (10)	0.0098 (4)	1
P40	4*e*	0.62070 (10)	0.30455 (8)	0.23249 (10)	0.0101 (4)	1
P41	4*e*	0.62233 (12)	0.36706 (10)	0.06104 (11)	0.0234 (5)	1
P42	4*e*	0.62357 (10)	0.23825 (8)	0.40919 (10)	0.0137 (4)	1
P43	4*e*	0.74562 (10)	0.18943 (8)	0.12546 (10)	0.0112 (4)	1
P44	4*e*	0.76399 (10)	0.48823 (8)	0.05891 (10)	0.0117 (4)	1
P45	4*e*	0.76724 (10)	0.39730 (8)	0.21428 (10)	0.0085 (4)	1
Si1	4*e*	0.01117 (10)	0.27316 (8)	0.13186 (10)	0.0088 (4)	1
Si2	4*e*	0.01202 (10)	0.14220 (9)	0.46790 (10)	0.0100 (4)	1
Si3	4*e*	0.01827 (10)	0.20960 (9)	0.30542 (10)	0.0101 (4)	1
Si4	4*e*	0.03003 (11)	0.05308 (9)	0.31959 (10)	0.0104 (4)	1
Si5	4*e*	0.03012 (10)	0.12333 (8)	0.14691 (11)	0.0101 (4)	1
Si6	4*e*	0.04200 (10)	0.52868 (8)	0.66480 (10)	0.0096 (4)	1
Si7	4*e*	0.12365 (10)	0.53941 (8)	0.33356 (10)	0.0093 (4)	1
Si8	4*e*	0.13538 (10)	0.62460 (9)	0.17537 (10)	0.0098 (4)	1
Si9	4*e*	0.13635 (10)	0.69416 (8)	0.34740 (10)	0.0091 (4)	1
Si10	4*e*	0.17152 (10)	0.35304 (8)	0.12048 (10)	0.0082 (4)	1
Si11	4*e*	0.17179 (10)	0.22445 (8)	0.45367 (10)	0.0089 (4)	1

Si12	4*e*	0.17239 (10)	0.28665 (8)	0.28746 (10)	0.0084 (4)	1
Si13	4*e*	0.18126 (11)	0.19865 (8)	0.12714 (10)	0.0096 (4)	1
Si14	4*e*	0.18490 (10)	0.06703 (8)	0.46854 (10)	0.0092 (4)	1
Si15	4*e*	0.19017 (11)	0.13606 (8)	0.30291 (10)	0.0100 (4)	1
Si16	4*e*	0.20287 (10)	0.05641 (8)	0.15101 (10)	0.0089 (4)	1
Si17	4*e*	0.20364 (10)	0.59919 (8)	0.66226 (10)	0.0091 (4)	1
Si18	4*e*	0.28263 (10)	0.60654 (8)	0.32513 (10)	0.0097 (4)	1
Si19	4*e*	0.47969 (10)	0.45022 (8)	0.17799 (10)	0.0105 (4)	1
Si20	4*e*	0.47986 (10)	0.38363 (8)	0.35190 (10)	0.0091 (4)	1
Si21	4*e*	0.49953 (10)	0.29424 (8)	0.20154 (10)	0.0088 (4)	1
Si22	4*e*	0.50095 (11)	0.35295 (9)	0.03556 (10)	0.0115 (4)	1
Si23	4*e*	0.50282 (10)	0.23432 (9)	0.37560 (10)	0.0104 (4)	1
Si24	4*e*	0.54501 (10)	0.03195 (8)	0.17517 (10)	0.0103 (4)	1
Si25	4*e*	0.62693 (10)	0.47416 (9)	0.33374 (11)	0.0117 (4)	1
Si26	4*e*	0.64515 (10)	0.38579 (9)	0.17841 (11)	0.0118 (4)	1
Si27	4*e*	0.64830 (10)	0.31588 (8)	0.35388 (10)	0.0099 (4)	1
Si28	4*e*	0.79975 (10)	0.48338 (8)	0.17803 (10)	0.0091 (4)	1
Na1	4*e*	0.07943 (18)	0.41807 (14)	0.23327 (18)	0.0280 (8)	1
Na2	4*e*	0.0949 (2)	0.36334 (16)	0.4564 (2)	0.0437 (10)	1
Na3	4*e*	0.0961 (2)	0.77335 (17)	0.0458 (2)	0.0413 (10)	1
Na4	4*e*	0.0969 (4)	0.5110 (3)	0.0654 (3)	0.086 (3)	0.800 (13)
Na5	4*e*	0.0980 (2)	0.53262 (15)	0.50053 (18)	0.0463 (11)	1
Na6	4*e*	0.10046 (19)	0.83248 (16)	0.2586 (2)	0.0408 (10)	1
Na7	4*e*	0.25194 (17)	0.73749 (14)	0.23042 (18)	0.0310 (8)	1
Na8	4*e*	0.2840 (3)	0.4096 (2)	0.4035 (4)	0.100 (2)	1
Na9	4*e*	0.2852 (3)	0.5481 (3)	0.0910 (3)	0.056 (2)	0.793 (12)
Na10	4*e*	0.2957 (2)	0.47480 (17)	0.2446 (2)	0.0429 (10)	1
Na11	4*e*	0.34425 (16)	0.36148 (14)	0.08820 (17)	0.0252 (7)	1
Na12	4*e*	0.34683 (16)	0.29341 (14)	0.27121 (19)	0.0289 (8)	1
Na13	4*e*	0.35073 (16)	0.23080 (14)	0.44277 (18)	0.0261 (7)	1
Na14	4*e*	0.3680 (3)	0.0408 (3)	0.4160 (2)	0.103 (2)	1
Na15	4*e*	0.3718 (3)	0.1792 (2)	0.1274 (3)	0.088 (3)	0.953 (14)
Na16	4*e*	0.4355 (2)	0.09648 (16)	0.27678 (19)	0.0462 (11)	1
Na17	4*e*	0.4749 (3)	0.1137 (4)	0.0232 (4)	0.133 (4)	0.905 (14)
Na18	4*e*	0.5516 (3)	0.0560 (2)	0.4467 (3)	0.0531 (19)	0.868 (12)

Na19	4*e*	0.5908 (2)	0.2239 (2)	0.0539 (2)	0.0579 (13)	1
Na20	4*e*	0.5947 (5)	0.0273 (3)	0.0052 (3)	0.160 (4)	1
Na21	4*e*	0.59964 (19)	0.16202 (17)	0.2787 (2)	0.0406 (10)	1
Na22	4*e*	0.7366 (2)	0.2933 (2)	0.0295 (3)	0.0667 (14)	1
Na23	4*e*	0.74298 (19)	0.11380 (15)	0.00752 (16)	0.0316 (8)	1
Na24	4*e*	0.8864 (4)	0.4058 (4)	0.0773 (4)	0.092 (4)	0.680 (13)

Table B4 Fractional atomic coordinates, equivalent thermal displacement parameters and occupation factors for $Na_{23}Si_{37}P_{57}$.

Atom	Wyckoff Symbol	*x*	*y*	*z*	U_{eq} / Å^2	Occ.
P1	8*f*	0.01693 (3)	0.15717 (5)	0.11897 (5)	0.01517 (17)	1
P2	8*f*	0.04189 (3)	0.42413 (5)	0.22558 (5)	0.01250 (16)	1
P3	8*f*	0.05413 (3)	0.12541 (5)	0.57707 (5)	0.01111 (16)	1
P4	8*f*	0.06201 (3)	0.30447 (5)	0.45991 (5)	0.01124 (16)	1
P5	8*f*	0.07898 (3)	0.16570 (5)	0.32672 (5)	0.01306 (17)	1
P6	8*f*	0.12913 (3)	0.40501 (5)	0.17870 (5)	0.01371 (17)	1
P7	8*f*	0.13552 (3)	0.03067 (5)	0.12583 (5)	0.01409 (17)	1
P8	8*f*	0.13989 (3)	0.54150 (5)	0.04112 (5)	0.01090 (15)	1
P9	8*f*	0.14781 (3)	0.14320 (5)	0.51777 (5)	0.01174 (16)	1
P10	8*f*	0.15507 (3)	0.31414 (5)	0.40911 (5)	0.01427 (17)	1
P11	8*f*	0.19849 (3)	0.04481 (5)	0.31944 (5)	0.00961 (15)	1
P12	8*f*	0.20089 (3)	0.21504 (5)	0.20782 (5)	0.01607 (18)	1
P13	8*f*	0.21270 (3)	0.38816 (5)	0.10741 (5)	0.00995 (15)	1
P14	8*f*	0.26952 (3)	0.03842 (5)	0.51590 (5)	0.01371 (17)	1
P15	8*f*	0.27351 (3)	0.20265 (5)	0.39862 (5)	0.01146 (16)	1
P16	8*f*	0.28048 (3)	0.37781 (5)	0.29646 (5)	0.01063 (15)	1
P17	8*f*	0.28532 (3)	0.05426 (5)	0.25675 (5)	0.01168 (16)	1
P18	8*f*	0.29100 (3)	0.22954 (5)	0.15188 (5)	0.01225 (16)	1
P19	8*f*	0.30316 (3)	0.39313 (5)	0.04463 (5)	0.01337 (17)	1
P20	8*f*	0.36481 (3)	0.21687 (5)	0.34297 (5)	0.01444 (17)	1
P21	8*f*	0.37467 (3)	0.07657 (5)	0.20201 (5)	0.01214 (16)	1
P22	8*f*	0.37472 (3)	0.39257 (5)	0.23414 (5)	0.01053 (15)	1
P23	8*f*	0.38392 (3)	0.25129 (5)	0.09558 (5)	0.01484 (17)	1
P24	8*f*	0.43493 (3)	0.49417 (5)	0.06067 (5)	0.01295 (16)	1
P25	8*f*	0.45776 (3)	0.24491 (5)	0.28523 (5)	0.01070 (16)	1

P26	8*f*	0.46157 (2)	0.08715 (5)	0.15020 (5)	0.00935 (15)	1
P27	8*f*	0.47103 (3)	0.22644 (6)	0.02029 (5)	0.01629 (18)	1
P28	8*f*	0.55020 (3)	0.06558 (5)	0.09656 (5)	0.01077 (15)	1
P29	4*e*	0.0000	0.00960 (7)	0.2500	0.0117 (2)	1
Si1	8*f*	0.01909 (3)	0.21413 (5)	0.48636 (5)	0.01033 (17)	1
Si2	8*f*	0.03180 (3)	0.08765 (5)	0.35114 (5)	0.01087 (17)	1
Si3	8*f*	0.08869 (3)	0.49821 (5)	0.20108 (5)	0.00987 (16)	1
Si4	8*f*	0.10159 (3)	0.06058 (5)	0.54088 (5)	0.01053 (17)	1
Si5	8*f*	0.10984 (3)	0.23162 (5)	0.43004 (5)	0.01066 (17)	1
Si6	8*f*	0.17461 (3)	0.47570 (5)	0.14800 (5)	0.01056 (17)	1
Si7	8*f*	0.24204 (3)	0.13244 (5)	0.29262 (5)	0.01021 (17)	1
Si8	8*f*	0.24838 (3)	0.29941 (5)	0.19697 (5)	0.01021 (17)	1
Si9	8*f*	0.26161 (3)	0.46607 (5)	0.08426 (5)	0.00984 (16)	1
Si10	8*f*	0.31321 (3)	0.11788 (5)	0.48831 (5)	0.01067 (17)	1
Si11	8*f*	0.31922 (3)	0.28811 (5)	0.37891 (5)	0.01162 (17)	1
Si12	8*f*	0.32953 (3)	0.45776 (5)	0.27655 (5)	0.00987 (16)	1
Si13	8*f*	0.32976 (3)	0.14542 (6)	0.24110 (6)	0.01592 (19)	1
Si14	8*f*	0.33913 (3)	0.31402 (5)	0.13598 (5)	0.01091 (17)	1
Si15	8*f*	0.40218 (3)	0.13296 (5)	0.43502 (5)	0.01084 (17)	1
Si16	8*f*	0.41004 (3)	0.30473 (5)	0.32247 (5)	0.01046 (17)	1
Si17	8*f*	0.41922 (3)	0.16965 (5)	0.18642 (5)	0.01036 (17)	1
Si18	8*f*	0.50871 (3)	0.16094 (5)	0.12029 (5)	0.00958 (16)	1
Si19	4*e*	0.0000	0.51187 (7)	0.2500	0.0090 (2)	1
Na1	8*f*	0.01769 (9)	0.40109 (14)	0.06994 (12)	0.0668 (8)	1
Na2	8*f*	0.07005 (6)	0.03221 (12)	0.19818 (12)	0.0431 (5)	1
Na3	8*f*	0.09140 (6)	0.43808 (11)	0.37815 (10)	0.0370 (4)	1
Na4	8*f*	0.10071 (18)	0.1613 (3)	0.0268 (2)	0.0661 (19)	0.512 (6)
Na5	8*f*	0.10649 (19)	0.2521 (2)	0.2278 (2)	0.159 (2)	1
Na6	8*f*	0.11016 (16)	0.3703 (3)	0.0134 (3)	0.0234 (15)	0.311 (5)
Na7	8*f*	0.13314 (6)	0.01924 (11)	0.39139 (10)	0.0325 (4)	1
Na8	8*f*	0.19901 (7)	0.3849 (2)	0.32441 (13)	0.0879 (11)	1
Na9	8*f*	0.21036 (8)	0.17317 (14)	0.45686 (16)	0.0338 (9)	0.681 (6)
Na10	8*f*	0.21516 (7)	0.0676 (2)	0.10465 (12)	0.0798 (10)	1
Na11	8*f*	0.2289 (2)	0.2790 (3)	0.0011 (3)	0.0491 (19)	0.373 (5)
Na12	8*f*	0.31971 (17)	0.1162 (3)	0.0490 (2)	0.0825 (19)	0.627 (5)

Na13	8*f*	0.46411 (7)	0.35697 (12)	0.15271 (14)	0.0580 (7)	1
Na14	4*e*	0.0000	0.26391 (16)	0.2500	0.0526 (9)	1
Na15	4*a*	0.0000	0.0000	0.0000	0.0602 (10)	1

Table B5 Fractional atomic coordinates, equivalent thermal displacement parameters and occupation factors for *LT*-$NaSi_2P_3$.

Atom	Wyckoff Symbol	*x*	*y*	*z*	U_{eq} / Å^2	Occ.
P1	16*f*	0.00325 (3)	0.01532 (3)	0.37758 (2)	0.01224 (11)	1
P2	16*f*	0.00358 (3)	0.38033 (3)	0.54724 (2)	0.00993 (10)	1
P3	16*f*	0.00721 (3)	0.03856 (3)	0.23647 (2)	0.00943 (10)	1
P4	16*f*	0.01871 (3)	0.04359 (3)	0.08615 (2)	0.00902 (10)	1
P5	16*f*	0.03762 (3)	0.16844 (3)	0.31112 (2)	0.01389 (11)	1
P6	16*f*	0.04085 (3)	0.17886 (3)	0.15817 (2)	0.00933 (10)	1
P7	16*f*	0.05092 (3)	0.16632 (3)	0.01303 (2)	0.00940 (10)	1
P8	16*f*	0.13319 (3)	0.12702 (3)	0.47610 (2)	0.00870 (10)	1
P9	16*f*	0.13438 (3)	0.11468 (3)	0.62674 (2)	0.00955 (10)	1
P10	16*f*	0.13934 (3)	0.25710 (3)	0.54859 (2)	0.00930 (10)	1
P11	16*f*	0.14063 (3)	0.01387 (3)	0.30778 (2)	0.00861 (10)	1
P12	16*f*	0.14527 (3)	0.01024 (3)	0.15893 (2)	0.01001 (10)	1
P13	16*f*	0.17502 (3)	0.14498 (3)	0.23887 (2)	0.01132 (11)	1
P14	16*f*	0.17546 (3)	0.13397 (3)	0.08557 (2)	0.00946 (10)	1
P15	16*f*	0.25992 (3)	0.52668 (3)	0.01774 (2)	0.01302 (11)	1
P16	16*f*	0.30116 (3)	0.11249 (3)	0.16167 (2)	0.01190 (11)	1
P17	16*f*	0.33771 (3)	0.23282 (3)	0.09083 (2)	0.01218 (11)	1
P18	16*f*	0.38099 (3)	0.01062 (3)	0.04924 (2)	0.01225 (11)	1
P19	8*e*	0.0000	0.2500	0.47272 (2)	0.01457 (16)	1
P20	4*b*	0.0000	0.2500	0.6250	0.0099 (2)	1
Si1	16*f*	0.06067 (3)	0.05602 (3)	0.58814 (2)	0.00907 (11)	1
Si2	16*f*	0.06513 (3)	0.19330 (3)	0.51356 (2)	0.00877 (11)	1
Si3	16*f*	0.06841 (3)	0.31626 (3)	0.58676 (2)	0.00822 (10)	1
Si4	16*f*	0.08716 (3)	0.09475 (3)	0.27131 (2)	0.00936 (11)	1
Si5	16*f*	0.09351 (3)	0.09493 (3)	0.12600 (2)	0.00871 (11)	1
Si6	16*f*	0.12232 (3)	0.21737 (3)	0.19787 (2)	0.00885 (11)	1
Si7	16*f*	0.12669 (3)	0.21960 (3)	0.05214 (2)	0.00849 (11)	1
Si8	16*f*	0.19079 (3)	0.05443 (3)	0.51645 (2)	0.00890 (11)	1

Si9	16*f*	0.19761 (3)	0.18680 (3)	0.58965 (2)	0.00892 (11)	1
Si10	16*f*	0.22072 (3)	0.06613 (3)	0.19805 (2)	0.01003 (11)	1
Si11	16*f*	0.25150 (3)	0.18830 (3)	0.12403 (2)	0.00894 (11)	1
Si12	16*f*	0.28548 (3)	0.30974 (3)	0.05497 (2)	0.00886 (11)	1
Si13	8*e*	0.0000	0.2500	0.27198 (2)	0.00908 (15)	1
Na1	16*f*	0.0250 (4)	0.0138 (3)	0.4822 (2)	0.102 (4)	0.242 (3)
Na2	16*f*	0.0430 (7)	0.1622 (3)	0.39636 (12)	0.075 (5)	0.422 (17)
Na3	16*f*	0.0957 (10)	0.1333 (7)	0.3854 (3)	0.089 (7)	0.272 (13)
Na4	16*f*	0.1384 (2)	0.0420 (2)	0.02678 (14)	0.0406 (18)	0.254 (4)
Na5	16*f*	0.15773 (7)	0.25349 (7)	0.30840 (5)	0.0626 (5)	1
Na6	16*f*	0.26924 (6)	0.01225 (6)	0.10398 (4)	0.0406 (3)	1
Na7	16*f*	0.35642 (13)	0.14604 (7)	0.02307 (4)	0.1003 (8)	1
Na8	16*f*	0.38552 (13)	0.50341 (10)	0.06227 (8)	0.1031 (13)	0.758 (3)
Na9	16*f*	0.41983 (6)	0.05155 (8)	0.19151 (4)	0.0545 (4)	1
Na10	16*f*	0.4789 (9)	0.1597 (6)	0.1019 (3)	0.130 (6)	0.300 (11)

Table B6 Fractional atomic coordinates, equivalent thermal displacement parameters and occupation factors for *HT*-$NaSi_2P_3$.

Atom	Wyckoff Symbol	*x*	*y*	*z*	U_{eq} / Å^2	Occ.
P1	32*g*	0.03874 (4)	0.06180 (4)	0.15553 (2)	0.0178 (2)	1
P2	32*g*	0.03979 (4)	0.05999 (4)	0.27855 (2)	0.01323 (19)	1
P3	32*g*	0.05032 (4)	0.19243 (4)	0.34671 (2)	0.01272 (18)	1
P4	32*g*	0.06298 (4)	0.19718 (4)	0.03587 (2)	0.0180 (2)	1
P5	32*g*	0.06831 (4)	0.31159 (4)	0.27854 (2)	0.01276 (18)	1
P6	32*g*	0.17881 (4)	0.18301 (4)	0.27740 (2)	0.01355 (18)	1
P7	32*g*	0.18592 (4)	0.08157 (4)	0.03437 (2)	0.01254 (18)	1
P8	32*g*	0.19673 (4)	0.32806 (4)	0.15752 (2)	0.01589 (19)	1
P9	32*g*	0.29607 (4)	0.05675 (4)	0.28044 (2)	0.01653 (19)	1
P10	32*g*	0.30377 (4)	0.07723 (4)	0.09519 (2)	0.01317 (18)	1
P11	32*g*	0.31183 (4)	0.19693 (4)	0.15923 (2)	0.01251 (18)	1
P12	32*g*	0.42365 (4)	0.06857 (4)	0.15775 (2)	0.01241 (18)	1
Si1	32*g*	0.11182 (4)	0.12280 (4)	0.37412 (2)	0.01161 (19)	1
Si2	32*g*	0.11842 (4)	0.24176 (4)	0.31211 (2)	0.01186 (19)	1
Si3	32*g*	0.12577 (4)	0.14470 (4)	0.00126 (2)	0.01303 (19)	1
Si4	32*g*	0.25008 (4)	0.14925 (4)	0.06338 (2)	0.01259 (19)	1

Si5	32*g*	0.25633 (4)	0.26490 (4)	0.12595 (2)	0.01227 (19)	1
Si6	32*g*	0.36738 (4)	0.01595 (4)	0.06165 (2)	0.01337 (19)	1
Si7	32*g*	0.37964 (4)	0.25719 (4)	0.06314 (2)	0.01160 (19)	1
Si8	16*e*	0.22772 (6)	0.0000	0.2500	0.0145 (3)	1
Si9	16*d*	0.0000	0.2500	0.00172 (3)	0.0127 (2)	1
Na1	32*g*	0.0206 (6)	0.0618 (3)	0.0435 (3)	0.093 (4)	0.532 (15)
Na2	32*g*	0.1568 (5)	0.0699 (5)	0.1127 (2)	0.093 (5)	0.323 (7)
Na3	32*g*	0.1634 (2)	0.30810 (16)	0.04093 (11)	0.1387 (19)	1
Na4	32*g*	0.1716 (4)	0.2749 (6)	0.2217 (2)	0.076 (4)	0.456 (15)
Na5	32*g*	0.3155 (2)	0.0374 (2)	0.36036 (12)	0.0614 (13)	0.5
Na6	32*g*	0.31554 (16)	0.08682 (16)	0.20814 (9)	0.0586 (12)	0.688 (7)
Na7	16*f*	0.0467 (6)	0.2967 (6)	0.1250	0.190 (11)	0.423 (14)
Na8	16*f*	0.4384 (4)	0.6884 (4)	0.1250	0.229 (10)	0.577 (14)

B.3 Structural Details on Supertetrahedral Sodium Phosphidosilicates

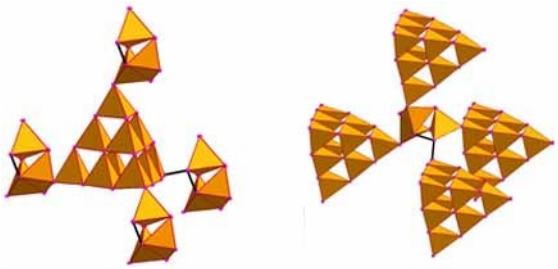

Figure B1 Building units of $Na_{19}Si_{13}P_{25}$ consisting of T3 supertetrahedral clusters and Si_3P_8 entities. Three Si_3P_8 units are connected with a T3 tetrahedron by common vertices. The forth supertetrahedral vertex is linked to another Si_3P_8 entity by one P–P single bond (left). The connection of four T3 tetrahedra to one Si_3P_8 unit is similar (right).

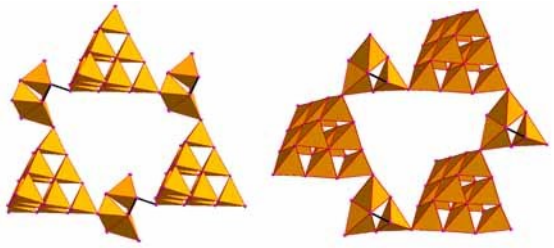

Figure B2 Two different ring motives formed of alternating building units in $Na_{19}Si_{13}P_{25}$. (left) Six-membered ring with four vertex and two homonuclear P–P single bond condensations. (right) All vertex shared six-membered ring.

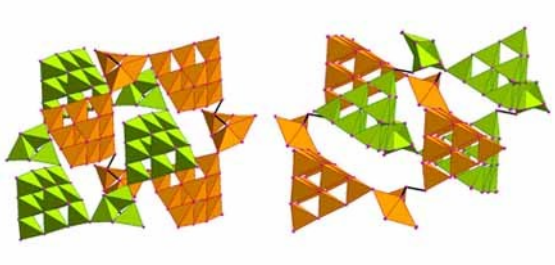

Figure B3 Two different interpenetration modes of symmetrically equivalent networks in $Na_{19}Si_{13}P_{25}$. Ring a (Fig. B2) is interpenetrated by ring b (Fig. B2) (left) and a homo-interpenetration of ring a (Fig. B2) can be observed (right).

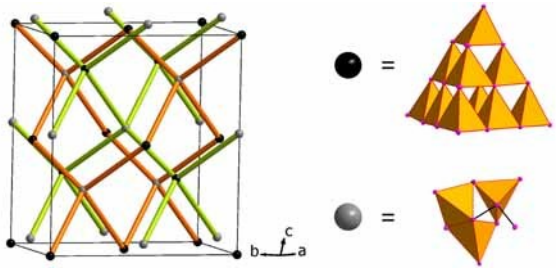

Figure B4 Topology of the two interpenetrating sphalerite-like networks. Nodes represent the centers of gravity of respective building units.

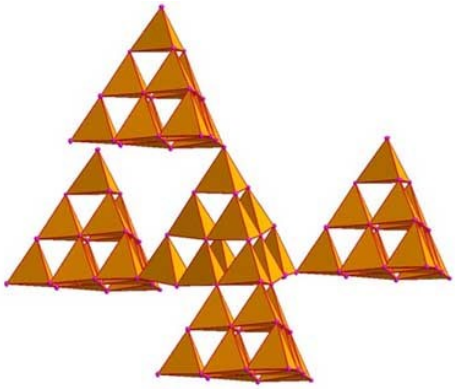

Figure B5 Supertetrahedral building unit of $Na_{23}Si_{19}P_{33}$. A T3 cluster is vertex shared with three other T3 entities and fused with another T3 supertetrahedron by one common SiP_4 unit.

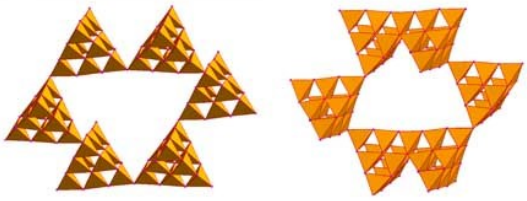

Figure B6 Two different ring motives formed by T3 clusters in $Na_{23}Si_{19}P_{33}$. (a) All vertex shared six-membered ring. (b) Six-membered ring consisting of T3 entities with four common vertices and two fusions.

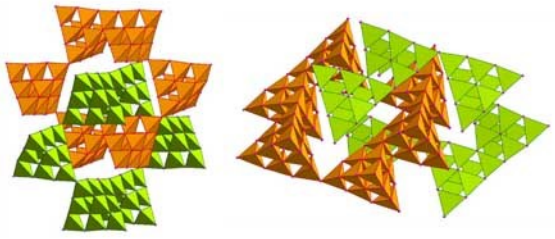

Figure B7 Two different interpenetration modes of symmetrically equivalent networks in $Na_{23}Si_{19}P_{33}$. Ring a (Fig. B6) is interpenetrated by ring b (Fig. B6) (left) and a homo-interpenetration of ring b (Fig. B6) can be observed (right).

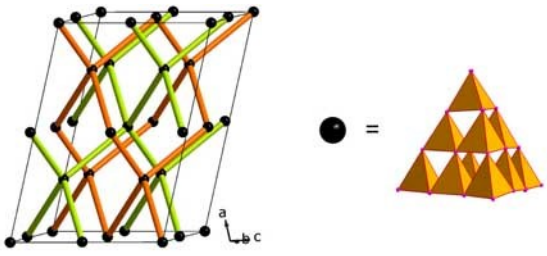

Figure B8 Topology of the two interpenetrating diamond-like networks. Nodes represent the centers of gravity of the T3 supertetrahedra.

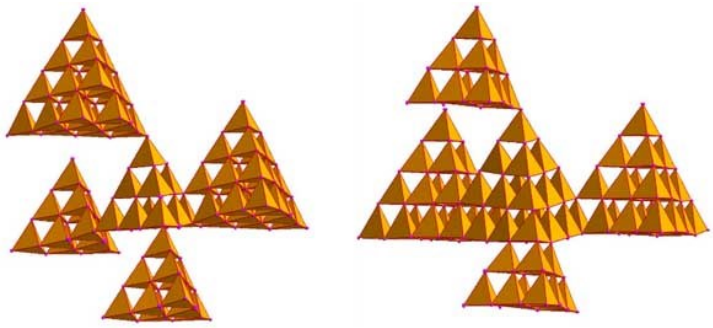

Figure B9 Basic building units of $Na_{23}Si_{28}P_{45}$ consisting of T3 and T4 clusters. Every T3 entity is connected to one T4 and two T3 entities by common vertices and fused with one T4 tetrahedron (left). Every T4 cluster is fused with two other T4 and one T3 entity and vertex shared with one T3 cluster (right).

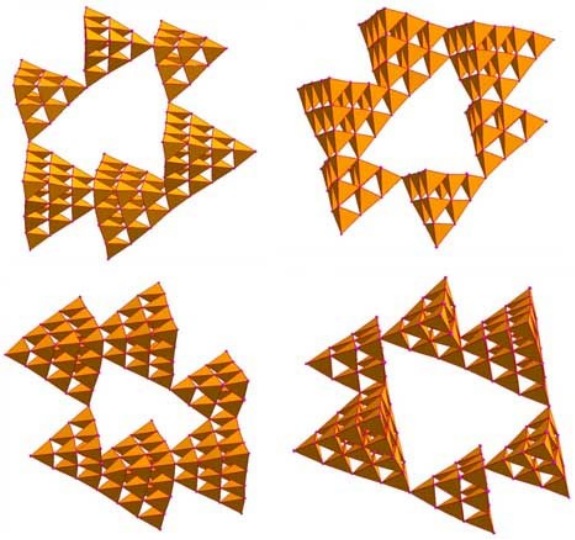

Figure B10 Four different six-membered ring motives are formed by T3 and T4 clusters in $Na_{23}Si_{28}P_{45}$. (top, left) Three sequent T3 entities are vertex shared and three T4 clusters are fused likewise. T3 and T4 entities are condensed by common vertices. (top, right) Ring derived from ring a by replacing vertex condensation between T3 and T4 supertetrahedra by fusion. (bottom, left) Two double units of fused T4 clusters which are turned by two T3 tetrahedra by two common vertices and two fusions into a ring motive. (bottom, right) Ring consisting of two double units of vertex shared T3 entities, which are twice fused and twice vertex shared with two T4 clusters.

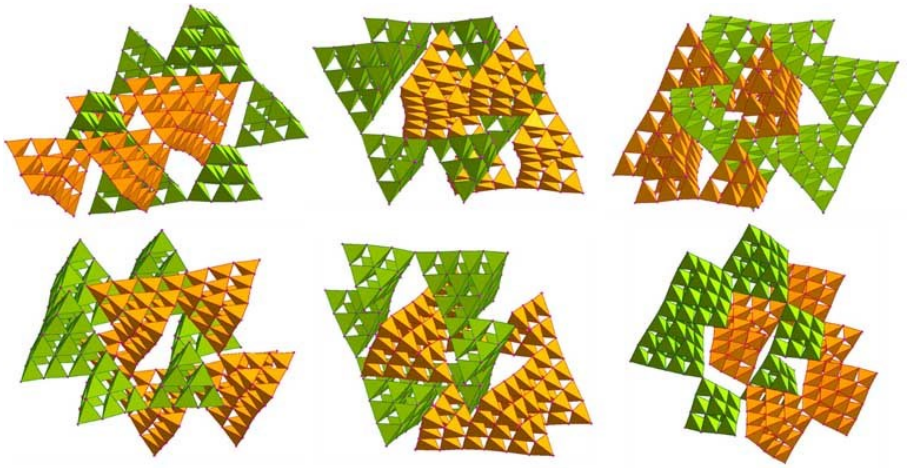

Figure B11 Six different interpenetration modes of symmetrically equivalent networks in $Na_{23}Si_{28}P_{45}$. Entanglement of rings a and d (top, left), rings b and d (top, middle), rings a and b (top, right), rings c and b (bottom, left), rings c and d (bottom middle) and a and c (bottom, right). No homo-interpenetration of one ring can be observed.

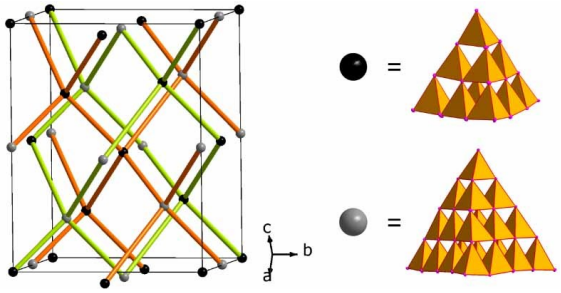

Figure B12 Topology of the two interpenetrating symmetrically equivalent networks, which are a hierarchically combination of the diamond- and the sphalerite-type structure. Nodes represent the centers of gravity of the T3 and T4 supertetrahedra.

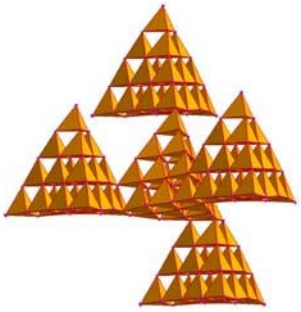

Figure B13 Supertetrahedral building unit of $Na_{23}Si_{37}P_{57}$. A T4 cluster is fused with three other T4 entities by one common SiP_4 unit and vertex shared with another T4 supertetrahedron.

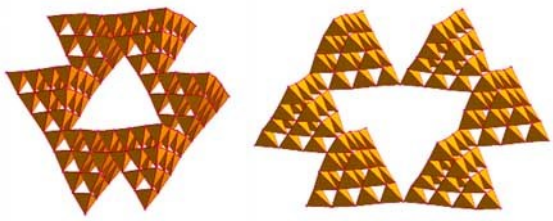

Figure B14 Two different ring motives formed by T4 clusters in $Na_{23}Si_{37}P_{57}$. (a) All fused six-membered ring. (b) Six-membered ring consisting of T4 entities with two common vertices and four fusions.

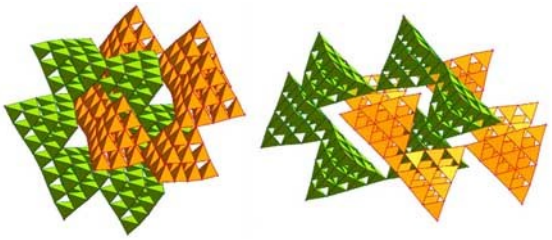

Figure B15 Two different interpenetration modes of symmetrically equivalent networks in $Na_{23}Si_{37}P_{57}$. Ring a is interpenetrated by ring b (left) and a homo-interpenetration of ring b can be observed (right).

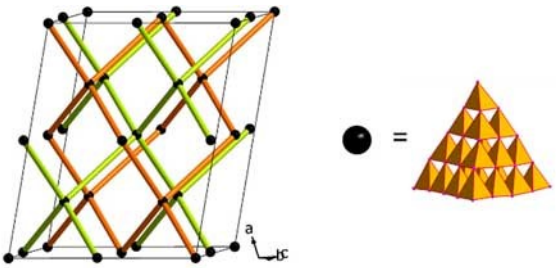

Figure B16 Topology of the two interpenetrating diamond-like networks of $Na_{23}Si_{37}P_{57}$. Nodes represent the centers of gravity of the T4 supertetrahedra.

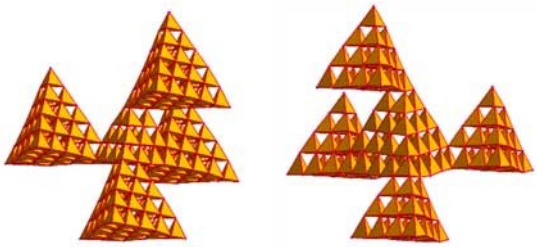

Figure B17 Building units of *LT*-$NaSi_2P_3$ consisting of T4 and T5 supertetrahedral clusters. Every T4 supertetrahedron is fused with four T5 entities by one common SiP_4 tetrahedron (left) and vice versa (right).

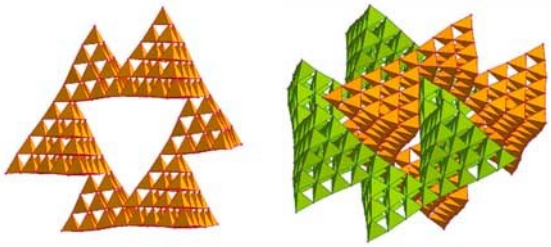

Figure B18 Six-membered ring motive of alternating T4 and T5 clusters connected by fusion the whole structure can be described with in *LT*-$NaSi_2P_3$ (left). Only one single interpenetration mode is existent (right).

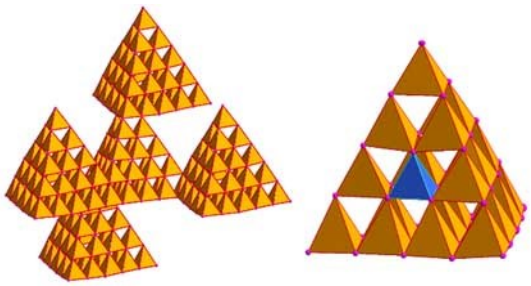

Figure B19 Building unit of *HT*-$NaSi_2P_3$ consisting of solely T5 supertetrahedral clusters. Every T5 supertetrahedron is fused with four other T5 entities by one common SiP_4 tetrahedron (left). T5 cluster with one missing silicon core, depicted as blue tetrahedron (right, top layer is not displayed due to a better view).

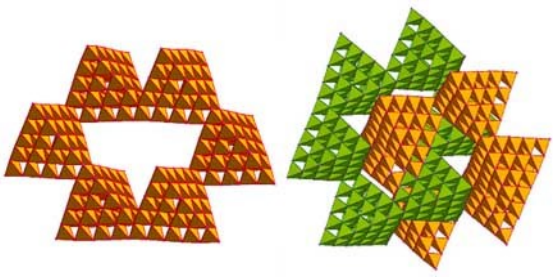

Figure B20 Six-membered ring motive of all-fused T5 supertetrahedra the whole structure can be described with in *HT*-$NaSi_2P_3$ (left). Only one single interpenetration mode is existent (right).

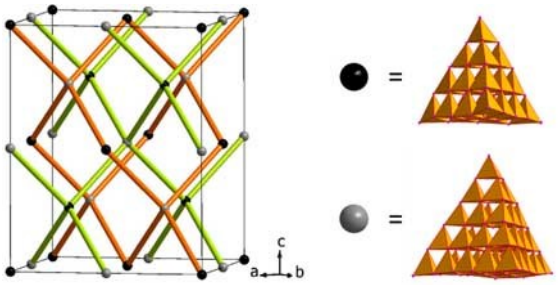

Figure B21 Topology of the two interpenetrating sphalerite-like networks of *LT*-$NaSi_2P_3$. Nodes represent the centers of gravity of the T4 and T5 supertetrahedra.

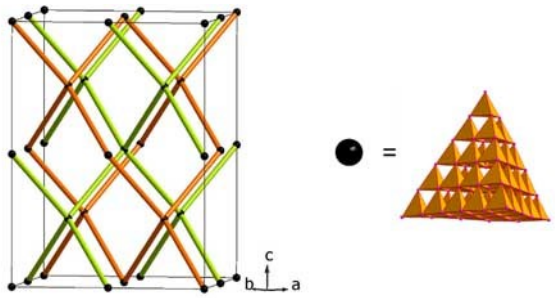

Figure B22 Topology of the two interpenetrating diamond-like networks of *HT*-$NaSi_2P_3$. Nodes represent the centers of gravity of the T5 supertetrahedra.

B.4 Powder Refinements of Supertetrahedral Sodium Phosphidosilicates

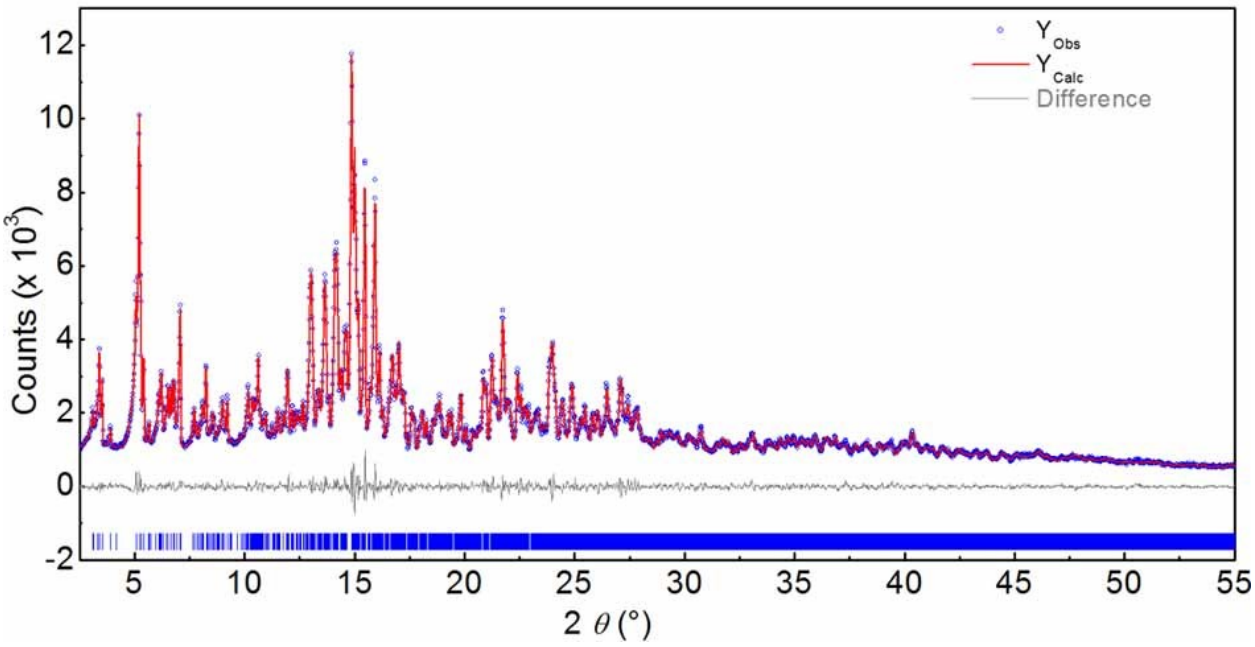

Figure B23 Observed (blue circles) and calculated (red line) powder diffraction pattern as well as difference plot (grey) of the Rietveld refinement of $Na_{19}Si_{13}P_{25}$.

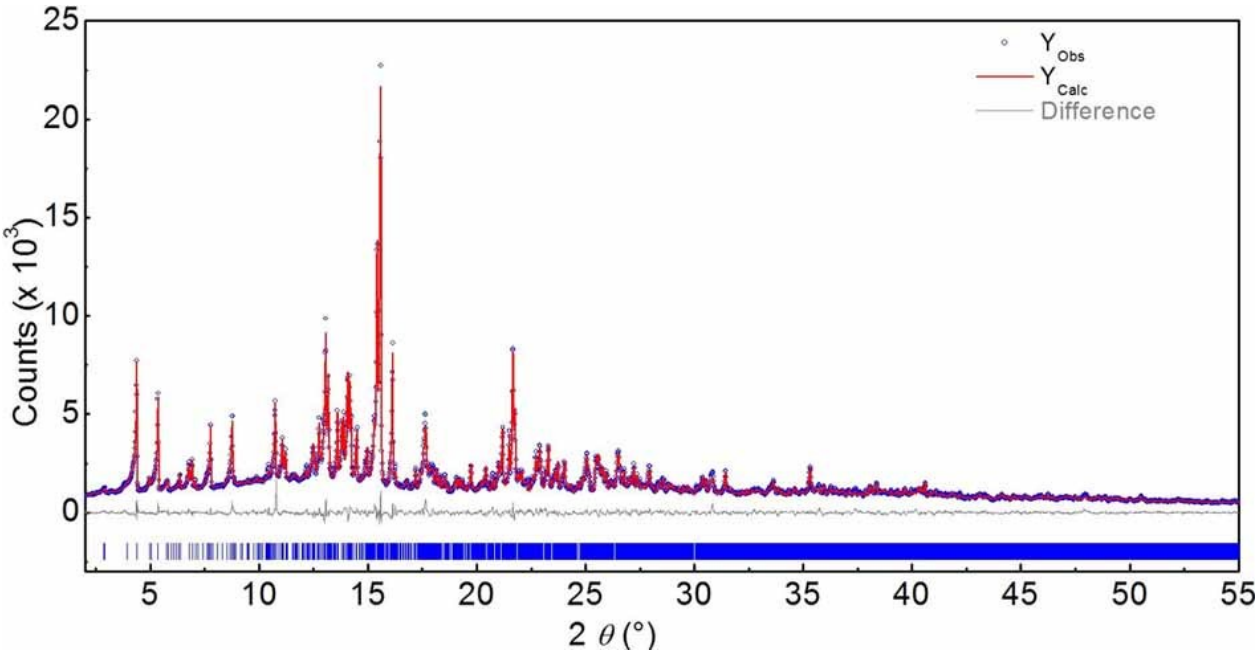

Figure B24 Observed (blue circles) and calculated (red line) powder diffraction pattern as well as difference plot (grey) of the Rietveld refinement of $Na_{23}Si_{19}P_{33}$. Peak positions are illustrated by vertical blue bars.

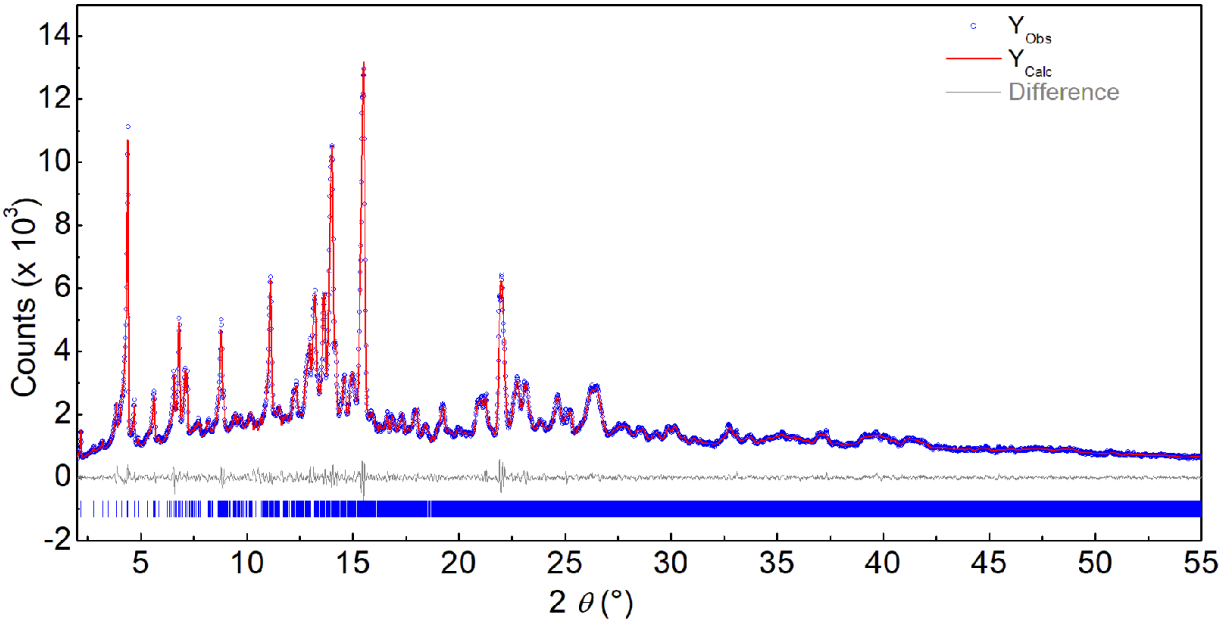

Figure B25 Observed (blue circles) and calculated (red line) powder diffraction pattern as well as difference plot (grey) of the Rietveld refinement of $Na_{23}Si_{28}P_{45}$. Peak positions are illustrated by vertical blue bars.

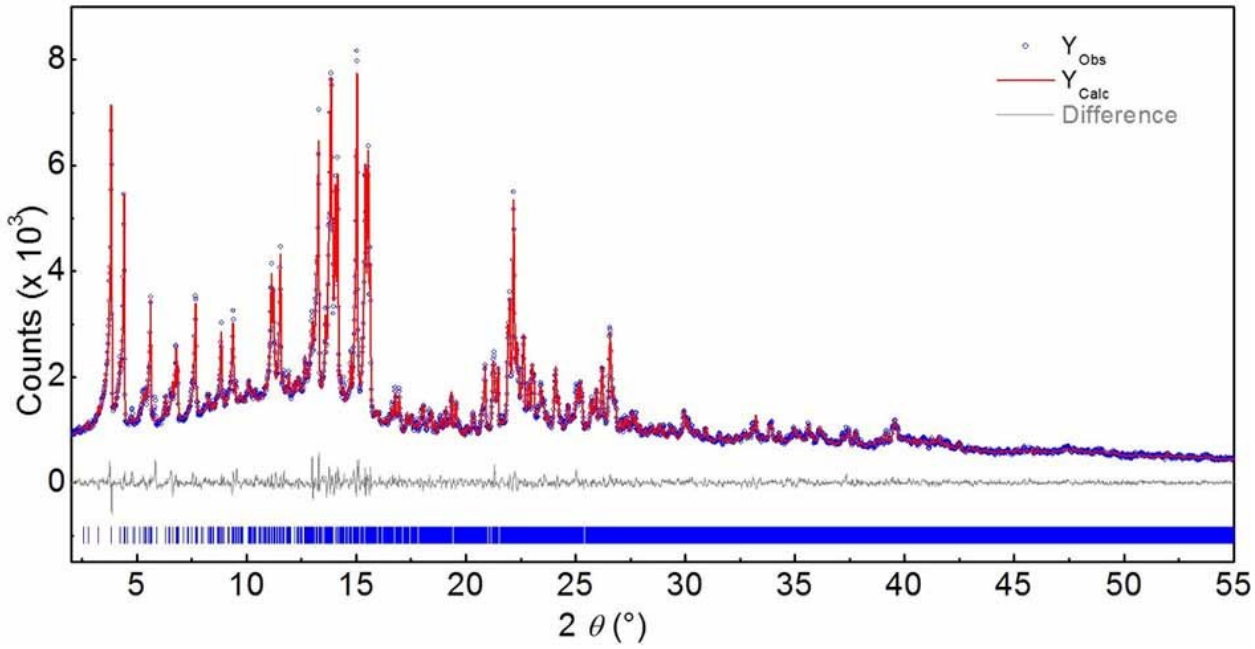

Figure B26 Observed (blue circles) and calculated (red line) powder diffraction pattern as well as difference plot (grey) of the Rietveld refinement of $Na_{23}Si_{37}P_{57}$. Peak positions are illustrated by vertical blue bars.

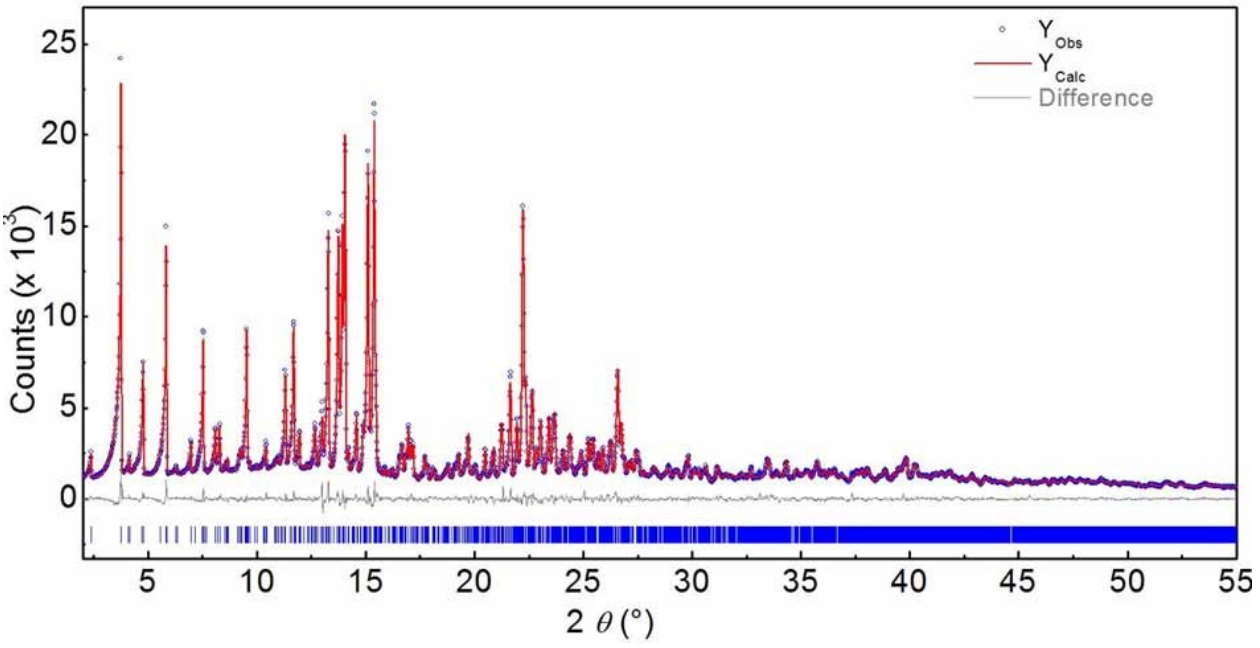

Figure B27 Observed (blue circles) and calculated (red line) powder diffraction pattern as well as difference plot (grey) of the Rietveld refinement of *LT*-$NaSi_2P_3$. Peak positions are illustrated by vertical blue bars.

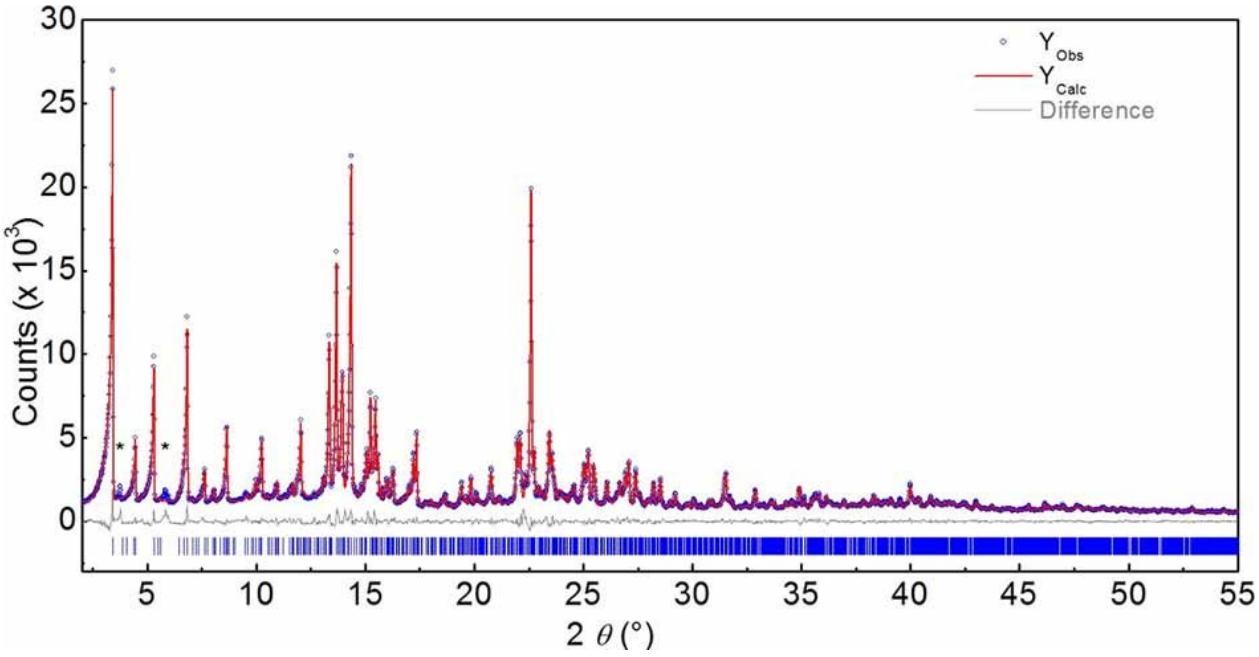

Figure B28 Observed (blue circles) and calculated (red line) powder diffraction pattern as well as difference plot (grey) of the Rietveld refinement of *HT*-$NaSi_2P_3$. Peak positions are illustrated by vertical blue bars. Asterisked peaks represent *LT*-$NaSi_2P_3$ as side phase (4.38 wt%).

B.5 Solid-State MAS-NMR of Supertetrahedral Sodium Phosphidosilicates

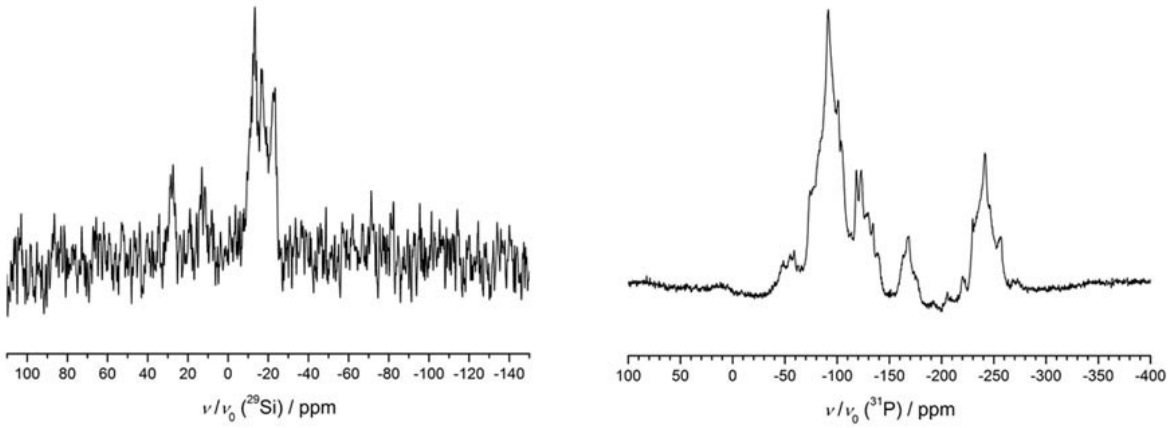

Figure B29 (left) ^{29}Si MAS NMR spectrum of $Na_{19}Si_{13}P_{25}$ with abroad resonance between δ = -23.39 and -13.34 ppm (ν_0 = 10 kHz). (right) ^{31}P MAS NMR spectrum of $Na_{19}Si_{13}P_{25}$ with broad resonances between δ = -263.69 and -229.74 ppm, -175.16 and -163.05 ppm and -139.12 and -48.58 ppm (ν_0 = 50 kHz). If the signal between δ = -175.16 and -163.05 is assigned to one phosphorus site then the integration of all signals yields 24 crystallographic P sites (25 cryst. distinct sites for P).

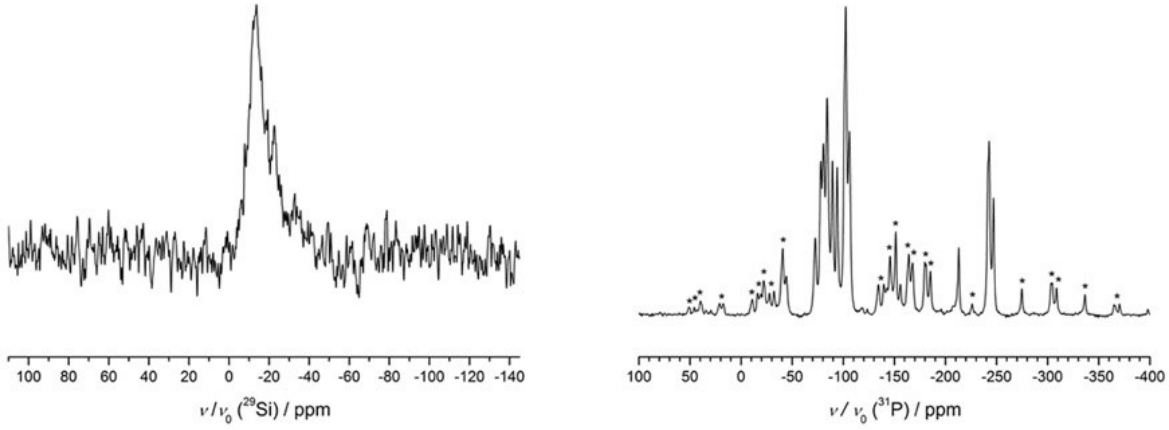

Figure B30 (left) ^{29}Si MAS NMR spectrum of $Na_{23}Si_{19}P_{33}$ with a broad resonance at δ = -13.68 ppm (ν_0 = 10 kHz). (right) ^{31}P MAS NMR spectrum of $Na_{23}Si_{19}P_{33}$ with resonances at δ = -247.00, -242.77, -213.04, -106.03, -102.43, -94.01, -89.47, -84.21, -80.66, -78.07, -72.67 ppm (ν_0 = 12.5 kHz). If the signal at δ = -247.00 ppm is assigned to one phosphorus site then the integration of all signals yields 17.5 crystallographic P sites (16.5 cryst. different sites for P). Rotational sidebands are marked with asterisks.

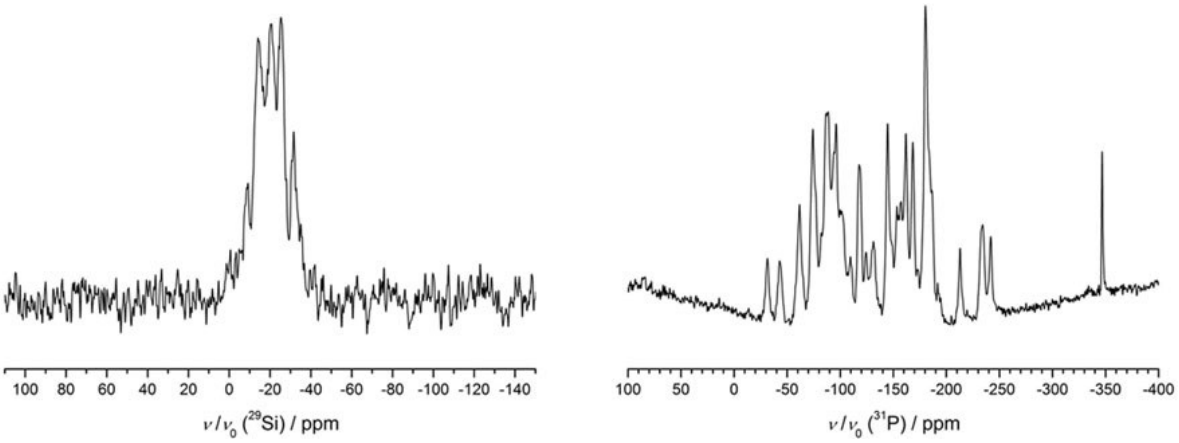

Figure B31 (left) ^{29}Si MAS NMR spectrum of $Na_{23}Si_{28}P_{45}$ with broad resonances at δ = -31.58, -25.39, -20.69, -14.14 and -9.14 ppm (ν_0 = 10 kHz). (right) ^{31}P MAS NMR spectrum of $Na_{23}Si_{28}P_{45}$ with resonances at δ = -346.71, -241.78, -234.08, -212.86, -180.34, -168.41, -161.90, -157.25, -144.63, -131.30, -117.86, -96.13, -88.53, -74.22, -61.65, -42.84 and -31.43 ppm (ν_0 = 50 kHz). If the signal at δ = -31.43 ppm is assigned to one phosphorus site then the integration of all signals yields in 48 crystallographic P sites (45 cryst. different sites for P).

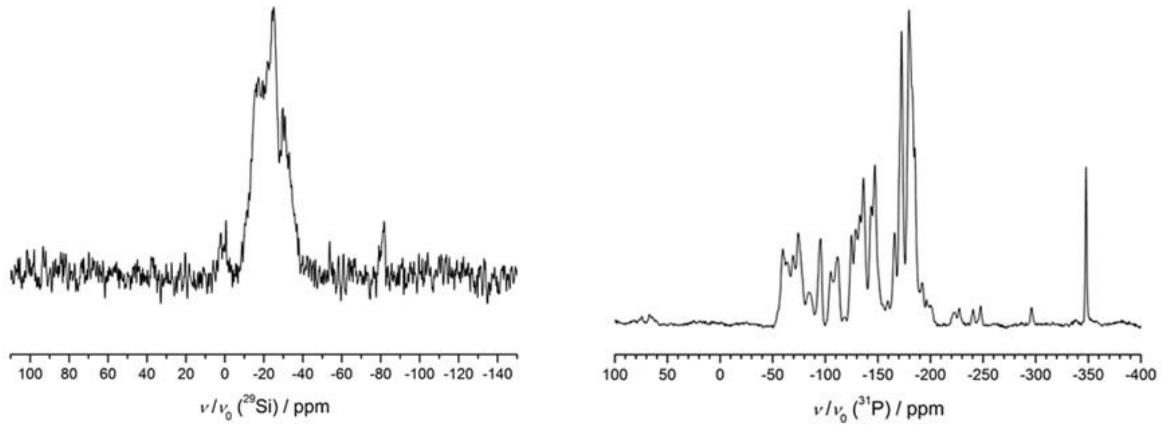

Figure B32 (left) ^{29}Si MAS NMR spectrum of $Na_{23}Si_{37}P_{57}$ with a broad resonance between δ = -38.49 and -9.49 ppm (ν_0 = 10 kHz). Additional small resonances at δ = -81.74 and -0.52 ppm are assigned to small amounts of impurities. (right) ^{31}P MAS NMR spectrum of $Na_{23}Si_{37}P_{57}$ with resonances at δ = -347.91, -179.58, -172.53, -165.94, -147.11, -136.25, -124.89, -111.70, -105.23, -95.45, -74.33, -69.51 and -59.66 ppm (ν_0 = 50 kHz). If the signal at δ = -347.91 ppm is assigned to one phosphorus site then the integration of all signals yields in 30.5 crystallographic P sites (desired value 28.5 sites for P). Resonances at δ = -296.03, -247.70, -240.51 and -227.45 ppm are assigned to small amounts of impurities.

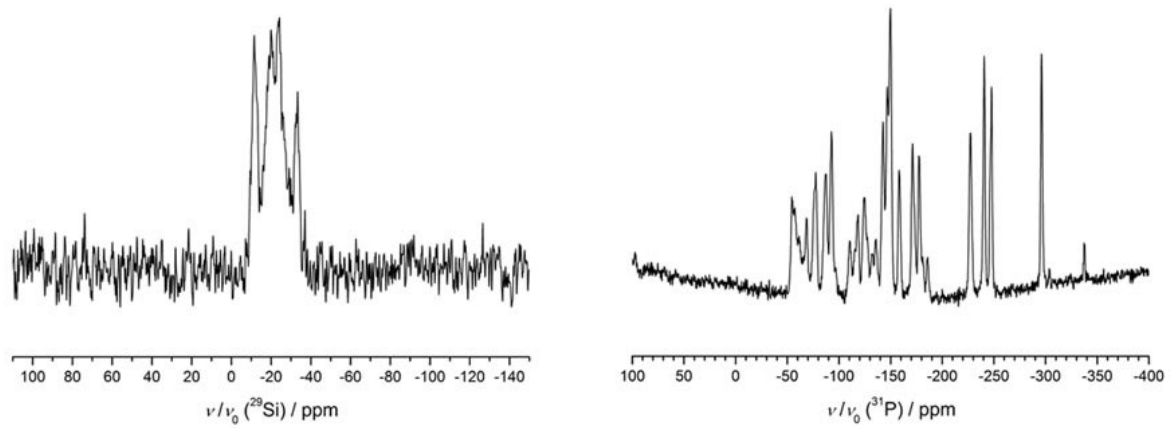

Figure B33 (left) ^{29}Si MAS NMR spectrum of *LT*-$NaSi_2P_3$ with broad resonances at δ = -33.34, -24.17, -19.95 and -11.47 ppm (ν_0 = 10 kHz). (right) ^{31}P MAS NMR spectrum of *LT*-$NaSi_2P_3$ with resonances at δ = -296.09, -247.76, -240.60, -227.41, -177.38, -171.35, -158.12, -149.77, -146.68, -142.71, -135.85, -124.97, -118.57, -110.42, -92.69, -87.18, -77.51, -68.64 and -54.39 ppm (ν_0 = 50 kHz). If the signal at δ = -296.09 ppm is assigned to one phosphorus site then the integration of all signals yields in 19 crystallographic P sites (18.75 cryst. different sites for P). The resonance at δ = -337.34 ppm is assigned to a small amount of impurity.

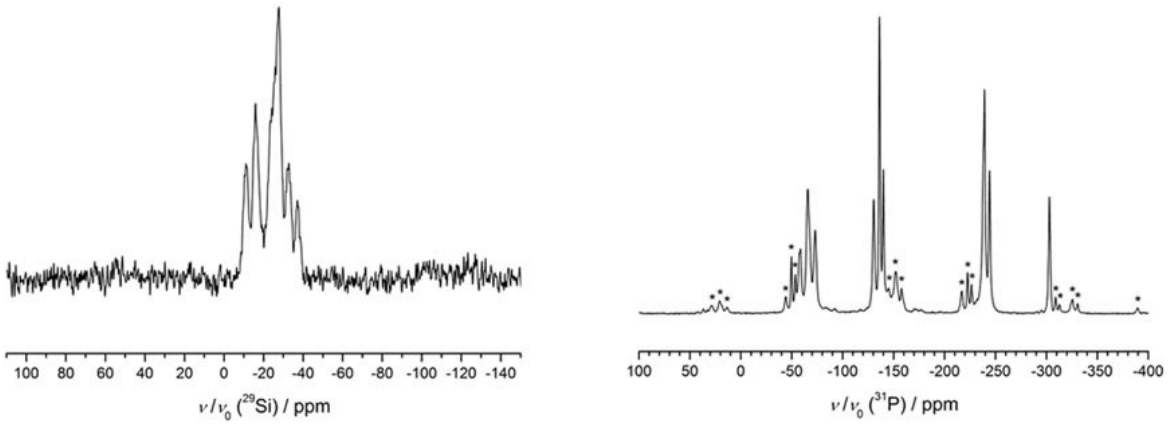

Figure B34 (left) ^{29}Si MAS NMR spectrum of *HT*-$NaSi_2P_3$ with broad resonances at δ = -37.09, -32.82, -27.71, -15.87 and -11.10 ppm (ν_0 = 10 kHz). (right) ^{31}P MAS NMR spectrum of *LT*-$NaSi_2P_3$ with resonances at δ = -302.12, -233.12, -239.38, -140.06, -135.98, -130.59, -73.33, -65.68, -58.52 ppm (ν_0 = 14 kHz). If the signal at δ = -302.12 ppm is assigned to one phosphorus site then the integration of all signals yields in 12 crystallographic P sites (12 cryst. different sites for P). Rotational sidebands are marked with asterisks.

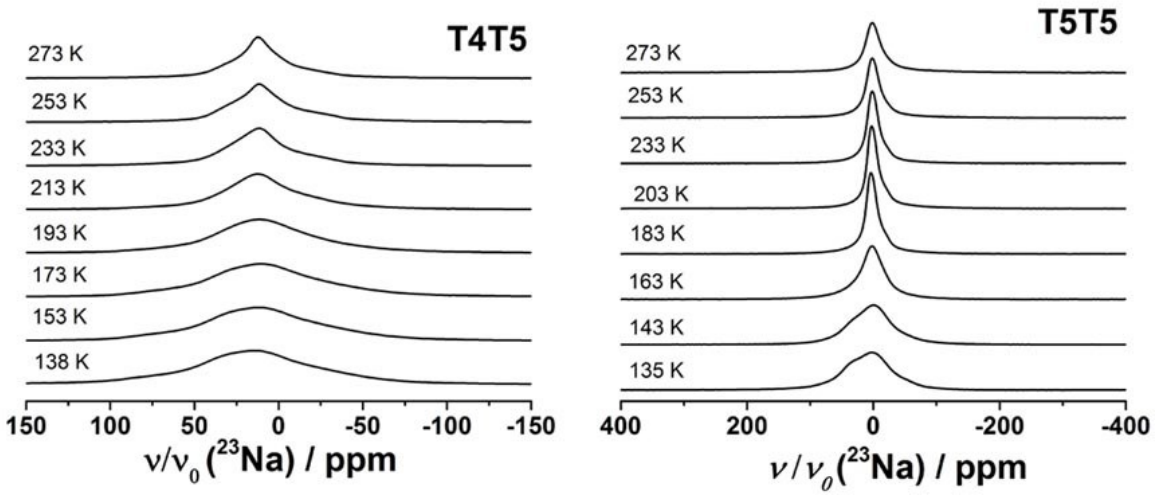

Figure B35 ^{23}Na-NMR spectra at the indicated temperatures of *LT*-$NaSi_2P_3$ (left) and *HT*-$NaSi_2P_3$ (right).

B.6 EDX Measurements of Supertetrahedral Sodium Phosphidosilicate

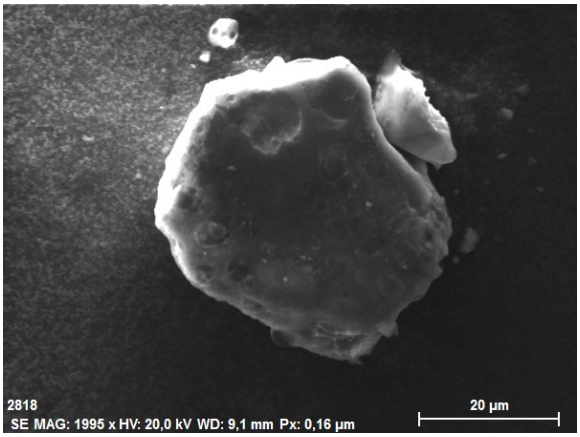

Figure B36 Scanning electron micrograph of $Na_{19}Si_{13}P_{25}$.

Table B7 EDX elemental analysis of $Na_{19}Si_{13}P_{25}$. Average of eight measuring points of a polycrystalline sample. Signals of oxygen were not taken into account due to hydrolysis by contact with air.

	Na	Si	P
EDX point 1 / atom%	31.98	24.16	43.86
EDX point 2 / atom%	33.05	21.13	45.82
EDX point 3 / atom%	33.10	22.03	44.88
EDX point 4 / atom%	33.36	21.33	45.30
EDX point 5 / atom%	33.04	23.51	43.44
EDX point 6 / atom%	33.45	25.19	41.36
EDX point 7 / atom%	34.64	23.94	41.42
EDX point 8 / atom%	33.18	22.24	44.58
Average / atom%	**33.23**	**22.94**	**43.83**
Calculated / atom%	**33.33**	**22.81**	**43.86**

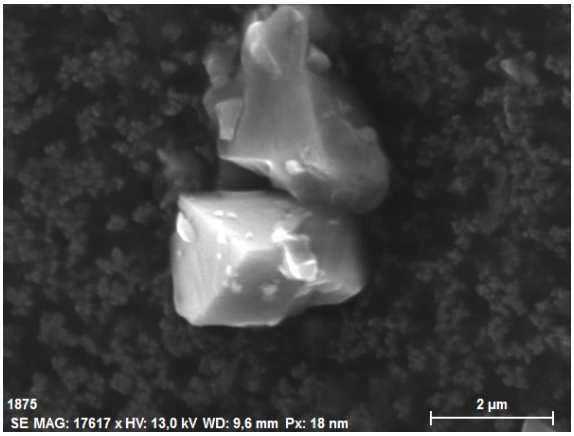

Figure B37 Scanning electron micrograph of $Na_{23}Si_{19}P_{33}$.

Table B8 EDX elemental analysis of $Na_{23}Si_{19}P_{33}$. Average of eight measuring points of a polycrystalline sample. Signals of oxygen were not taken into account due to hydrolysis by contact with air.

	Na	Si	P
EDX point 1 / atom%	30.74	23.77	45.49
EDX point 2 / atom%	30.68	23.65	45.67
EDX point 3 / atom%	29.01	26.13	44.86
EDX point 4 / atom%	30.33	25.10	44.57
EDX point 5 / atom%	29.27	25.81	44.92
EDX point 6 / atom%	29.90	26.83	43.27
EDX point 7 / atom%	30.71	26.42	42.87
EDX point 8 / atom%	29.58	25.52	44.89
Average / atom%	**30.03**	**25.40**	**44.57**
Calculated / atom%	**30.66**	**25.33**	**44.00**

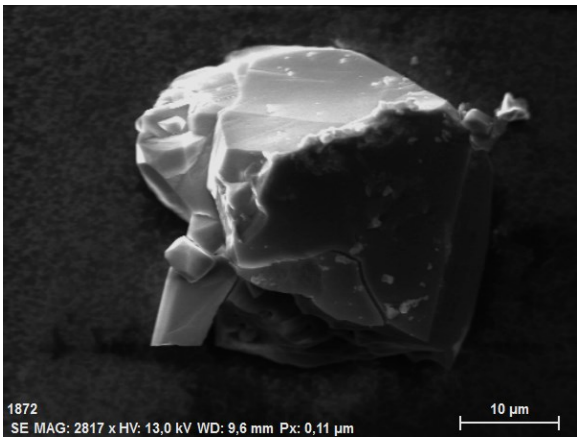

Figure B38 Scanning electron micrograph of $Na_{23}Si_{28}P_{45}$.

Table B9 EDX elemental analysis of $Na_{23}Si_{28}P_{45}$. Average of eight measuring points of a polycrystalline sample. Signals of oxygen were not taken into account due to hydrolysis by contact with air.

	Na	Si	P
EDX point 1 / atom%	24.47	28.11	47.42
EDX point 2 / atom%	22.89	30.50	46.62
EDX point 3 / atom%	25.23	28.69	46.08
EDX point 4 / atom%	24.88	27.80	47.32
EDX point 5 / atom%	21.46	30.51	48.04
EDX point 6 / atom%	25.05	28.64	46.31
EDX point 7 / atom%	23.03	30.34	46.63
EDX point 8 / atom%	22.46	30.72	46.82
Average / atom%	**23.68**	**29.41**	**46.91**
Calculated / atom%	**23.96**	**29.17**	**46.88**

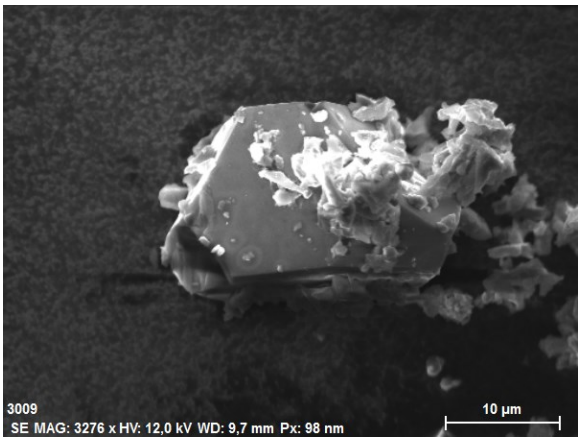

Figure B39 Scanning electron micrograph of $Na_{23}Si_{37}P_{57}$.

Table B10 EDX elemental analysis of $Na_{23}Si_{37}P_{57}$. Average of eight measuring points of a polycrystalline sample. Signals of oxygen were not taken into account due to hydrolysis by contact with air.

	Na	Si	P
EDX point 1 / atom%	17.68	33.63	48.69
EDX point 2 / atom%	19.55	32.22	48.22
EDX point 3 / atom%	19.60	31.94	48.47
EDX point 4 / atom%	20.18	31.59	48.23
EDX point 5 / atom%	20.67	31.19	48.14
EDX point 6 / atom%	19.78	31.77	48.46
EDX point 7 / atom%	18.99	31.67	49.35
EDX point 8 / atom%	19.29	31.15	49.56
Average / atom%	**19.47**	**31.89**	**48.64**
Calculated / atom%	**19.66**	**31.62**	**48.72**

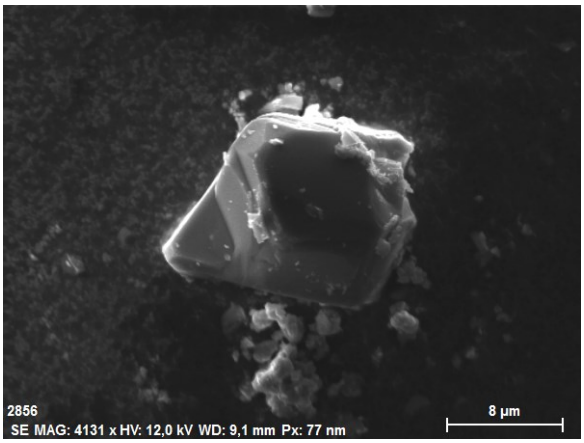

Figure B40 Scanning electron micrograph of *LT*-$NaSi_2P_3$.

Table B11 EDX elemental analysis of *LT*-$NaSi_2P_3$. Average of eight measuring points of a polycrystalline sample. Signals of oxygen were not taken into account due to hydrolysis by contact with air.

	Na	Si	P
EDX point 1 / atom%	16.65	35.90	47.46
EDX point 2 / atom%	17.31	33.11	49.57
EDX point 3 / atom%	17.21	32.86	49.92
EDX point 4 / atom%	15.67	34.87	49.46
EDX point 5 / atom%	17.46	32.85	49.69
EDX point 6 / atom%	17.01	33.06	49.94
EDX point 7 / atom%	18.09	33.29	48.62
EDX point 8 / atom%	16.71	34.35	48.94
Average / atom%	**17.01**	**33.79**	**49.20**
Calculated / atom%	**16.67**	**33.33**	**50.00**

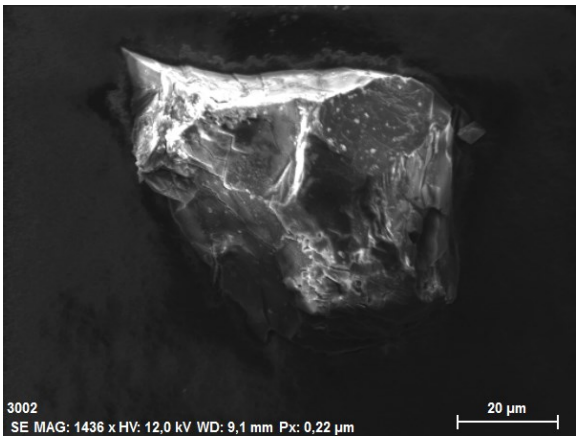

Figure B41 Scanning electron micrograph of *HT*-$NaSi_2P_3$.

Table B12 EDX elemental analysis of *HT*-$NaSi_2P_3$. Average of eight measuring points of a polycrystalline sample. Signals of oxygen were not taken into account due to hydrolysis by contact with air.

	Na	Si	P
EDX point 1 / atom%	14.79	34.34	50.87
EDX point 2 / atom%	15.38	34.47	50.14
EDX point 3 / atom%	15.18	34.37	50.45
EDX point 4 / atom%	15.97	33.77	50.26
EDX point 5 / atom%	15.12	34.02	50.86
EDX point 6 / atom%	15.08	33.79	51.13
EDX point 7 / atom%	14.66	34.46	50.88
EDX point 8 / atom%	16.16	33.99	49.86
Average / atom%	**15.29**	**34.15**	**50.56**
Calculated / atom%	**16.67**	**33.33**	**50.00**

B.7 Geometrical Sodium Pathway Analysis

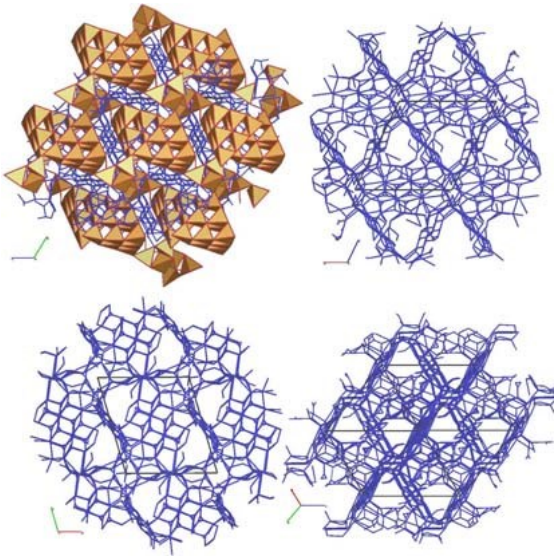

Figure B42 Calculated possible sodium ion pathways according to the voids in the structure of $Na_{19}Si_{13}P_{25}$. View along [100] (top, left), [010] (top, right), [001] (bottom, left) and [111] (bottom, right).

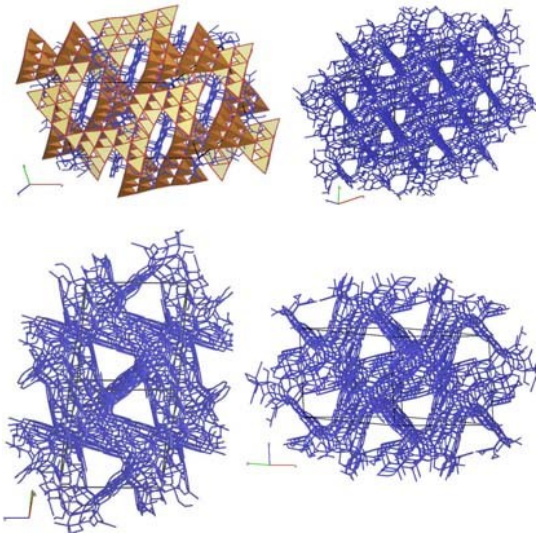

Figure B43 Calculated possible sodium ion pathways according to the voids in the structure of $Na_{23}Si_{19}P_{33}$. View along [112] (top, left), [1-12] (top, right), [1-10] (bottom, left) and [110] (bottom, right).

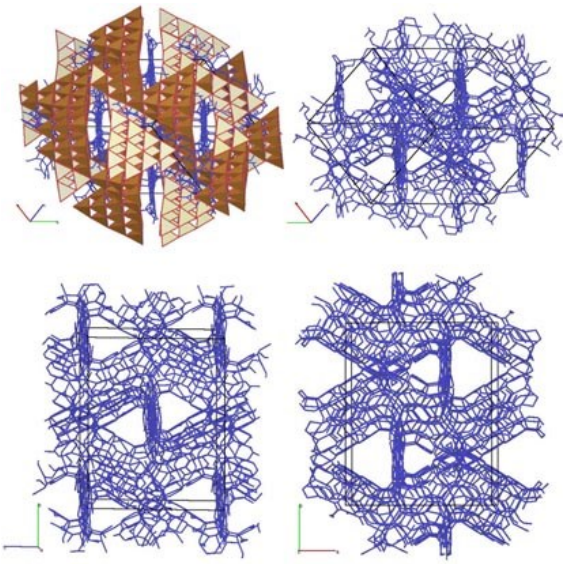

Figure B44 Calculated possible sodium ion pathways according to the voids in the structure of $Na_{23}Si_{28}P_{45}$. View along [11-1] (top, left), [-111] (top, right), [100] (bottom, left) and [001] (bottom, right).

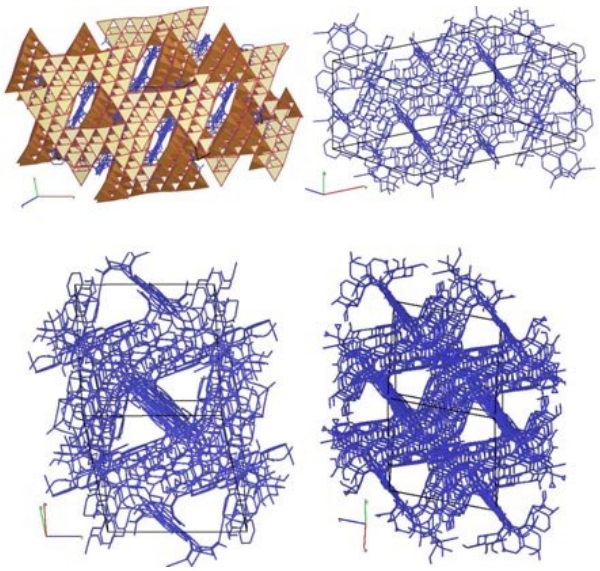

Figure B45 Calculated possible sodium ion pathways according to the voids in the structure of $Na_{23}Si_{37}P_{57}$. View along [112] (top, left), [1-12] (top, right), [1-10] (bottom, left) and [110] (bottom).

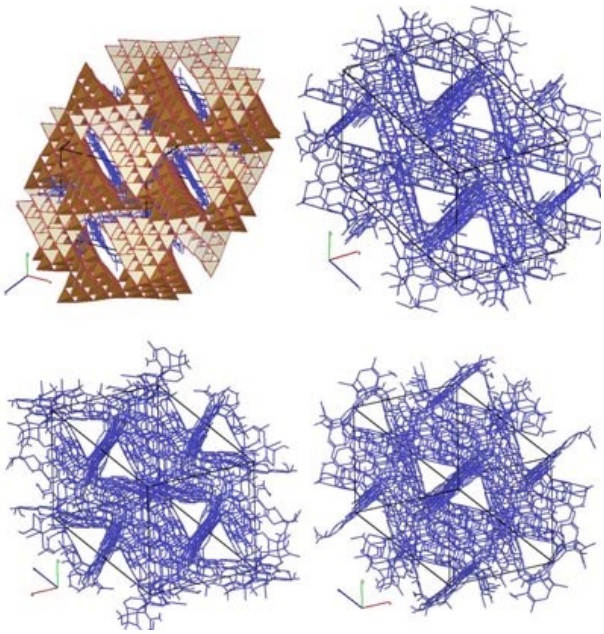

Figure B46 Calculated possible sodium ion pathways according to the voids in the structure of *LT*-$NaSi_2P_3$. View along [111] (top, left), [-111] (top, right), [11-1] (bottom, left) and [1-11] (bottom, right).

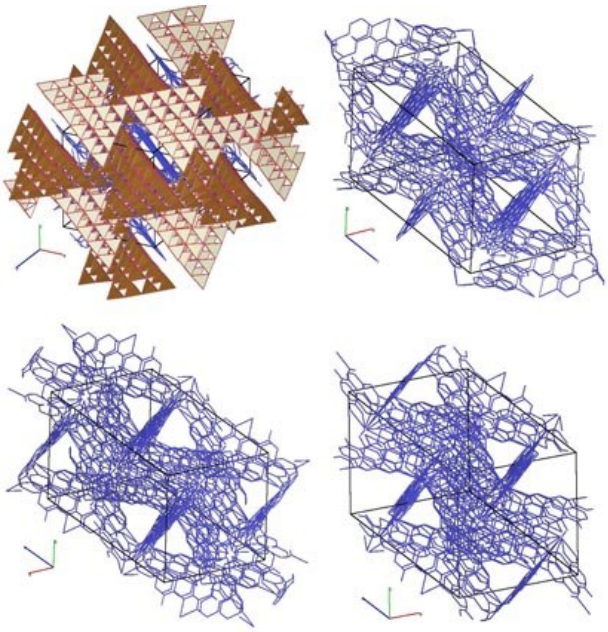

Figure B47 Calculated possible sodium ion pathways according to the voids in the structure of *HT*-$NaSi_2P_3$. View along [111] (top, left), [-111] (top, right), [11-1] (bottom, left) and [1-11] (bottom, right)

B.8 Details on Electrical Conductivity Measurements

To determine the electronic conductivities and ionic transference numbers, DC galvanostatic polarization measurements with ion-blocking electrodes (Indium metal) were conducted on all samples. No reactions between In and the samples were observed under these conditions. A current of 10 nA was always turned on between 1000-1500 s (each data point was collected in an interval of 0.1 s). Therefore, the samples except the T3T4 sample did not reach a steady state and the estimation of the electronic conductivity represents an upper limit. From the polarization in the EIS measurements it is clear that ions are the majority charge carrier in these systems. According to Maier,[1-2] the processes in an ionically and electronically conducting sample between two ion blocking electrodes can be described with the simplified equivalent circuit model in Figure B48 as parallel arrangement of electrical R_{eon} and ionic resistance R_{ion} with the bulk capacitor C_{bulk} and the ion blocking capacitor C_{block}.

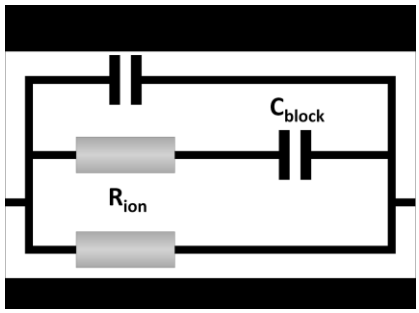

Figure B48 Equivalent circuit model of an ionic and electronic conducting sample between two ion blocking electrodes.

The initial sharp IR-drop in the DC polarization experiment after turning on the current contains the total resistance of the sample (V_{IR}=IR_{tot}). The total resistance R_{tot} includes R_{ion} and R_{eon} in parallel:

$$\frac{1}{R_{tot}} = \frac{1}{R_{eon}} + \frac{1}{R_{ion}} \quad (1)$$

After a long time of current flow the saturation voltage V_s, which can be assigned to the electronic resistance (V_s=IR_{eon}), is obtained. With the value for R_{eon} the ionic resistance R_{ion} can be calculated from R_{tot}. But this methods exhibits some problems for materials with high ionic conducitivity, because the resistance of the IR-drop measured after an interval time of 0.1 s is equivalent with the impedance at a frequency of 10 Hz and thus includes grain boundary contributions and polarization effects. For the fast ionic conductors (T3, T4T4, T4T5, T5T5), the ionic conductivity was approximated by the value obtained by EIS at room temperature. This allows the determination of the ionic transference numbers t_i, which depends on the ionic (σ_{ion}) and electronic (σ_{eon}) conductivity of all samples according to the following equation:

$$t_i = \frac{\sigma_{ion}}{\sigma_{ion} + \sigma_{eon}} \quad (2)$$

For a good ionic conductor, the transference number is ideally as close as possible to 1.0. If t_i is much greater than zero, but much smaller than one, a material is considered to be a mixed conductor.[3]

The DC measurements of all samples are shown in Figure S48 and the electronic conductivity and ionic transference number for each compound is listed in Table B13. All samples except T3T3 (t_i=0.6507), show a transference number that is close to 1. The sample T3T3 shows the behavior of a mixed ionic-electronic conductor because of its relatively low ionic conductivity.

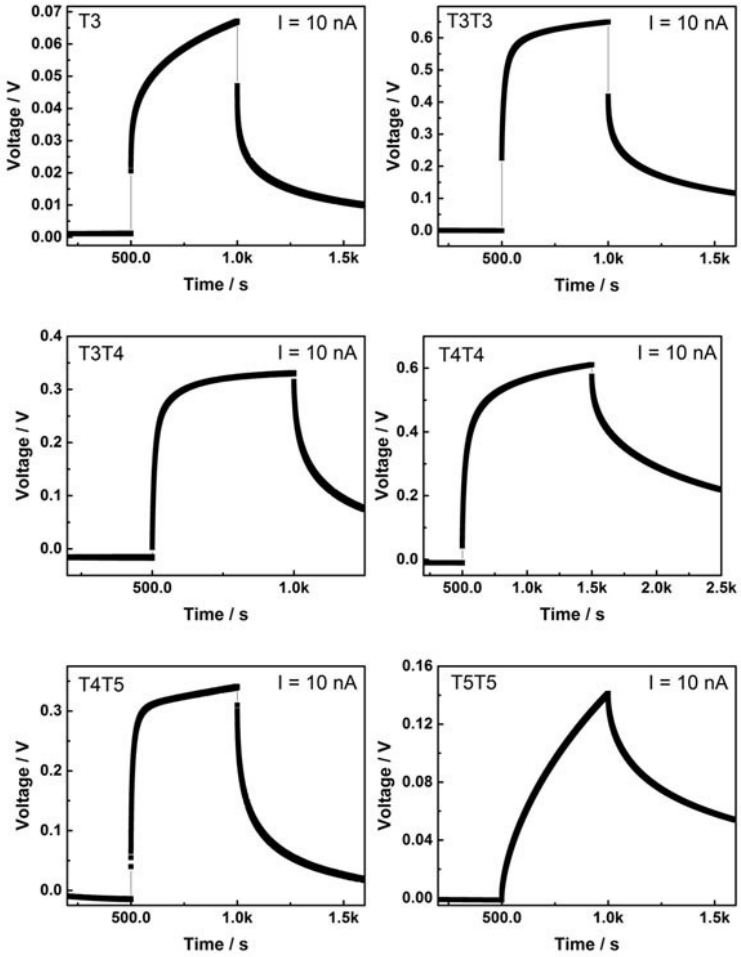

Figure B49 Plots of DC galvanostatic polarization measurements at RT with a current of 10 nA turned on between 1000-1500 s. The DC measurements were conducted with the same samples right after the EIS measurements.

Table B13 Results of DC galvanostatic polarization measurements including ionic transference number and upper limit of electronic conductivity.

Sample	σ_{eon} / Scm^{-1}	t_i
T3	$1.5 \cdot 10^{-7}$	0.9851
T3T3	$1.4 \cdot 10^{-8}$	0.6507
T3T4	$2.7 \cdot 10^{-8}$	0.9868
T4T4	$8.2 \cdot 10^{-9}$	0.9967
T4T5	$1.3 \cdot 10^{-8}$	0.9746
T5T5	$3.2 \cdot 10^{-8}$	0.9993

Temperature dependent EIS and and equivalent circuit modelling of T3, T3T3, T3T4, T4T4, T4T5, T5T5. The representative impedance spectra of the samples $Na_{19}Si_{13}P_{25}$ (T3), $Na_{23}Si_{19}P_{33}$ (T3T3),

$Na_{23}Si_{28}P_{45}$ (T3T4), $Na_{23}Si_{37}P_{57}$ (T4T4) *LT*-$NaSi_2P_3$ (T4T5) and *HT*-$NaSi_2P_3$ (T5T5) in Figure B50-S55 contain one to two semicircles at high frequencies and a spike at low frequencies. In general, the semicircles can be attributed to bulk or to grain boundary conductivity. In the simplest case, the impedance of one semicircle can be described with an equivalent circuit model containing a parallel arrangement of a resistor R and a capacitor C resembling the capacitive and conductive behavior of a solid electrolyte.[4-5] If the semicircles are depressed, the capacitor can be replaced by a constant phase element (CPE). This element takes a dispersion of relaxations times ($\tau=1/RC$) caused for instance by surface roughness of the sample or electrodes or non-uniform current distribution into consideration.[6] If the CPE is placed in parallel to a resistance, an effective capacitance C_{eff} can be calculated from the fitted values of *Q*, *R* and the factor α by:[7]

$$C_{eff} = \frac{(RQ)^{1/\alpha}}{R} \quad (3)$$

At low frequencies the spectra show a capacitive spike in the µF range due to the accumulation of Na^+-ions at the interface between pellet and metal electrode. This polarization is a typical characteristic of a solid ionic conductor and can be modeled by a capacitor or CPE in series to the RC-element.[4-5] By estimating the intersection of the semicircle with the real part of the impedance (Z_{Re}) in a Nyquist plot, the resistance (*R*) of the conduction process is obtained. The ionic conductivity (σ) is the inverse of *R* depending on the thickness (*l*) of the sample and the surface area of the electrodes (*A*):[3, 7]

$$\sigma = \frac{l}{AR} \quad (4)$$

By measuring the conductivity as function of temperature information about the activation energy E_a of the ion hopping through the structure of the solid (activated jump process) can be obtained in an Arrhenius-type function with *R* being the ideal gas constant, σ_0 an pre-exponential factor and *T* the temperature:[7-10]

$$\sigma = \frac{\sigma_0}{T} \cdot e^{\frac{-E_a}{RT}} \quad (5)$$

In Figure B50-B55 the spectra were fitted with an equivalent circuit containing a capacitor parallel to the serial connection of RC elements. This accounts for cable and stray capacitance of the measurement setup and was kept constant at 20 pF during the fitting routine.[11]

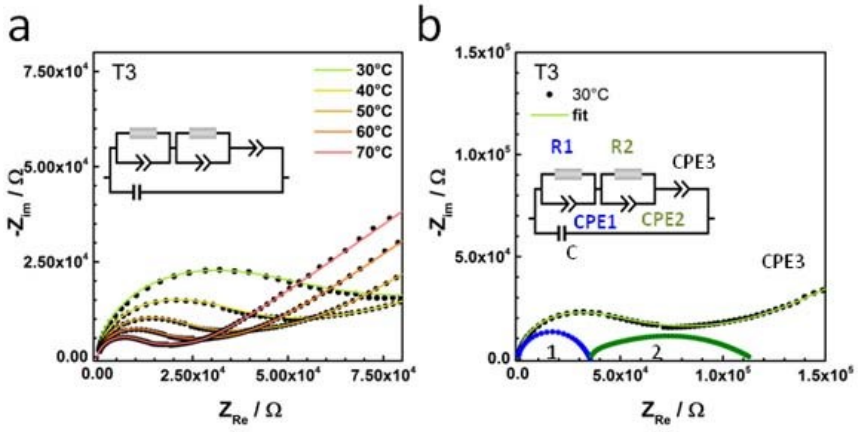

Figure B50 Representative EIS measurements of the sample T3 sintered at 400 °C (a) measurements and fits at different temperatures (b) fit of data measured at 30 °C with visualization of contributions to the fit with the shown model.

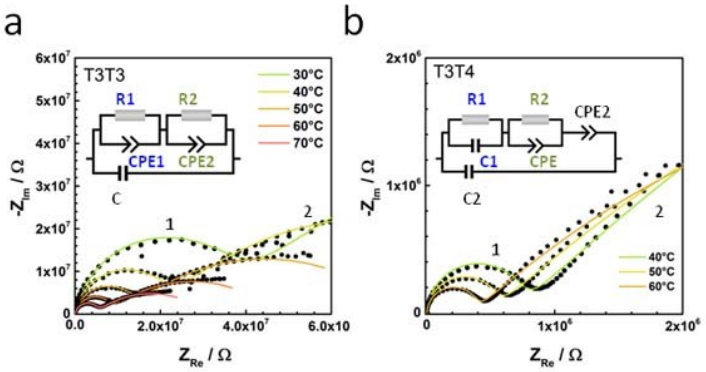

Figure B51 Representative EIS measurements with fits and applied model of the samples (a) T3T3, (b) T3T4 sintered at 400 °C. The contributions to the fit are indicated with the numbers 1 and 2 corresponding to the R1-CPE1 and R2-CPE2 elements.

For the capacitance of all contributions in the samples T3, T3T3 and T3T4 only values in the range of 10 nF to 0.1 nF were obtained. The R-CPE elements at higher frequencies (R1-CPE1 in S49-50) showed capacitances of about 10-100nF and at lower frequencies at least one order of magnitude larger. Thus, only conductivities limited by grain boundary properties were measured.[4] The activation energies for the observed processes shown in the main text were different for each Na-Si-P compound. For sample $Na_{19}Si_{13}P_{25}$ (T3) the activation energy for the sum of both processes inside the extremely broad semicircle

(cf. Figure B50a and b) was 0.36 eV. A clear deconvolution of the processes in the broad semicircle in T3 was difficult. Therefore, only the total conductivity was considered. For sample T3T3 the activation energies for both semicircles were very similar with 0.47 eV and 0.44 eV. Interestingly, no polarization spike was observed for T3T3 (cf. B51a). This corroborates the assumption that T3T3 is a mixed ionic-electronic conductor due to its comparable low ionic conductivity. For sample T3T4 the semicircle at lower frequencies (Figure B51b R2-CPE2) showed a much higher E_a and higher resistance than the one at high frequencies (0.69 eV for R2-CPE2 vs. 0.38 eV for R1-CPE1). This can indicate highly resistive layers at grain-to-grain contacts.[12-13]

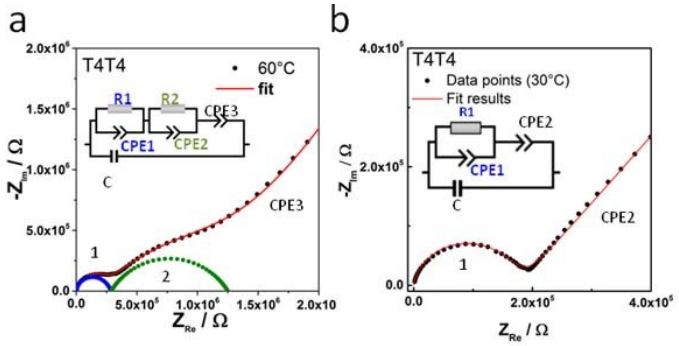

Figure B52 Representative EIS measurements of the sample T4T4 sintered at 400 °C (a) average sample showing two semicircles in the EIS, (b) best sample of T4T4 showing only one semicircle.

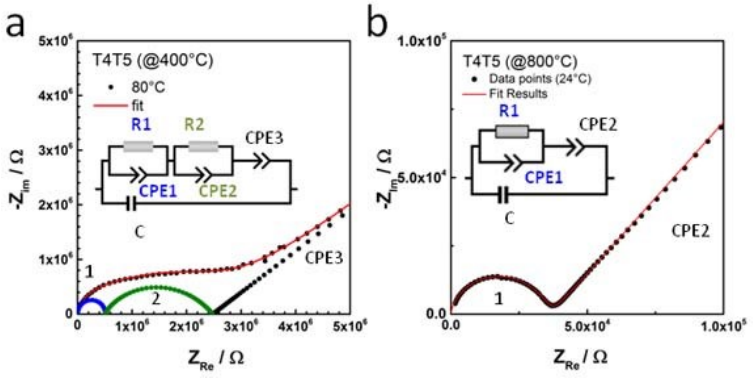

Figure B53 Representative EIS measurements of the sample T4T5 sintered at (a) 400 °C, (b) 800 °C.

The samples T4T4, T4T5 and T5T5 sintered at 400 °C show similar properties as T3T4 but have higher conductivities and lower E_a (cf. Figure B52a and B53a). For the presented best samples of T4T4 and T4T5 in Figure B52b and B53b only one semicircle is visible, probably because this sample received the

optimal sintering and pressing treatment. The capacitance of the R1-CPE1 element of the best samples of T4T4 and T4T5 was 20 pF, thus still higher as expected for bulk properties.

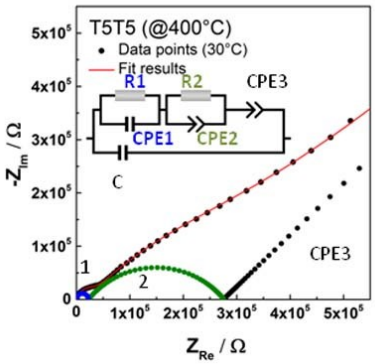

Figure B54 Representative EIS impedance measurement of the samples T5T5 sintered at 400 °C showing two semicircles.

Especially, for samples T4T5 (Figure B53a) and T5T5 (Figure B54) a non ideal microstructure of the pellets was noticed. Subsequently, for improving the microstructure the pellets were sintered at 800 °C (cf. Figure B57). For the other compounds (T3, T3T3, T3T4, T4T4) phase transitions occurred at such high sintering temperatures leading to a mixture of compounds in the pellet. Hence, they were sintered at 400 °C only.

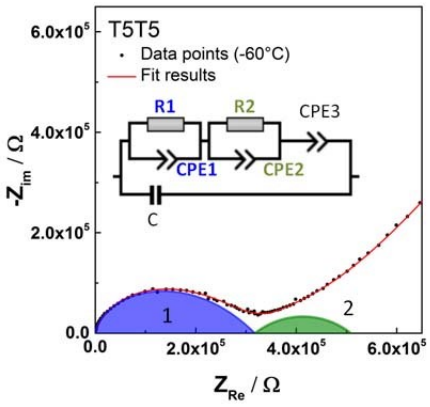

Figure B55 The electrochemical impedance of the T5T5 samples was measured at -60 °C showing a capacitance of about 20 pF ($C_{eff}1$ calculated from R1 and CPE1). The extraction of the capacitance from the measurement at 25 °C was difficult due to the small resistance and the influence of cable induction on the spectrum.

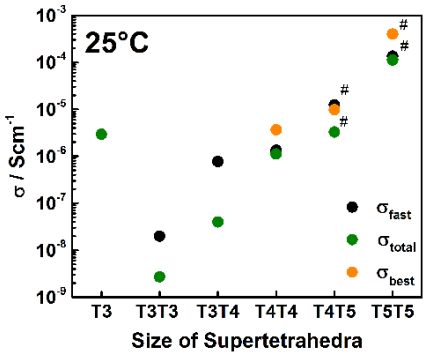

Figure B56 Ionic conductivities at 25 °C increases with the size of the supertetrahedral entities in the Na-Si-P structures. The samples T3-T4T4 were sintered at 400 °C. T4T5 and T5T5 were sintered at 800 °C (marked with a hash). σ_{fast} (black) refers to the average conductivity of at least four samples calculated from the resistance of the high frequency arc (cf. R1-CPE1 in Figure B50-B54). σ_{total} (green) refers to the corresponding total conductivity (sum of the resistances of both semicircles; R1+R2). Additionally, the conductivities of the samples showing only one semicircle in the EIS are plotted in orange (σ_{best}).

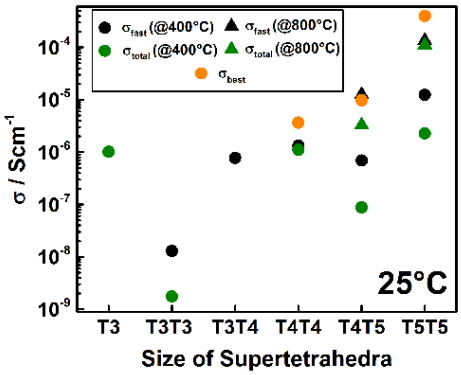

Figure B57 Comparison of the ionic conductivity of all samples at 25 °C. The conductivity increases with the size of the supertetrahedral entities in the Na-Si-P structures. The samples T3-T4T4 were sintered at 400 °C (points). This Figure also includes the conductivity values of T4T5 and T5T5 sintered at 400 °C (points) and at 800 °C (triangles). Especially for the sample T4T5 it is obvious that the microstructure is not optimal for impedance measurements and the performance is reduced in comparison to the samples sintered at 800 °C

C Appendix – Supporting Information for Chapter 5

C.1 Experimental Procedures

Synthesis. Like most of alkaline and alkaline-earth phosphidosilicates the title compound is highly moisture sensitive leading to hydrolysis within a few minutes by contact with air. Therefore, all manipulations were conducted under inert conditions.

KSi_2P_3-*mC*928 can be obtained as an air sensitive and dark red polycrystalline powder by reacting directly a stoichiometric elemental mixture. To this end, metallic potassium (1 eq., 0.0208 g, 99.95 %), silicon powder (2 eq., 0.0299 g, 99.999 %) and red phosphorus (3 eq., 0.0494 g, 99.999+ %) were mixed in an argon filled glovebox and loaded into an alumina crucible and sealed in silica ampoules under argon atmosphere. To prevent bursting of the ampoule the temperature of the tube furnace was raised slowly to 200 °C with a 20 °C/h rate before the mixture was reacted for 60 h at 1060 °C. To produce larger amounts of KSi_2P_3-*mC*928 we synthesized the known T3 compound as precursor. Therefore, we mixed potassium (1 eq., 0.1039 g), silicon (2 eq., 0.1495 g) and phosphorus (3 eq., 0.2471 g), and heated the mixture to 700 °C with a 10 °C/h rate for 30 h. The intermediate was ground and reheated again to 700 °C for 30 h yielding in a phase-pure precursor. This precursor was inserted in a preheated furnace at 1060 °C and reacted for 2 h before the temperature settled to 25 °C with 40 °C/h. Since we failed to produce the polymorphs KSi_2P_3-*oF*1952 and KSi_2P_3-*tI*960 by different temperature programs, we were able to intercept small amounts of these by applying three equivalents of an in situ formed crystallization agent of K_3P. To this end, a mixture of potassium (5 eq., 0.0618 g), silicon (1 eq., 0.0085 g) and phosphorus (3 eq., 0.0294 g) was prepared likewise and heated to 100 °C within 5 h before the temperature was raised to 800 °C or 950 °C with 100 °C/h for 60 h, respectively.

Single-Crystal X-ray Diffraction. The crystal structure of the T5 compound was successfully solved and refined only for the KSi_2P_3-*tI*960 polymorph. Due to the sensitivity to air and moisture, single-crystals were prepared under dried paraffin oil and transferred into oil filled and sealed glass capillaries (Hilgenberg GmbH) with an inner diameter of 0.2 mm. Diffraction data of the whole Ewald's sphere were collected with a Bruker D8 Quest device with Mo-Kα radiation, Photon II detector and Göbel mirror optics. With the software package APEX3 the data reduction and absorption correction were processed before the structure was solved by direct methods and refined with the SHELX package.

Powder X-ray Diffraction. Phase-pure polycrystalline samples of each polymorph were ground, filled and sealed in Hilgenberg glass capillaries with an inner diameter of 0.2 mm under argon atmosphere. Diffraction data were obtained from a StadiP powder diffractometer (STOE & Cie GmbH) with Cu-$K\alpha_1$radiation and Mythen 1K detector (Dectris) and a Ge (111) monochromator in Debye-Scherrer

geometry. Based on the single-crystal structure of KSi_2P_3-*tI*960 the according diffractogram was refined with the Rietveld method implemented in the TOPAS software. For the Rietveld refinement of the KSi_2P_3-*oF*1952 polymorph the single-crystal structure of KSi_2P_3-*tI*960 was solved assuming an orthorhombic unit cell. Based on these data, the powder pattern was indexed and refined with manually adjusted cell parameters. The powder refinement of the KSi_2P_3-*mC*928 polymorph was processed likewise.

Temperature-Dependent Powder X-ray Diffraction. For the investigation of phase transitions the respective polycrystalline samples were ground and loaded in Hilgenberg silica glass capillaries with an inner diameter of 0.4 mm and sealed with grease for pressure compensation. Diffraction data collection under argon atmosphere was also performed on a STOE StadiP diffractometer with Mo-Kα_1 radiation, Ge monochromator, a resistance graphite furnace and IP-PSD detector. For the transition of the T3 compound described by Feng *et al.* to KSi_2P_3-*tI*960 (Figure 5.1) a sample was heated beginning at room temperature to 1045 °C in steps of 20 °C with a 5 °C/min heating rate. At each step the temperature was kept constant and a diffractogram was collected. For the phase transitions solely involving the T5 compounds in Figure 5.5 the sample was heated to 350 °C and cooled to room temperature with the same heating rate but every 5 °C a diffraction pattern was recorded.

EDX Analysis. The elemental composition of KSi_2P_3-*mC*928 was verified by energy dispersive X-ray spectroscopy with an EVO-MA10 Zeiss scanning electron microscope with a field emission gun and X-Flash 410-M X-ray detector. Polycrystalline samples were prepared under inert conditions in a glovebox on electronic conducting and adhesive carbon pads. These were inserted in the SEM quickly due to hydrolysis. The collected data were processed with QUANTAX200 software in which signals of oxygen and carbon were not taken to account.

Solid-State NMR. A X-ray pure sample of KSi_2P_3-*mC*928 was loaded into a zirconia rotor of 4 mm in diameter for the silicon and into a 2.5 mm rotor for the phosphorus spectra and placed into a Bruker Avance III 500 spectrometer with a magnetic field strength of 11.74 T. The sample was rotated with 10 kHz and 25 kHz for the respective silicon and phosphorus spectra under MAS conditions with Larmor frequencies of ν_0 (^{31}P) = 202.5 MHz and ν_0 (^{29}Si) = 99.38 MHz. All spectra were indirectly referenced to ^{1}H at 0 ppm in 0.1 % TMS (4 mm rotor) and -0.1240 ppm in 100 % TMS (2.5 mm rotor).

Conductivity Measurements. The KSi_2P_3-*mC*928 samples were ground thoroughly and compacted to a pellet of about 0.5-1.0 mm thickness and 5 mm in diameter by uniaxial cold pressing (10 kN) and then

annealed under argon at 800 °C for 10 h. The large thickness of the pellets was required for sputtering and annealing. The pellets had densities of about 78±3 % (Table C9). The pellets were sputtered with ruthenium as ion-blocking electrodes on both sides. Electrochemical impedance spectroscopy (EIS) for every sample was measured for several temperature cycles between 25 and -20 °C with 5 °C steps inside a glovebox under argon atmosphere. Higher temperatures were avoided to avoid phase changes influencing the performance. The samples were subsequently used for the polarization measurements to extract the electronic partial conductivity at 25 °C. For these a voltage of 0.25 and 0.5 V was applied for 5-10 h each and the drop in resulting current measured. The resistance was calculated from the current measured at a steady state after several hours. EIS and polarization measurements were performed with an IVIUM compactstat.h (24 bit instrument) in a two-electrode setup using a RHD INSTRUMENTS Microcell HC cell stand loaded with RHD INSTRUMENTS TSC Battery cells. The spectra were recorded in a frequency range of 1 MHz–0.01 Hz and rms AC voltage of 50 mV was applied. The analysis of the impedance spectra was carried out with the RelaxIS3 software from RHD INSTRUMENTS. The linearity, stability and causality were checked by the Kramers-Kronig-relation before fitting the data.

Geometrical Pathway Analysis. The identification of possible potassium migration pathways was conducted with the ToposPro software package. Therefore, based on the crystal structures the voids accessible for potassium ions were calculated using the ionic radius for potassium and covalent radius for phosphorus atoms since calculations on Ba_2SiP_4 showed predominantly covalent behavior of the anionic Si-P network. Afterwards the channels were calculated connecting the possible potassium voids with at least 3.1 Å in diameter. The results are shown in Figure C6-C8.

C.2 Crystallographic Data on KSi_2P_3 Modifications

Table C1 Fractional atomic coordinates, equivalent displacement parameters (Å²) and occupancy factors of KSi_2P_3-*tI*960.

atom	Wyckoff	*x*	*y*	*z*	U_{eq}	Occ. (<1)
Si1	32*g*	0.01336 (3)	0.13475 (3)	0.31216 (2)	0.01251 (11)	
Si2	32*g*	0.11118 (3)	0.26473 (3)	0.31162 (2)	0.01299 (11)	
Si3	32*g*	0.12699 (3)	0.34243 (3)	0.00244 (2)	0.01433 (12)	
Si4	32*g*	0.12716 (3)	0.15085 (3)	0.37593 (2)	0.01241 (11)	
Si5	32*g*	0.25467 (3)	0.33227 (3)	0.06290 (2)	0.01332 (11)	
Si6	32*g*	0.26842 (3)	0.22218 (3)	0.12512 (2)	0.01347 (11)	

Si7	32*g*	0.28474 (3)	0.11150 (3)	0.18786 (2)	0.01398 (12)	
Si8	16*e*	0.29477 (4)	0	¼	0.01299 (15)	
Si9	16*d*	0	¼	0.00359 (2)	0.01502 (16)	
P1	32*g*	0.05818 (3)	0.20620 (3)	0.40372 (2)	0.01319 (10)	
P2	32*g*	0.06423 (3)	0.29646 (3)	0.03746 (2)	0.02339 (14)	
P3	32*g*	0.06794 (3)	0.19514 (3)	0.27753 (2)	0.01429 (11)	
P4	32*g*	0.08297 (3)	0.08147 (3)	0.34163 (2)	0.01326 (11)	
P5	32*g*	0.09091 (3)	0.03417 (3)	0.09325 (2)	0.01942 (12)	
P6	32*g*	0.18135 (3)	0.21133 (3)	0.34107 (2)	0.01352 (11)	
P7	32*g*	0.19082 (3)	0.39756 (3)	0.03518 (2)	0.01286 (10)	
P8	32*g*	0.19672 (3)	0.02117 (3)	0.02977 (2)	0.01887 (12)	
P9	32*g*	0.19967 (3)	0.27053 (3)	0.09466 (2)	0.01848 (12)	
P10	32*g*	0.31478 (3)	0.27727 (3)	0.02760 (2)	0.01449 (11)	
P11	32*g*	0.33477 (3)	0.17519 (3)	0.22294 (2)	0.01504 (11)	
P12	32*g*	0.34720 (3)	0.05309 (3)	0.15492 (2)	0.01351 (11)	
K1	32*g*	0.0305 (2)	0.06606 (13)	0.02603 (11)	0.108 (3)	0.409 (5)
K2	32*g*	0.07481 (19)	0.18388 (14)	0.10302 (14)	0.142 (3)	0.436 (4)
K3	32*g*	0.07998 (6)	0.08214 (14)	0.21173 (5)	0.1581 (16)	0.820 (5)
K4	32*g*	0.1508 (2)	0.3851 (3)	0.13536 (14)	0.170 (5)	0.427 (4)
K5	32*g*	0.18701 (11)	0.2800 (2)	0.19937 (10)	0.105 (2)	0.468 (5)
K6	32*g*	0.20248 (8)	0.01439 (9)	0.14389 (6)	0.0651 (6)	0.5
K7	32*g*	0.2161 (3)	0.1692 (5)	0.2668 (3)	0.111 (5)	0.163 (4)
K8	32*g*	0.3209 (6)	0.0292 (4)	0.0672 (5)	0.113 (9)	0.189 (8)
K9	32*g*	0.34676 (15)	0.04711 (12)	0.04386 (10)	0.0569 (10)	0.459 (8)
K10	16*e*	0.0999 (3)	0	¼	0.058 (4)	0.125 (5)
K11	16*d*	0	¼	0.1075 (3)	0.186 (13)	0.193 (7)

Table C2 Atomic displacement parameters (Å^2) of KSi_2P_3-*tl*960.

atom	U^{11}	U^{22}	U^{33}	U^{12}	U^{13}	U^{23}
Si1	0.0125 (3)	0.0124 (2)	0.0126 (2)	−0.00107 (19)	−0.00011 (19)	−0.0002 (2)
Si2	0.0137 (3)	0.0120 (3)	0.0133 (3)	−0.00081 (19)	−0.0003 (2)	0.0002 (2)
Si3	0.0140 (3)	0.0155 (3)	0.0135 (3)	−0.0032 (2)	−0.0015 (2)	−0.0005 (2)
Si4	0.0123 (2)	0.0124 (2)	0.0125 (2)	−0.00036 (19)	−0.0007 (2)	0.0001 (2)
Si5	0.0128 (3)	0.0127 (3)	0.0144 (3)	0.0010 (2)	−0.0015 (2)	0.0005 (2)
Si6	0.0124 (2)	0.0131 (3)	0.0149 (3)	0.0005 (2)	−0.0003 (2)	0.0014 (2)
Si7	0.0138 (3)	0.0135 (3)	0.0147 (3)	0.0001 (2)	0.0008 (2)	0.0016 (2)
Si8	0.0119 (3)	0.0136 (4)	0.0135 (3)	0	0	0.0024 (3)
Si9	0.0142 (4)	0.0176 (4)	0.0132 (4)	−0.0041 (3)	0	0
P1	0.0128 (2)	0.0132 (2)	0.0135 (2)	0.00034 (18)	−0.00005 (18)	−0.00033 (18)
P2	0.0226 (3)	0.0339 (4)	0.0136 (3)	−0.0140 (3)	−0.0016 (2)	0.0008 (2)
P3	0.0162 (2)	0.0135 (2)	0.0132 (2)	−0.00242 (19)	0.00104 (19)	−0.00036 (19)
P4	0.0123 (2)	0.0127 (2)	0.0148 (2)	−0.00039 (18)	−0.00019 (18)	−0.00054 (19)

P5	0.0209 (3)	0.0134 (2)	0.0240 (3)	−0.0002 (2)	0.0086 (2)	0.0006 (2)
P6	0.0130 (2)	0.0130 (2)	0.0146 (2)	−0.00006 (18)	0.00024 (18)	0.00081 (19)
P7	0.0130 (2)	0.0122 (2)	0.0134 (2)	−0.00055 (18)	−0.00209 (18)	−0.00035 (18)
P8	0.0216 (3)	0.0118 (2)	0.0233 (3)	0.0014 (2)	0.0099 (2)	0.0009 (2)
P9	0.0136 (2)	0.0190 (3)	0.0229 (3)	0.0002 (2)	−0.0022 (2)	0.0064 (2)
P10	0.0142 (2)	0.0144 (2)	0.0148 (2)	0.00248 (19)	−0.00186 (19)	−0.00053 (19)
P11	0.0168 (3)	0.0137 (2)	0.0146 (2)	−0.00091 (19)	0.0011 (2)	0.00096 (19)
P12	0.0129 (2)	0.0135 (2)	0.0141 (2)	−0.00012 (18)	−0.00010 (18)	0.00136 (19)
K1	0.160 (5)	0.0456 (14)	0.119 (3)	−0.0022 (18)	−0.113 (4)	0.0196 (16)
K2	0.088 (3)	0.0397 (15)	0.298 (7)	−0.0017 (14)	−0.026 (3)	−0.017 (3)
K3	0.0359 (7)	0.303 (4)	0.1350 (17)	0.0462 (12)	−0.0338 (8)	−0.149 (2)
K4	0.0581 (19)	0.220 (8)	0.231 (8)	0.004 (3)	0.022 (3)	−0.200 (7)
K5	0.0507 (13)	0.143 (4)	0.122 (3)	−0.0142 (15)	0.0403 (15)	−0.097 (3)
K6	0.0391 (8)	0.0557 (10)	0.1003 (15)	0.0023 (7)	−0.0236 (9)	−0.0492 (10)
K7	0.061 (5)	0.134 (8)	0.136 (8)	−0.027 (5)	0.058 (5)	−0.097 (7)
K8	0.100 (8)	0.041 (4)	0.199 (18)	0.037 (5)	−0.118 (11)	−0.069 (7)
K9	0.0648 (15)	0.0371 (10)	0.069 (2)	0.0009 (10)	−0.0448 (14)	−0.0176 (11)
K10	0.012 (3)	0.073 (7)	0.090 (9)	0	0	0.014 (6)
K11	0.24 (2)	0.26 (3)	0.058 (6)	−0.15 (2)	0	0

Table C3 Fractional atomic coordinates, equivalent displacement parameters (Å^2) and occupancy factors of KSi_2P_3- *oF*1952.

atom	Wyckoff	*x*	*y*	*z*	U_{eq}	Occ. (<1)
Si1	32*h*	0.00479 (2)	0.27318 (2)	0.12527 (2)	0.01361 (11)	
Si2	32*h*	0.01178 (2)	0.11103 (2)	0.37389 (2)	0.01247 (11)	
Si3	32*h*	0.01526 (2)	0.14230 (2)	0.00260 (2)	0.01448 (12)	
Si4	32*h*	0.05198 (2)	0.33666 (2)	0.18803 (2)	0.01406 (12)	
Si5	32*h*	0.06065 (2)	0.17594 (2)	0.43765 (2)	0.01250 (11)	
Si6	32*h*	0.06200 (2)	0.17319 (2)	0.31147 (2)	0.01304 (11)	
Si7	32*h*	0.07404 (2)	0.06072 (2)	0.31200 (2)	0.01261 (11)	
Si8	32*h*	0.07675 (2)	0.06208 (2)	0.43818 (2)	0.01300 (11)	
Si9	32*h*	0.13900 (2)	0.01191 (2)	0.37575 (2)	0.01251 (11)	
Si10	32*h*	0.28886 (2)	0.20650 (2)	0.31273 (2)	0.01341 (11)	
Si11	32*h*	0.29344 (2)	0.03874 (2)	0.06307 (2)	0.01337 (11)	
Si12	32*h*	0.35270 (2)	0.10252 (2)	0.00017 (2)	0.01303 (11)	
Si13	32*h*	0.35775 (2)	0.26533 (2)	0.25226 (2)	0.01437 (12)	
Si14	32*h*	0.41345 (2)	0.05176 (2)	0.06233 (2)	0.01397 (11)	
Si15	32*h*	0.47694 (2)	0.00462 (2)	0.12505 (2)	0.01355 (11)	
Si16	16*g*	⅛	⅛	0.00375 (2)	0.01510 (16)	
Si17	16*g*	⅛	⅛	0.50341 (2)	0.01498 (16)	
P1	32*h*	0.00084 (2)	0.33225 (2)	0.09179 (2)	0.01325 (10)	

P2	32*h*	0.00490 (2)	0.17015 (2)	0.27689 (2)	0.01504 (11)	
P3	32*h*	0.01494 (2)	0.03536 (2)	0.15519 (2)	0.01840 (12)	
P4	32*h*	0.01490 (2)	0.05368 (2)	0.40875 (2)	0.01353 (10)	
P5	32*h*	0.01870 (2)	0.04604 (2)	0.27746 (2)	0.01453 (11)	
P6	32*h*	0.04995 (2)	0.39708 (2)	0.15509 (2)	0.01344 (10)	
P7	32*h*	0.06266 (2)	0.27846 (2)	0.15691 (2)	0.01947 (12)	
P8	32*h*	0.06356 (2)	0.11848 (2)	0.47231 (2)	0.01426 (11)	
P9	32*h*	0.06966 (2)	0.13391 (3)	0.03762 (2)	0.02356 (14)	
P10	32*h*	0.07398 (2)	0.11781 (2)	0.34612 (2)	0.01319 (10)	
P11	32*h*	0.07974 (2)	0.00505 (2)	0.47276 (2)	0.01508 (11)	
P12	32*h*	0.13154 (2)	0.06365 (2)	0.27737 (2)	0.01437 (11)	
P13	32*h*	0.13220 (2)	0.07403 (2)	0.40355 (2)	0.01314 (10)	
P14	32*h*	0.13389 (3)	0.06969 (2)	0.53729 (2)	0.02334 (14)	
P15	32*h*	0.14092 (2)	0.33790 (2)	0.02959 (2)	0.01892 (12)	
P16	16*g*	0.14654 (2)	0.45586 (2)	0.03499 (2)	0.01285 (10)	
P17	16*g*	0.19640 (2)	0.01505 (2)	0.34091 (2)	0.01353 (10)	
P18	32*h*	0.28553 (2)	0.26483 (2)	0.34449 (2)	0.01857 (12)	
P19	32*h*	0.29425 (2)	0.10329 (2)	0.03535 (2)	0.01282 (10)	
P20	32*h*	0.29600 (2)	0.26879 (2)	0.22222 (2)	0.01444 (11)	
P21	32*h*	0.35297 (2)	0.04977 (2)	0.09525 (2)	0.01352 (10)	
P22	32*h*	0.41233 (2)	0.10883 (2)	0.02994 (2)	0.01882 (12)	
P23	32*h*	0.41780 (2)	0.00069 (2)	0.15852 (2)	0.01320 (10)	
P24	32*h*	0.47171 (2)	0.06245 (2)	0.09341 (2)	0.01939 (12)	
K1	32*h*	0.01614 (10)	0.04712 (12)	0.05120 (9)	0.0984 (13)	0.4524 (13)
K2	32*h*	0.0241 (3)	0.4426 (3)	0.0171 (3)	0.119 (4)	0.180 (2)
K3	32*h*	0.04659 (12)	0.51614 (11)	0.05070 (9)	0.0979 (13)	0.4524 (13)
K4	32*h*	0.04759 (13)	0.01829 (13)	0.02654 (11)	0.1260 (19)	0.4524 (13)
K5	32*h*	0.0498 (2)	0.3002 (2)	0.0001 (2)	0.085 (3)	0.180 (2)
K6	32*h*	0.05293 (8)	0.39980 (8)	0.04371 (7)	0.0536 (7)	0.433 (3)
K7	32*h*	0.07121 (12)	0.25495 (16)	0.03342 (10)	0.0793 (15)	0.433 (3)
K8	32*h*	0.0748 (3)	0.39580 (18)	0.0670 (3)	0.114 (5)	0.180 (2)
K9	32*h*	0.10838 (6)	0.34408 (6)	0.10600 (6)	0.0574 (6)	0.4524 (13)
K10	32*h*	0.1170 (2)	0.48199 (13)	0.11428 (15)	0.181 (4)	0.4524 (13)
K11	32*h*	0.12912 (12)	0.05465 (11)	0.10258 (15)	0.144 (2)	0.4524 (13)
K12	32*h*	0.15791 (14)	0.00681 (13)	0.04421 (12)	0.0903 (14)	0.4524 (13)
K13	32*h*	0.24512 (16)	0.32121 (12)	0.28301 (9)	0.0837 (15)	0.4524 (13)
K14	32*h*	0.25704 (14)	0.34247 (14)	0.29456 (12)	0.0953 (16)	0.4524 (13)
K15	32*h*	0.26800 (13)	0.1326 (2)	0.11486 (16)	0.178 (4)	0.4524 (13)
K16	32*h*	0.3079 (3)	0.2264 (4)	0.0167 (3)	0.145 (6)	0.180 (2)
K17	32*h*	0.35030 (8)	0.19656 (8)	0.04419 (7)	0.0596 (9)	0.475 (5)
K18	32*h*	0.35428 (19)	0.1742 (3)	0.0681 (4)	0.107 (5)	0.180 (2)
K19	32*h*	0.40601 (6)	0.14139 (6)	0.10622 (6)	0.0586 (6)	0.4524 (13)
K20	32*h*	0.51814 (13)	0.04806 (13)	0.02635 (11)	0.115 (2)	0.433 (3)

K21	32*h*	0.55468 (11)	0.12945 (12)	0.10261 (15)	0.143 (2)	0.4524 (13)

Table C4 Atomic displacement parameters (Å^2) of KSi_2P_3- *oF*1952.

atom	U^{11}	U^{22}	U^{33}	U^{12}	U^{13}	U^{23}
Si1	0.0134 (3)	0.0121 (3)	0.0154 (3)	0.0004 (2)	−0.0009 (2)	−0.0012 (2)
Si2	0.0129 (3)	0.0120 (2)	0.0125 (3)	−0.0001 (2)	−0.0006 (2)	−0.0005 (2)
Si3	0.0119 (3)	0.0181 (3)	0.0134 (3)	0.0008 (2)	0.0016 (2)	−0.0006 (2)
Si4	0.0137 (3)	0.0135 (3)	0.0149 (3)	−0.0002 (2)	−0.0019 (2)	−0.0005 (2)
Si5	0.0135 (3)	0.0114 (3)	0.0126 (3)	0.0002 (2)	0.0001 (2)	−0.0002 (2)
Si6	0.0122 (3)	0.0136 (3)	0.0133 (3)	−0.0007 (2)	0.0001 (2)	−0.0002 (2)
Si7	0.0116 (3)	0.0137 (3)	0.0125 (3)	−0.0001 (2)	−0.0003 (2)	0.0000 (2)
Si8	0.0137 (3)	0.0120 (3)	0.0134 (3)	0.0008 (2)	−0.0005 (2)	0.0000 (2)
Si9	0.0120 (2)	0.0127 (3)	0.0128 (3)	0.0000 (2)	−0.0004 (2)	0.0006 (2)
Si10	0.0119 (3)	0.0139 (3)	0.0144 (3)	−0.0002 (2)	0.0015 (2)	0.0009 (2)
Si11	0.0140 (3)	0.0118 (3)	0.0144 (3)	0.0001 (2)	−0.0005 (2)	0.0013 (2)
Si12	0.0126 (3)	0.0128 (3)	0.0137 (3)	−0.0009 (2)	−0.0018 (2)	0.0017 (2)
Si13	0.0178 (3)	0.0115 (3)	0.0137 (3)	−0.0009 (2)	0.0006 (2)	0.0015 (2)
Si14	0.0136 (3)	0.0138 (3)	0.0145 (3)	0.0001 (2)	−0.0007 (2)	0.0017 (2)
Si15	0.0123 (3)	0.0132 (3)	0.0152 (3)	−0.0002 (2)	−0.0013 (2)	0.0006 (2)
Si16	0.0119 (4)	0.0201 (4)	0.0133 (4)	0.0016 (3)	0	0
Si17	0.0196 (4)	0.0119 (4)	0.0134 (4)	0.0018 (3)	0	0
P1	0.0130 (2)	0.0123 (2)	0.0145 (2)	−0.00027 (19)	0.00018 (19)	−0.00056 (19)
P2	0.0145 (2)	0.0163 (3)	0.0144 (3)	−0.0016 (2)	−0.0016 (2)	0.0002 (2)
P3	0.0165 (3)	0.0162 (3)	0.0225 (3)	−0.0027 (2)	0.0032 (2)	−0.0060 (2)
P4	0.0130 (2)	0.0130 (2)	0.0146 (2)	−0.00002 (19)	−0.00054 (19)	0.00062 (19)
P5	0.0121 (2)	0.0169 (3)	0.0146 (3)	0.0000 (2)	−0.00100 (19)	−0.0016 (2)
P6	0.0130 (2)	0.0133 (2)	0.0139 (2)	0.00030 (19)	−0.00125 (19)	−0.00099 (19)
P7	0.0170 (3)	0.0175 (3)	0.0239 (3)	0.0038 (2)	−0.0066 (2)	−0.0057 (2)
P8	0.0172 (3)	0.0123 (2)	0.0132 (2)	0.0011 (2)	0.0010 (2)	0.00041 (19)
P9	0.0145 (3)	0.0425 (4)	0.0137 (3)	0.0058 (3)	0.0007 (2)	−0.0018 (3)
P10	0.0128 (2)	0.0134 (2)	0.0134 (2)	−0.00020 (19)	0.00014 (19)	−0.00022 (19)
P11	0.0161 (3)	0.0142 (2)	0.0149 (3)	0.0016 (2)	0.0002 (2)	0.0014 (2)
P12	0.0125 (2)	0.0175 (3)	0.0131 (2)	−0.0013 (2)	0.00052 (19)	−0.0010 (2)
P13	0.0134 (2)	0.0128 (2)	0.0132 (2)	0.00020 (19)	−0.00040 (19)	−0.00018 (19)
P14	0.0418 (4)	0.0143 (3)	0.0140 (3)	0.0054 (3)	−0.0017 (3)	0.0007 (2)
P15	0.0183 (3)	0.0153 (3)	0.0232 (3)	−0.0050 (2)	−0.0079 (2)	0.0063 (2)
P16	0.0130 (2)	0.0121 (2)	0.0135 (2)	−0.00039 (19)	−0.00125 (19)	0.00153 (19)
P17	0.0130 (2)	0.0133 (2)	0.0142 (2)	0.00003 (19)	0.00083 (19)	0.00052 (19)
P18	0.0163 (3)	0.0165 (3)	0.0229 (3)	−0.0028 (2)	0.0062 (2)	−0.0030 (2)
P19	0.0121 (2)	0.0132 (2)	0.0132 (2)	−0.00044 (19)	−0.00187 (19)	0.00136 (19)
P20	0.0166 (3)	0.0120 (2)	0.0147 (3)	−0.0002 (2)	0.0015 (2)	0.00097 (19)

P21	0.0134 (2)	0.0131 (2)	0.0140 (2)	−0.00039 (19)	−0.00103 (19)	0.00084 (19)
P22	0.0154 (3)	0.0181 (3)	0.0230 (3)	−0.0049 (2)	−0.0066 (2)	0.0076 (2)
P23	0.0122 (2)	0.0130 (2)	0.0145 (2)	0.00020 (19)	−0.00060 (19)	−0.00031 (19)
P24	0.0173 (3)	0.0171 (3)	0.0238 (3)	−0.0036 (2)	−0.0057 (2)	0.0063 (2)
K1	0.0762 (18)	0.103 (2)	0.116 (3)	−0.0385 (17)	−0.0327 (17)	0.090 (2)
K2	0.137 (8)	0.079 (5)	0.141 (8)	−0.044 (5)	0.115 (7)	−0.032 (5)
K3	0.102 (2)	0.0782 (18)	0.113 (2)	−0.0404 (17)	0.089 (2)	−0.0344 (18)
K4	0.117 (3)	0.123 (3)	0.138 (3)	−0.072 (2)	−0.082 (3)	0.110 (3)
K5	0.064 (4)	0.067 (4)	0.125 (7)	−0.038 (3)	−0.005 (4)	0.004 (4)
K6	0.0485 (13)	0.0471 (12)	0.0653 (15)	−0.0129 (9)	0.0423 (11)	−0.0179 (11)
K7	0.072 (2)	0.103 (3)	0.063 (2)	−0.062 (2)	0.0267 (16)	−0.0345 (19)
K8	0.109 (6)	0.029 (2)	0.206 (11)	−0.028 (3)	0.139 (8)	−0.033 (4)
K9	0.0437 (10)	0.0392 (9)	0.0894 (15)	−0.0076 (7)	0.0477 (10)	−0.0163 (9)
K10	0.149 (6)	0.152 (3)	0.243 (8)	−0.088 (4)	0.168 (6)	−0.132 (5)
K11	0.0635 (19)	0.0707 (19)	0.298 (7)	−0.0248 (16)	−0.031 (3)	0.007 (3)
K12	0.100 (3)	0.070 (2)	0.101 (3)	−0.053 (2)	−0.053 (2)	0.024 (2)
K13	0.109 (3)	0.078 (2)	0.0634 (19)	0.067 (2)	0.0371 (19)	0.0278 (16)
K14	0.073 (2)	0.107 (3)	0.105 (3)	0.059 (2)	0.027 (2)	0.056 (2)
K15	0.148 (3)	0.140 (6)	0.245 (8)	−0.082 (4)	0.131 (5)	−0.162 (6)
K16	0.086 (6)	0.162 (9)	0.186 (11)	−0.051 (6)	0.046 (6)	−0.147 (9)
K17	0.0502 (12)	0.0544 (14)	0.0741 (17)	−0.0147 (10)	0.0201 (11)	−0.0476 (13)
K18	0.036 (3)	0.100 (6)	0.185 (10)	−0.031 (3)	0.035 (4)	−0.120 (7)
K19	0.0392 (9)	0.0448 (10)	0.0918 (16)	−0.0081 (7)	0.0168 (9)	−0.0497 (10)
K20	0.110 (3)	0.110 (3)	0.124 (3)	−0.063 (2)	0.097 (3)	−0.072 (2)
K21	0.0715 (19)	0.0630 (19)	0.294 (7)	−0.0253 (16)	0.004 (3)	−0.027 (3)

Table C5 Fractional atomic coordinates, equivalent displacement parameters (Å^2) and occupancy factors of KSi_2P_3- *m*C928.

atom	Wyckoff	*x*	*y*	*z*	Ueq	Occ. (<1)
Si1	8f	0.01059 (3)	0.08657 (3)	0.12466 (4)	0.01386 (14)	
Si2	8f	0.02438 (3)	0.20656 (3)	0.12618 (4)	0.01322 (14)	
Si3	8f	0.10233 (3)	0.14729 (3)	0.49963 (4)	0.01295 (14)	
Si4	8f	0.10506 (3)	0.26526 (3)	0.49476 (4)	0.01428 (15)	
Si5	8f	0.12044 (3)	0.02307 (3)	0.25011 (4)	0.01345 (14)	
Si6	8f	0.12122 (3)	0.37501 (3)	0.49248 (4)	0.01509 (15)	
Si7	8f	0.12393 (3)	0.07676 (3)	0.12365 (4)	0.01288 (14)	
Si8	8f	0.13614 (3)	0.13901 (3)	0.24847 (4)	0.01235 (14)	
Si9	8f	0.13643 (3)	0.18935 (3)	0.12471 (4)	0.01237 (14)	
Si10	8f	0.14792 (3)	0.49521 (3)	0.24947 (4)	0.01353 (14)	
Si11	8f	0.14847 (3)	0.25478 (3)	0.25055 (4)	0.01348 (14)	
Si12	8f	0.14864 (3)	0.44801 (3)	0.12396 (4)	0.01392 (14)	

Si13	8f	0.23715 (3)	0.01178 (3)	0.25221 (4)	0.01226 (14)
Si14	8f	0.23828 (3)	0.06065 (3)	0.12467 (4)	0.01238 (14)
Si15	8f	0.24875 (3)	0.07406 (3)	0.37603 (4)	0.01247 (14)
Si16	8f	0.24976 (3)	0.17326 (3)	0.12365 (4)	0.01280 (14)
Si17	8f	0.26510 (3)	0.23824 (3)	0.25222 (4)	0.01245 (14)
Si18	8f	0.26536 (3)	0.18800 (3)	0.37708 (4)	0.01292 (14)
Si19	8f	0.26760 (3)	0.39226 (3)	0.00456 (4)	0.01411 (14)
Si20	8f	0.26922 (3)	0.46115 (3)	0.12545 (4)	0.01330 (14)
Si21	8f	0.27472 (3)	0.30198 (3)	0.37606 (4)	0.01400 (14)
Si22	8f	0.35179 (3)	0.04344 (3)	0.12612 (4)	0.01324 (14)
Si23	8f	0.35270 (3)	0.10271 (3)	0.00033 (4)	0.01294 (14)
Si24	8f	0.36027 (3)	0.01527 (3)	0.50518 (4)	0.01438 (15)
Si25	8f	0.36173 (3)	0.06201 (3)	0.37704 (4)	0.01282 (14)
Si26	8f	0.36236 (3)	0.11099 (3)	0.24850 (4)	0.01243 (14)
Si27	8f	0.36412 (3)	0.16344 (3)	0.12466 (4)	0.01384 (14)
Si28	8f	0.37728 (3)	0.17595 (3)	0.37597 (4)	0.01244 (14)
Si29	8f	0.37842 (3)	0.37498 (3)	0.00686 (4)	0.01496 (15)
Si30	8f	0.37971 (3)	0.22693 (3)	0.25012 (4)	0.01336 (14)
Si31	8f	0.39381 (3)	0.28885 (3)	0.37456 (4)	0.01329 (14)
Si32	8f	0.48691 (3)	0.35773 (3)	0.00452 (4)	0.01427 (15)
P1	8f	0.03099 (3)	0.02827 (3)	0.18682 (4)	0.01930 (15)
P2	8f	0.03229 (3)	0.07973 (3)	0.05445 (4)	0.01497 (14)
P3	8f	0.04549 (3)	0.14704 (2)	0.19048 (4)	0.01341 (13)
P4	8f	0.04657 (3)	0.20399 (3)	0.05552 (4)	0.01434 (13)
P5	8f	0.05946 (3)	0.26497 (3)	0.18963 (4)	0.01828 (15)
P6	8f	0.06791 (3)	0.20577 (2)	0.42927 (4)	0.01281 (13)
P7	8f	0.07346 (3)	0.26873 (2)	0.55486 (4)	0.01437 (13)
P8	8f	0.07845 (4)	0.31966 (3)	0.42477 (4)	0.02338 (18)
P9	8f	0.07888 (3)	0.08767 (3)	0.44013 (4)	0.01865 (15)
P10	8f	0.07908 (3)	0.14653 (2)	0.56998 (4)	0.01280 (13)
P11	8f	0.09628 (4)	0.43033 (3)	0.42477 (4)	0.02333 (18)
P12	8f	0.10673 (3)	0.50489 (2)	0.05379 (4)	0.01495 (14)
P13	8f	0.11747 (4)	0.39092 (3)	0.05920 (4)	0.01889 (15)
P14	8f	0.11985 (4)	0.48503 (3)	0.31045 (4)	0.01827 (15)
P15	8f	0.12153 (4)	0.43733 (3)	0.18618 (4)	0.01935 (15)
P16	8f	0.14496 (3)	0.01491 (2)	0.18250 (4)	0.01334 (13)
P17	8f	0.14615 (3)	0.06357 (3)	0.05536 (4)	0.01407 (13)
P18	8f	0.15788 (3)	0.08221 (2)	0.31708 (4)	0.01310 (13)
P19	8f	0.15922 (3)	0.18644 (3)	0.05537 (4)	0.01408 (13)
P20	8f	0.17049 (3)	0.13220 (2)	0.19288 (4)	0.01299 (13)
P21	8f	0.17405 (3)	0.25082 (2)	0.18358 (4)	0.01318 (13)
P22	8f	0.17417 (3)	0.19640 (2)	0.31820 (4)	0.01342 (13)
P23	8f	0.18538 (3)	0.31265 (3)	0.31383 (4)	0.01931 (15)

P24	8f	0.19167 (3)	0.14093 (3)	0.55918 (4)	0.01873 (15)	
P25	8f	0.24046 (3)	0.49917 (2)	0.31644 (4)	0.01304 (13)	
P26	8f	0.24088 (3)	0.39653 (2)	0.07003 (4)	0.01281 (13)	
P27	8f	0.24198 (3)	0.45005 (2)	0.18982 (4)	0.01328 (13)	
P28	8f	0.25895 (3)	0.04599 (3)	0.05550 (4)	0.01437 (13)	
P29	8f	0.26860 (3)	0.01870 (2)	0.44511 (4)	0.01446 (13)	
P30	8f	0.27172 (3)	0.07398 (2)	0.30776 (4)	0.01310 (13)	
P31	8f	0.27221 (3)	0.17027 (3)	0.05450 (4)	0.01497 (14)	
P32	8f	0.27243 (3)	0.11780 (2)	0.19289 (4)	0.01303 (13)	
P33	8f	0.28609 (3)	0.17602 (2)	0.30777 (4)	0.01310 (13)	
P34	8f	0.28633 (3)	0.13155 (2)	0.44530 (4)	0.01427 (13)	
P35	8f	0.28759 (3)	0.23508 (2)	0.18251 (4)	0.01349 (13)	
P36	8f	0.30217 (3)	0.29995 (2)	0.31017 (4)	0.01332 (13)	
P37	8f	0.30297 (3)	0.24510 (2)	0.44625 (4)	0.01493 (14)	
P38	8f	0.35696 (3)	0.38389 (3)	0.07458 (4)	0.02317 (18)	
P39	8f	0.35932 (3)	0.46447 (3)	0.18895 (4)	0.01838 (15)	
P40	8f	0.38865 (3)	0.04425 (2)	0.07067 (4)	0.01267 (13)	
P41	8f	0.38875 (4)	0.16234 (3)	0.05984 (4)	0.01876 (15)	
P42	8f	0.39406 (3)	0.05361 (2)	0.31818 (4)	0.01334 (13)	
P43	8f	0.39503 (3)	0.10297 (2)	0.19049 (4)	0.01341 (13)	
P44	8f	0.40587 (4)	0.22172 (3)	0.18682 (4)	0.01915 (15)	
P45	8f	0.40924 (3)	0.16779 (2)	0.31705 (4)	0.01304 (13)	
P46	8f	0.42037 (3)	0.28552 (3)	0.31104 (4)	0.01847 (15)	
P47	8f	0.46757 (3)	0.36610 (3)	0.07458 (4)	0.02309 (18)	
P48	8f	0.59099 (3)	0.11846 (2)	0.05470 (4)	0.01410 (13)	
K1	8f	0.00400 (11)	0.48393 (13)	0.1022 (2)	0.1009 (17)	0.4651 (13)
K2	8f	0.00821 (12)	0.45226 (17)	0.0528 (3)	0.132 (3)	0.4651 (13)
K3	8f	0.0348 (2)	0.04687 (15)	0.6016 (2)	0.0987 (16)	0.4651 (13)
K4	8f	0.03536 (14)	0.09404 (8)	0.28768 (16)	0.0602 (8)	0.4651 (13)
K5	8f	0.03740 (8)	0.33105 (12)	0.07673 (15)	0.1671 (19)	0.889 (3)
K6	8f	0.0477 (3)	0.37071 (16)	0.2044 (5)	0.154 (3)	0.4651 (13)
K7	8f	0.0504 (4)	0.2998 (3)	−0.0002 (6)	0.088 (3)	0.180 (2)
K8	8f	0.0798 (15)	0.0219 (12)	0.534 (2)	1.25 (4)	0.778 (5)
K9	8f	0.0935 (3)	0.37923 (16)	0.2960 (5)	0.155 (3)	0.4651 (13)
K10	8f	0.1088 (7)	0.1461 (2)	0.3666 (8)	0.111 (5)	0.180 (2)
K11	8f	0.14408 (14)	0.05317 (10)	0.58778 (18)	0.0575 (8)	0.4651 (13)
K12	8f	0.1517 (2)	0.26613 (13)	0.3977 (2)	0.1011 (16)	0.4651 (13)
K13	8f	0.15285 (16)	0.14977 (11)	0.41214 (18)	0.0589 (9)	0.4651 (13)
K14	8f	0.19353 (11)	0.30305 (10)	0.08763 (17)	0.0574 (8)	0.4651 (13)
K15	8f	0.1998 (4)	0.0499 (3)	0.4998 (6)	0.089 (3)	0.180 (2)
K16	8f	0.20003 (10)	0.35828 (8)	0.21193 (16)	0.0594 (8)	0.4651 (13)
K17	8f	0.2056 (3)	0.29772 (17)	0.4472 (3)	0.129 (2)	0.4651 (13)
K18	8f	0.2101 (7)	0.1921 (4)	0.4667 (7)	0.127 (6)	0.180 (2)

K19	8f	0.2095 (4)	0.2738 (4)	0.0338 (6)	0.108 (5)	0.180 (2)
K20	8f	0.21050 (14)	0.41881 (12)	0.42323 (15)	0.1666 (18)	0.889 (3)
K21	8f	0.2136 (4)	0.3258 (4)	0.1362 (8)	0.108 (5)	0.180 (2)
K22	8f	0.23815 (12)	0.39179 (8)	0.28818 (16)	0.0584 (8)	0.4651 (13)
K23	8f	0.31688 (14)	0.29675 (15)	0.1016 (2)	0.0995 (16)	0.4651 (13)
K24	8f	0.32425 (14)	0.26794 (16)	0.0523 (3)	0.122 (2)	0.4651 (13)
K25	8f	0.3278 (5)	0.4242 (4)	0.3638 (8)	0.105 (5)	0.180 (2)
K26	8f	0.35392 (18)	0.37509 (13)	0.2502 (3)	0.214 (3)	0.778 (5)
K27	8f	0.36922 (18)	0.49889 (9)	0.07631 (15)	0.1726 (19)	0.889 (3)
K28	8f	0.45716 (9)	0.25098 (9)	0.07616 (15)	0.1722 (19)	0.889 (3)
K29	8f	0.4730 (3)	0.44538 (15)	0.2048 (4)	0.148 (3)	0.4651 (13)
K30	8f	0.4791 (3)	0.48160 (17)	0.0533 (3)	0.126 (2)	0.4651 (13)
K31	8f	0.4819 (2)	0.30457 (15)	0.2049 (4)	0.145 (3)	0.4651 (13)
K32	8f	0.49076 (10)	0.10036 (10)	0.08816 (17)	0.0579 (8)	0.4651 (13)
K33	8f	0.4921 (3)	0.1041 (2)	0.1348 (8)	0.107 (5)	0.180 (2)
K34	8f	0.4930 (3)	0.0582 (4)	0.0339 (8)	0.135 (7)	0.180 (2)
K35	8f	0.49767 (8)	0.15602 (8)	0.21243 (16)	0.0602 (8)	0.4651 (13)
K36	4e	0	0.22907 (15)	¼	0.199 (3)	0.778 (5)
K37	4e	0	0.52111 (15)	¼	0.199 (4)	0.778 (5)

Table C6 Atomic displacement parameters (Å^2) of KSi_2P_3- *mC*928.

atom	U^{11}	U^{22}	U^{33}	U^{12}	U^{13}	U^{23}
Si1	0.0122 (3)	0.0135 (3)	0.0144 (3)	0.0005 (3)	0.0074 (3)	0.0008 (3)
Si2	0.0111 (3)	0.0139 (3)	0.0142 (3)	0.0003 (3)	0.0076 (3)	0.0006 (3)
Si3	0.0114 (3)	0.0126 (3)	0.0133 (3)	−0.0005 (3)	0.0068 (3)	−0.0018 (3)
Si4	0.0155 (3)	0.0119 (3)	0.0132 (3)	−0.0014 (3)	0.0077 (3)	−0.0016 (3)
Si5	0.0131 (3)	0.0123 (3)	0.0153 (4)	0.0006 (3)	0.0089 (3)	0.0012 (3)
Si6	0.0175 (4)	0.0118 (3)	0.0132 (3)	−0.0013 (3)	0.0080 (3)	0.0000 (3)
Si7	0.0127 (3)	0.0134 (3)	0.0133 (3)	0.0011 (3)	0.0084 (3)	0.0005 (3)
Si8	0.0118 (3)	0.0120 (3)	0.0128 (3)	0.0002 (3)	0.0073 (3)	0.0003 (3)
Si9	0.0115 (3)	0.0134 (3)	0.0126 (3)	0.0002 (3)	0.0076 (3)	0.0000 (3)
Si10	0.0145 (3)	0.0132 (3)	0.0154 (4)	−0.0009 (3)	0.0104 (3)	−0.0010 (3)
Si11	0.0123 (3)	0.0131 (3)	0.0153 (4)	−0.0002 (3)	0.0086 (3)	−0.0008 (3)
Si12	0.0145 (3)	0.0135 (3)	0.0149 (4)	−0.0010 (3)	0.0096 (3)	−0.0018 (3)
Si13	0.0124 (3)	0.0126 (3)	0.0123 (3)	0.0003 (3)	0.0079 (3)	0.0006 (3)
Si14	0.0121 (3)	0.0132 (3)	0.0127 (3)	−0.0001 (3)	0.0081 (3)	−0.0001 (3)
Si15	0.0131 (3)	0.0113 (3)	0.0126 (3)	0.0001 (3)	0.0077 (3)	0.0003 (3)
Si16	0.0123 (3)	0.0136 (3)	0.0129 (3)	0.0005 (3)	0.0080 (3)	−0.0004 (3)
Si17	0.0117 (3)	0.0129 (3)	0.0124 (3)	−0.0004 (3)	0.0072 (3)	−0.0007 (3)
Si18	0.0129 (3)	0.0121 (3)	0.0131 (3)	−0.0006 (3)	0.0076 (3)	0.0001 (3)
Si19	0.0135 (3)	0.0178 (4)	0.0134 (3)	0.0003 (3)	0.0095 (3)	−0.0006 (3)

Si20	0.0149 (3)	0.0117 (3)	0.0144 (3)	−0.0007 (3)	0.0095 (3)	−0.0013 (3)
Si21	0.0136 (3)	0.0136 (3)	0.0147 (4)	−0.0013 (3)	0.0087 (3)	−0.0020 (3)
Si22	0.0139 (3)	0.0136 (3)	0.0144 (3)	−0.0002 (3)	0.0099 (3)	−0.0006 (3)
Si23	0.0145 (3)	0.0126 (3)	0.0135 (3)	−0.0018 (3)	0.0095 (3)	−0.0019 (3)
Si24	0.0171 (4)	0.0115 (3)	0.0134 (3)	0.0004 (3)	0.0088 (3)	0.0017 (3)
Si25	0.0134 (3)	0.0120 (3)	0.0131 (3)	−0.0007 (3)	0.0082 (3)	−0.0001 (3)
Si26	0.0135 (3)	0.0118 (3)	0.0128 (3)	−0.0002 (3)	0.0084 (3)	−0.0004 (3)
Si27	0.0155 (3)	0.0135 (3)	0.0142 (3)	−0.0004 (3)	0.0099 (3)	−0.0008 (3)
Si28	0.0131 (3)	0.0115 (3)	0.0124 (3)	−0.0003 (3)	0.0077 (3)	−0.0004 (3)
Si29	0.0124 (3)	0.0196 (4)	0.0134 (3)	0.0015 (3)	0.0082 (3)	0.0001 (3)
Si30	0.0144 (3)	0.0121 (3)	0.0150 (4)	−0.0009 (3)	0.0097 (3)	−0.0012 (3)
Si31	0.0129 (3)	0.0120 (3)	0.0144 (3)	−0.0011 (3)	0.0081 (3)	−0.0016 (3)
Si32	0.0108 (3)	0.0176 (4)	0.0136 (3)	0.0012 (3)	0.0071 (3)	0.0007 (3)
P1	0.0133 (3)	0.0173 (4)	0.0236 (4)	0.0006 (3)	0.0094 (3)	0.0055 (3)
P2	0.0131 (3)	0.0160 (3)	0.0146 (3)	0.0011 (3)	0.0079 (3)	−0.0001 (3)
P3	0.0126 (3)	0.0133 (3)	0.0140 (3)	0.0002 (2)	0.0080 (3)	0.0009 (2)
P4	0.0119 (3)	0.0166 (3)	0.0146 (3)	0.0011 (2)	0.0082 (3)	0.0016 (3)
P5	0.0123 (3)	0.0164 (3)	0.0225 (4)	0.0003 (3)	0.0088 (3)	−0.0031 (3)
P6	0.0119 (3)	0.0121 (3)	0.0131 (3)	−0.0009 (2)	0.0070 (3)	−0.0018 (2)
P7	0.0141 (3)	0.0119 (3)	0.0143 (3)	−0.0006 (2)	0.0073 (3)	−0.0009 (2)
P8	0.0297 (4)	0.0144 (4)	0.0135 (4)	−0.0050 (3)	0.0069 (3)	−0.0006 (3)
P9	0.0121 (3)	0.0153 (3)	0.0228 (4)	−0.0003 (3)	0.0079 (3)	−0.0066 (3)
P10	0.0110 (3)	0.0131 (3)	0.0134 (3)	−0.0003 (2)	0.0070 (3)	−0.0010 (2)
P11	0.0331 (5)	0.0144 (4)	0.0135 (3)	−0.0044 (3)	0.0097 (3)	0.0006 (3)
P12	0.0154 (3)	0.0144 (3)	0.0142 (3)	0.0003 (3)	0.0086 (3)	−0.0015 (3)
P13	0.0245 (4)	0.0181 (4)	0.0232 (4)	−0.0088 (3)	0.0193 (3)	−0.0079 (3)
P14	0.0241 (4)	0.0164 (3)	0.0224 (4)	−0.0037 (3)	0.0184 (3)	−0.0029 (3)
P15	0.0254 (4)	0.0169 (3)	0.0237 (4)	−0.0070 (3)	0.0191 (3)	−0.0066 (3)
P16	0.0129 (3)	0.0128 (3)	0.0141 (3)	0.0003 (2)	0.0082 (3)	0.0005 (2)
P17	0.0122 (3)	0.0170 (3)	0.0130 (3)	0.0001 (3)	0.0078 (3)	−0.0011 (3)
P18	0.0138 (3)	0.0120 (3)	0.0145 (3)	0.0005 (2)	0.0092 (3)	0.0006 (2)
P19	0.0130 (3)	0.0170 (3)	0.0130 (3)	0.0015 (3)	0.0083 (3)	0.0009 (3)
P20	0.0129 (3)	0.0133 (3)	0.0131 (3)	0.0006 (2)	0.0081 (3)	0.0005 (2)
P21	0.0125 (3)	0.0129 (3)	0.0144 (3)	−0.0002 (2)	0.0085 (3)	0.0001 (2)
P22	0.0131 (3)	0.0130 (3)	0.0142 (3)	−0.0005 (2)	0.0084 (3)	−0.0009 (2)
P23	0.0144 (3)	0.0170 (3)	0.0237 (4)	−0.0010 (3)	0.0102 (3)	−0.0066 (3)
P24	0.0122 (3)	0.0179 (4)	0.0231 (4)	−0.0010 (3)	0.0094 (3)	−0.0079 (3)
P25	0.0133 (3)	0.0129 (3)	0.0143 (3)	0.0002 (2)	0.0092 (3)	0.0001 (2)
P26	0.0140 (3)	0.0129 (3)	0.0136 (3)	−0.0012 (2)	0.0095 (3)	−0.0014 (2)
P27	0.0142 (3)	0.0130 (3)	0.0137 (3)	−0.0009 (2)	0.0090 (3)	−0.0012 (2)
P28	0.0139 (3)	0.0165 (3)	0.0148 (3)	−0.0006 (3)	0.0098 (3)	−0.0015 (3)
P29	0.0177 (3)	0.0117 (3)	0.0147 (3)	0.0006 (3)	0.0103 (3)	0.0010 (2)
P30	0.0135 (3)	0.0128 (3)	0.0134 (3)	−0.0004 (2)	0.0084 (3)	−0.0002 (2)

P31	0.0159 (3)	0.0158 (3)	0.0148 (3)	0.0013 (3)	0.0102 (3)	0.0001 (3)
P32	0.0127 (3)	0.0131 (3)	0.0132 (3)	−0.0001 (2)	0.0079 (3)	−0.0004 (2)
P33	0.0131 (3)	0.0125 (3)	0.0135 (3)	−0.0002 (2)	0.0081 (3)	0.0001 (2)
P34	0.0167 (3)	0.0126 (3)	0.0128 (3)	−0.0013 (3)	0.0088 (3)	−0.0006 (2)
P35	0.0140 (3)	0.0131 (3)	0.0144 (3)	−0.0004 (2)	0.0093 (3)	−0.0005 (2)
P36	0.0126 (3)	0.0127 (3)	0.0138 (3)	−0.0005 (2)	0.0077 (3)	−0.0012 (2)
P37	0.0157 (3)	0.0145 (3)	0.0144 (3)	−0.0024 (3)	0.0091 (3)	−0.0017 (3)
P38	0.0145 (3)	0.0417 (5)	0.0138 (3)	0.0033 (3)	0.0090 (3)	−0.0017 (3)
P39	0.0160 (3)	0.0162 (3)	0.0227 (4)	−0.0017 (3)	0.0117 (3)	−0.0062 (3)
P40	0.0144 (3)	0.0118 (3)	0.0133 (3)	−0.0016 (2)	0.0093 (3)	−0.0019 (2)
P41	0.0270 (4)	0.0154 (3)	0.0230 (4)	−0.0079 (3)	0.0200 (3)	−0.0065 (3)
P42	0.0139 (3)	0.0128 (3)	0.0140 (3)	0.0005 (2)	0.0089 (3)	0.0008 (2)
P43	0.0142 (3)	0.0133 (3)	0.0139 (3)	−0.0009 (2)	0.0092 (3)	−0.0010 (2)
P44	0.0254 (4)	0.0170 (4)	0.0233 (4)	−0.0065 (3)	0.0192 (3)	−0.0055 (3)
P45	0.0131 (3)	0.0119 (3)	0.0143 (3)	−0.0001 (2)	0.0085 (3)	−0.0006 (2)
P46	0.0218 (4)	0.0159 (3)	0.0230 (4)	−0.0060 (3)	0.0165 (3)	−0.0062 (3)
P47	0.0134 (3)	0.0414 (5)	0.0137 (3)	0.0053 (3)	0.0080 (3)	0.0017 (3)
P48	0.0147 (3)	0.0122 (3)	0.0129 (3)	0.0009 (2)	0.0072 (3)	−0.0004 (2)
K1	0.0221 (11)	0.078 (2)	0.119 (3)	−0.0107 (13)	0.0011 (15)	0.032 (2)
K2	0.0230 (12)	0.122 (4)	0.147 (4)	−0.0064 (17)	−0.0007 (18)	0.087 (3)
K3	0.122 (3)	0.104 (3)	0.114 (3)	0.084 (3)	0.095 (3)	0.087 (3)
K4	0.113 (2)	0.0407 (12)	0.093 (2)	0.0177 (13)	0.097 (2)	0.0178 (12)
K5	0.0533 (11)	0.227 (3)	0.141 (2)	−0.0290 (15)	0.0193 (12)	0.133 (2)
K6	0.155 (5)	0.067 (3)	0.323 (10)	0.001 (3)	0.189 (7)	0.035 (4)
K7	0.100 (7)	0.066 (5)	0.128 (9)	−0.040 (5)	0.086 (7)	−0.011 (5)
K8	1.02 (7)	1.16 (8)	1.74 (11)	−0.16 (6)	0.93 (8)	−0.36 (8)
K9	0.177 (6)	0.068 (3)	0.327 (10)	0.043 (3)	0.209 (7)	0.036 (4)
K10	0.268 (15)	0.030 (3)	0.198 (11)	0.042 (6)	0.226 (12)	0.033 (6)
K11	0.0756 (19)	0.0529 (16)	0.0699 (18)	0.0382 (14)	0.0577 (17)	0.0451 (14)
K12	0.200 (5)	0.078 (2)	0.119 (3)	0.051 (3)	0.145 (4)	0.033 (2)
K13	0.104 (2)	0.0518 (15)	0.0717 (19)	0.0235 (17)	0.080 (2)	0.0204 (14)
K14	0.0390 (13)	0.0525 (16)	0.0711 (18)	0.0169 (11)	0.0290 (13)	0.0452 (14)
K15	0.086 (6)	0.066 (5)	0.135 (9)	0.030 (5)	0.077 (7)	−0.004 (5)
K16	0.0437 (12)	0.0450 (13)	0.092 (2)	0.0236 (10)	0.0433 (14)	0.0487 (14)
K17	0.237 (6)	0.122 (4)	0.140 (4)	0.108 (4)	0.173 (5)	0.082 (3)
K18	0.263 (17)	0.084 (7)	0.156 (11)	0.059 (9)	0.191 (13)	0.040 (7)
K19	0.071 (6)	0.121 (9)	0.125 (9)	0.029 (6)	0.056 (6)	0.098 (8)
K20	0.216 (3)	0.228 (3)	0.142 (2)	0.192 (3)	0.154 (2)	0.134 (2)
K21	0.060 (5)	0.102 (7)	0.191 (12)	0.056 (5)	0.091 (7)	0.127 (9)
K22	0.0751 (17)	0.0441 (12)	0.091 (2)	0.0344 (12)	0.0686 (17)	0.0471 (13)
K23	0.0601 (19)	0.104 (3)	0.117 (3)	0.0241 (19)	0.046 (2)	0.090 (3)
K24	0.0500 (18)	0.116 (3)	0.132 (4)	0.010 (2)	0.022 (2)	0.100 (3)
K25	0.112 (8)	0.102 (7)	0.182 (12)	0.092 (7)	0.131 (9)	0.122 (8)

K26	0.199 (4)	0.178 (3)	0.363 (6)	0.143 (3)	0.223 (5)	0.232 (4)
K27	0.340 (5)	0.133 (2)	0.149 (2)	−0.168 (3)	0.204 (3)	−0.0889 (18)
K28	0.0656 (12)	0.135 (2)	0.148 (2)	−0.0593 (14)	−0.0194 (13)	0.0890 (19)
K29	0.188 (6)	0.074 (3)	0.304 (9)	−0.024 (3)	0.212 (7)	−0.006 (3)
K30	0.202 (6)	0.119 (3)	0.139 (4)	−0.119 (4)	0.147 (4)	−0.106 (3)
K31	0.124 (5)	0.071 (3)	0.299 (9)	−0.018 (2)	0.159 (6)	0.004 (3)
K32	0.0154 (9)	0.0486 (15)	0.0725 (19)	0.0004 (8)	0.0082 (11)	0.0192 (14)
K33	0.016 (3)	0.032 (3)	0.190 (13)	−0.003 (2)	0.021 (5)	0.029 (6)
K34	0.030 (4)	0.091 (8)	0.164 (12)	−0.016 (4)	−0.002 (5)	0.047 (8)
K35	0.0155 (8)	0.0404 (12)	0.094 (2)	0.0040 (8)	0.0178 (11)	0.0172 (12)
K36	0.435 (9)	0.098 (3)	0.337 (7)	0	0.375 (8)	0
K37	0.0228 (12)	0.100 (3)	0.337 (8)	0	0.041 (3)	0

C.3 Powder Refinements of KSi_2P_3 Modifications

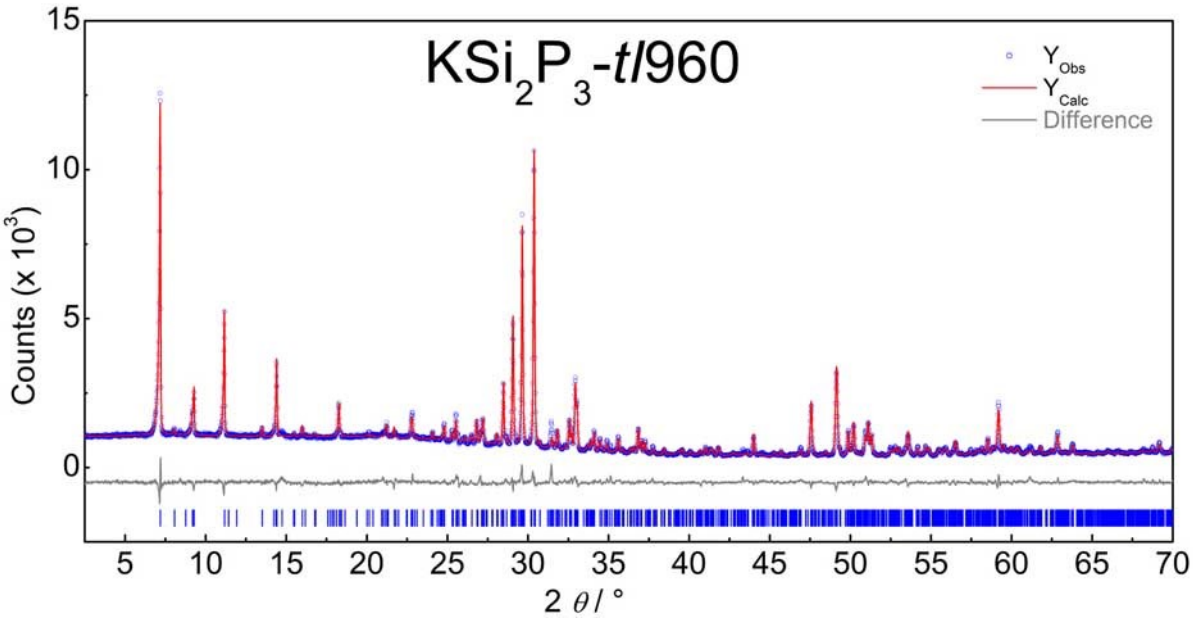

Figure C1 Cu-Kα_1 X-ray powder diffraction pattern of KSi_2P_3-*tl*960 (blue) with Rietveld fit (red line) and difference plot (grey).

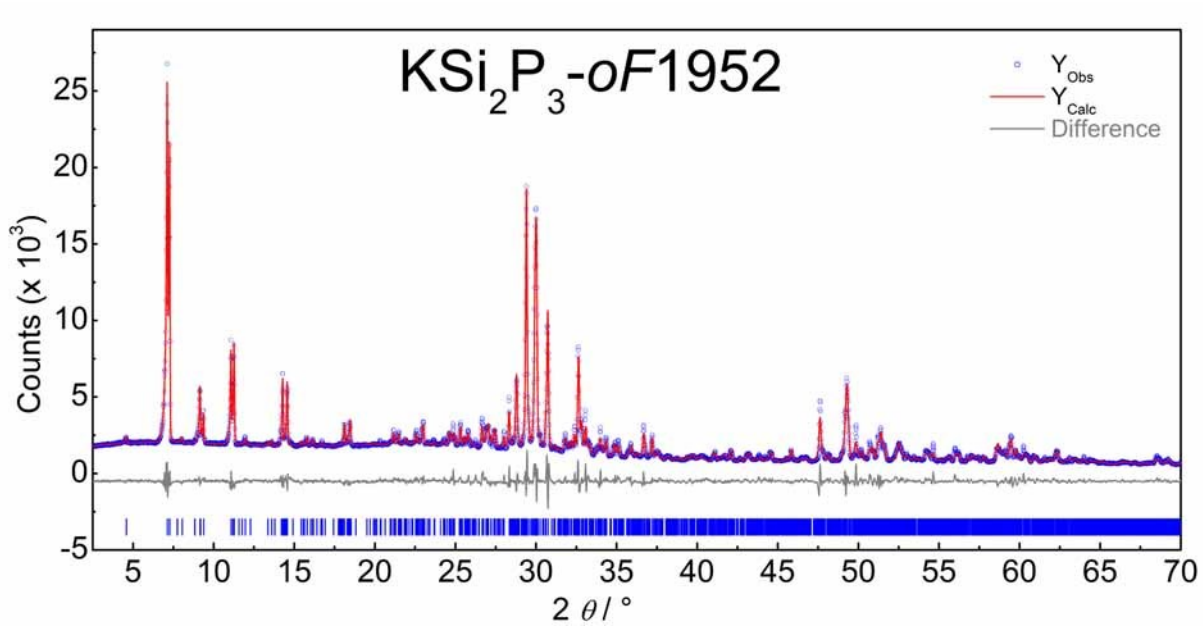

Figure C2 Cu-Kα$_1$ X-ray powder diffraction pattern of KSi_2P_3- *oF*1952 (blue) with Rietveld fit (red line) and difference plot (grey).

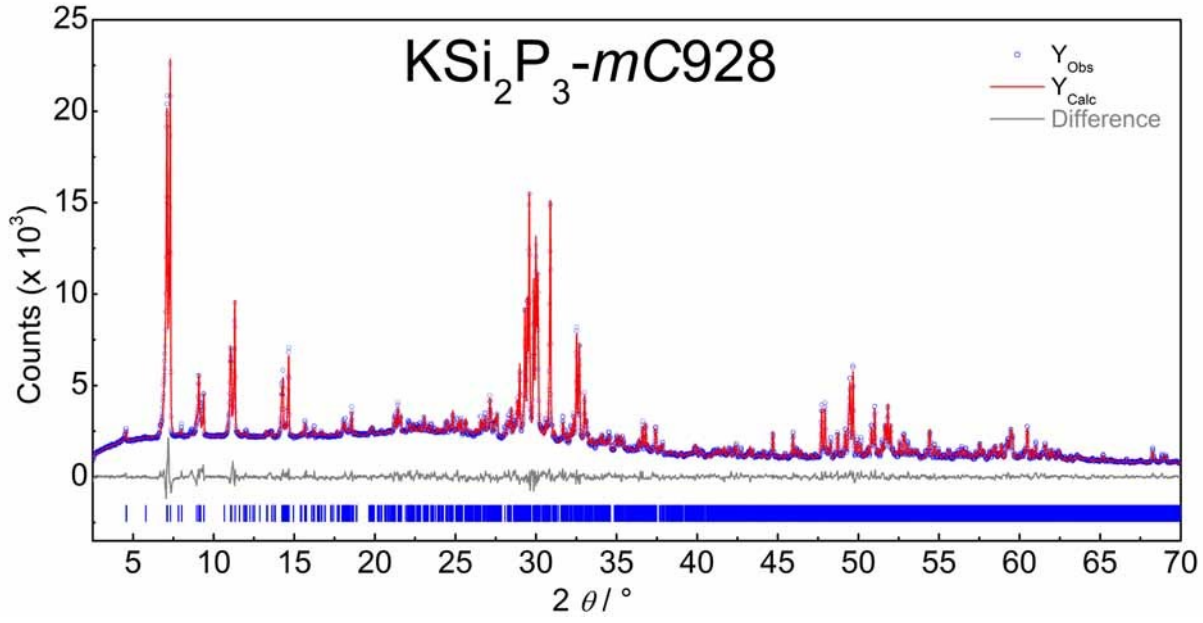

Figure C3 Cu-Kα$_1$ X-ray powder diffraction pattern of KSi_2P_3- *mC*928 (blue) with Rietveld fit (red line) and difference plot (grey).

C.4 Elemental Analysis of monoclinic KSi_2P_3

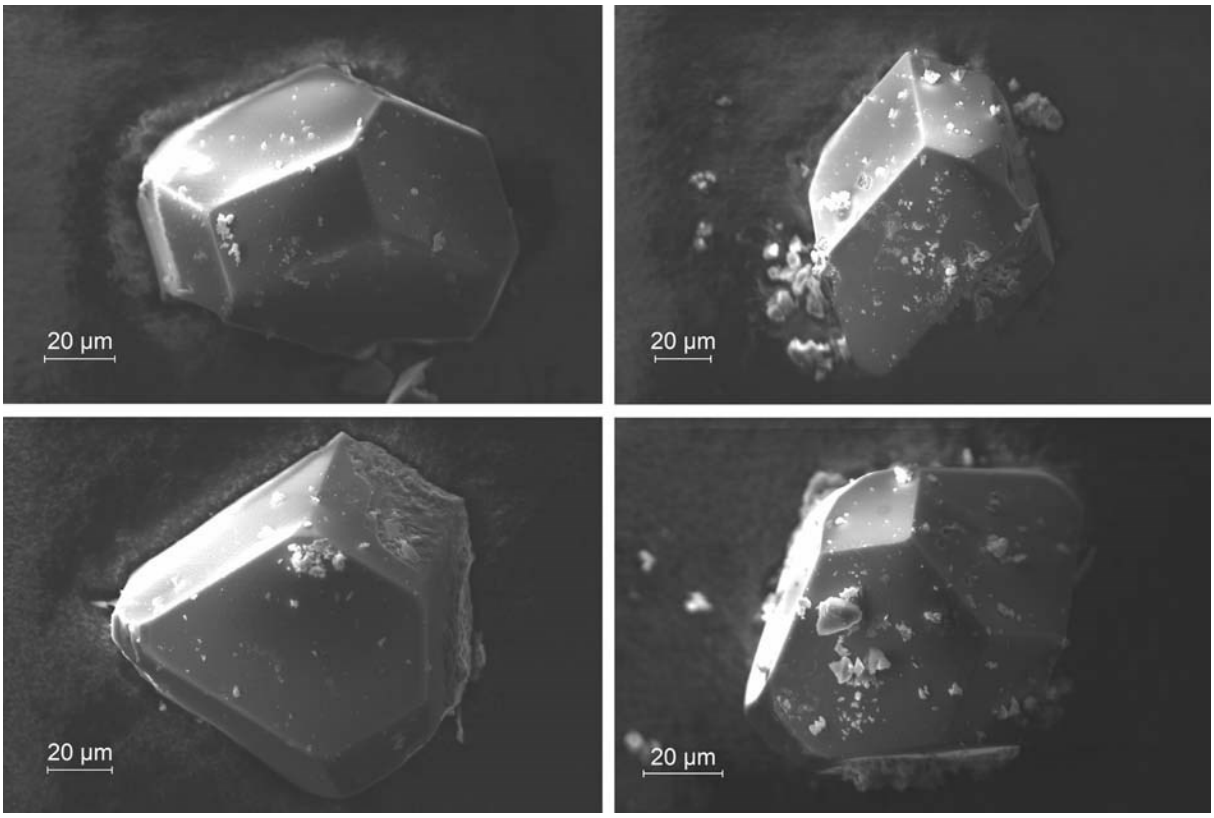

Figure C4 Representative scanning electron microscopic photographs of KSi_2P_3- *mC*928.

Table C7 Elemental analysis by EDX of KSi_2P_3-*mC*928, signals of oxygen were not taken into account due to hydrolysis.

	K	**Si**	**P**
EDX point 1 / atom-%	18.65	31.51	49.84
EDX point 2 / atom-%	17.23	31.86	50.91
EDX point 3 / atom-%	18.21	31.09	50.71
EDX point 4 / atom-%	15.82	33.82	50.36
EDX point 5 / atom-%	16.23	32.17	51.59
EDX point 6 / atom-%	18.83	31.19	49.98
EDX point 7 / atom-%	17.30	30.54	52.16
EDX point 8 / atom-%	16.98	30.98	52.04
EDX point 9 / atom-%	18.61	30.54	50.85
EDX point 10 / atom-%	19.08	30.06	50.87
EDX point 11 / atom-%	16.41	32.46	51.12
EDX point 12 / atom-%	17.38	32.08	50.54
EDX point 13 / atom-%	18.00	30.22	51.78
EDX point 14 / atom-%	17.96	32.50	49.54
Average / atom-%	**17.62**	**31.50**	**50.88**
Calculated / atom-%	**16.66**	**33.33**	**50.00**

C.5 ^{29}Si Solid-State MAS NMR of monoclinic KSi_2P_3

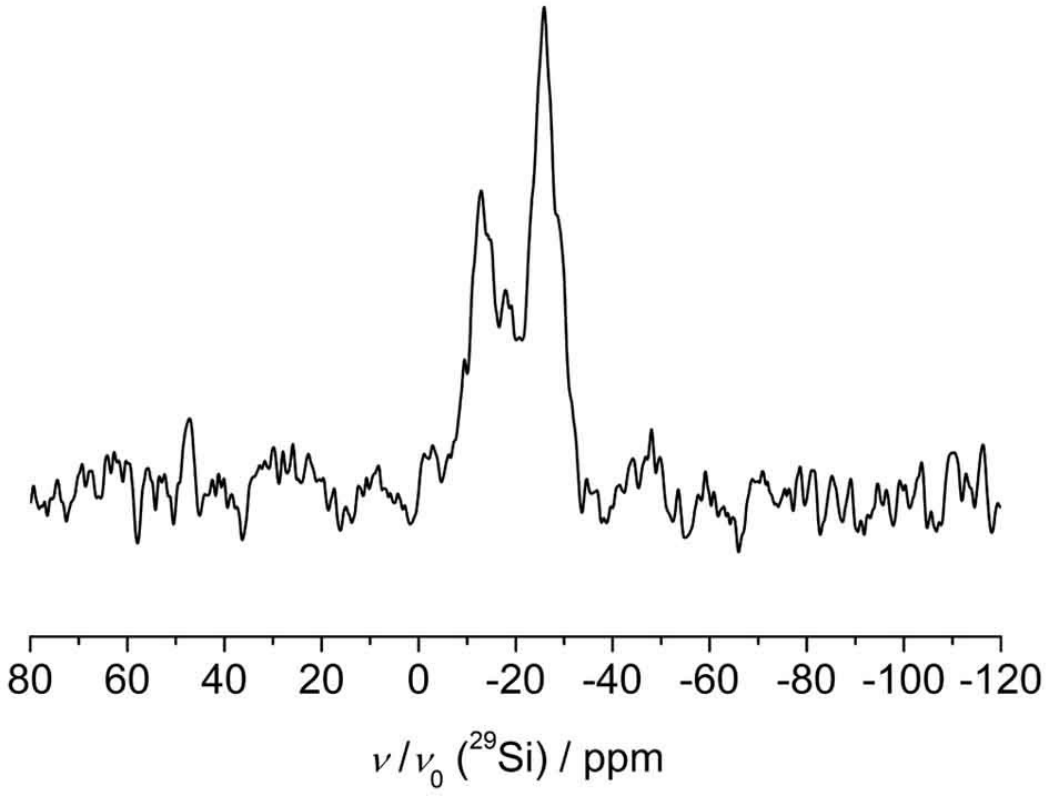

Figure C5 ^{29}Si-MAS-NMR spectrum of a KSi_2P_3-*m*C928 sample with a rotation frequency of 10 kHz acquired at a magnetic field of 11.7 T. Three very broad signals are visible at δ (^{29}Si) = -12.9, -17.9 and -25.9 ppm resulting from 32 crystallographically independent Si atoms on general Wyckoff sites. The chemical shift is comparable to known phosphidosilicates.

C.6 Geometrical Potassium Pathway Analysis

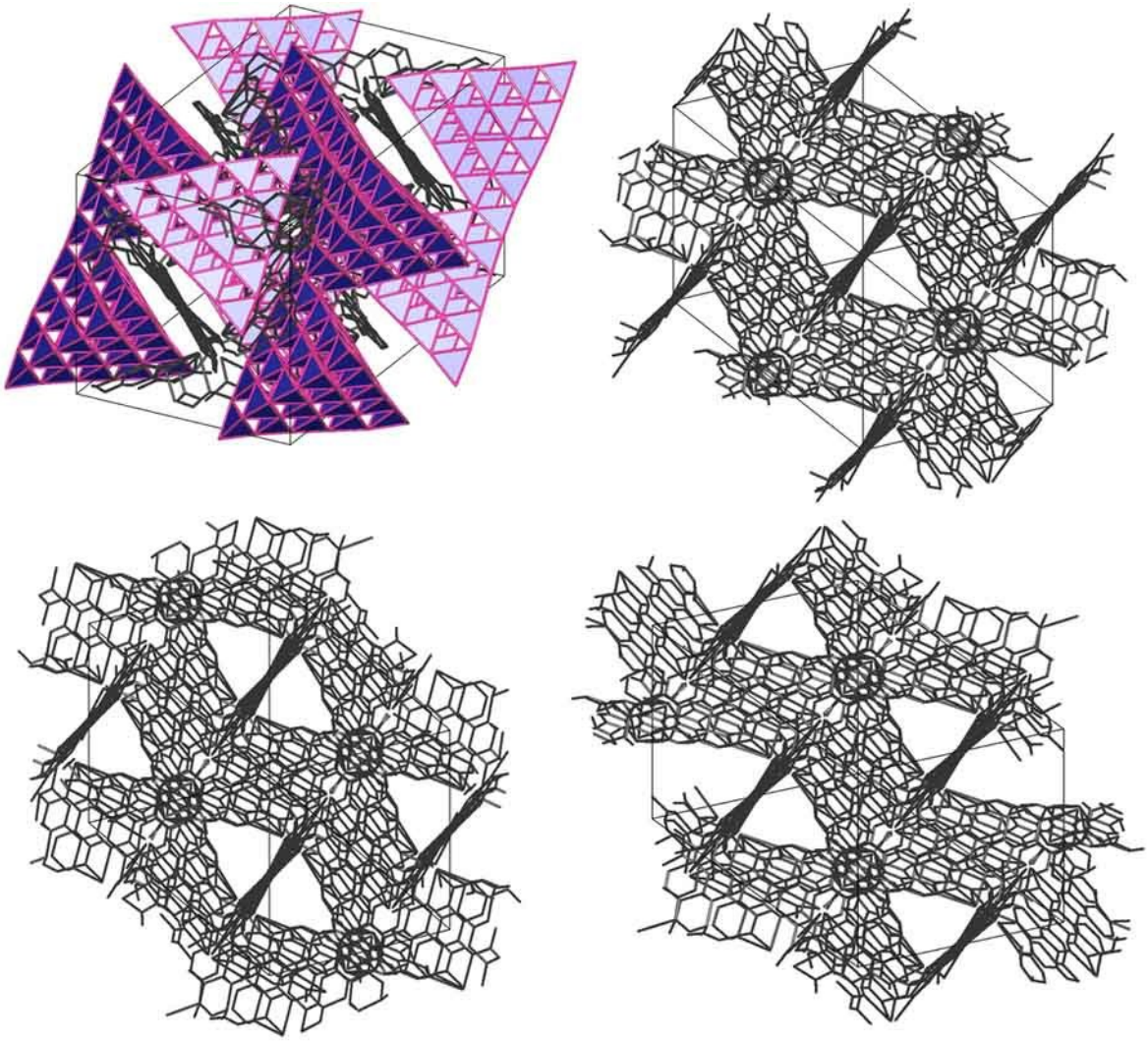

Figure C6 Geometrically calculated pathways for potassium ion migration in KSi_2P_3-*tI*960. Four main channels are formed along [111] (top, left), [-111] (top, right), [1-11] (bottom left) and [11-1] (bottom, right), which are connected by shorter passages along every supertetrahedral face resulting in an isotropic 3D ion conduction.

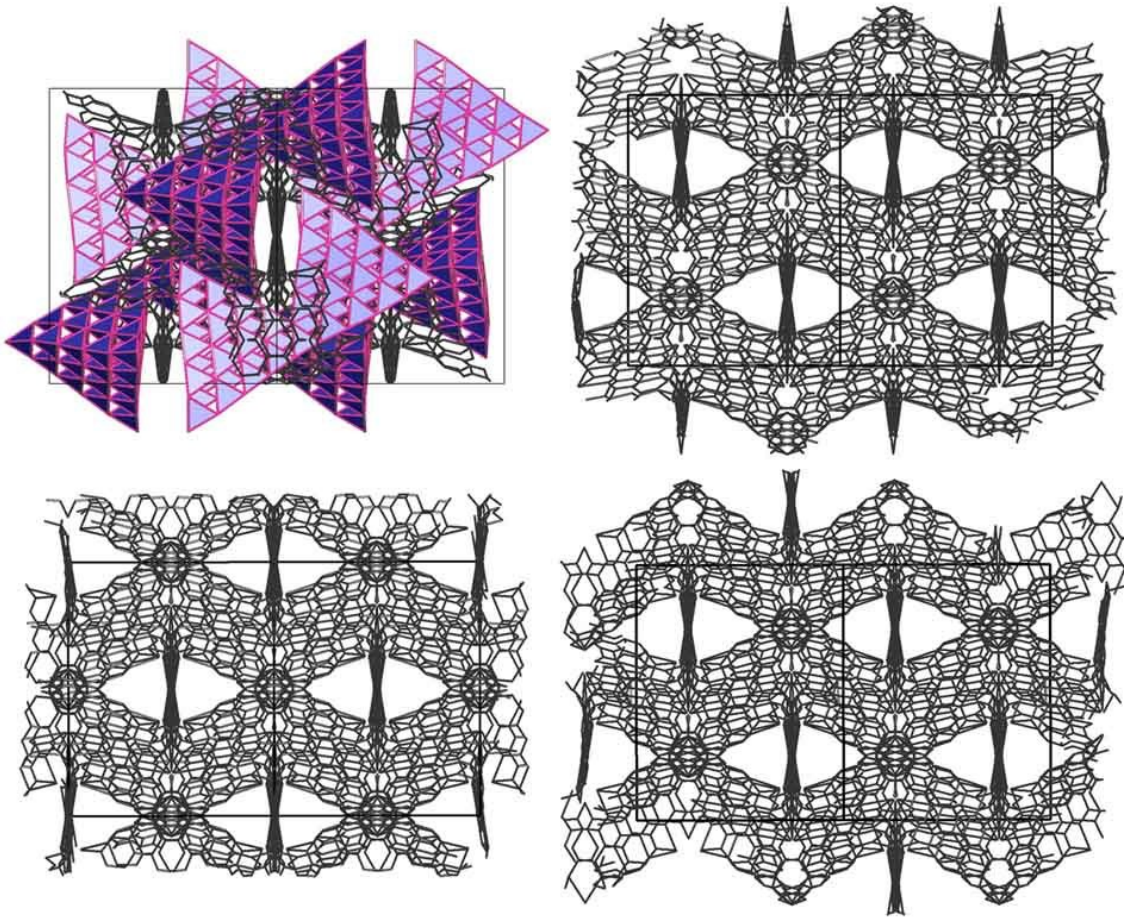

Figure C7 Geometrically calculated pathways for potassium ion migration in KSi_2P_3-*oF*1952. Four main channels are formed along [101] (top, left), [-101] (top, right), [011] (bottom left) and [0-11] (bottom, right), which are connected by shorter passages along every supertetrahedral face resulting in an isotropic 3D ion conduction.

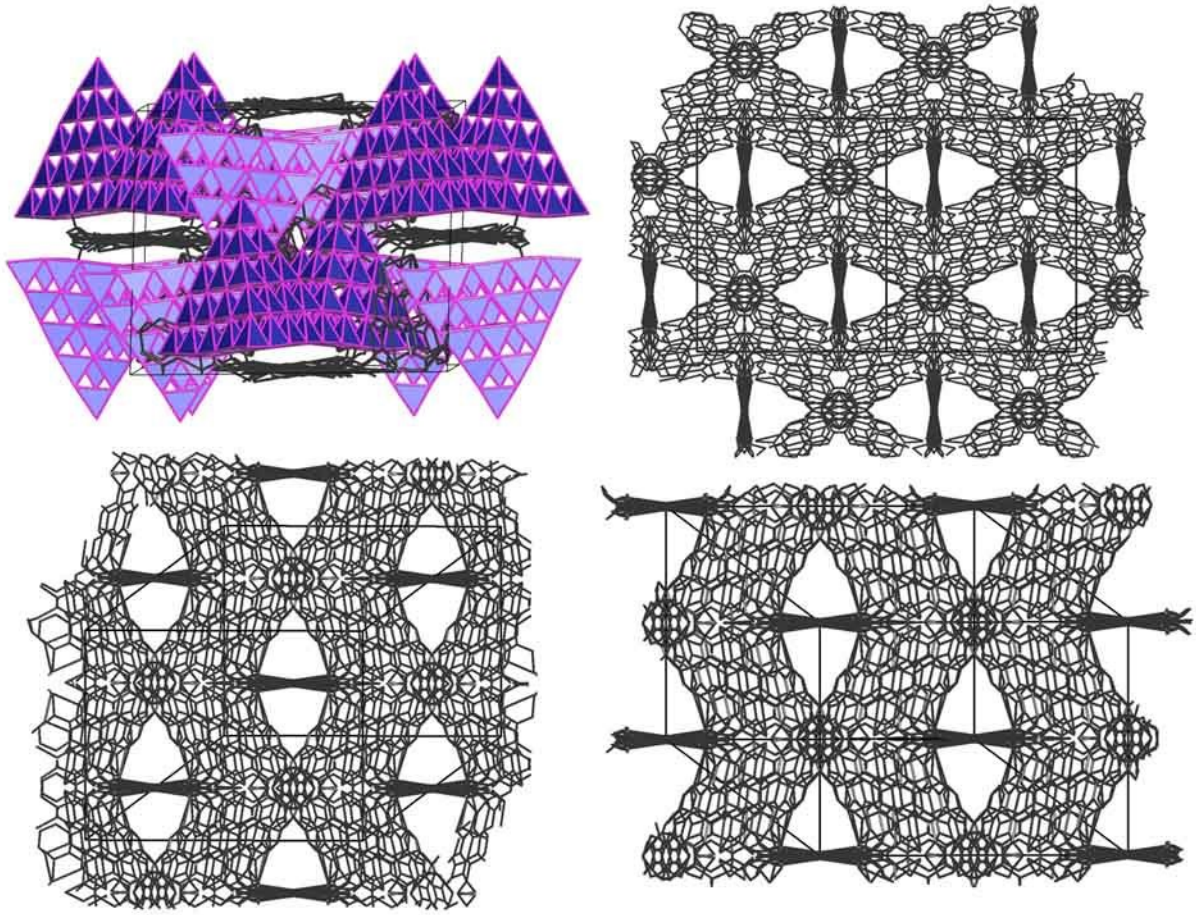

Figure C8 Geometrically calculated pathways for potassium ion migration in KSi_2P_3-*mC*928. Four main channels are formed along [001] (top, left), [101] (top, right), [112] (bottom left) and [1-12] (bottom, right), which are connected by shorter passages along every supertetrahedral face resulting in an isotropic 3D ion conduction.

C.7 Known Potassium Ion Conductors and Impedance Spectroscopy

Table C8 Ionic conductivity and activation energy of selected solid potassium ion conductors; a visualization is shown in Figure 5.1 main text.

Compound	T / °C	$\sigma(K^+)$ / Scm^{-1}	E_a / eV	Reference
KSi_2P_3	25	1x10^{-4}	0.20	*This work*
$K_2Fe_4O_7$	25	5x10^{-2}	0.08[*]	[1]
K-β-Alumina*	25	6.5x10^{-5}	0.29	[1-2]
$KFeO_2$	300	3x10^{-4}	-	[3]
$K_{0.7}Cd_{0.15}FeO_2$	300	2x10^{-3}	0.24	[3]
$K_{0.4}Cd_{0.3}FeO_2$	300	2.5x10^{-2}	0.24	[3]
$KGaO_2$	400	1x10-4	0.47	[3-4]
$K_{0.89}Pb_{0.1}GaO_2$	400	1x10^{-3}	0.47	[4-5]
$K_{0.7}Sr_{0.15}GaO_2$	400	1x10^{-2}	0.23	[4-5]
$KAlO_2$	400	1x10^{-3}	-	[4, 6]
$K_{1.90}Pb_{0.05}AlO_2$	400	2.5x10^{-3}	0.29	[6]
$K_{1.90}Ba_{0.05}AlO_2$	400	5.8x10^{-2}	0.23	[6]
γ-$K_{1.8}Al_{1.9}M_{0.1}O_4$ (M =Ta, Nb)	300	5-8x10^{-3}	0.23-0.26	[6-7]
$K_{1.8}Ga_{1.9}V_{0.1}O_4$	400	1x10^{-3}	0.47	[7-8]
$K_{1.8}Fe_{1.9}P_{0.1}O_4$	300	76x10^{-3}	0.35	[8-9]
$K_{1.8}Al_{1.9}P_{0.1}O_4$	200	5x10^{-3}	0.21	[9-10]
$K_{0.9}Al_{0.9}Ti_{0.1}O_2$	400	4x10^{-3}	-	[10-11]
$K_xM_{x/2}Ti_{8-x/2}O_{16}$ (M =Zn, Ni) x=1.6	300	1x10^{-4}	0.23	[11-12]
$K_{1.6}Mg_{0.8}Ti_{7.2}O_{16}$	300	1x10^{-4}	0.29	[12-13]
0.8 $La_2O_2SO_4$ −0.2 (0.8 K_2SO_4 −0.2 $CaSO_4$)	>800	1x10^{-2}	-	[13-14]
0.35 Gd_2O_3–0.3KNO_2	600	2x10^{-1}	-	[14-15]
$K_3Sb_4BO_{13}$	300	3x10^{-5}	0.33	[15-17]
K_2SbPO_6	400	4x10^{-6}	0.82	[16, 18]
$K_3Sb_3P_2O_{14}$	400	6x10^{-6}	0.59	[16, 18]
$K_5Sb_5P_2O_{20}$	300	2x10^{-5}	0.52	[16, 18]

[#] Data extrapolated. [*] Data of single crystals.

Table C9 Results of electrochemical impedance spectroscopy and polarization measurements of KSi_2P_3-*m*C928 of three batches (1-3) of KSi_2P_3.

Sample	Relative pellet density / %	σ_{bulk} / Scm^{-1}	σ_{Tot} / Scm^{-1}	E_a (σ_{bulk}) / eV	E_a (σ_2) / eV	C_{eff1} / F	C_{eff2} / F	$\varepsilon = \frac{Cd}{\varepsilon_0 A}$
1a	79	1.3E-05	4.8E-06	0.23	0.34*	1.4E-10	3.3E-05	442
1b	81	2.7E-05	7.2E-06	0.21	0.19	9.9E-11	1.8E-05	381

1c	73	1.9E-05	4.5E-06	0.12	0.39*	2.4E-11	2.4E-05	92
2a	77	5.4E-05	1.1E-05	0.18	0.16	1.6E-11	2.0E-06	64
2b	72	4.5E-05	7.7E-06	0.22	0.19	7.8E-12	9.0E-07	24
2c	80	1.1E-04	1.8E-05	0.20	0.23	4.5E-11	1.0E-06	178
2d	80	2.5E-04	4.1E-05	0.22	0.16	5.8E-11	1.30E-06	211.52
3a	79	2.6E-04	1.4E-05	0.21	0.22	3.4E-11	4.20E-06	90.94
3b#	80	2.0E-04	2.0E-04	0.28	n.a.	3.0E-11	n.a.	92.15
Average	**78**	**1.1E-04**	**3.4E-05**	**0.20**	**0.19**			
St. dev.	**3**	**9.6E-05**	**6.0E-05**	**0.04**	**0.03**			

*Outlier not used for averaging #data fitted with R(1)CPE(1)-CPE(2) Model.

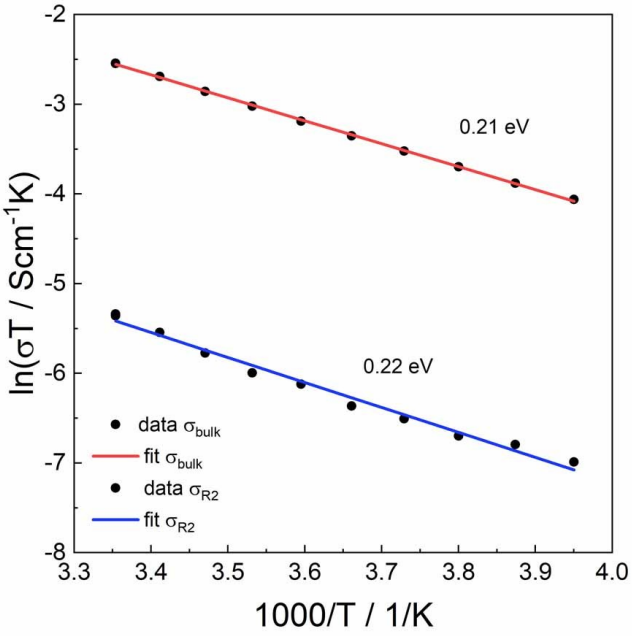

Figure C9 Plot of Arrhenius plot of sample 3a in Table C8 showing very similar activation energies of the high frequency process (bulk) and the low frequency process (R2).

C.8 References

[1] H. Yuan, H. Li, T. Zhang, G. Li, T. He, F. Du, S. Feng, *J. Mater. Chem. A* **2018**, *6*, 8413-8418.

[2] M. S. Whittingham, R. A. Huggins in *Proceedings of the 5th Material Research Symposium, Vol. 364*, Nat. Bur. Standard Pub., Solid State Chemistry, **1972**, pp. 139-154.

[3] E. I. Burmakin, B. D. Antonov, G. S. Shekhtman, *Inorg. Mater.* **2010**, *46*, 540-544.

[4] G. V. Nechaev, E. I. Burmakin, *Russ. J. Electrochem.* **2011**, *47*, 1411-1414.

[5] G. V. Nechaev, E. I. Burmakin, *Russ. J. Electrochem.* **2011**, *47*, 457-460.

[6] E. I. Burmakin, G. V. Nechaev, G. S. Shekhtman, *Russ. J. Electrochem.* **2008**, *44*, 1386-1392.

[7] E. I. Burmakin, G. V. Nechaev, G. S. Shekhtman, S. V. Plaksin, *Russ. J. Electrochem.* **2009**, *45*, 934-937.

[8] E. I. Burmakin, G. V. Nechaev, *Russ. J. Electrochem.* **2013**, *49*, 1001-1003.

[9] E. I. Burmakin, G. S. Shekhtman, *Inorg. Mater.* **2008**, *44*, 882-885.

[10] E. I. Burmakin, G. S. Shekhtman, *Russ. J. Electrochem.* **2005**, *41*, 1341-1344.

[11] E. I. Burmakin, V. I. Voronin, L. Z. Akhtyamova, I. F. Berger, G. S. Shekhtman, *Russ. J. Electrochem.* **2005**, *41*, 783-788.

[12] T. Takahashi, K. Kuwabara, *Electrochim. Acta* **1978**, *23*, 375-379.

[13] T. Takahashi, K. Kuwabara, *Nippon Kagaku Kaishi* **1974**, *1974*, 1883-1887.

[14] S. Yamamoto, S. Tamura, N. Imanaka, *J. Alloys Compd.* **2006**, *418*, 226-229.

[15] Y.-W. Kim, A. Oda, N. Imanaka, *Electrochem. Commun.* **2003**, *5*, 94-97.

[16] J.-M. Doux, N. Stephant, A. L. G. La Salle, O. Joubert, D. Guyomard, E. Quarez, *CrystEngComm* **2019**, *21*, 594-601.

[17] J.-M. Doux, L. Leguay, A. Le Gal La Salle, O. Joubert, E. Quarez, *Solid State Ionics* **2018**, *324*, 260-266.

[18] E. Wang, M. Greenblatt, *Chem .Mater.* **1991**, *3*, 542-546.

D Appendix – Supporting Information for Chapter 9

D.1 Crystallographic Data of $Na_{1.25}Ba_{0.875}Si_3P_5$ and $Na_{31}Ba_5Si_{52}P_{83}$

Table D1 Fractional atomic coordinates, equivalent displacement parameters (Å^2) and occupancy factors of $Na_{1.25}Ba_{0.875}Si_3P_5$.

atom	Wyckoff	*x*	*y*	*z*	U_{eq}	Occ. (<1)
Ba1	8*f*	0.000000	0.20847 (2)	0.08780 (4)	0.01843 (16)	0.4052 (19)
Ba2	4*c*	0.000000	0.41347 (2)	0.250000	0.0391 (2)	0.808 (3)
Ba3	4*c*	0.000000	0.79762 (2)	0.250000	0.01851 (9)	
Na1	8*f*	0.000000	0.20847 (2)	0.08780 (4)	0.01843 (16)	0.595 (2)
Na2	8*e*	0.2456 (5)	0.000000	0.000000	0.0399 (8)	0.823 (5)
Na3	4*c*	0.000000	0.41347 (2)	0.250000	0.0391 (2)	0.192 (3)
Na4	4*c*	0.000000	0.91409 (13)	0.250000	0.0478 (15)	0.733 (11)
Si1	16*h*	0.25116 (9)	0.10945 (2)	0.08484 (6)	0.01093 (13)	
Si2	8*f*	0.000000	0.32129 (3)	0.07770 (9)	0.01184 (18)	
Si3	4*c*	0.000000	0.03358 (4)	0.250000	0.0114 (2)	
Si4	4*c*	0.000000	0.53264 (4)	0.250000	0.0116 (2)	
Si5	4*c*	0.000000	0.68381 (4)	0.250000	0.0118 (2)	
P1	16*h*	0.26239 (9)	0.35654 (2)	0.08266 (6)	0.01537 (14)	
P2	8*g*	0.23757 (13)	0.14767 (3)	0.250000	0.01199 (16)	
P3	8*g*	0.25204 (13)	0.49366 (3)	0.250000	0.01388 (17)	
P4	8*f*	0.000000	0.06891 (3)	0.07724 (8)	0.01158 (16)	
P5	8*f*	0.000000	0.27958 (3)	0.58292 (9)	0.0243 (2)	
P6	8*f*	0.000000	0.56828 (3)	0.07749 (8)	0.01209 (17)	
P7	4*c*	0.000000	0.28421 (4)	0.250000	0.0148 (2)	

Table D2 Atomic displacement parameters (Å^2) of $Na_{1.25}Ba_{0.875}Si_3P_5$.

atom	U^{11}	U^{22}	U^{33}	U^{12}	U^{13}	U^{23}
Ba1	0.0253 (3)	0.0157 (2)	0.0143 (2)	0.000	0.000	0.00122 (15)
Ba2	0.0799 (5)	0.0163 (2)	0.0211 (2)	0.000	0.000	0.000
Ba3	0.02080 (16)	0.01630 (15)	0.01843 (16)	0.000	0.000	0.000
Na1	0.0253 (3)	0.0157 (2)	0.0143 (2)	0.000	0.000	0.00122 (15)
Na2	0.070 (2)	0.0303 (12)	0.0192 (11)	0.000	0.000	−0.0053 (9)
Na3	0.0799 (5)	0.0163 (2)	0.0211 (2)	0.000	0.000	0.000
Na4	0.048 (3)	0.030 (2)	0.066 (3)	0.000	0.000	0.000
Si1	0.0089 (3)	0.0139 (3)	0.0100 (3)	−0.0006 (2)	−0.0002 (2)	0.0011 (2)
Si2	0.0118 (4)	0.0136 (4)	0.0101 (4)	0.000	0.000	0.0010 (3)
Si3	0.0089 (5)	0.0128 (6)	0.0127 (6)	0.000	0.000	0.000
Si4	0.0098 (6)	0.0126 (6)	0.0125 (6)	0.000	0.000	0.000
Si5	0.0116 (6)	0.0135 (6)	0.0103 (6)	0.000	0.000	0.000
P1	0.0111 (3)	0.0220 (3)	0.0131 (3)	−0.0019 (2)	−0.0018 (2)	0.0060 (2)
P2	0.0097 (4)	0.0154 (4)	0.0108 (4)	−0.0001 (3)	0.000	0.000

P3	0.0095 (4)	0.0130 (4)	0.0191 (4)	−0.0003 (3)	0.000	0.000
P4	0.0094 (4)	0.0130 (4)	0.0124 (4)	0.000	0.000	0.0005 (3)
P5	0.0485 (7)	0.0136 (4)	0.0109 (4)	0.000	0.000	−0.0003 (3)
P6	0.0100 (4)	0.0140 (4)	0.0123 (4)	0.000	0.000	0.0003 (3)
P7	0.0212 (6)	0.0145 (6)	0.0086 (5)	0.000	0.000	0.000

Table D3 Selected bond distances in $Na_{1.25}Ba_{0.875}Si_3P_5$ in Å.

atoms	distance	atoms	distance	atoms	distance	atoms	distance
Ba1—P5^{i}	3.0749 (11)	Ba2—Na4^{ix}	3.5840 (1)	Na2—P4^{xx}	3.057 (2)	Si1—P4	2.2707 (9)
Ba1—P7	3.1458 (12)	Ba2—Na4^{x}	3.5840 (1)	Na2—P6^{ix}	3.078 (2)	Si2—P1	2.2323 (9)
Ba1—P2	3.2290 (9)	Ba2—Si2^{i}	3.6762 (11)	Na2—P6^{iv}	3.078 (2)	Si2—P1^{viii}	2.2324 (9)
Ba1—P2^{ii}	3.2290 (9)	Ba2—Si2	3.6764 (11)	Na2—Si3^{xx}	3.4777 (17)	Si2—P5^{i}	2.2785 (14)
Ba1—P1^{iii}	3.3735 (8)	Ba2—P6^{xi}	3.6844 (9)	Na2—Si3	3.4777 (17)	Si2—P7	2.2904 (12)
Ba1—P1^{iv}	3.3735 (8)	Ba2—P6^{vii}	3.6844 (9)	Na2—Si4^{ix}	3.4995 (18)	Si3—P3^{x}	2.2382 (12)
Ba1—Ba1^{i}	3.5971 (9)	Ba3—P5^{xii}	3.2174 (11)	Na2—Si4i^{v}	3.4995 (18)	Si3—P3^{xix}	2.2382 (12)
Ba1—P5^{v}	3.6074 (2)	Ba3—P5^{xiii}	3.2174 (11)	Na2—Na2^{xx}	3.521 (7)	Si3—P4	2.2626 (12)
Ba1—P5^{vi}	3.6074 (2)	Ba3—P1^{xiv}	3.2210 (7)	Na2—Na2^{xxi}	3.646 (7)	Si3—P4^{i}	2.2627 (12)
Ba1—Ba3^{vii}	3.7517 (5)	Ba3—P1^{xv}	3.2210 (7)	Na4—P1^{xvii}	3.192 (3)	Si4—P3	2.2424 (12)
Ba1—Si1	3.8241 (8)	Ba3—P1^{xvi}	3.2210 (7)	Na4—P1^{xvi}	3.192 (3)	Si4—P3^{ii}	2.2425 (12)
Ba1—Si1^{viii}	3.8242 (8)	Ba3—P1^{xvii}	3.2210 (7)	Na4—P1^{xiv}	3.192 (3)	Si4—P6	2.2658 (12)
Ba2—P3^{ii}	3.2754 (10)	Ba3—P7^{xvii}	3.6129 (2)	Na4—P1^{xv}	3.192 (3)	Si4—P6^{i}	2.2658 (12)
Ba2—P3	3.2755 (10)	Ba3—P7^{xviii}	3.6129 (2)	Na4—P3^{xiv}	3.242 (4)	Si5—P5^{xiii}	2.2336 (13)
Ba2—P1^{viii}	3.2775 (8)	Ba3—Na4	3.968 (5)	Na4—P3^{xvii}	3.242 (4)	Si5—P5^{xii}	2.2336 (13)
Ba2—P1^{ii}	3.2775 (8)	Na2—P3^{xix}	2.7807 (1)	Si1—P1^{iv}	2.1913 (9)	Si5—P2^{xvii}	2.2483 (12)
Ba2—P1^{i}	3.2775 (8)	Na2—P3^{iv}	2.7807 (1)	Si1—P2	2.2492 (8)	Si5—P2^{xiv}	2.2483 (12)
Ba2—P1	3.2776 (8)	Na2—P4	3.057 (2)	Si1—P6^{ix}	2.2707 (9)	Si1—P4	2.2707 (9)

Symmetry codes: (i) x, *y*, −*z*+1/2; (ii) −*x*, *y*, −*z*+1/2; (iii) *x*−1/2, −*y*+1/2, −*z*; (iv) −*x*+1/2, −*y*+1/2, −*z*; (v) −*x*+1/2, −*y*+1/2, *z*−1/2; (vi) −*x*−1/2, −*y*+1/2, *z*−1/2; (vii) −*x*, −*y*+1, −*z*; (viii) −*x*, *y*, *z*; (ix) *x*+1/2, *y*−1/2, *z*; (x) *x*−1/2, *y*−1/2, *z*; (xi) −*x*, −*y*+1, *z*+1/2; (xii) −*x*, −*y*+1, *z*−1/2; (xiii) −*x*, −*y*+1, −*z*+1; (xiv) −*x*+1/2, *y*+1/2, −*z*+1/2; (xv) *x*−1/2, *y*+1/2, −*z*+1/2; (xvi) −*x*+1/2, *y*+1/2, *z*; (xvii) *x*−1/2, *y*+1/2, *z*; (xviii) *x*+1/2, *y*+1/2, *z*; (xix) −*x*+1/2, *y*−1/2, −*z*+1/2; (xx) −*x*, −*y*, −*z*; (xxi) −*x*+1, −*y*, −*z*; (xxii) −*x*, −*y*, *z*+1/2; (xxiii) −*x*+1/2, −*y*+1/2, *z*+1/2; (xxiv) −*x*−1/2, −*y*+1/2, *z*+1/2.

Table D4 Fractional atomic coordinates, equivalent displacement parameters (Å^2) and occupancy factors of $Na_{31}Ba_5Si_{52}P_{83}$.

atom	Wyckoff	*x*	*y*	*z*	U_{eq}	Occ. (<1)
Ba1	8*f*	0.03838(3)	0.28816(2)	0.44990(3)	0.03319(13)	0.5
Ba2	8*f*	0.42512(2)	0.12558(2)	0.29605(2)	0.02363(6)	

Ba3	8*f*	0.43398(2)	0.00233(2)	0.06545(2)	0.03283(7)	
Na1	8*f*	0.00223(14)	0.10926(17)	0.49733(14)	0.1048(16)	
Na2	8*f*	0.00686(11)	0.16477(9)	0.36852(12)	0.0533(6)	
Na3	8*f*	0.0430(3)	0.30328(17)	0.4023(4)	0.083 (2)	0.5
Na4	8*f*	0.0624(7)	0.3881(3)	0.2299(5)	0.135(5)	0.5
Na5	8*f*	0.0636(3)	0.4140 (3)	0.2057 (4)	0.082 (2)	0.5
Na6	8*f*	0.0721 (4)	0.2081 (2)	0.5718 (3)	0.0715 (18)	0.5
Na7	8*f*	0.0875 (2)	0.44421 (11)	0.11510 (16)	0.0598 (13)	0.743 (8)
Na8	8*f*	0.24210 (12)	0.39581 (6)	0.19832 (9)	0.0392 (5)	
Na9	8*f*	0.24662 (15)	0.33869 (11)	0.32971 (16)	0.0814 (11)	
Na10	8*f*	0.2477 (2)	0.44216 (9)	0.04221 (14)	0.0820 (10)	
Na11	8*f*	0.2522 (3)	0.2775 (2)	0.4487 (4)	0.224 (4)	
Na12	8*f*	0.25708 (15)	0.30915 (7)	0.00968 (9)	0.0502 (6)	
Na13	8*f*	0.3839 (2)	0.39190 (13)	0.1225 (2)	0.110 (2)	0.892 (10)
Na14	8*f*	0.40704 (13)	0.14171 (8)	0.07478 (9)	0.0459 (5)	
Na15	8*f*	0.41501 (15)	0.34166 (8)	0.29286 (11)	0.0545 (6)	
Na16	8*f*	0.43369 (13)	0.25448 (7)	0.09847 (8)	0.0443 (5)	
Na17	8*f*	0.4914 (2)	0.4690 (2)	0.1078 (2)	0.130 (3)	0.878 (10)
Na18	4*e*	0.000000	0.0063 (2)	0.250000	0.096 (2)	0.972 (15)
Na19	4*e*	0.000000	0.23869 (13)	0.250000	0.0637 (11)	
Si1	8*f*	0.12797 (5)	0.35015 (3)	0.06876 (4)	0.01613 (19)	
Si2	8*f*	0.14325 (6)	0.23599 (3)	0.06283 (4)	0.01532 (19)	
Si3	8*f*	0.14759 (5)	0.29167 (3)	0.19249 (4)	0.01338 (17)	
Si4	8*f*	0.15704 (5)	0.12513 (3)	0.05375 (4)	0.01428 (18)	
Si5	8*f*	0.16056 (5)	0.01184 (3)	0.04449 (4)	0.01362 (18)	
Si6	8*f*	0.16119 (5)	0.06083 (3)	0.17363 (4)	0.01297 (17)	
Si7	8*f*	0.16278 (5)	0.10598 (3)	0.54268 (4)	0.01372 (18)	
Si8	8*f*	0.16296 (5)	0.17611 (3)	0.18630 (4)	0.01279 (17)	
Si9	8*f*	0.16315 (5)	0.04632 (3)	0.41873 (4)	0.01474 (18)	
Si10	8*f*	0.16454 (5)	0.22990 (3)	0.31329 (4)	0.01346 (18)	
Si11	8*f*	0.16732 (5)	0.11122 (3)	0.30336 (4)	0.01368 (18)	
Si12	8*f*	0.16750 (5)	0.16597 (3)	0.42771 (4)	0.01435 (18)	
Si13	8*f*	0.18625 (5)	0.45145 (3)	0.36336 (4)	0.01375 (18)	
Si14	8*f*	0.29282 (5)	0.30290 (3)	0.15019 (4)	0.01311 (17)	
Si15	8*f*	0.30819 (5)	0.18534 (3)	0.15002 (4)	0.01325 (17)	
Si16	8*f*	0.31110 (5)	0.06675 (3)	0.14294 (4)	0.01319 (17)	
Si17	8*f*	0.31122 (5)	0.00422 (3)	0.26096 (4)	0.01410 (18)	
Si18	8*f*	0.31121 (5)	0.23848 (3)	0.27591 (4)	0.01215 (17)	
Si19	8*f*	0.31647 (5)	0.05175 (3)	0.39075 (4)	0.01445 (18)	
Si20	8*f*	0.32087 (5)	0.10468 (3)	0.51419 (4)	0.01544 (18)	
Si21	8*f*	0.32141 (5)	0.16746 (3)	0.39691 (4)	0.01361 (18)	
Si22	8*f*	0.33889 (5)	0.49532 (3)	0.20764 (4)	0.01324 (17)	
Si23	8*f*	0.34165 (5)	0.44621 (3)	0.33394 (4)	0.01315 (17)	

Si24	8*f*	0.44033 (5)	0.24940 (3)	0.23187 (4)	0.01304 (17)
Si25	8*f*	0.44218 (5)	0.00773 (3)	0.22698 (4)	0.01398 (18)
Si26	8*f*	0.53629 (6)	0.10431 (4)	0.01670 (5)	0.0208 (2)
P1	8*f*	0.06627 (5)	0.39356 (4)	0.44006 (4)	0.0225 (2)
P2	8*f*	0.07249 (6)	0.54290 (4)	0.06602 (5)	0.0279 (2)
P3	8*f*	0.07437 (5)	0.44766 (3)	0.32417 (4)	0.01828 (18)
P4	8*f*	0.07790 (5)	0.40785 (3)	0.01360 (4)	0.01930 (19)
P5	8*f*	0.09242 (5)	0.29268 (3)	0.00918 (4)	0.01777 (18)
P6	8*f*	0.09491 (5)	0.34891 (3)	0.14242 (4)	0.01832 (18)
P7	8*f*	0.10536 (5)	0.23290 (3)	0.13459 (4)	0.01500 (17)
P8	8*f*	0.10650 (6)	0.18167 (3)	0.00068 (4)	0.0220 (2)
P9	8*f*	0.11451 (5)	0.00588 (3)	0.11124 (4)	0.01454 (17)
P10	8*f*	0.11484 (5)	0.12101 (3)	0.12364 (4)	0.01305 (16)
P11	8*f*	0.11639 (5)	0.04637 (3)	0.48593 (4)	0.01397 (16)
P12	8*f*	0.11657 (5)	0.05668 (3)	0.24087 (4)	0.01412 (16)
P13	8*f*	0.11874 (5)	0.17174 (3)	0.25340 (4)	0.01327 (16)
P14	8*f*	0.11905 (5)	0.29095 (3)	0.26748 (4)	0.01677 (18)
P15	8*f*	0.12014 (5)	0.10811 (3)	0.36871 (4)	0.01485 (17)
P16	8*f*	0.12105 (5)	0.11210 (3)	0.61046 (4)	0.01588 (17)
P17	8*f*	0.12370 (5)	0.16694 (3)	0.49356 (4)	0.01713 (18)
P18	8*f*	0.12431 (5)	0.22756 (3)	0.38152 (4)	0.01681 (18)
P19	8*f*	0.22142 (5)	0.39077 (3)	0.41677 (4)	0.01363 (16)
P20	8*f*	0.22370 (5)	0.49260 (3)	0.16714 (4)	0.01396 (16)
P21	8*f*	0.22584 (5)	0.44311 (3)	0.29334 (4)	0.01382 (16)
P22	8*f*	0.24177 (5)	0.36008 (3)	0.09607 (4)	0.01576 (17)
P23	8*f*	0.25854 (5)	0.24264 (3)	0.09306 (4)	0.01516 (17)
P24	8*f*	0.26254 (5)	0.29965 (3)	0.22710 (4)	0.01323 (16)
P25	8*f*	0.27277 (5)	0.12761 (3)	0.08910 (4)	0.01386 (16)
P26	8*f*	0.27463 (5)	0.06746 (3)	0.21473 (4)	0.01354 (16)
P27	8*f*	0.27620 (5)	0.01137 (3)	0.07962 (4)	0.01393 (16)
P28	8*f*	0.27732 (5)	0.17644 (3)	0.22442 (4)	0.01289 (16)
P29	8*f*	0.27839 (5)	0.04335 (3)	0.46111 (4)	0.01609 (17)
P30	8*f*	0.28076 (5)	0.23274 (3)	0.35208 (4)	0.01360 (16)
P31	8*f*	0.28253 (5)	0.11168 (3)	0.33466 (4)	0.01478 (17)
P32	8*f*	0.28390 (5)	0.16936 (3)	0.46901 (4)	0.01530 (17)
P33	8*f*	0.37585 (6)	0.48831 (3)	0.13755 (4)	0.01998 (19)
P34	8*f*	0.37902 (5)	0.42929 (3)	0.00814 (4)	0.01809 (18)
P35	8*f*	0.38405 (5)	0.43940 (3)	0.26701 (4)	0.01661 (17)
P36	8*f*	0.40505 (5)	0.31098 (3)	0.18038 (4)	0.01743 (18)
P37	8*f*	0.42026 (5)	0.18631 (3)	0.18168 (4)	0.01638 (17)
P38	8*f*	0.42198 (5)	0.01163 (4)	0.30508 (4)	0.0211 (2)
P39	8*f*	0.42275 (5)	0.24213 (3)	0.31297 (4)	0.01698 (18)
P40	8*f*	0.42381 (5)	0.06940 (3)	0.17732 (4)	0.01710 (18)

P41	8*f*	0.56460 (5)	0.16504 (4)	0.07307 (4)	0.0209 (2)	
P42	8*f*	0.01904 (15)	0.28372 (9)	0.51020 (13)	0.0397 (6)	0.5

Table D5 Atomic displacement parameters (Å^2) of $Na_{31}Ba_5Si_{52}P_{83}$.

atom	U^{11}	U^{22}	U^{33}	U^{12}	U^{13}	U^{23}
Ba1	0.0237(3)	0.0350(3)	0.0402(3)	-0.0194(2)	0.0120(2)	-0.0034(2)
Ba2	0.02674(12)	0.02313(11)	0.02034(11)	-0.00194(9)	0.00866(9)	0.00406(9)
Ba3	0.04358(16)	0.03085(14)	0.02699(13)	0.00248(10)	0.01716(12)	-0.01025(12)
Na1	0.0256(13)	0.215(5)	0.0616(19)	0.040(2)	0.0052(12)	-0.0109(19)
Na2	0.0267(11)	0.0564(15)	0.0757(18)	0.0158(13)	0.0191(11)	0.0037(10)
Na3	0.044(3)	0.033(3)	0.143(6)	-0.037(3)	0.008(3)	0.013(2)
Na4	0.253(14)	0.088(6)	0.120(8)	-0.025(6)	0.134(9)	0.029(8)
Na5	0.053(3)	0.074(5)	0.125(7)	-0.057(5)	0.040(4)	0.001(3)
Na6	0.103(5)	0.074(4)	0.062(3)	0.015(3)	0.059(4)	0.035(4)
Na7	0.068(3)	0.045(2)	0.056(2)	-0.0191(16)	0.0137(18)	0.0057(17)
Na8	0.0652(14)	0.0238(9)	0.0351(10)	-0.0108(8)	0.0268(10)	-0.0058(9)
Na9	0.0657(18)	0.085(2)	0.109(3)	-0.074(2)	0.0513(18)	-0.0390(16)
Na10	0.135(3)	0.0385(14)	0.076(2)	0.0078(14)	0.047(2)	-0.0253(17)
Na11	0.106(4)	0.241(7)	0.362(10)	-0.255(8)	0.129(5)	-0.090(4)
Na12	0.109(2)	0.0258(10)	0.0343(11)	0.0027(8)	0.0480(13)	0.0058(11)
Na13	0.067(3)	0.062(2)	0.181(5)	0.066(3)	0.029(3)	0.0077(18)
Na14	0.0687(16)	0.0470(13)	0.0329(11)	0.0021(9)	0.0319(11)	0.0095(11)
Na15	0.0839(19)	0.0336(11)	0.0441(13)	-0.0131(10)	0.0237(13)	0.0032(12)
Na16	0.0727(16)	0.0352(11)	0.0205(9)	-0.0003(8)	0.0138(10)	0.0047(10)
Na17	0.046(2)	0.237(7)	0.111(4)	-0.058(4)	0.037(2)	-0.031(3)
Na18	0.037(2)	0.155(6)	0.084(4)	0.000	0.011(2)	0.000
Na19	0.0260(16)	0.056(2)	0.105(3)	0.000	0.0208(19)	0.000
Si1	0.0208(19)	0.0145(4)	0.0148(4)	0.0043(3)	0.0037(4)	0.0006(4)
Si2	0.0228(5)	0.0103(4)	0.0115(4)	0.0012(3)	0.0053(4)	0.0012(4)
Si3	0.0159(4)	0.0115(4)	0.0137(4)	0.0013(3)	0.0070(4)	0.0010(3)
Si4	0.0203(5)	0.0105(4)	0.0123(4)	0.0003(3)	0.0068(4)	-0.0001(3)
Si5	0.0176(5)	0.0116(4)	0.0117(4)	-0.0004(3)	0.0059(4)	0.0008(3)
Si6	0.0168(4)	0.0118(4)	0.0110(4)	-0.0002(3)	0.0064(4)	0.0002(3)
Si7	0.0173(5)	0.0138(4)	0.0112(4)	0.0008(3)	0.0068(4)	-0.0010(3)
Si8	0.0163(4)	0.0113(4)	0.0117(4)	0.0000(3)	0.0065(4)	-0.0006(3)
Si9	0.0215(5)	0.0127(4)	0.0116(4)	-0.0008(3)	0.0083(4)	-0.0023(4)
Si10	0.0168(4)	0.0127(4)	0.0131(4)	0.0004(3)	0.0083(4)	-0.0001(3)
Si11	0.0194(5)	0.0116(4)	0.0109(4)	0.0002(3)	0.0068(4)	0.0000(3)
Si12	0.0192(5)	0.0133(4)	0.0123(4)	0.0007(3)	0.0082(4)	-0.0007(4)
Si13	0.0170(4)	0.0130(4)	0.0121(4)	0.0006(3)	0.0067(4)	0.0002(3)
Si14	0.0161(4)	0.0108(4)	0.0129(4)	0.0012(3)	0.0063(4)	0.0015(3)

Si15	0.0178(5)	0.0107(4)	0.0134(4)	-0.0006(3)	0.0084(4)	-0.0008(3)
Si16	0.0170(4)	0.0115(4)	0.0117(4)	0.0005(3)	0.0065(4)	0.0002(3)
Si17	0.0155(4)	0.0132(4)	0.0131(4)	-0.0001(3)	0.0051(4)	-0.0006(3)
Si18	0.0143(4)	0.0119(4)	0.0117(4)	0.0001(3)	0.0067(3)	-0.0003(3)
Si19	0.0183(5)	0.0128(4)	0.0120(4)	-0.0019(3)	0.0058(4)	-0.0019(3)
Si20	0.0184(5)	0.0168(4)	0.0130(4)	0.0005(3)	0.0082(4)	-0.0008(4)
Si21	0.0158(4)	0.0130(4)	0.0124(4)	0.0008(3)	0.0061(4)	-0.0005(3)
Si22	0.0174(4)	0.0121(4)	0.0109(4)	0.0009(3)	0.0063(4)	0.0012(3)
Si23	0.0166(4)	0.0121(4)	0.0114(4)	0.0011(3)	0.0063(4)	0.0010(3)
Si24	0.0147(4)	0.0114(4)	0.0151(4)	0.0003(3)	0.0082(4)	0.0004(3)
Si25	0.0163(4)	0.0131(4)	0.0115(4)	0.0006(3)	0.0044(4)	-0.0002(3)
Si26	0.0170(5)	0.0225(5)	0.0209(5)	0.0072(4)	0.0055(4)	0.0035(4)
P1	0.0206(5)	0.0272(5)	0.0191(5)	-0.0008(4)	0.0072(4)	-0.0039(4)
P2	0.0181(5)	0.0269(5)	0.0313(6)	0.0105(4)	0.0019(4)	0.0008(4)
P3	0.0168(4)	0.0168(4)	0.0196(4)	0.0011(3)	0.0056(4)	0.0002(3)
P4	0.0162(4)	0.0161(4)	0.0239(5)	0.0091(4)	0.0061(4)	0.0030(3)
P5	0.0233(5)	0.0156(4)	0.0120(4)	0.0015(3)	0.0046(4)	0.0019(4)
P6	0.0222(5)	0.0156(4)	0.0186(4)	0.0041(3)	0.0096(4)	0.0060(4)
P7	0.0189(4)	0.0123(4)	0.0130(4)	0.0011(3)	0.0055(3)	-0.0008(3)
P8	0.0379(6)	0.0111(4)	0.0122(4)	0.0004(3)	0.0050(4)	0.0008(4)
P9	0.0193(4)	0.0124(4)	0.0125(4)	-0.0003(3)	0.0070(3)	0.0004(3)
P10	0.0167(4)	0.0111(4)	0.0111(4)	0.0003(3)	0.0052(3)	0.0004(3)
P11	0.0180(4)	0.0129(4)	0.0115(4)	0.0008(3)	0.0064(3)	-0.0009(3)
P12	0.0186(4)	0.0128(4)	0.0123(4)	-0.0006(3)	0.0076(3)	-0.0004(3)
P13	0.0171(4)	0.0118(4)	0.0120(4)	0.0003(3)	0.0069(3)	0.0001(3)
P14	0.0218(5)	0.0145(4)	0.0170(4)	0.0014(3)	0.0109(4)	0.0027(3)
P15	0.0195(4)	0.0140(4)	0.0127(4)	0.0001(3)	0.0081(3)	-0.0005(3)
P16	0.0219(5)	0.0145(4)	0.0129(4)	0.0029(3)	0.0088(4)	0.0043(3)
P17	0.0230(5)	0.0169(4)	0.0146(4)	0.0028(3)	0.0108(4)	0.0017(4)
P18	0.0237(5)	0.0144(4)	0.0170(4)	0.0019(3)	0.0131(4)	0.0020(3)
P19	0.0171(4)	0.0130(4)	0.0115(4)	-0.0002(3)	0.0065(3)	-0.0007(3)
P20	0.0178(4)	0.0117(4)	0.0121(4)	0.0010(3)	0.0056(3)	0.0009(3)
P21	0.0170(4)	0.0130(4)	0.0121(4)	0.0002(3)	0.0064(3)	0.0007(3)
P22	0.0184(4)	0.0122(4)	0.0181(4)	0.0040(3)	0.0087(4)	0.0026(3)
P23	0.0230(5)	0.0112(4)	0.0134(4)	0.0003(3)	0.0095(4)	-0.0005(3)
P24	0.0160(4)	0.0112(4)	0.0135(4)	0.0005(3)	0.0070(3)	0.0005(3)
P25	0.0195(4)	0.0110(4)	0.0123(4)	0.0002(3)	0.0076(3)	0.0000(3)
P26	0.0172(4)	0.0125(4)	0.0119(4)	-0.0005(3)	0.0068(3)	-0.0001(3)
P27	0.0183(4)	0.0120(4)	0.0124(4)	-0.0006(3)	0.0071(3)	0.0001(3)
P28	0.0158(4)	0.0114(4)	0.0125(4)	0.0001(3)	0.0069(3)	-0.0002(3)
P29	0.0222(5)	0.0150(4)	0.0120(4)	0.0003(3)	0.0077(4)	-0.0002(3)
P30	0.0169(4)	0.0132(4)	0.0128(4)	0.0004(3)	0.0082(3)	-0.0001(3)
P31	0.0203(4)	0.0130(4)	0.0122(4)	-0.0002(3)	0.0077(3)	-0.0004(3)

P32	0.0198(4)	0.0146(4)	0.0133(4)	-0.0004(3)	0.0086(3)	-0.0016(3)
P33	0.0310(5)	0.0171(4)	0.0174(4)	0.0053(3)	0.0156(4)	0.0086(4)
P34	0.0265(5)	0.0118(4)	0.0126(4)	-0.0004(3)	0.0044(4)	0.0013(3)
P35	0.0227(5)	0.0143(4)	0.0160(4)	0.0035(3)	0.0109(4)	0.0047(3)
P36	0.0187(4)	0.0133(4)	0.0221(5)	0.0038(3)	0.0101(4)	0.0010(3)
P37	0.0177(4)	0.0134(4)	0.0202(4)	-0.0028(3)	0.0098(4)	-0.0001(3)
P38	0.0174(4)	0.0298(5)	0.0156(4)	0.0018(4)	0.0062(4)	-0.0011(4)
P39	0.0145(4)	0.0234(5)	0.0142(4)	0.0022(3)	0.0069(3)	0.0002(3)
P40	0.0169(4)	0.0152(4)	0.0183(4)	0.0026(3)	0.0061(4)	-0.0004(3)
P41	0.0192(5)	0.0285(5)	0.0153(4)	0.0008(4)	0.0071(4)	0.0080(4)
P42	0.0367(14)	0.0346(13)	0.0413(15)	-0.0076(11)	0.0087(12)	0.0005(11)

Table D6 Selected bond distances in $Na_{31}Ba_5Si_{52}P_{83}$ in Å.

atoms	distance	atoms	distance	atoms	distance	atoms	distance
Ba1—Na3	1.331 (9)	Na5—P6	2.802 (6)	Na14—P4^{vii}	2.828 (2)	Si9—P33^{vi}	2.2232 (14)
Ba1—P42	1.738 (3)	Na5—P3^{ii}	2.912 (6)	Na14—P5^{vii}	2.931 (2)	Si9—P29	2.2518 (15)
Ba1—P41^{i}	3.2732 (12)	Na5—P38^{ix}	3.035 (9)	Na14—P37	2.945 (2)	Si9—P15	2.2604 (14)
Ba1—P1	3.3141 (13)	Na5—P3	3.093 (8)	Na14—P25	3.050 (3)	Si9—P11	2.2879 (13)
Ba1—P5^{ii}	3.3367 (12)	Na5—Si25^{ix}	3.370 (6)	Na14—P40	3.324 (2)	Si10—P14	2.2120 (14)
Ba1—P7^{ii}	3.4030 (11)	Na5—P21	3.395 (7)	Na14—Si1^{vii}	3.416 (2)	Si10—P18	2.2142 (13)
Ba1—P6^{ii}	3.4190 (12)	Na5—Na8	3.916 (7)	Na14—P41	3.444 (3)	Si10—P30	2.2687 (14)
Ba1—P18	3.5097 (11)	Na5—Na5^{ii}	4.144 (16)	Na14—Na16	3.518 (3)	Si10—P13	2.2919 (13)
Ba1—Si26^{i}	3.7149 (12)	Na6—P42	2.771 (7)	Na15—P36	2.926 (3)	Si11—P13	2.2521 (13)
Ba1—P32^{iii}	3.7435 (11)	Na6—P17	2.908 (5)	Na15—P35	3.083 (3)	Si11—P15	2.2537 (13)
Ba1—Na6	3.781 (6)	Na6—P16	3.147 (6)	Na15—P39	3.088 (3)	Si11—P31	2.2548 (14)
Ba1—Na2	4.233 (3)	Na6—P39^{iii}	3.257 (6)	Na15—P16^{iii}	3.177 (3)	Si11—P12	2.2597 (13)
Ba2—P28	3.3255 (9)	Na6—Na16^{i}	3.468 (6)	Na15—P24	3.262 (3)	Si12—P17	2.2111 (13)
Ba2—P37	3.4105 (10)	Na6—Na15^{iii}	3.662 (6)	Na15—Si24	3.369 (2)	Si12—P18	2.2190 (14)
Ba2—P41^{iv}	3.4525 (10)	Na6—Na9^{iii}	3.935 (7)	Na16—P5v^{ii}	2.937 (2)	Si12—P32	2.2735 (14)
Ba2—P40	3.4557 (10)	Na6—Na11^{iii}	3.997 (8)	Na16—P36	2.947 (2)	Si12—P15	2.2795 (14)
Ba2—P40^{iv}	3.4672 (10)	Na7—P4	2.734 (4)	Na16—P39^{iv}	3.006 (3)	Si13—P3	2.1858 (14)
Ba2—P38	3.5049 (12)	Na7—P38^{ix}	2.954 (3)	Na16—P8^{vii}	3.026 (2)	Si13—P19	2.2465 (13)
Ba2—P26	3.5224 (10)	Na7—P6	2.994 (4)	Na16—P37	3.062 (2)	Si13—P21	2.2604 (13)
Ba2—P31	3.5639 (10)	Na7—P20	3.048 (4)	Na16—Si24	3.328 (2)	Si13—P27^{ix}	2.2761 (13)
Ba2—P39	3.6035 (11)	Na7—P2	3.239 (4)	Na17—P9^{x}	2.821 (5)	Si14—P36	2.2112 (14)
Ba2—P37^{iv}	3.6230 (10)	Na7—Si1	3.354 (3)	Na17—P33	2.906 (4)	Si14—P22	2.2243 (13)
Ba2—Na14^{iv}	3.792 (3)	Na7—P1^{ii}	3.379 (4)	Na17—P34	2.958 (5)	Si14—P23	2.2802 (13)
Ba2—Ba2^{iv}	4.6383 (5)	Na7—Na8	3.455 (4)	Na17—Si23^{iv}	3.331 (5)	Si14—P24	2.2843 (13)
Ba3—P2^{v}	3.1927 (12)	Na8—P22	2.809 (2)	Na17—P35^{iv}	3.346 (6)	Si15—P37	2.1913 (14)

Ba3—P3^{vi}	3.3247 (11)	Na8—P21	2.946 (2)	Na17—Na18^{x}	3.715 (5)	Si15—P28	2.2454 (13)
Ba3—P1^{vi}	3.3394 (12)	Na8—P24	3.028 (2)	Na18—P12	3.007 (4)	Si15—P23	2.2519 (13)
Ba3—P4^{vii}	3.3551 (10)	Na8—P20	3.057 (2)	Na18—P12^{ii}	3.007 (4)	Si15—P25	2.2708 (13)
Ba3—Na7^{v}	3.485 (4)	Na8—P35	3.121 (2)	Na18—P33^{xi}	3.0645 (17)	Si16—P40	2.2016 (14)
Ba3—P38^{iv}	3.4937 (11)	Na8—P6	3.216 (3)	Na18—P33^{vi}	3.0645 (17)	Si16—P26	2.2434 (13)
Ba3—P27	3.5256 (10)	Na8—Si14	3.438 (2)	Na18—Si22^{xi}	3.1744 (13)	Si16—P27	2.2489 (13)
Ba3—P2^{vii}	3.5583 (14)	Na8—Si1	3.502 (2)	Na18—Si22^{vi}	3.1744 (13)	Si16—P25	2.2630 (13)
Ba3—P40	3.5769 (10)	Na8—Na9	3.727 (5)	Na18—P35^{xi}	3.366 (4)	Si17—P38	2.1797 (14)
Ba3—P29^{viii}	3.5948 (10)	Na8—Na15	3.872 (4)	Na18—P35^{vi}	3.366 (4)	Si17—P26	2.2389 (13)
Ba3—Na10^{vii}	4.106 (4)	Na9—P14	2.929 (3)	Na19—P14^{ii}	2.878 (2)	Si17—P20^{vi}	2.2524 (13)
Ba3—Na14	4.332 (2)	Na9—P19	2.940 (3)	Na19—P14	2.878 (2)	Si17—P21^{vi}	2.2718 (13)
Na1—P16	2.971 (3)	Na9—P24	3.000 (3)	Na19—Si10	3.2275 (11)	Si18—P39	2.1785 (14)
Na1—P34^{i}	2.986 (3)	Na9—P16^{iii}	3.016 (3)	Na19—Si10^{ii}	3.2275 (11)	Si18—P28	2.2564 (13)
Na1—P10^{ii}	3.103 (3)	Na9—P21	3.313 (4)	Na19—P13	3.229 (3)	Si18—P24	2.2581 (13)
Na1—Si7	3.140 (3)	Na9—P30	3.329 (4)	Na19—P13^{ii}	3.230 (3)	Si18—P30	2.2732 (13)
Na1—Si4^{ii}	3.145 (3)	Na9—Si7^{iii}	3.474 (3)	Na19—P18^{ii}	3.3432 (11)	Si19—P2^{vi}	2.1884 (15)
Na1—P17	3.164 (4)	Na9—Na11	3.515 (11)	Na19—P18	3.3432 (11)	Si19—P29	2.2467 (13)
Na1—P11	3.203 (4)	Na9—Na15	4.046 (4)	Si1—P6	2.2410 (14)	Si19—P31	2.2584 (13)
Na1—P8^{ii}	3.221 (5)	Na10—P22	2.890 (3)	Si1—P4	2.2431 (14)	Si19—P20^{vi}	2.2741 (13)
Na1—Na6	3.567 (9)	Na10—P29^{ix}	3.148 (3)	Si1—P5	2.2461 (14)	Si20—P1^{iii}	2.2112 (15)
Na1—Na2	3.715 (4)	Na10—P33	3.165 (4)	Si1—P22	2.2572 (14)	Si20—P19^{iii}	2.2673 (13)
Na1—Na17^{i}	3.761 (6)	Na10—Na13	3.195 (5)	Si2—P5	2.2062 (14)	Si20—P32	2.2684 (14)
Na2—P15	2.969 (3)	Na10—P27^{vii}	3.249 (3)	Si2—P8	2.2100 (14)	Si20—P29	2.2790 (14)
Na2—P10^{ii}	2.992 (2)	Na10—P34	3.260 (4)	Si2—P7	2.2647 (14)	Si21—P41^{iv}	2.2344 (14)
Na2—P18	3.066 (3)	Na10—Na12	4.183 (4)	Si2—P23	2.2681 (15)	Si21—P31	2.2488 (13)
Na2—Si12	3.137 (2)	Na11—P32^{iii}	2.978 (5)	Si3—P6	2.1937 (13)	Si21—P32	2.2660 (13)
Na2—P7^{ii}	3.150 (3)	Na11—P17^{iii}	2.989 (4)	Si3—P14	2.2126 (13)	Si21—P30	2.2941 (13)
Na2—P17	3.151 (3)	Na11—P18	2.992 (4)	Si3—P24	2.2578 (14)	Si22—P33	2.2197 (13)
Na2—P13^{ii}	3.184 (3)	Na11—P30	3.070 (5)	Si3—P7	2.2705 (13)	Si22—P35	2.2300 (13)
Na2—Si8^{ii}	3.331 (2)	Na11—Na11^{iii}	3.124 (19)	Si4—P8	2.1947 (14)	Si22—P20	2.2489 (14)
Na2—Na19	3.718 (4)	Na11—P32	3.380 (8)	Si4—P34^{vii}	2.2074 (13)	Si22—P12^{ix}	2.2704 (13)
Na3—P1	2.907 (5)	Na11—Si12^{iii}	3.384 (5)	Si4—P25	2.2605 (14)	Si23—P16^{iii}	2.2180 (13)
Na3—P6^{ii}	3.032 (5)	Na11—Si10	3.503 (6)	Si4—P10	2.2849 (13)	Si23—P35	2.2247 (13)
Na3—P42	3.032 (10)	Na12—P22	2.811 (2)	Si5—P34^{vii}	2.2024 (13)	Si23—P9i^{x}	2.2612 (13)
Na3—P18	3.064 (5)	Na12—P23	2.927 (2)	Si5—P27	2.2575 (14)	Si23—P21	2.2614 (14)
Na3—Na19	4.102 (7)	Na12—P23^{vii}	2.952 (2)	Si5—P11^{viii}	2.2713 (13)	Si24—P39	2.2405 (13)
Na3—Na4^{ii}	4.124 (13)	Na12—P25^{vii}	3.026 (2)	Si5—P9	2.2738 (13)	Si24—P36	2.2475 (13)
Na3—Na11	4.202 (7)	Na12—P8^{vii}	3.029 (3)	Si6—P26	2.2234 (14)	Si24—P37	2.2603 (13)
Na4—Na5	1.009 (11)	Na12—Si14	3.334 (2)	Si6—P10	2.2331 (13)	Si24—Si24^{iv}	2.330 (2)

Na4—P6	2.837 (7)	Na12—Si4^{vii}	3.510 (2)	Si6—P9	2.2522 (13)	Si25—P38	2.1882 (14)
Na4—P3	2.936 (8)	Na12—Na14^{vii}	3.616 (4)	Si6—P12	2.2595 (13)	Si25—P3^{vi}	2.1986 (14)
Na4—Na4^{ii}	3.20 (2)	Na12—Na12^{vii}	3.658 (4)	Si7—P17	2.2159 (14)	Si25—P40	2.2182 (13)
Na4—P14	3.212 (11)	Na12—Na16	3.904 (4)	Si7—P16	2.2327 (13)	Si25—Si25^{iv}	2.263 (2)
Na4—P3^{ii}	3.241 (12)	Na12—Na13	3.967 (6)	Si7—P19^{iii}	2.2615 (14)	Si26—P2v	2.2215 (15)
Na4—Na7	3.597 (11)	Na13—P36	2.826 (4)	Si7—P11	2.2914 (13)	Si26—P4^{vii}	2.2675 (15)
Na4—Na5^{ii}	3.735 (12)	Na13—P22	2.988 (4)	Si8—P7	2.2294 (13)	Si26—P1^{xii}	2.2727 (16)
Na4—Na9	4.017 (14)	Na13—P33	2.995 (4)	Si8—P28	2.2308 (14)	Si26—P41	2.2768 (16)
Na4—Na8	4.212 (12)	Na13—P34	3.078 (5)	Si8—P13	2.2505 (13)	P5—P42^{ii}	2.238 (3)
Na5—Na7	2.706 (11)	Na13—Na17	3.412 (7)	Si8—P10	2.2643 (13)	P41—P42^{xii}	2.171 (3)

Symmetry codes: (i) x−1/2, −*y*+1/2, *z*+1/2; (ii) −*x*, *y*, −*z*+1/2; (iii) −*x*+1/2, −*y*+1/2, −*z*+1; (iv) −*x*+1, *y*, −*z*+1/2; (v) *x*+1/2, *y*−1/2, *z*; (vi) −*x*+1/2, *y*−1/2, −*z*+1/2; (vii) −*x*+1/2, −*y*+1/2, −*z*; (viii) *x*, −*y*, *z*−1/2; (ix) −*x*+1/2, *y*+1/2, −*z*+1/2; (x) *x*+1/2, *y*+1/2, *z*; (xi) *x*−1/2, *y*−1/2, *z*; (xii) *x*+1/2, −*y*+1/2, *z*−1/2.

D.2 Topology and ball-stick models of the anionic network of $Na_{1.25}Ba_{0.875}Si_3P_5$ and $Na_{31}Ba_5Si_{52}P_{83}$

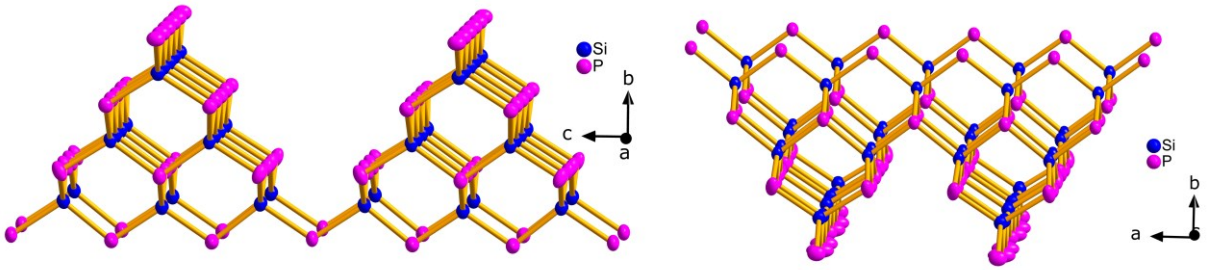

Figure D1 Ball-stick models of T3 supertetrahedra in $Na_{1.25}Ba_{0.875}Si_3P_5$ along the crystallographic *a*- and *c*-axis showing their connectivity by a common vertex (left) and by a common SiP_4 tetrahedron (right). Ellipsoids are drawn with 90 % probability.

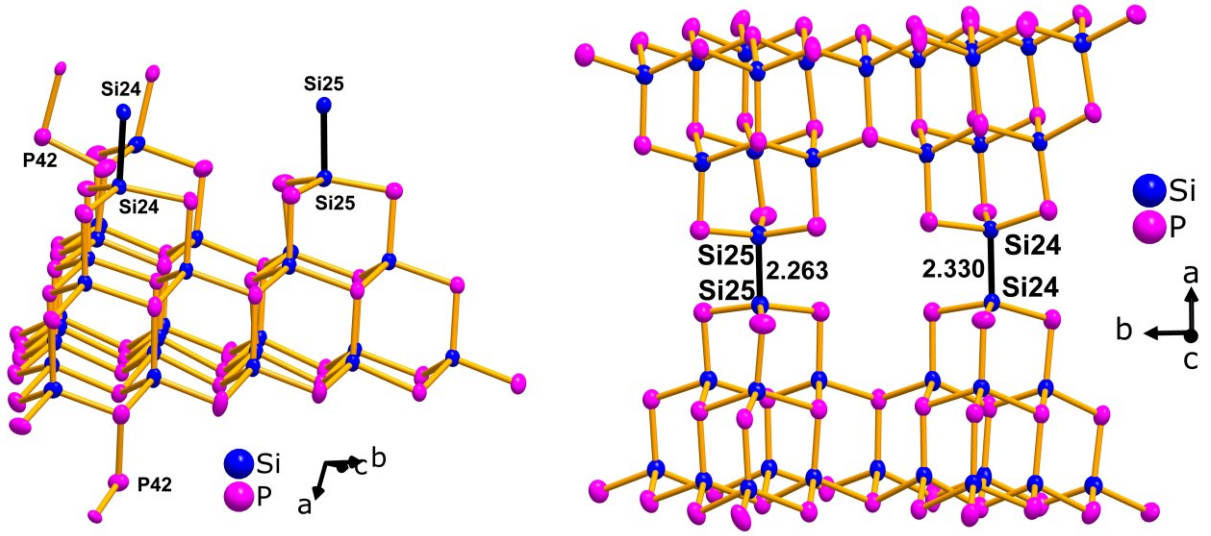

Figure D2 Ball-stick models of T3 supertetrahedra in $Na_{31}Ba_5Si_{52}P_{83}$ showing their connectivity by common SiP_4 tetrahedra to defect T5 supertetrahedra (left) and the condensation to a three dimensional anionic network by homonuclear silicon bonds (right). Ellipsoids are drawn with 90 % probability and the homonuclear silicon bonds are depicted in black.

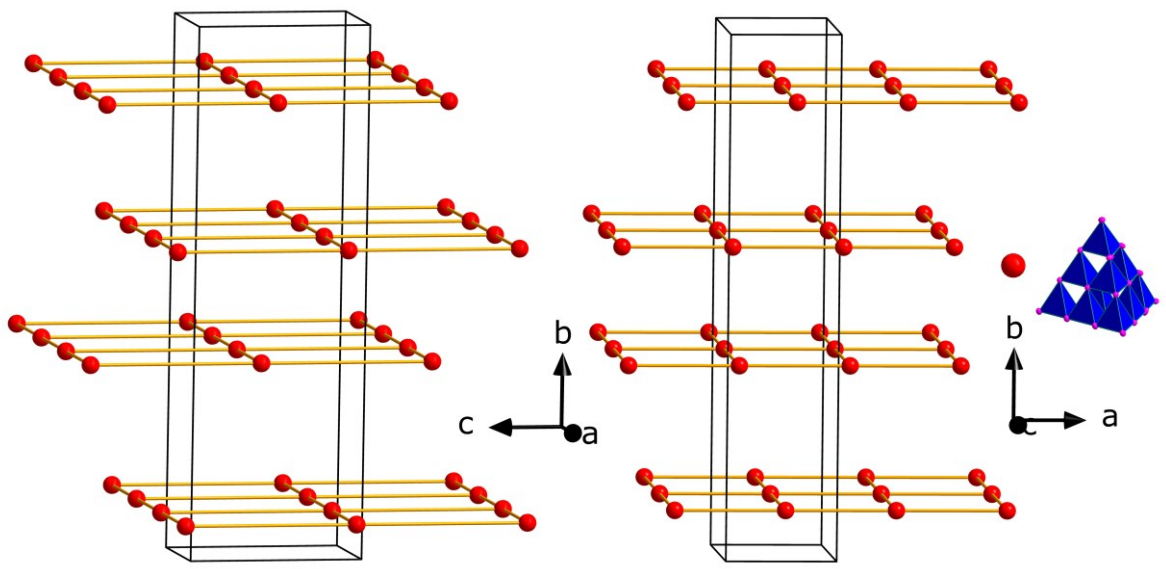

Figure D3 Topology of the anionic sheets in $Na_{1.25}Ba_{0.875}Si_3P_5$, which can be assigned to distorted sql-nets. Every red position corresponds to a T3 supertetrahedron. The distortion arises from different condensations of the T3 supertetrahedra either by common vertices or by fusion.

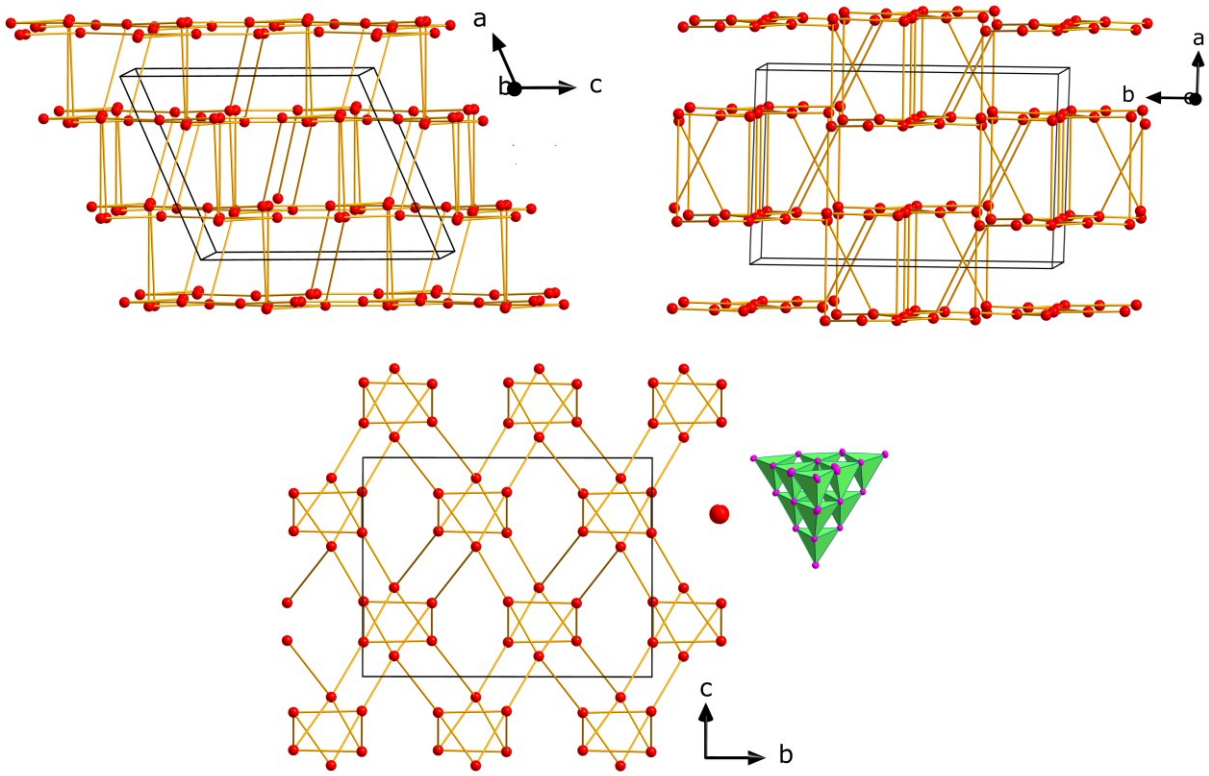

Figure D4 Topology of the anionic 26-nodal network (TD10 = 596) in Na31Ba5Si52P83 in b (left), c (right) and a (bottom) direction. Every red position corresponds to a T3 supertetrahedron either with a SiP4 or a SiP_3Si vertex.

D.3 Powder Diffraction and Rietveld Refinements of $Na_{1.25}Ba_{0.875}Si_3P_5$ and $Na_{31}Ba_5Si_{52}P_{83}$

The preparation of polycristalline samples was conducted in an argon filled glovebox due to the high sensitivity towards air and moisture of the compounds. Respective samples were ground and filled in silica capillaries with a diameter of 0.2 mm and subsequently sealed. The according powder X-ray diffractograms were obtained by using the setup described in the publication for this Supporting Information and the fundamental parameter approach. Based on the structure models of the single-crystal X-ray structure determination and refinement the according powder diffraction patterns were fitted. Therefore, the unit cell parameters were refined as well as the atom positions of barium, silicon and phosphorus with no significant changes. The occupancies derived from the single-crystal refinement were not refined and the peak shapes and background were fitted using pseudo-Voigt and shiftedChebyshev, respectively. For the $Na_{31}Ba_5Si_{52}P_{83}$samples the difference curve revealed a side phase

beside unreacted silicon (1.4 %), which we were able to refine with the single-crystal structure model of $Na_{23}Si_{37}P_{57}$ (9.8 %). The according results are compiled in Table D7.

Table D7 Crystallographic data of powder Rietveld refinements of $Na_{1.25}Ba_{0.875}Si_3P_5$ and $Na_{31}Ba_5Si_{52}P_{83}$.

Formula	**$Na_{1.25}Ba_{0.875}Si_3P_5$**	**$Na_{31}Ba_5Si_{52}P_{83}$**
Space group	*Cmcm* (No. 63)	*C*2/*c* (No. 15)
a / Å	7.1682(2)	21.279(1)
b / Å	34.158(2)	30.688(2)
c / Å	11.0886(3)	25.341(1)
β / °	90	113.559(5)
V_{cell} / Å³	2715.1(2)	15168(2)
$\rho_{X\text{-}ray}$ / g·cm^{-1}	2.733(5)	2.3751(2)
Diffractometer	Stoe Stadi P	
Radiation	Mo-Kα1 (λ = 0.709319 Å)	
Detector	Mythen 1K	
Monochromator	Ge(111)	
2Θ - range / °	2.000 – 55.940	1.000 - 57.145
Data points	3597	3744
Background function	Shifted Chebyshev	
Refined parameters (background parameters)	48 (18)	234 (20)
GooF	3.302	3.019
R_p; R_{wp}	0.040; 0.053	0.033; 0.044
R_{exp}; R_{Bragg}	0.016; 0.027	0.014; 0.012

D.4 Elemental Analysis of $Na_{1.25}Ba_{0.875}Si_3P_5$ and $Na_{31}Ba_5Si_{52}P_{83}$

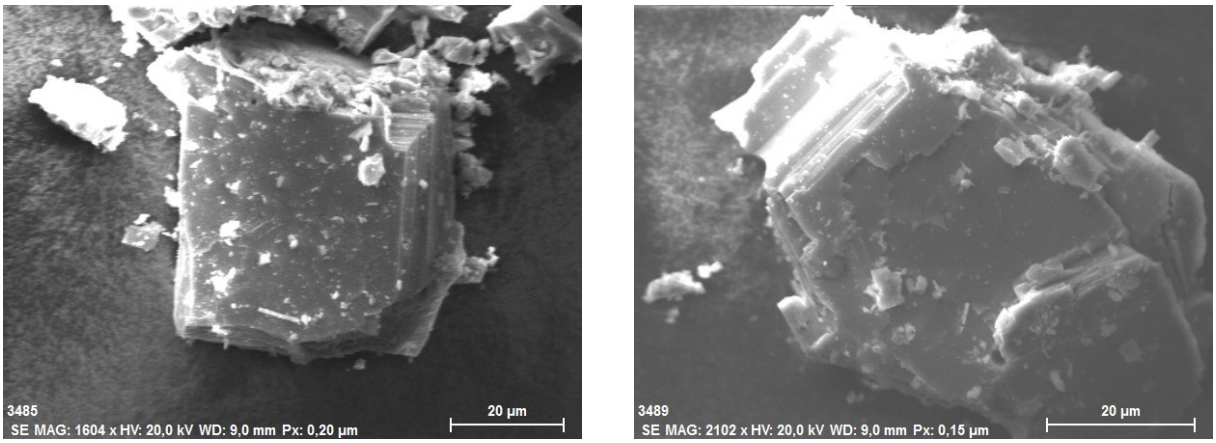

Figure D5 Representative scanning electron microscopic photographs of $Na_{1.25}Ba_{0.875}Si_3P_5$.

Table D8 Elemental analysis by EDX of $Na_{1.25}Ba_{0.875}Si_3P_5$, signals of oxygen were not taken into account due to hydrolysis.

	Na	**Ba**	**Si**	**P**
EDX point 1 / atom-%	13.09	8.35	26.52	52.04
EDX point 2 / atom-%	12.49	9.28	26.48	51.75
EDX point 3 / atom-%	12.85	9.73	26.42	51.00
EDX point 4 / atom-%	12.51	9.45	26.49	51.55
EDX point 5 / atom-%	12.26	8.28	26.78	52.68
EDX point 6 / atom-%	12.55	8.08	26.96	52.41
EDX point 7 / atom-%	12.15	9.14	26.86	51.85
EDX point 8 / atom-%	12.38	9.48	26.65	51.48
EDX point 9 / atom-%	12.25	9.28	26.79	51.68
EDX point 10 / atom-%	12.28	8.65	26.81	52.27
EDX point 11 / atom-%	11.47	8.78	27.04	52.70
EDX point 12 / atom-%	12.05	8.01	27.18	52.76
EDX point 13 / atom-%	10.11	8.73	28.91	52.24
EDX point 14 / atom-%	13.08	9.18	26.49	51.25
EDX point 15 / atom-%	12.24	9.53	26.23	52.00
Average / atom-%	**12.25**	**8.93**	**26.84**	**51.98**
Calculated / atom-%	**12.4**	**8.6**	**29.6**	**49.4**

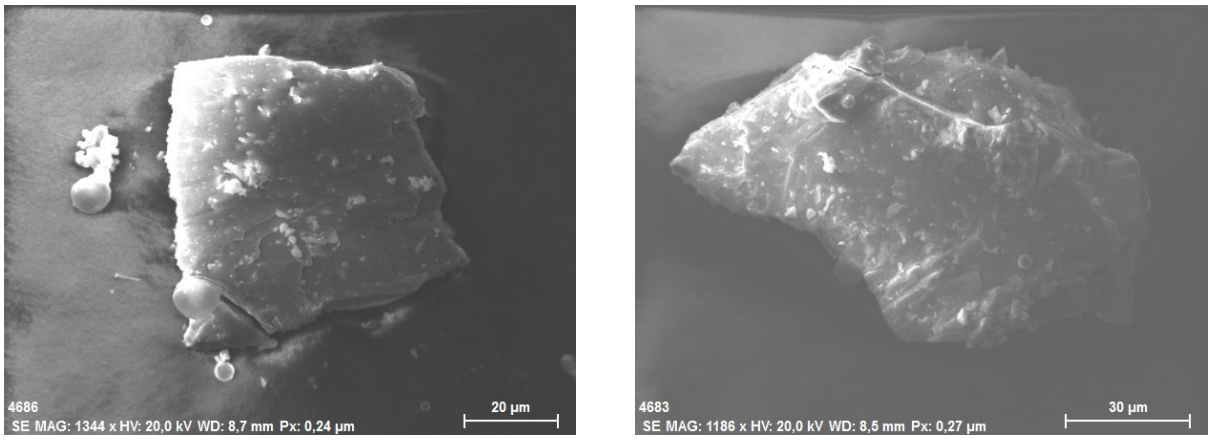

Figure D6 Representative scanning electron microscopic photographs of $Na_{31}Ba_5Si_{52}P_{83}$.

Table D9 Elemental analysis by EDX of $Na_{31}Ba_5Si_{52}P_{83}$, signals of oxygen were not taken into account due to hydrolysis.

	Na	**Ba**	**Si**	**P**
EDX point 1 / atom-%	17.27	3.56	27.54	51.64
EDX point 2 / atom-%	18.81	3.54	26.51	51.14
EDX point 3 / atom-%	18.69	3.42	26.09	51.80
EDX point 4 / atom-%	18.35	3.76	26.79	51.10
EDX point 5 / atom-%	18.21	2.85	26.42	52.52
EDX point 6 / atom-%	19.48	3.81	26.03	50.69
EDX point 7 / atom-%	17.92	3.41	26.87	51.80
EDX point 8 / atom-%	18.22	3.15	26.29	52.34
EDX point 9 / atom-%	15.64	3.24	28.65	52.47
EDX point 10 / atom-%	17.99	3.45	26.59	51.97
EDX point 11 / atom-%	17.51	3.28	27.71	51.51
EDX point 12 / atom-%	17.62	3.61	28.83	49.94
EDX point 13 / atom-%	15.56	3.52	29.52	51.40
EDX point 14 / atom-%	20.53	3.30	24.25	51.92
EDX point 15 / atom-%	18.44	3.24	27.02	51.31
Average / atom-%	**18.0**	**3.4**	**27.0**	**51.6**
Calculated / atom-%	**18.13**	**2.92**	**30.41**	**48.54**

D.5 Geometrical Sodium Pathway Analysis for $Na_{31}Ba_5Si_{52}P_{83}$

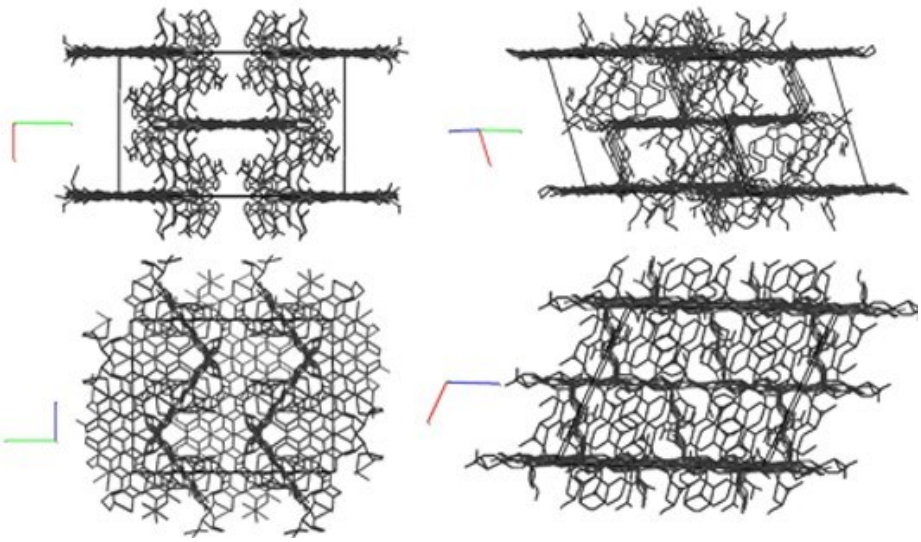

Figure D7 Geometrically calculated possible sodium migration paths for $Na_{31}Ba_5Si_{52}P_{83}$. Wide channels along *c* are formed which are connected by narrow and short passages along the T3 faces assuming predominantly one-dimensional sodium ion conduction.

D.6 T_1-relaxometry of $Na_{31}Ba_5Si_{52}P_{83}$

To obtain the ^{23}Na-NMR spin-lattice relaxation time (T_1) at different temperatures, the saturation recovery technique was used. For an estimate of the activation energies, the characteristic correlation times τ_c of the dynamic processes causing the spin relaxation are assumed to follow an Arrhenius type of behavior with activation energy E_A:

$$\tau_c = \tau_0 \exp\left(\frac{E_A}{k_B T}\right)$$

In the so-called low-temperature regime ($\omega_0\tau_c >> 1$), the relaxation rate $1/T_1$ for a single dynamic process is given by the following form, which can be linearized and fitted to extract the activation energy:

$$R_1 = \frac{1}{T_1} = \frac{4}{3} G(0) \frac{1}{\omega_0^2 \tau_0} \exp\left(-\frac{E_A}{k_B T}\right)$$

For a single dynamic process, the integrated signal intensities are expected to follow a mono-exponential function. As may be seen from Figure D8 (left), using a mono-exponential does not lead to a good fit for

$Na_{31}Ba_5Si_{52}P_{83}$. In contrast, a bi-exponential fit describes the data much better, see Figure D8 (right). The existence of a second exponential function implies the presence of at least one more dynamic process on a much slower time scale. From the M_0 values returned by the bi-exponential fit it may be seen that slow process constitutes the minority component of the signal by a factor of about one quarter. Therefore, this process could be due to sodium ions in the side phase or related to non-mobile or slow moving sodium in the target structure.

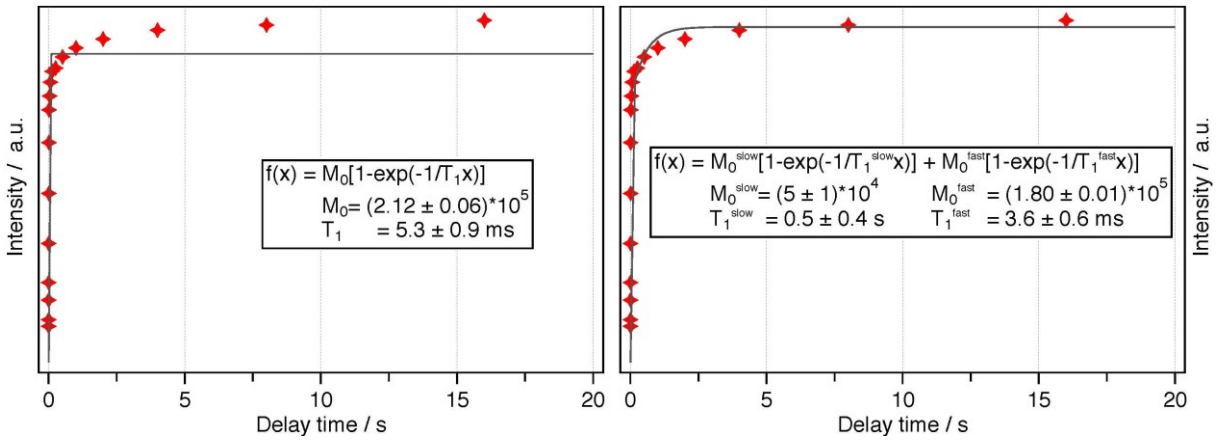

Figure D8 ^{23}Na-NMR spin-lattice relaxation time (T_1) data for $Na_{31}Ba_5Si_{52}P_{83}$ at 274K. The integrated signal intensities were fitted with either a mono-exponential (left) or bi-exponential (right) function.

E Appendix – Miscellaneous

E.1 List of Publications

The following list comprises all publications within this thesis.

1. **Supertetrahedral Networks and Lithium-Ion Mobility in Li_2SiP_2 and LSi_2P_3**

   Arthur Haffner, Thomas Bräuniger, Dirk Johrendt

   published in: *Angew. Chem. Int. Ed.* **2016**, *55*, 13585.

   For this publication, the synthesis, sample preparation, EDX measurements, single-crystal and powder X-ray diffraction of the title compounds were performed by Arthur Haffner. NMR measurements were done by Christian Minke and Thomas Bräuniger. The manuscript was written in equal parts by Arthur Haffner, Thomas Bräuniger, and Dirk Johrendt.

2. **Fast Sodium-Ion Conductivity in Supertetrahedral Phosphidosilicates**

   Arthur Haffner, Anna-Katharina Hatz, Igor Moudrakovski, Battina V. Lotsch, Dirk Johrendt

   published in: *Angew. Chem. Int. Ed.* **2018**, *57*, 6155.

   For this publication, the synthesis, sample preparation, EDX measurements, single-crystal and powder X-ray diffraction of the title compounds were performed by Arthur Haffner. Electrical measurements and their analyses were done by Anna-Katharina Hatz. Christian Minke performed the NMR measurements and Igor Moudrakovski conducted the temperature dependent NMR measurements. The manuscript was written in equal parts by Arthur Haffner, Anna-Katharina Hatz, Bettina V. Lotsch, and Dirk Johrendt.

3. **Synthesis and Structure of the Sodium Phosphidosilicate Na_2SiP_2**

   Arthur Haffner, Anna-Katharina Hatz, Constantin Hoch, Battina V. Lotsch, Dirk Johrendt

   published in: *Eur. J. Inorg. Chem.* **2020**, 617.

   For this publication, the synthesis, sample preparation, single-crystal and powder X-ray diffraction of the title compound were performed by Arthur Haffner. Electrical measurements and their analyses were done by Anna-Katharina Hatz. Constantin Hoch contributed crystallographic discussions and reviewed the structure elucidation. NMR Measurements were conducted by Christian Minke and Otto E. O. Zeman assisted with interpretation of NMR spectra. The manuscript was written in equal parts by Arthur Haffner, Anna-Katharina Hatz, and Dirk Johrendt.

4. Polymorphism and Fast Potassium-Ion Conduction in the T5 Supertetrahedral Phosphidosilicate KSi_2P_3

Arthur Haffner, Anna-Katharina Hatz, Otto E. O. Zeman, Constantin Hoch, Bettina V. Lotsch, Dirk Johrendt

published in: *Angew. Chem. Int. Ed.* **2021**, *60*, 13641.

For this publication, the synthesis, EDX measurements, sample preparation, single-crystal and powder X-ray diffraction of the title compound were performed by Arthur Haffner. Electrical measurements and their analyses were done by Anna-Katharina Hatz. NMR measurements were performed by Christian Minke and Otto E. O. Zeman. Constantin Hoch contributed crystallographic discussions and reviewed the structure elucidation. Bettina V. Lotsch assisted with electrochemical discussions and the review of the manuscript, which was written in equal parts by Arthur Haffner, Anna-Katharina Hatz, and Dirk Johrendt.

5. The Phosphidosilicates $SrSi_7P_{10}$ and $BaSi_7P_{10}$

Arthur Haffner, Valentin Weippert, Dirk Johrendt

published in: *Z. Anorg. Allg. Chem.* **2021**, *647*, 326.

For this publication, the synthesis, sample preparation, EDX measurements, single-crystal and powder X-ray diffraction of the title compounds were performed by Arthur Haffner with assistance of Valentin Weippert. NMR spectra were recorded by Christian Minke and the theoretical calculations were conducted by Dirk Johrendt. The manuscript was written in equal parts by all authors.

6. Synthesis, Crystal Structure, and Chemical Bonding of Ba_2SiP_4

Arthur Haffner, Dirk Johrendt

published in: *Z. Anorg. Allg. Chem.* **2017**, *643*, 1717.

For this publication, the synthesis, sample preparation, EDX measurements, single-crystal and powder X-ray diffraction of the title compounds were performed by Arthur Haffner. NMR spectra were recorded by Christian Minke and the theoretical calculations were conducted by Dirk Johrendt. The manuscript was written in equal parts by both authors.

7. **Polymorphism of Ba_2SiP_4**

   Arthur Haffner, Valentin Weippert, Dirk Johrendt

   published in: *Z. Anorg. Allg. Chem.* **2020**, *646*, 120.

   For this publication, the synthesis, sample preparation, EDX measurements, single-crystal and powder X-ray diffraction of the title compounds were performed by Arthur Haffner with assistance of Valentin Weippert. NMR spectra were recorded by Christian Minke and the theoretical calculations were conducted by Dirk Johrendt. The manuscript was written in equal parts by all authors.

8. **Exotic Supertetrahedral Anions in the Silicates $Na_{1.25}Ba_{0.875}Si_3P_5$ and $Na_{16}Ba_{2.5}Si_{26}P_{41}$**

   Arthur Haffner, Otto E. O. Zeman, Thomas Bräuniger, Dirk Johrendt

   published in: *Dalton Trans.* **2021**, DOI: 10.1039/D1DT01234G

   For this publication, the synthesis, sample preparation, EDX measurements, single-crystal and powder X-ray diffraction of the title compounds were performed by Arthur Haffner. NMR spectra were recorded by Christian Minke, Otto E. O. Zeman, and Thomas Bräuniger. Otto E. O. Zeman and Thomas Bräuniger assisted with the interpretation of these spectra. The manuscript was written in equal parts by all authors.

E.2 Publications beyond this Thesis

The following list comprises all publications with scientific contribution excluding this thesis

1. **Supertetrahedral Layers Based on GaAs and InAs**

   Valentin Weippert, **Arthur Haffner**, Alexis Stamatopoulos, Dirk Johrendt

   published in: *J. Am. Chem. Soc.* **2019**, *141*, 11245.

2. **Preparation of Iron(IV) Nitridoferrate Ca_4FeN_4 through Azide-Mediated Oxidation under High-Pressure Conditions**

   Simon D. Kloß, **Arthur Haffner**, Pascal Manuel, Masato Goto, Yuichi Shimakawa, J. Paul Attfield

   published in: *Nature Commun.* **2021**, *12*, 571.

3. **New Layered Supertetrahedral Compounds T2-*M*SiAs$_2$, T3-*M*GaSiAs$_3$ and polytypic T4-*M*$_4$Ga$_5$SiAs$_9$ (M = Sr; Eu)**

   Valentin Weippert, **Arthur Haffner**, Dirk Johrendt

   published in: *Z. Naturforsch.* **2020**, *75*, 983.

E.3 Deposited Crystallographic Data

Single-crystal structures of the compounds contained in this dissertation are deposited as crystallographic information files (CIF) at the Fachinformationszentrum (FIZ) in Karlsruhe or the Cambridge Crystallographic Data Centre and can be obtained by quoting the corresponding CSD or CCDC deposition number given in Table E.1.

Table E1: Results of DC galvanostatic polarization measurements including ionic transference number and upper limit of electronic conductivity.

Compound	CSD-Number	CCDC-Number
Li_2SiP_2	431573	
$LiSi_2P_3$	431584	
$Na_{19}Si_{13}P_{25}$		1816421
$Na_{23}Si_{19}P_{33}$		1816422
$Na_{23}Si_{28}P_{45}$		1816423
$Na_{23}Si_{37}P_{57}$		1816420
LT-$NaSi_2P_3$		1816424
HT-$NaSi_2P_3$		1816425
Na_2SiP_2		1946908
KSi_2P_3-*tl*960		2058594
$SrSi_7P_{10}$	2022066	
$BaSi_7P_{10}$	2022067	
Ba_2SiP_4-*tl*28	433493	
Ba_2SiP_4-*oP*56		1946350
$Na_{1.25}Ba_{0.875}Si_3P_5$		2076577
$Na_{31}Ba_5Si_{52}P_{83}$		2076578